THÈSE

En vue de l'obtention du

DOCTORAT DE L'UNIVERSITÉ DE TOULOUSE

Délivré par :

Institut National Polytechnique de Toulouse (INP Toulouse)

Discipline ou spécialité :

Dynamique des fluides

Présentée et soutenue par :

M. LUIS MIGUEL SEGUI TROTH

le mardi 14 novembre 2017

Titre :

Multiphysics coupled simulations of gas turbines

Ecole doctorale :

Mécanique, Energétique, Génie civil, Procédés (MEGeP)

Unité de recherche :

Centre Européen de Recherche et Formation Avancées en Calcul Scientifique (CERFACS)

Directeur(s) de Thèse :

M. LAURENT GICQUEL

Rapporteurs :

M. EDWIN VAN DER WEIDE, UNIV. TWENTE ENSCHEDE PAYS-BAS

M. GUILLAUME HOUZEAUX, BARCELONA SUPERCOMPUTING CENTER

Membre(s) du jury :

M. NICOLAS GOURDAIN, ISAE-SUPAERO, Président

M. FRANCK NICOUD, UNIVERSITE DE MONTPELLIER, Membre

M. LAURENT GICQUEL, CERFACS, Membre

Mme KARINE TRUFFIN, IFPEN, Membre

M. TONY ARTS, VON KARMAN INSTITUTE RHODE SAINT GENESE, Membre

Acknowledgements

I would like to start thanking the members of the Jury for accepting to evaluate my work and for their time to review the manuscript. Their comments and punctualizations have helped to improve the quality of the manuscript and also provided paths to follow in the future.

I cannot neglect the importance of the Marie Curie Project *COPA-GT* that allowed me to come to CERFACS in the first place. The financial support from the European Union changed my life by granting me the chance of coming to France and joining such an incredible team.

More specifically, a special thank you goes to my supervisors Laurent and Florent for their support and help from the first day. We encountered a tough subject but after hard work from all parts, I want to think we have managed to put another stone towards the improvement of numerical schemes and to the understanding of turbine blade flows. Their contribution was not only limited to these topics but also to other soft skills and their insistence to believe in myself; something that I am still working on.

This thesis would not be the same without the contribution from Guillaume and Julien to the numerical part. Thank you for your time on a subject that did not concern you directly, for your patience and time for discussions that were so fruitful but also enjoyable.

Also, a great contributor to this thesis has been Jérôme. Many discussions concerning a large variety of themes have taken place during these years and have proven to be very useful. I don't think I can mention all of them so I'll just say that they were a lot.

Of course, I cannot forget the whole permanent CFD (and COOP) team of CERFACS, led so well by Thierry. I have had the opportunity to interact with the whole team (Benedicte, Olivier, Gab, Eléonore, Jérôme, Antony and Antoine) during or after the PhD. Also to the 'externals' such as Franck and Stéphane who helped me both before and during the PhD.

To all the administration team, it has been great to share the corridors of the first floor with you that were always full of laughter which translated into a great atmosphere. Nothing would be the same without Chantal, Michèle, Dominique, Marie, Nicole, Brigitte, Lydia...

It is indispensable to mention all the CSG team who are always helpful in the moments of greatest need (something that happens quite often). Their patience and knowledge is without doubt one of the most important assets of the whole group.

I had the opportunity to coincide with many PhD students and PostDocs with which I had not only the luck to work with but also to spend time outside our offices. Both to the ones who were already here when I arrived (Dimitris, Ignacio, Corentin, Lucas, Laure, Manqi...) and to those who I met after (Pierre, Omar, Dario, Luc, Franchine, Félix, Lulu, Nico, Mélissa, Majd, Romain, Pamphile...). A special mention goes to Francis and Thomas whom I had the luck to share the office with. To all members of the EAC: I'm sure this next season will be better than the last, we just need to keep recruiting!

To all my friends from Tenerife, Seville and Toulouse who have understood the difficulty behind what I was confronting and weren't too hard on me when I turned down a beer because I had to work. We will have more time now.

Finally, I want to thank my family for their support during so many years. To my parents for their patience and continuous support even in the distance and on days when my temper wasn't the best. To my brother, I'm sorry to have been so hard during our math lessons when we were younger. I really am trying to improve this last part now that Olivia is here.

Lidia, thank you for your unconditional help and encouragement; this thesis is also yours.

You are part of my small family, which has grown in number during the last years, and I would like to say I'm sorry for all the hours I've spent in front of a computer. From now on I just want to enjoy what comes next beside you and Olivia.

Let's get down to business.

La inspiración existe, pero tiene que encontrarte trabajando.

Pablo Picasso

To my family

Contents

List of Figures

List of Tables

Nomenclature

Δ	Filter width
Δ_x	Cell length in x direction, m
λ	Wavelength, m
λ_t	Thermal diffusivity, W/(m.K)
$\mathbb{R}_{\Omega_j}$	Cell-based residual
$\mathbf{U}$	Conservative variables vector
ν	Kinematic viscosity, m^2/s
ν_τ	Turbulent viscosity, m^2/s
ϕ_i	Shape functions
ρ	Density, kg/m^3
τ_w	Wall shear stress, Pa
$\vec{\mathcal{F}}^C$	Convective fluxes
$\vec{\mathcal{F}}^V$	Viscous fluxes
$D^k_{\Omega_j}$	Distribution Matrix
f	Frequency, Hz
H	Total enthalpy
K	Von Karman constant
L	Length, m
M_{is}	Isentropic Mach number
p	Pressure, Pa
P_t	Total pressure, Pa
r	Mixture gas constant, J/(kg.K)

Re	Reynolds number
T	Temperature, K
t	Time, sec
T_t	Total temperature, K
TKE	Turbulent kinetic energy, J
Tu	Turbulence Intensity
V_{Ω_j}	Cell volume
x^+	Non-dimensional streamwise distance
y^+	Non-dimensional wall-normal distance
z^+	Non-dimensional spanwise distance
(U)RANS	(Unsteady) Reynolds Averaged Navier-Stokes
CFD	Computational Fluid Dynamics
CFL	Courant-Friedrichs-Lewy number
DNS	Direct Numerical Simulations
FFT	Fast Fourier Transform
GT	Gas Turbines
HPT	High-Pressure Turbine
LES	Large Eddy Simulation
NSCBC	Navier-Stokes Characteristic Boundary Conditions
PSD	Power Spectral Density
R	Radius, m
RMS	Root Mean Square
SGS	Sub-Grid Scale
TTG	Two-step Taylor Galerkin

Chapter 1

General introduction

Contents

1.1 CFD, how did we get here?

To understand the development of humanity up to its present state, it would be difficult to contextualize the world as in 2017 without talking about Fluid Mechanics. Transport in ancient and current societies, energy transformation for common use or even developments in biomedical research would not be possible without fluids. Fundamental of Fluid Mechanics started with the hydrostatic theory, a contribution that is known to the non-specialized public such as Archimedes' principle. The principle implies an incompressible fluid, an acceptable hypothesis for liquids, and allowed to develop architectural elements such as aqueducts or cisterns but also to explain the buoyant forces that keep a boat afloat. Likewise, to understand the atmosphere that surrounds the planet, it is necessary to balance the different forces applied to the air and the different pressures encountered in each layer. This is now known thanks to the contribution of Pascal who introduced the concept of hydrostatic pressure. This same principle can be extended to many other fields such as biomechanics where equilibrium processes take place in the body of any human being. In short, many engineering applications rely on the most basic principles of fluids without even introducing the applications of fluid dynamics.

Of course, one might be tempted to think that considering the large space of time since the first developments done over more than 2000 years, the basics are today well understood. The problem of fluids is that even with all the powerful tools available today, predicting how a flow will establish still remains the greatest unresolved problem of classical physics. The ideal would be to find a general model capable of predicting the behaviour of any type of flow and solve it for each particular case. The first step in itself, although achieved in the context of Newtonian fluids, was not at all trivial and it took many centuries to be able to define the problem to

be solved. The validity of this model, represented by a set of equations, is currently one of the Seven Problems of the Millennium of the Clay Institute that questions the existence of the solutions and their unicity. However and despite the lack of such validation or demonstration, these equations are currently being heavily used and are the starting point of anybody willing to study flows in a Computational Fluid Dynamics (CFD) context.

Historically, the governing equations at hand are the today well-known set of Navier-Stokes equations, named after both Claude Navier and George Stokes. Their individual contributions were to introduce respectively, the viscous transport equations for an incompressible fluid and its extension to compressible fluids [14] responsible for the shear stress or heat transfer effects. Not mentioned explicitly, the reader may note that there is a loop in the process as only the viscous part of the equations is mentioned and so, an inviscid part must also exist. Due to the great number of publications and theorems already assigned to his name, Leonhard Euler is mentioned only for the inviscid part of the equations.

Many applications of these equations were found during the 19th Century and solutions to specific problems of interest were developed. To mention some, the solution to a laminar channel done by Poiseuille, or Reynolds, who determined that different flows could be classified depending on the ratio of inertial forces to viscous forces. Additionally, Reynolds introduced the idea of separating a mean component and a fluctuating component for a turbulent flow, leading to a Reynolds-average way of dealing with turbulence. The resolution of such complex problems required a reasonable hypothesis in each case, and thus, a limited applicability of the solution. From a physical point of view, it was important for the understanding of certain principles that although still not well mastered, set a ground for the study of many engineering applications such as turbomachines. From a mathematical point of view however, developments did not advance as fast as in the coming 20th century. One of the reasons for these mathematical difficulties can be found in the nature of the equations.

The equations are written in terms of partial derivatives and some of the shortcomings of the methodologies developed until the 20th century were in part due to the lack of techniques to solve Partial Differential Equations (PDE). These relate to the the inability to find a mathematical functional space for an adequate solution to the problem. Indeed, although infinitesimal calculus had been developed by notable mathematicians such as Newton or Leibniz, applications to this field were not found until many centuries later. The realization that the continuous equations could not be solved resurfaced the possibility to study them in a discrete way through numerical schemes or algebraic relationships. In that respect, contributions by Banach and Sobolev to functional analysis [27] and their future application to Finite Elements, were fundamental to a larger variety of spatial discretization techniques.

In terms of developments and associated interest from industry, one can easily identify the presence of an inflection point in the resolution of the system of equations' history; before and after World War II. There is a general consensus that the first work in the context of what today is known as CFD was published by Richardson [149] and consisted in solving the Laplace equation using a relaxation technique. Another important achievement before this period was done by Lewy et al. [108] who defined one of the stability requirements for the resolution schemes.

The definition of the CFL number, known to any CFD practitioner, is due to this paper. Other contributions were done by Lax [103] who stated the theorem that produces the sufficient conditions of *consistency* and *stability* to guarantee the convergence of the discretization. The stability of the different methods was then continued by von Neumann and Richtmeyer in [188] who developed a methodology capable of determining the stability of the scheme under certain hypotheses.

Nowadays, past World War II progress still remains the panorama as no numerical scheme has yet managed to impose itself over others. And it is still in continuous development as the problems to be solved become more and more complex. Classical methods for spatial discretizations such as Finite Differences, Finite Elements or Finite Volumes coupled with a time integration scheme are nowadays used regularly, as well as other methods such as the multi-grid approach. More recent methods such as Spectral schemes [195] or Lattice-Boltzmann [77] are increasing their presence in publications. The current tendency is to increase the order of the scheme, meaning that a higher accuracy is attained for the same number of degrees of freedom, compensated of course by a larger number of operations. However, there is a limit to these developments which introduces significant difficulties. This was found thanks to Godunov [70] who published in his thesis the theorem that carries his name. He stated that a scheme of order equal or higher than two is non-monotonic. This affirmation is a strong one as it requires for practically all type of schemes to introduce flux limiters or to suffer the consequences, namely the node-to-node oscillations, a deadbeat and purely numerical artifact.

While computers might seem the sine qua non of CFD as explicitly noted in its name, initial computations such as the ones done by Richardson [149] were not performed by a machine. It was after the war that developments in the military industry led to more powerful tools for the resolution of repetitive tasks. The classical Turing machines started to literally fill laboratories and Universities, see Fig. 1.1. Some of the most convinced precursors of machine-resolved task resolution were some of the great names in CFD, von Neumann and Lax. The arrival of machines capable of solving costly operations for humans increased the interest in this discipline. This induced the growth in the number of publications focusing on numerical simulations, but also the number of groups developing new mathematical methods and applying them to problems of industrial interest. The main initial issue from a coding point of view at the time was the difficulty of implementing the desired code and worst of all, the portability of this code for future machines. This issue might once again be of relevance as in recent years, the existence of GPU architectures or even quantum machines have shown their power and possible advantages. The exploitation of these machines seems to be the future and requires to adapt most codes to these new systems.

In any case, the future of scientific computing seems guaranteed and so, the continuous development of tools and results that may one day be of use.

Figure 1.1: IBM computer in 1955, capable of performing 3750 operations per second. Total memory of approximately 10 kbytes.

1.2 Industrial interest for CFD

The rate of development of CFD has been greatly impacted by industrial needs. Developments in CFD required an investment that industry could provide while industry required means to reduce their costs using improved or complimentary methods to the traditional experimental procedures. This process is still taking place today because many tasks may not be put in place using industrial configurations, or at least not as regularly as required at an assumable cost. Industrial applications represent a challenge both in terms of geometry and flow physics. Geometrical difficulties arise as a result of the global optimization process leading to curved shapes which are difficult to represent. Flow physics are also a problem as highly turbulent flows are encountered in most of these industrial configurations. Higher levels of turbulence require more computational power and it was clear from the beginning to the precursors of CFD that computational power available at the time would inevitably limit the industrial applications. To circumvent this limit, the development of turbulence models appeared and contributions from Spalding [174] with the k-ϵ model allowed to address turbulent flows. The model used at the time is still widely applied today and many variants have been developed since its first appearance [122].

In term of process and effective use of CFD by industry, one has to realize that in the aeronautical industry, the first complete aircraft simulations were performed using potential flow theory in the 60-70s. Euler equations were then successfully applied in the following decade to a whole aircraft configuration. The optimization process did not start until the decade 90-00 using Euler equations, the Navier-Stokes equations being applied in the past decade [88] for the whole aircraft, see Fig. 1.2. Note that qualifying the simulation of a complete aircraft does not mean taking into account all of its components. In fact, most of the time the use of CFD is more or less frequent depending on the difficulty to capture the physics around the targeted domain and its relevance to the overall design process. For example, the ventilation system is important for the cooling of components and optimal comfort of passengers but of great difficulty to model due to all the possible sub-components of an aircraft present in a large configuration. This being

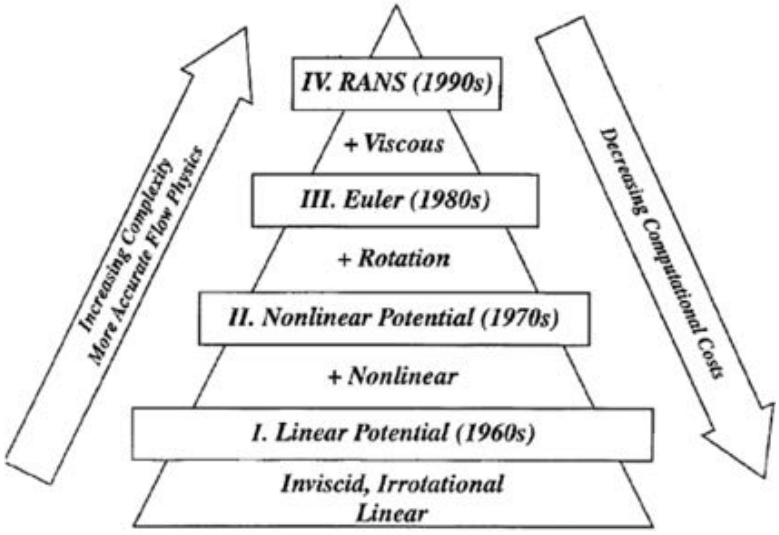

Figure 1.2: Evolution of equations solved for similar problems throughout the years [83].

the case, use of CFD for this specific problem has been largely neglected until recently. Fuselage design or performance envelopes on the other hand have always been targeted since the gain in optimization is much more important. Today, it is possible to model complete aircrafts or cars but difficulties are still present when simulating vortex dominated transitional flows. This is the case for internal engine aerodynamics. Unsteady effects however govern most processes in a flow and turbulence models are in most cases insufficient for the correct prediction of the associated physics. It seems however clear to most of the community that the correct representation of these unsteady effects is critical to the manufacturers to produce better products.

To this end, it is necessary to have a solver as well as the means to perform these simulations and the expertise required to analyze the results. Generally, CFD codes are not developed by the industry that uses them. If the problem is a multiphysics problem, it could be necessary to acquire multiple codes. In fact, each CFD code depending on its numerical approach inherently limits the range of problems it will be optimal for. The existence of dedicated codes for each discipline is hence common.

The appearance of the first CFD general-purpose code was *PHOENICS*, contemporary to one of the best-known commercial software that appeared a few years later and named *FLUENT*. Although the existence of solvers alone does not guarantee a sufficient basis for adequate CFD simulations, pre-processing and post-processing softwares are also required to create the necessary meshes and to be able to analyze the results. Large editors such as *ANSYS* provide the whole chain so it is a good option for many good manufacturers. The existence of such an offer could seem discouraging for smaller research groups to find their place in the industry market. However, future trends are always pursued by research groups, public or private, and remains their strength. It has been said that unsteady effects contribute largely to flows and Large Eddy Simulation (LES) is an alternative turbulence modeling approach to Reynolds-Averaged Navier Stokes (RANS), one that is feasible for industry in the coming years. The

gain behind this new approach is that modeling is reduced and more degrees of freedom are used, the fluid being treated as a fully dynamic and unsteady system. This different formalism usually requires different schemes and so, a completely different code. Additionally, LES requires an expertise that can be found in research groups and not so often in industry as the use of this methodology is still not common. Even with larger computers, a great effort must still be done to increase the efficiency and the applicability range for industry, namely through code parallelism. The access to this type of supercomputers is also an issue and although research groups are granted access to a large volume of CPU hours provided by national governments for research means, industrial partners must pay these accesses. This gives an edge to research departments to gain expertise that is then published and applied in future configurations coming from industry.

The industrial configurations of interest are here limited to gas turbines for the following. The interest of this thesis focuses on the possible means to obtain the solutions to the Navier-Stokes equations within the context of gas turbines. The study of gas turbines is bounded by the formalism chosen and corresponds to Large Eddy Simulations (LES) for the present document. There are two main questions to be answered in relation to the output provided by any CFD code when performing a gas turbine component simulation. First of all, is the code capable of producing an acceptable prediction of the flow at hand? Many codes *presume* they possess the required properties to be a usable code in industry. Some of these properties are that it is optimally parallelized, that it is portable on a large range of machines or that it contains the latest and most robust numerical methods. This last point is interesting as a perfect comparison between codes and their numerical schemes is never possible, or complicated at the very least, for complex configurations. If however it is assumed that a fair comparison can be done, it is reasonable to ask how well each code behaves when confronted to the complex cases they must solve and for which they were designed and *financed*. The second question relates precisely to the numerical methods behind each simulation: which is the best choice? For this document, the comparison between numerical methods is limited to only one code. Nevertheless, various numerical methods implemented in this same code are compared in simple and in complex configurations. These methods will be notably low-order versus high-order schemes (see Chap. 3) and comparisons to literature results are performed when available.

1.3 Gas Turbines

Gas Turbines (GT) have been used to power aircraft since the 1930s when thrust generating aeroengines were first used. Due to their higher power-to-weight ratio these engines are extensively used either to power aircraft or produce electrical energy in an effective and adaptive way. Aircraft engines are subject to a large range of operating conditions on a daily basis where it must perform safely. From take-off to cruise, from the Andes to the Sahara desert the variability of the atmosphere must not interfere with the performance limits of the aircraft and thereby its engines. This large envelope of operating points introduces difficulties in many aspects including combustion requirements. It is necessary to operate and maintain an efficient but at the same time quiet and 'green' combustion.

Historically, there has been little need for clean combustion requirements, so liability and efficiency have been the main targets of existing aircraft engine designs. Reliability was an easily measured parameter which has mainly been addressed by performing multiple tests for the different modules of the engine. The exercise hence, resumed to finding the best compromise to operate the engine for as long as possible. When dealing with efficiency, it began to be a problem once the aircraft industry started to grow exponentially and fuel reservoirs were no longer considered as infinite. Industry became more competitive and companies began to find out that preservation of their market shares started to be a difficult exercise which forced them to be in continuous evolution, a context where research becomes crucial. At the same time, external agents such as governments or regulation agencies started adding more constraints to the whole process of design and operation. A direct consequence of such a stringent industrial context is that it is no longer possible to produce and test all the thought innovations that might occur within an engineering process. Experience can provide an approximative assessment of a given design but such an intuitive decision making carries either a lot of risks or conversely prevent disruptive and potentially highly efficient solutions. Decision taking is definitely not eased by the flow encountered in such systems which results from the different aspects of the physics in the engine which are highly coupled. Despite this fact, it is still necessary to manufacturers to know which is the most constraining factor for each individual component that will constitute its final product that is the engine.

An aircraft engine works as a whole and so, it must be carefully integrated meaning a careful assembly of all its different components. Each component of a gas turbines has its limitations; in some cases restricted by the aerodynamic loading it is capable of sustaining, some limited by global weight constraints, and others are subject to restrictions given by other components. In the case of high-pressure turbines, the focus of this work, the most limiting factor is bound by the heat transfer due to their proximity to the combustor exit plane [118]. From an efficiency point of view, it is convenient to increment the temperature of the system and so increase the work available for the turbine to extract from the cycle. This temperature thus, represents a critical issue. Material sciences have remained behind in comparison to the evolution rate of other fields. Nickel superalloys seem to have been exploited to the limit for the time being although recent approaches show a promising margin of improvement in Smith et al. [169]. In the meantime, increasing the life span of turbine blades relies mainly on the engineer's capacity to predict the correct temperature and heat flux that the blades are subject to. If done adequately, the key remaining step is to correctly optimize the different cooling systems. In such a context, Computational Fluid Dynamics (CFD) is an ideal tool to complement and even surpass experiments while reducing global costs.

As stated in Sec. 1.2, simulations in this document, including the high-pressure turbine, are done using LES. The final goal is to correctly predict the thermal fields associated to the surface of the blade using a code that is *supposed* to simulate accurately the flow. It will be seen in Part II that one of the main problems associated to the heat transfer coefficient prediction is the capacity of the proposed solution to capture laminar to turbulent transition. Special focus is thus paid to boundary layer turbulence in terms of statistics and visualization.

1.4 Objectives

The objectives of this thesis are to assess LES for turbine flow predictions and to continue the improvement of numerical schemes to ease LES of complex geometries. Towards this goal, the developments are performed in the context of a validated LES solver **AVBP** [161] (developed by CERFACS and IFP-EN). The objective is in fine to assess numerics versus modelling effects on the LES prediction of a turbomachinery flow, all in the context of non-reactive LES. In the majority of simulations the unsteadiness of the flow is a preponderant effect. However, it is necessary to assess that this unsteadiness does not have a numerical origin due to boundary effects or Gibbs type oscillations. In this application, specific interest focuses on the sensitivity of the near wall bounded flows to inflow specifications as well as near wall numerical treatments.

The main objectives of the thesis are hence:

- The study of a complex geometry for various operating points: the LS89 turbine vane [7]. The study of one of the richest databases in turbomachinery and the different operating points is a key element to understand the physics of boundary layer transition around blades, an objective not attained to date for a number of cases of this database by most conventional CFD tools. From the analysis, it is observed that acoustic waves, wake interactions and turbulence in boundary layers are potentially of great importance towards the prediction of the flow pursued during this work.

- The study of current numerical schemes in **AVBP** and their implementation. Special focus is paid to stability issues and prediction methodologies, the influence of physical borders being taken into account through specific developments. The implementation of boundary conditions and the equations behind the numerical scheme closure terms are analyzed and tested. Also, the multi-element context and the meshes encountered in complex configurations are analyzed.

The work is decomposed into the following parts:

Part I

- Chapter 2: Introduction to Modelling and Numerics

  Different turbulence modelling approaches such as Reynolds Averaged Navier-Stokes (RANS), Direct Numerical Simulation (DNS) or Large Eddy Simulation (LES) are detailed, from then on focalising on the LES formalism. Special attention is then devoted to the specific need for modelling in the case of wall-bounded flows where the previous models miss some unsteady effects, the associated necessary grid resolution requirements being discussed. Numerics is then addressed. Various discretizations methods, both spatial and temporal are also seen in this section, distinction being made between the different possible solvers and the way the data stored is addressed. The most used Finite Differences (FD), Finite Elements (FE) or Finite Volumes (FV) spatial discretization methods are described and different methods for time advancement are presented.

- Chapter 3: Numerics of AVBP

  Once the state-of-the art has been presented, the cell-vertex context, its properties and the metrics associated to the approach are first shown. Then for AVBP in particular, both the convective and diffusive schemes are introduced highlighting the importance of each operator used. Time advancement limits and the necessary artificial terms to control possible numerical instabilities are discussed. Finally, boundary conditions are appraised in both a physical and a numerical context.

- Chapter 4: Spectral properties of the AVBP schemes

  The properties of numerical schemes are studied in many different ways and the main methods are presented here. Stability is analyzed to try to determine the origin of numerical instabilities in the present code. A von Neumann analysis is done in both 1D and 2D type elements for the main convective schemes in AVBP. Dissipation and dispersion properties are also available from the Fourier analysis done.

Part II

- Chapter 5: Introduction to LS89 simulations

  First, a brief introduction on the composition and applications of aeroengines is provided with special attention to high-pressure turbine blades. Performance issues stress the importance towards the correct prediction of thermal fields in an unsteady flow. Explicitly in the context of high pressure turbines in academic but realistic operating conditions, the LS89 test case [7] arises as an ideal case for the evaluation of the physical effects observed and their origin, numerical effects included.

- Chapter 6: LES predictions of MUR129 and MUR235

  Two operating points of the LS89 database have been simulated and are analyzed in this section. The physical analysis performed depends on the difficulty to understand the complex flow physics behind each operating point, the effects of turbulence injection, boundary layer interactions or acoustics generated from the wakes are appraised.

- Chapter 7: LS89 Numerical Aspects and associated analyses

  Aside from the aerodynamical response of the flow predictions that are observed to be of great interest, mesh dependency and numerical observations point to the need for an in-depth numerical analysis of the schemes for the specific problem at hand. To do so, an amplification matrix method is implemented due to the impossibility to treat boundary conditions by more conventional methods and tests are performed for its validation. The methodology used to perform such an analysis is general to all types of linearized equations. It is capable of determining the stability in a case-dependent situation at a reasonable cost but proportional to the number of degrees of freedom. Following the applications of such a tool which was not able as of today to analyze bounded numerical instabilities, a series of numerical experiments are performed to demonstrate the importance of a rigorous mathematical formalism. In this case, emphasis is put on boundary closure terms and new mathematical procedures are proposed to close the higher order

terms at boundaries to reduce numerical issues. This discussion led to study the importance of accurate spatial derivatives proposing improvement strategies and directions to alleviate the impact of the observed numeric instabilities.

This thesis was funded by the European Union Project COPA-GT as part of the Marie Sklodovska-Curie Initial Training Networks (ITN). It has also had a strong link with the CN2020 project conducted by the Safran group to impulse the use of LES for turbines by the year 2020.
A list of publications done during this thesis is provided below.

List of publications

- Segui, L., Gicquel, L., Duchaine, F., & de Laborderie, J. (2017). LES of the LS89 cascade: influence of inflow turbulence on the flow predictions. In 12th European Conference on Turbomachinery Fluid dynamics & Thermodynamics, Stockholm, Sweden.
- Roy, P., Segui, L., Jouhaud, J.C. Gicquel, L. Resampling Strategies to Improve Surrogate Model-based Uncertainty Quantification - Application to LES of LS89. Submitted.
- Segui, L., Gicquel, L., Duchaine, F., & de Laborderie, J. (2018). Importance of boundary layer transition in a high-pressure turbine cascade using LES. Submitted to ASME TurboExpo 2018.

Part I

Modelling and Numerics

Daily circumstances of big industrial companies often impose to newcomers or even people with a certain experience in the domain of CFD to simulate complex devices. In fact, your new boss, whatever your engineer's background will have you to rapidly answer the question: " can you do a flow simulation of this 'new engine' that explains this problem as soon as possible?" Assuming your company computing account is active, you know where the coffee machine stands and you have a desk already assigned, the natural next step is to ask yourself *'how shall I perform this task?'* Although a first reflex is to jump onto the geometry definition, mesh generation... and the need for the mastering of the associated softwares and manipulation steps which are very time consuming and require expertise often to be acquired, one should instead wonder if *the code* X, *that one you've heard so much about that is widely used in your company, optimal for this simulation?*. Or even simpler, *is code X capable of performing such a simulation?* Of course, the definition of optimal is not trivial. In most cases such questions never arise because the choice of code might be limited to *the only one available*. Assume now that X is a set. Say there are two codes that are used by your office colleagues, one that has been around for quite a few years but is based on a more classical approach and another that has been developed more recently and is state of the art. Which one to choose? What are the differentiating features between codes that make one *a priori* better than the other? By intuition or experience, the problem identified is here to be linked to a fluid dynamics problem and as discussed in the introduction, not all CFD solutions (if none) is valid for the whole range of known flow physics. Specific tools, modelling and codes are usually the only guarantee for a reliable prediction. You hence need to know what is effectively behind the human friendly interfaces. Imagine now that you are researcher with many years of experience and you must perform a comparison between these two previously mentioned codes. Someone will probably try to convince you that the state of the art code is clearly superior. Or maybe the contrary, that all these new codes are not sufficiently mature to compete with the more classical and tuned approaches which have comprehensively been studied in the literature and have been used over the years in the design process of your new company. An objective way to determine how well all these codes perform is naturally to select a set of test cases and check the predictions' accuracies. What seems clear is that using a code as a 'black box' is likely to blow up on you and this will depend on your understanding of flows, codes and the various difficulties encountered.

The objective of the following chapters of Part I is to provide the necessary background to answer these questions. First, a description of the different options that exist in terms of modelling and resolution approaches is given in Chapter 2. This chapter allows to answer questions such as what features differentiate one approach from another. One must know which are the aspects attention must be paid to, these being the numerical modelling (if necessary) of turbulence, the associated grids used to discretize the domain and the separation of spatial and temporal operators. In chapter 3 focus is set upon a single code, AVBP, and a comprehensive description of the operators, as well as specific aspects associated to the control volumes where the equations that are solved are detailed. Finally, in Chapter 4 answers are provided for the properties that characterize the methods used in AVBP in particular. Only when all of these aspects have been addressed is it possible to move on to more complicated problems such as positioning a code, AVBP, with respect to others in a content of a series of complex test cases a subject that is left to Part II.

Chapter 2

Introduction to Modelling and Numerics

Contents

The interest of Computational Fluid Dynamics (CFD) is to obtain a representative flow of a given configuration determined by the Boundary Conditions and a geometry of the problem. To do this requires the resolution of a set of equations capable of representing the fluid behaviour. These are the previously mentioned Navier-Stokes (NS) equations,

$$\frac{\partial \rho}{\partial t} + \frac{\partial \rho u_i}{\partial x_i} = 0 \tag{2.1}$$

$$\frac{\partial}{\partial t}\rho u_i + \frac{\partial}{\partial x_j}\rho u_i u_j = -\frac{\partial P}{\partial x_j}\delta_{ij} + \frac{\partial T_{ij}^{(v)}}{\partial x_i} \tag{2.2}$$

$$\frac{\partial \rho E}{\partial t} + \frac{\partial}{\partial x_j}(\rho u_j E) = \frac{\partial q_i}{\partial x_i} + \frac{\partial}{\partial x_j}(u_i(P\delta_{ij} + T_{ij}^{(v)})) + \dot{\mathcal{Q}} \tag{2.3}$$

where ρ is the density, u is the velocity vector, E the total energy, $T_{ij}^{(v)}$ is the viscous stress tensor, P represents the pressure, q the heat flux and $\dot{\mathcal{Q}}$ is the heat source term.

The previous equations Eqs. (2.1), (2.2), (2.3) represent a continuity equation. This last concept is useful because based on the local conservation laws it allows to write the whole set of equations as a transport equation,

$$\frac{\partial U}{\partial t} + \vec{\nabla} \cdot \vec{F} = S, \tag{2.4}$$

where U corresponds to the vector containing the conservative variables of the solution; F represents the fluxes matrix and S represents the possible source terms. These equations are comprehensively detailed in App. A and will be filtered to obtain the Large Eddy Simulation (LES) equations to be solved which is the focus of this thesis, see App. A.1.

It is arguable that the NS equations at the root of CFD are already a model of the physical behaviour but will be nonetheless accepted as being exact for the rest of this document. When discussing modelling of the equations a new step is added and this one refers to the fact that it is not the continuous Partial Differential Equation (PDE) problem which is solved. The numerical methods solve only the discrete equations and depending on the resolution (see Sec. 2.3) there is more or less "numerical" modelling to perform. Equivalently and as detailed hereafter for high Reynolds (Re) number flows, directly discretizing Eq. (2.4) which results from Eqs. (2.1)-(2.3) is not practiced. "Turbulence" modelling is to be introduced which will substitute Eqs. (2.1)-(2.3) be recast in the form of Eq. (2.4) and then be "numerically" modelled or discretized. In particular, the filtering of the LES equations indicates that there is a part of the equations that is differs from the resolution algorithms. Two other approaches to treat high Re flows are also possible and are described to show how LES is a more powerful source of information compared to Reynolds Averaged Navier-Stokes (RANS) or Direct Numerical Simulations (DNS). Modelling requirements for the turbulence are presented in following sections. How the equations are solved and the different strategies to decompose the equations into the spatial and temporal parts that arise naturally from the equations are then discussed.

2.1 Free-stream turbulence based modelling

Nowadays, there is a great number of CFD codes able to provide an approximation of the flow in an industrial configuration, with more or less accuracy, by solving a larger or smaller part of the original geometry. The objective of these models is to capture the necessary physics for the simulation to be representative of the flow at the lowest cost possible. The representative part of the flow is clearly a subjective matter as in some cases the global trend might be enough for the description of the problem at hand. This has however clear limits since it is now known that a small local change in a flow can affect dramatically the main flow state or field. The question that arises is then how much of the flow is necessary to be solved to obtain an acceptable representation of the actual solution. This *a priori* choice clearly influences the final result obtained and users must be aware of the limitations when analyzing the results. Difficulties are nonetheless not limited to this choice. The key difficulty, in a fluid mechanics simulation, is **turbulence** and its definition is not trivial. Following the proposal of Bradshaw [25] *"Turbulence is a three dimensional time-dependent motion in which vortex stretching causes velocity fluctuations to spread to all wavelengths"*, the mathematical terms responsible for this process are the non-linear terms present in the governing equations Eqs. (2.1)-(2.3). These non-linear terms are more or less important depending on the Reynolds number of the flow, a number that quantifies the importance of the non-linearities with respect to the diffusion process. A

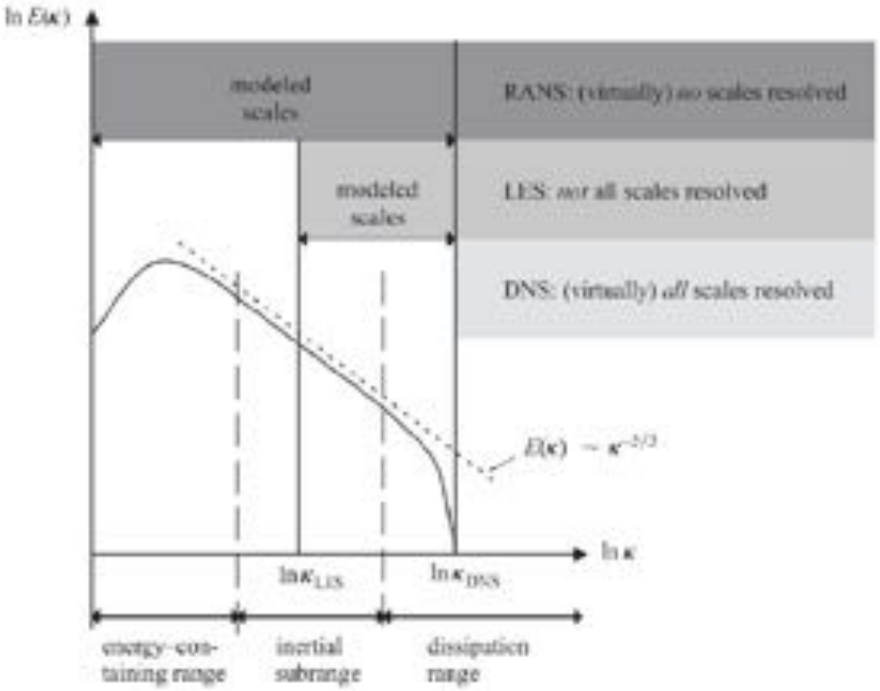

Figure 2.1: Spectrum of an homogeneous isotropic turbulent flow [194].

higher Reynolds number implies more non-linearities and thus, a more turbulent flow which is inconvenient from a mathematical point of view. In practice it requires accurate spatial and temporal discretizations or equivalently large meshes and small time steps. Most of the industrial configurations are high-Reynolds number flows so tackling the problem is inevitably expensive numerically unless artificial manipulations or models are introduced.

Different types of simulations are possible depending on the amount of turbulence that is resolved by the numerical model [141]. Note that such a choice only alleviates the high Reynolds number difficulty since in the end, the turbulence defined as resolved is inevitably influenced by the number of degrees of freedom used to solve each wavelength. Logically, a larger number of points leads to a more resolved simulation and a higher cost. How to determine which type of simulation to perform and more importantly, how reliable the information is in each case needs to be quantified. Very early on, effort has been done towards developing models capable of reproducing the non-resolved turbulence. Reviews such as Boussinesq [23] who developed what is now a very popular approach, has led to many classes of models [171, 109]. Today, there exists three main types of turbulent flow simulations which can be recast using the energy spectrum of a turbulent flow seen in Fig. 2.1; i.e. RANS, DNS and LES.

RANS - Reynolds Averaged Navier-Stokes approach

The first model historically applied and less expensive approach is the Reynolds-Averaged Navier Stokes (RANS) method. It consists in modelling the whole turbulence spectrum, a

hypothesis only valid if a temporal or ensemble average is performed over a set of realizations of the same flow [141]. The equations to be solved are different from the general Navier-Stokes equations. It is the averaged Navier Stokes equations which model all the turbulent scales and a large variety of closure models can be found, some of them being based on the Boussinesq closure method [173].

It is a powerful tool as many simulations can be performed at a very reasonable cost. The main disadvantage of this approach is that it is not capable of capturing the most subtle effects of a turbulent flow. So, even if it is based on averaged fields, these might be completely off if there is a transitional effect strong enough to create an instability. Such a case can easily be found for combustion instabilities for example [22]. In the end, it should be stressed that although RANS is effectively cheap in terms of computer cost, corresponding simulations can become expensive. The results may be unexploitable, or even worse, exploited under the wrong hypotheses or disregarding the risks induced by the inherent limitations present in the derivation of such models.

DNS - Direct Numerical Simulation

The most precise approach in terms of resolution of the equations is to solve the whole turbulent spectrum. This however is the most expensive approach and is known in the literature as Direct Numerical Simulations (DNS) [87]. Even with the increasing power of computational resources, it is extremely costly to solve the problem in this fashion due to the amount of points required to solve the smaller length scales that might be found in the flow. Theory of Homogeneous Isotropic Turbulence (HIT) indicates that the smallest length scales are those defined by the Kolmogorov scales [95], i.e.

$$l_{\mathcal{K}} = \left(\nu^3/\epsilon\right)^{0.25}, \tag{2.5}$$

where $l_{\mathcal{K}}$ is the Kolmogorov lengthscale, ν is the kinematic viscosity of the fluid and ϵ is the turbulence dissipation rate. By definition, the grid minimum cell size should be of the same order of magnitude as $l_{\mathcal{K}}$ or smaller to represent correctly the complete spectrum. Likewise, the size of the computational domain should allow the representation of multiple most energetic length scales or integral length scales resulting into an overall mesh size scaling as $Re^{9/4}$ for adequate DNS (where Re is the non-dimensional Reynolds number). The advantage provided by this method however is the possibility to gain insight into the turbulent structure [49] in a way considered as exact. This also allows to compare results obtained with other methods such as LES or RANS and to help validating the latter that do include some modelling.

Note that depending on the turbulent flow addressed, turbulence dissipation will not be the same and will evolve spatially contrarily to HIT: i.e. free-stream jets will have lower dissipation values than wall-confined flows. In the HIT case the cost of the simulation scales with a relation of $Re^{9/4}$ as mentioned earlier. It increases at a higher rate in the second case as a result of the the viscous effects in the near-wall region for example or in an inhomogeneous flow. Such scaling rules are the primary reasons why most publications address only academic problems

by use of DNS although there are some recent articles [192] where DNS is effectively used in complex configurations. Nevertheless, it is still regarded as an impossible approach for industry and very difficult for research of complex configurations.

LES - Large Eddy Simulation

LES is an alternative modelling approach to RANS which solves the larger scales of turbulence responsible for the interaction with the mean flow [140] while modeling the smallest scales. The difficulty in LES is to determine *a priori* the size of the filter used, Δ, that limits the quantity of turbulence to be modelled. This parameter should be taken small enough to solve approximately 80% of the turbulent kinetic energy (TKE) as stated in Pope [141]. Nevertheless, not knowing the full solutions implies a clear difficulty and an arbitrary choice of Δ will need verification. Just like in RANS note that, the solved equations are also modified to take into account the filter effects and additional terms arise for which dedicated models will have to be introduced.

Numerically, this formalism implies additional problems. Depending on the cell size, Δx, if numerics are required to have a negligible effect on the prediction, the ratio between the filter size and grid size should be large. Ideally, an explicit filter of size $2\Delta x$ is recommended [107] to avoid numerical issues with the non-resolved waves but in most practical approaches this recommendation is far from being met due to the resulting cost increase. In many codes the filter size is set to be the cell size and no explicit filtering is performed. Doing so implies introducing numerical scheme errors in the resolution of the equations, errors which are larger for the smallest wavelengths as less points are available for their resolution. The absence of an explicit filter is seen by some as the optimal option [142], as some numerical bias is acceptable and does not, in general, pollute the global simulation. It is important however to be able to ensure a low-dissipation scheme. Since there is no cut-off frequency, the smallest wavelengths must be both correctly predicted in terms of amplitude but also correctly transported. This requires a low-dispersion scheme for the waves to propagate at the correct speed.

Although there are different approaches to address the problem of turbulence, experienced researchers are able to know approximately which are the minimum requirements to correctly capture the global behaviour of a given configuration. This isn't true for the local flow aspects that are different in certain areas (wall region notably). Thus, mesh convergence is often a required step in any LES. However and in practice, an appropriate or sufficient mesh is a requirement not always met even when performing a convergence test today. For such issues, human experience will never be as good as a proper optimisation algorithm. In fact and to ease use of such CFD tools by engineers, mesh adaptation research is expected to upgrade LES performance in the future [64, 46] as long as adequate metrics are proposed which are still to be found for turbulent flows.

The previous modelling considerations for LES are true assuming the model is used in regions of free-stream turbulence. The accuracy of different models have been compared for a number of flows [69] but in most cases they are universally used without the necessary rigor, this implying that errors can come from this initial choice (such as the model used for unresolved

terms, see App. B) that may be difficult to trace. Nevertheless, the resolution of most structures (that correspond to the largest part of the spectrum) is a much better option than modelling the whole spectrum as done in the RANS approach. It must be stressed that the theory behind these models is HIT which is by no means applicable in near wall regions. For regions where the turbulence is anisotropic, as in the proximity of walls, additional models are required or must be modified locally to take into account the turbulent properties of the flow. This represents an advantage for RANS nonetheless because the whole spectrum is modelled and thus, only requires switching the model, from isotropic in the free-stream to anisotropic close to the wall. LES on the other hand requires to couple instantaneous data to a model that predicts the values at the wall when a sufficient resolution is not acquired. How to do this in LES is discussed in the following section.

2.2 Near-wall turbulence modelling

As mentioned in the previous section, regions close to the walls suppose an additional problem for RANS and LES in terms of modelling, DNS not requiring any modelling. RANS has been well-adapted for this different modelling with more or less success as stated in the previous section. Equivalently, LES relies on a certain amount of modelling to close the equations to be solved as shown in App. B. Thus, unresolved terms rely upon these models to account for missing physics. Adequate models may be found in cases where turbulence is isotropic, but these need usually to be adapted for strongly sheared flows such as those encountered near walls. Even for sub-grid scale models that are designed for wall-resolved situations, like the WALE model in App. B.3, these require additional hypotheses if meshes aren't sufficiently fine. This implies that any unresolved physics will either be wrongly modelled (Smagorinsky model) or neglected (WALE, SIGMA) if no other condition is added. There are thus two options; either define a mesh sufficiently fine to account for the smallest scales or to use an additional model. Simulations done in Chap. 6 are done in a wall-resolved context but the most widely used alternatives in industry are nevertheless presented.

Two main great families of modelling exist in the context of LES,

- Wall-modelled LES

  Modelling results from the need to determine the interaction between the smaller and the larger scales of the flow which are filtered and resolved respectively. This applies to the whole domain, however, it is of great importance in the near-wall region as the boundary layer physics dominate this area. The problem is that subgrid-scale models by themselves are not able to account for the shear stresses at the wall if y^+, a non-dimensional distance parameter, is larger than a certain value $\mathcal{O}(10)$. On the other hand, from the universal velocity distribution law in the presence of walls it is possible to provide a relation to account for the wall influence. Taking this law and the associated velocity distribution, it is possible to estimate the shear stress. This has been a historical problem initially approached by Schumann and Deardorff [163, 47] that has led to many laws and their variants. The common feature to all laws is that they require information of the velocity field outside of what is known as the viscous sublayer (see Chap. 5). The mesh must be

adapted so the position at which the information is extracted has a physical meaning as it is crucial to the correct behaviour of the wall law. The wall-modelled LES approach is thus based on predicting the shear stress (from a purely aerodynamical point of view) using a velocity value given at a normal distance from the wall to surpass the need for a high resolution in the proximity of the wall.

- Wall-resolved LES

  In this approach, the objective is to capture the dynamics of the locally most energetic scales. This imposes that the mesh cell size decreases in the near-wall region to account for the smaller scales present in the flow. The problem associated to this reduction is the increase in cost of the simulation. The estimation of the cost associated to this type of simulation is linked to the value of the Reynolds number and scales as $Re^{13/7}$ following Choi and Moin [31]. This implies that the cost is near to that of a DNS as the value of y^+, should not be higher than 5 for channel simulations [140] and even lower when curvature effects are present. In this low value y^+ region, contributions from the subgrid-scale models should be well adapted and an adequate SGS model (cf. the *P1 property* in App. B) has to be used.

It is known that different levels of refinement and discretization lead to different predictions and the only way to correctly assess this influence is by comparing different grids. This is especially critical if a wall-resolved approach is chosen, which increases the number of degrees of freedom, but more importantly, limits the time step to be used. This observation has led some authors to qualify such predictions as Quasi-Direct Numerical Simulations (QDNS) [171].

It is of note to underline the fact that in a wall model context, the effort required to obtain a good near-wall model is especially critical for blade flows characterized by an adverse pressure gradient. Most industrial-like application of LES relies on the use of laws-of-the-wall [189]. The main issue in this approach is the existence of pressure gradients which are not taken into account in classical approaches [148] or more recently [115] for example. The importance of taking into account the local effects of tangential pressure gradient was first noted by Wang and Moin [190] and good agreement has been found in papers such as Duprat et al. [60] and Maheu et al. [114]. In all approaches however, there is still the issue of the prediction of the transition position. The law-of-the-wall is designed to behave properly in turbulent boundary layers, whereas this might not be the case on the whole blade surface being then necessary to deactivate the model. Only the wall-resolved approach provides a sufficient degree of confidence today for such near wall flow predictions around blades where a transitioning flow is expected. Indeed, the solution provided by a well designed wall-resolved LES allows to capture all the effects provided an adequate local grid resolution. The main difficulty is hence not so much the physics in the boundary layer but the capability to capture effects such as strain or curvature [172] as well as rely on adequate SGS models.

Although the subject of this discussion stresses the importance of the turbulence formalism, it is important to note and this is especially evidenced in the context of LES, grid resolution is of foremost importance. The cell grid size parameter determines the filter size and in the case

of wall bounded flows qualifies the prediction as a wall-resolved simulation. Great care on grid generation is hence needed but different numerical solutions call for different code capabilities on this specific matter as detailed in the next section.

2.3 Meshes for LES

The choice of mesh determines to a large degree the quality of a LES. The use of different numerical schemes may lead to different solutions for the same mesh, more accurate results being attained for higher-order schemes. However, a high-order scheme in an insufficiently resolved near-wall region will never reproduce the correct physics by itself and so, the number of degrees of freedom must be well adapted locally in the domain. An important aspect to take into account before tackling the discretization methods is the way the information is stored relative to the available mesh and how the code will access the information stored at each degree of freedom. The set of elements that conform the domain may in general overlap [79] although this is not the case for AVBP. There are two main approaches defining a grid:

- **Structured mesh**
  A structured mesh is an approach where the mesh has a regular connectivity meaning side nodes are known so there is a direct data addressing. The main strength of this type of meshes resides in the simplicity to construct high order schemes compared to unstructured meshes as it is easier to find neighbour nodes. An example of structured mesh is shown in Fig. 2.2a. The main drawback is that structured meshes are in many cases limited to simple geometries. Also and in the most general case, it requires very long human time to generate the more complex meshes which in many cases limits its use especially for industrial applications. In this specific context most common type of meshes are H-mesh, O-mesh and C-meshes [78] which allow to follow a curved geometries more easily if needed.

- **Unstructured mesh**
  It is a more expensive approach in terms of memory as it requires to read an irregular connectivity table to exchange information on all elements. However, it is possible to generate all type of geometries in an acceptable amount of time and it allows to use different types of elements easily (hybrid meshes), although the use of tetrahedra is generally privileged. Note however that the use of hybrid meshes can be important when solving a boundary layer flow as presented in Auffray [9] where a structured type set of elements is highly beneficial. Another characteristic of unstructured meshes is that in end usage it is useful to be able to locally improve the mesh. In many cases this leads to the addition of nodes which increases the number of degrees of freedom. The objective of such strategies is to affect the quality of the mesh which if insufficient, can cause numerical artifacts. As stated in Section 2.1, the observation and improvement of meshes is a very subjective issue and algorithms based on certain fields must be used to optimise and enter this paradigm. A typical unstructured mesh is shown in Fig. 2.2b.

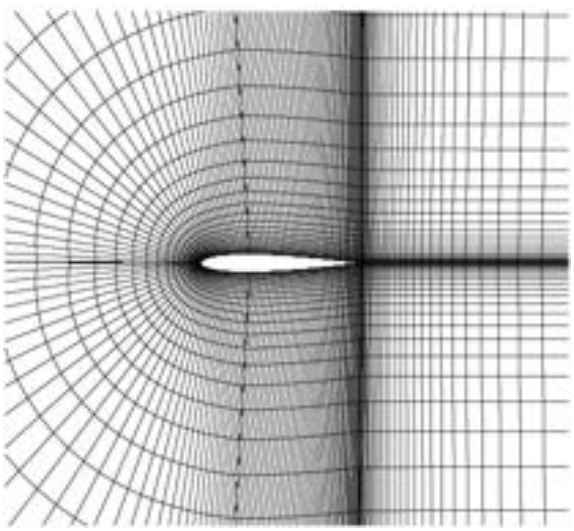

(a) Structured mesh of an airfoil.

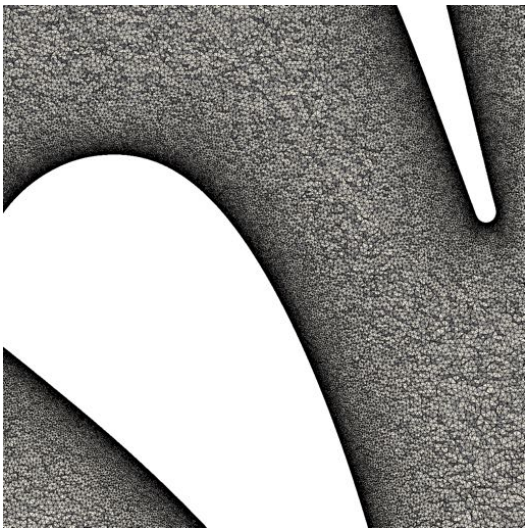

(b) Unstructured mesh around a vane profile.

Figure 2.2: Mesh comparison between structured and unstructured meshes.

Recent strategies try to take advantage of both formalisms, that is to have hybrid meshes composed of two blocks, some structured and others unstructured that are coupled to conform one global mesh. For the rest of this document, the concept of hybrid mesh is restrained to fully unstructured multi-element meshes composed of tetrahedra and prisms for example. Note finally that confusion must be avoided when referring to the isotropy or regularity of the mesh. These specifications are not limited to structured grids but may as well be obtained with an unstructured mesh.

Having established the existing mesh types available to a LES solver, the following fundamental step in solving the modelled LES equations resides for a given mesh and associated degrees of freedom in the introduction of numerical operators. For LES, there is no doubt that a time-dependent operator must be used but it is also clear that it is necessary to introduce the spatial operator of the problem. The way both discretizations are done will condition the properties of the scheme [9] and are shown in the following sections. The different sections to follow address first the spatial discretization in Sec. 2.4 while Sec. 2.5 addresses the temporal problem.

2.4 Spatial Discretization

The spatial discretization is first tackled in this section. Before introducing the different families of discretization that can be used, the integral form of the conservation laws of the continuity equations, see Eqs. (2.1)-(2.3), are presented as it is used in the next steps. The application of the integral conservation laws requires to define a sub-domain, namely a *cell*, where the conservation law has to hold. Naturally if this is law is directly applied the discretization conservativeness is automatically guaranteed in the cell. Mathematically this can be written through Eq. (2.6) with no source terms (after the use of Green's theorem),

$$\frac{\partial}{\partial t}\int_{\Omega} U d\Omega + \int_{S} \vec{F}\vec{n} dS = 0. \tag{2.6}$$

where U represents the conservative variables, $\vec{F}$ are the fluxes $\vec{n}$ is the normal vector. Also, Ω is the domain of interest: i.e. cell or computational domain and S represents the boundary of the domain.

The interpretation of the previous expression is that summing over all the elements that form the domain, the internal fluxes (faces of cells that do not correspond to boundary domain faces) must not contribute to the internal volume sources. If this is verified, the formulation is indeed conservative. However, calculating the direct integral of the fluxes is not the only way to proceed. It is also possible to obtain an approximate solution of the problem that is bounded but does not hold absolutely. This corresponds to a weak formulation (also known as weighted residuals) based on the *Lax-Milgram* theorem [27]. Finding these approximate functions remains the most challenging aspect of the method and is explained in the corresponding section.

An additional comment must also be done in terms of control volumes and their storage. The elements in which the domain is divided into, how the control volumes are defined and the spatial discretization used have to be clarified. These three approaches are shown in Fig. 2.3. Different algorithms exist to this end, cell-centered, vertex-centered and cell-vertex methods. The cell-centered method was the first to be used in the context of finite volumes. The domain is discretized using a series of cells that connect the nodes of the mesh, known as primary cells. For this method, the variables to be solved (one per cell) are stored at the center of each primary cell. This is different from cell-vertex methods which use the same primary cell to solve the equations, but will however store the information at a different location. The most usual locations are the vertices that define the primary cell. The control volume where the equations are solved is not necessarily the primary cell, an alternative being the vertex based approach. In this case, one requires an additional cell to be defined using the centroids of the neighbouring cells around a given node and define what is known as the dual cell. In this way, it is similar to the cell-centered method as it solves and stores the information at the same point with the additional cost of defining the dual cell.

For both cell-centered and vertex-centered approaches, the evaluation of the discretized variables requires to obtain information from its neighbours to compute the fluxes on each cell face. This is not necessary for the cell-vertex approach as the values are already stored at the vertices that define the cell. The counterpart to this is that once the computation in each cell has been performed, the cell-vertex method requires to send the information to each vertex. In all cases, information will need to be exchanged. Nowadays, CFD codes are run on a large number of processors, which requires good partitioning algorithms to optimize the exchange of information. The partitioning strategy will greatly determine the methodology to be used and vice versa. If the primary cells are kept, meaning that the boundaries of the partitioning coincide with the primary cell faces as in Fig. 2.4, the cell-vertex method would be a more appropriate choice. As nodes on the partitioning limits will be duplicated, each cell will contain

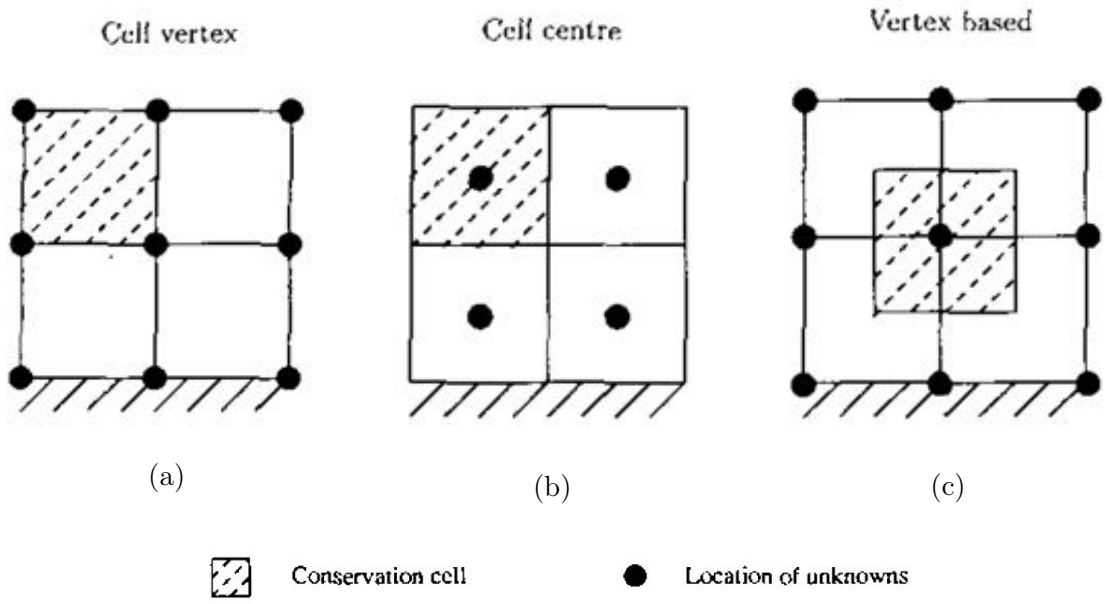

Figure 2.3: Discretization approaches [45], a) cell-vertex, b) cell-centre and c) vertex-based approach.

the required information for the resolution of Eq. (2.6). Of course, the node update will require partitioning information exchange. However, the time required for the computation of gradients will be much larger than just the update, concluding thus that for this type of partitioning the cell-vertex method will be more efficient. It is also of note that the boundary treatment performed in the cell-vertex method is in general, more precise and cheaper than for the other methods. It has also been shown for a large number of cases that the cell-vertex method is also the most accurate of the three methods [126] as well as more robust to distorted meshes [177]. All of these reasons justify the choice of methodology done for AVBP and is studied by numerous research groups still today [2]. The details of the cell-vertex method are developed in Section 3.1.

Once these concepts have been defined, it is possible to go on to define each particular discretization strategy. The spatial discretizations can be divided into three different families. These families are, by chronological development, Finite Differences, Finite Element and Finite Volumes. They are here presented to show their advantages and disadvantages regarding mainly their applicability, greatly limited depending on the type of mesh and their accuracy.

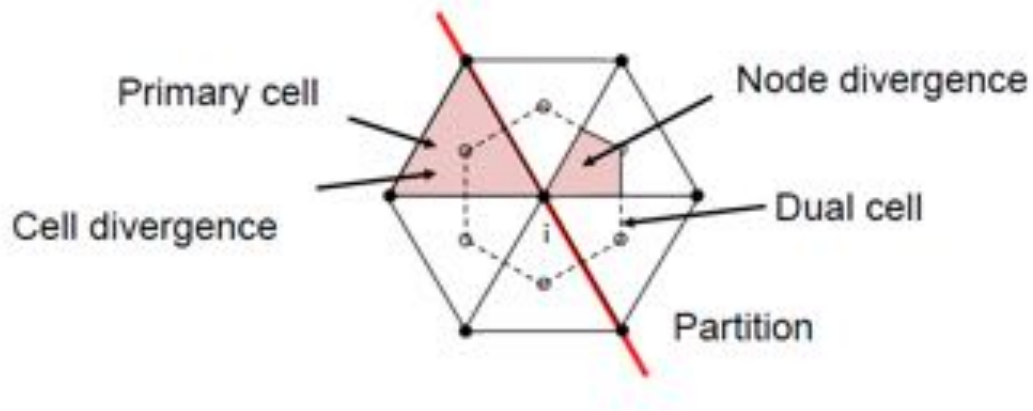

Figure 2.4: Partitioning of cells in AVBP [29] duplicates the number of nodes affected by the partition. Definition of primary and dual cells around a target node are also shown.

2.4.1 Finite Differences (FD)

Finite Differences was the first method developed and it is not based on an integral form but on a Taylor expansions of the spatial derivative of a function $f(x)$ around x_0,

$$f(x) = f(x_0) + \frac{\Delta x}{1!} f'(x_0) + \frac{\Delta x^2}{2!} f^{2)}(x_0) + \mathcal{O}\left(\Delta x^3\right). \tag{2.7}$$

It therefore addresses Eqs. (2.1)-(2.3) instead of Eq. (2.6) different expressions of the derivatives are obtained by truncating the development at the required order. If an infinite number of degrees of freedom were to be used, no truncation error would be present. The difficulty associated with this approach is the increase of stencil size or equivalently, the number of neighbouring nodes required to obtain the derivative approximation at a given order of accuracy. For structured type meshes this is not an issue except at boundaries, but as it has been seen, it will introduce difficulties in the discretization of complex geometries. Based on this type of development, the most common schemes are the compact or generalized Padé schemes [107] that allow to have reduced stencils compared to the classical Taylor expansion at the same **order of accuracy**. The first derivative in this case would be written as,

$$\beta f'_{j-2} + \alpha f'_{j-1} + f'_j + \alpha f'_{j+1} + \beta f'_{j+2} = c\frac{f_{j+3} - f_{j-3}}{6\Delta x} + b\frac{f_{j+2} - f_{j-2}}{4\Delta x} + a\frac{f_{j+1} - f_{j-1}}{2\Delta x} \tag{2.8}$$

where j is the target node and $j + k$ are their k^{th} neighbours. Depending on the values assigned to the coefficients β, α, a, b, c, the order of the scheme will be different. There is a clear inconvenience in this formulation due to the presence of neighbour node derivatives. This

requires to know the values taken by the derivative at these points and implies the use of a matrix that must be inverted, making it an implicit method. This inversion adds an additional cost from a purely computational point of view but it also presents computational difficulties due to memory requirements and eventually, partitioning issues. The great improvement issued by such approaches is however seen in both the lower dissipation and dispersion errors of such schemes justifying their wide use. General difficulties encountered for this type of schemes relate to aliasing errors leading to optimization studies that provide the best possible combinations [164].

2.4.2 Finite Elements (FE)

This method was originally derived for structural mechanics in the 1940s although the first applications to CFD appeared in the early 1980s. It is based on functional analysis and will resolve the weak form of the equations, i.e.: Eq. (2.6). Numerically, Finite Elements requires to discretize space into control volumes, known as elements (in Finite Differences although the domain is discretized artificially by elements, there is no other notion than nodes). These elements or cells will at the same time be delimited by vertices. Associated to these cells and vertices, shape functions are introduced to carry the spatial information associated to each variable. So, for each cell,

$$u\left(\vec{x}\right) = \sum_{k} u_k \vec{\phi}_k\left(\vec{x}\right) \tag{2.9}$$

$\vec{\phi}$ being the shape function containing the information of how the variable u is distributed inside the cell. Performing this operation in all cells contained in the domain, the spatial discretization is complete and a temporal integration can be applied. The construction of the entire spatial approximation based on each element representation is known as the assembly process. The local information is expressed in a global form so the problem is reduced to solving a matrix system. The shape functions can be of various types, interpolating, splines... [147]. If the trial functions are taken to be equal to the test functions, the method is known as Bubnov-Galerkin or simply the Galerkin approach. This numerical approach is applied for certain schemes in the AVBP solver and will be detailed in Section 3.2.2.

2.4.3 Finite Volumes (FV)

The most widely used discretization method in CFD relies on the direct application of the integral form of the governing equations, see Eq. (2.6). Introduced by Rizzi and Inouye [150] among others, its popularity comes from its ease and applicability to both structured and unstructured meshes. To obtain the update from step n to $n+1$ the fluxes must be evaluated through each face that composes the element. Fluxes will hence only depend on their surface values, which need to be approximated using the conservative values in each cell or its neighbours. How these fluxes are evaluated varies between the algorithm used (cell-centered, cell-vertex or vertex-centered) and each particular code implementation. Once the surface fluxes have been calculated, Eq. (2.6) can be rearranged to read,

$$\frac{\partial}{\partial t}\int_{\Omega} U d\Omega = -\int_{S} \vec{F}\vec{n} dS = R_{\Omega}. \tag{2.10}$$

where the surface integral is defined as the *residual* R_{Ω} of the control volume. This residual can then be used to advance in time and move on to the next iteration.

The three main families of discretization methods have been described as well as the different control volumes that exist and how this information is stored. Although robust, in the context of FE and FV the direct application of these methods lead to low-order schemes (equal or lower than two). The trend in the numerical community has been to increase this order as a result of its numerous advantages [182] which although more expensive in terms of operations pays off in terms of number of degrees of freedom necessary to obtain the same solution. The obtention of high-order distribution schemes has been a challenge for a large number of years now and in the context of classical CFD there are two main approaches today, Residual Distribution schemes (RD) and Discontinuous Galerkin (DG). They both have local formulations but the number of degrees of freedom increases slower in the RD case compared to DG. For the remaining of this thesis only the RD method, originally developed by Roe [152], is studied as it is the method applied in AVBP.

2.4.4 Residual distribution schemes (RD)

Residual distribution schemes, or fluctuation splitting schemes usually have associated to the nodes as degrees of freedom exclusively, so it has similarities with the cell-vertex approach and can be closely related to both finite volume and finite element schemes. The objective for the development was to increase the accuracy of the standard Finite Volume methods while keeping the linearity preservation properties [28]. This type of schemes tries to bring together the optimal properties of both methods. The difficulty of residual distribution schemes resides in extending the problem to the complete Navier-Stokes problem as it was initially designed for advection problems [3].

Considering no source terms as in Eq. (2.6), it can be shown that the spatial discretization for one element leads to Eq. (2.11). Based on the calculation of a residual or fluctuation from a non-stationary solution, in the case of a Finite Volume method, integrating the divergence of the fluxes over an element will lead to a value that will be different from zero:

$$R_{\Omega} = \frac{1}{V_{\Omega}}\int_{\Omega} \vec{\nabla}\cdot\vec{F} dV, \tag{2.11}$$

expression that can be transformed using the Gauss-Ostrogradskii theorem to obtain what is known as the *residual* previously seen.

The difference between Finite Volumes and RD is that the fluxes in the RD schemes are not considered to vary along the edge or face of the element, but are concentrated on the degree

of freedom. For a cell-vertex context this corresponds to a node. The key to the development of high-order schemes is that the gradients reconstructed must be of higher-order. This step provides the main interest in the method but also poses most of the problems. The calculation of the residual is however done at the center of the element and uses all the neighbour vertices. For a cell-vertex method, this value must now be distributed back to each node through the *scatter* operation. This operation can be characterized mathematically by a distribution matrix $D_{j,\Omega}$ that is related to the temporal advancement of the conservative variables by,

$$\frac{dU_j}{dt} = -N_j, \tag{2.12}$$

where N_j is,

$$N_j = \frac{1}{V_j} \sum_{\Omega \in D_j} D_{j,\Omega} V_\Omega R_\Omega, \tag{2.13}$$

and V_j represents the nodal volume. The way the $D_{j,\Omega}$ matrix is chosen define the different schemes and is discussed in Chapter 3 as each distribution will have very different properties.

Note that in all cases the spatial discretizations presented have always been ended by obtaining a *residual*. This is because the temporal advancement has still not been performed but is of course necessary. Section 2.5 presents the different ways this step can be done in the cell-vertex context used in AVBP.

2.5 Temporal integration

The advancement from time step n to $n+1$ is by adding a weighted residual to the conservative variables U^n to obtain U^{n+1} . There are two main ways to advance a temporal step, either in an explicit or in an implicit way.

- Explicit schemes

  Explicit schemes reside on finding a finite time step Δt to move from an instance n to *n+1* for it to remain stable. The schemes are conditionally stable (if not unstable) and are limited by the CFL number. The CFL value is due to [41] that defined the criterion for a compressible flow as

  $$CFL = \frac{(u+c)\,\Delta t}{\Delta x}. \tag{2.14}$$

  with u is the convection velocity and c is the sound speed. Typical order of magnitude of CFL stable values is $CFL \approx \mathcal{O}(1)$. As an example, in the case of a compressible flow where $u << c$ a typical time step could be of the order of $\Delta t\ \alpha\ \frac{\Delta x}{c}$. It is especially critical if a small Δx is required such as in the proximity of walls as already discussed.

- Implicit schemes

  Implicit schemes on the other hand are unconditionally stable which implies that large values of Δt may be used, the limit not being related to numerical issues but to the correct capture of the physics involved and the accuracy of the solution. Cases where strong non-linearities are present require small time steps losing thus part of the advantages associated to this family of schemes. This being the case, it seems unusual that explicit schemes still be used today. This may be explained by the cost of the operations associated to each family. Implicit schemes use backward time advancement which introduces a matrix inversion which is both costly and memory intensive. Additionally, it is much more difficult to parallelize which is a clear disadvantage considering the current machine architectures status. Both methods have however their advantages and disadvantages so it is a choice to make which will depend on the application targeted.

As specified for the spatial discretization, there is a need to increase the order of the temporal numerical schemes to reduce the global cost of the simulation. In hyperbolic systems where waves are transported there is a duality between space and time that must not be forgotten. However, effort has seemingly been focused much more on spatial discretization than on temporal integration schemes. This is a great mistake as it is the coupling of both that leads to the final properties of a numerical scheme [78]. Thus, temporal integration schemes require to increase their order too. To this end, many methods are available and can be further classified into three different families:

- Runge-Kutta methods

  The most popular integration method [84, 33] can be either explicit or implicit. It is an iterative method family where intermediate steps are used to approximate the solution. This way it is possible to increase the temporal stencil and thus, increase the order of the scheme and cancel out lower order error terms. They are simple to code and have good robustness properties.

- Multi-step methods

  They have a similar principle to Runge-Kutta methods except that multi-step methods rely on different time steps to approximate the solution at instant $n + 1$. The main issue concerning this type of integration is that the unsteady effects are not well captured for large CFL numbers [17] and thus of small interest for LES.

- Predictor-corrector methods

  The idea behind these approaches is to make a first estimation using generally an explicit integration method. This predicted value is then evaluated and used in a following step to combine it with either the same or another integrator in time. The number of optimal predictor or corrector steps in combination with different spatial discretization methods can be found in Lambert [102]. It is commonly used for non-linear problems for its robustness as it also deals better with stiff type problems.

As seen in this chapter, schemes can be classified in a large variety of ways. The way this is done depends mainly on: a) the way a solver addresses the data storage b) the spatial

discretization c) the temporal discretization. From now on and throughout the remaining part of this document, the numerics used are related exclusively to the AVBP code which uses:

- Unstructured data addressing,
- Finite Volume/ Finite Element discretization method,
- Explicit time integration based on predictor-corrector methods to increase the temporal order.

All these points can be justified from an application point of view. AVBP is a solver widely used in industry, so it requires to be able to deal with complex geometries limiting the choice to an unstructured solver. Accordingly, this discards the possibility to use finite differences and schemes are obtained either in a Finite Element or Finite Volume formalism. The temporal discretization makes use of the spatial derivatives to update the time step and is a characteristic of the Lax-Wendroff type methods. All these aspects are described in deeper details in the following chapters.

Chapter 3

Numerics of AVBP

Contents

A detailed description of the numerical methods implemented in AVBP, a cell-vertex FE/FV unstructured solver are presented in this chapter. The cell-vertex approach introduces many particular aspects inherent to the method that are less intuitive compared to standard FE/FV methods. This adds a layer of complexity in terms of notation and operations which require additional studies. Both the convection and diffusion operators are described highlighting the various difficulties present and which need to be be well-adapted to LES. The unstructured meshes make difficult the finding of high-order schemes which is the current trend in LES related literature. In AVBP, the convection operators are based on a Taylor expansion that allows to increase the temporal order of the scheme on such meshes. Note also that since the cell-vertex algorithm is known to be prone to small-amplitude oscillations a numerical treatment is introduced to improve the convergence towards the solution. This treatment is known as

artificial viscosity and is detailed here. Finally, the boundary conditions either physical or numerical are also described since needed to close the problem. Note that physical boundary conditions are certainly necessary for the correct definition of the problem but some schemes will require additional information. Identifying the terms, an introduction on how to tackle these closes the chapter.

3.1 The cell-vertex approach

Cell-vertex methods were first introduced by Ni [130] and were used along with the Lax-Wendroff scheme. It has been extensively studied by Crumpton et al. [45] or Deconinck et al. [48]. It is a residual method that stores information at each mesh node, j, while the equations are solved using the primary control volumes as indicated in Fig. 3.1, where the primary cell is that confined by the edges connecting the black dots and the dual cell is the shaded cell confined by the white dots. Two types of residuals are defined; the cell residual R_{K_e} is calculated using the flux values at each node balancing the equations on the primary cell. This cell residual is then redistributed to the nodes using the scatter operator to obtain the node residual R_j. Details on how this residual is obtained are provided in the following sections.

The main properties and advantages compared to other approaches are:

- **Accuracy on degenerated meshes** The use of a control volume defined by the primary cell is important when using complex geometries. In such cases, the dual cell might be greatly distorted while the primary cells are adequate, an observation which is even more present and critical for hybrid meshes. In that respect, accuracy has been shown to be much greater when compared to cell-centred or vertex-centred approaches [44, 154].
- **Memory intensive** In complex geometries it is a fact that the number of cells is always larger than the number of nodes if elements such as tetrahedra are used. This privileges the cell-vertex method as it will need to store less information.

It is necessary to introduce now the metrics that may be encountered in AVBP as well as the calculation of the residual on a single primary cell and how it is redistributed to the node.

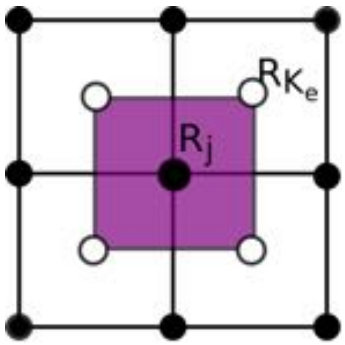

Figure 3.1: Residuals at primary (white) and dual (shaded) cells.

3.1.1 Cells and metric definition

In the cell-vertex context, the existence of a cell duality is present due to the primary and dual cells. This duality introduces an extensive need notations that must be clarified. To do this, it is first necessary to introduce the different types of elements found in the AVBP code in two and three dimensions:

- 2-D

  Triangles,

  Quadrilaterals,

- 3-D

  Tetrahedra,

  Pyramids,

  Prisms,

  Hexahedra.

A simple 2D hybrid mesh is presented in Fig. 3.2a to provide all the necessary definitions required. Throughout the following discussion, the definitions hereafter provided will refer to Fig. 3.2.

- $j \in [1, N_{node}]$ is the index used for the global node numbering where N_{node} is the total number of nodes of the mesh.
- K_e represents the primary cells of the mesh. The cell is defined by the edges that connect its nodes thanks to the connectivity table of the mesh.
- C_j represents the dual cell of the mesh. It is defined by the centroids of the primary cells and the half-lengths of the primary cell edges.
- ∂C_j represents the boundary of the dual cell. The same applies to the primary cell for ∂K_e.
- $k \in [1, n_v(K_e)]$ is the local numbering of the vertices of a cell K_e, with $n_v(K_e)$ the number of vertices of the cell K_e.
- $f \in [1, n_f(K_e)]$ is the local numbering of the faces of a cell K_e, with $n_f(K_e)$ the number of total faces of the cell K_e.
- $\vec{F}_k$ is an approximation of $\vec{F}$ (a vector field) at the vertices.
- $\vec{s}$ represents the normal vector. It is defined at each face and each vertex.
- R_j is the global nodal residual.
- R_{K_e} is the primary cell residual.

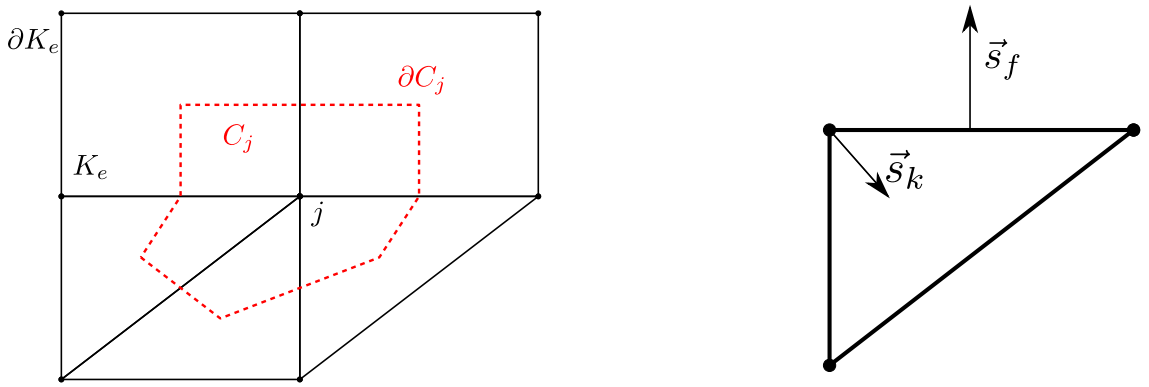

(a) Detail of mesh dual cell.

(b) Definition of normals to face and nodes.

Figure 3.2: Definition of cell-vertex metric.

- $\vec{x}$ is a vector representing the vertex coordinates.
- *Linear element* is a metric element whose shape function is linear, e.g. triangles or tetrahedra.
- *Bilinear or trilinear elements* are metric elements whose shape functions are bilinear or trilinear, e.g. quadrilaterals, prisms, hexahedra.

To define the volume V_{K_e} consistently it is necessary to define it in a way such that,

$$V_{K_e} = -\frac{1}{n_d^2} \sum_{k|k\in K_e} \vec{x}_k \cdot \vec{s}_k, \tag{3.1}$$

since $\nabla \cdot \vec{x} = n_d$ with n_d the number of dimensions. The control volume around the node j (median dual cell) is thus defined as : $V_j = \sum_{j|k\in K_e} V_{K_e}/n_{v(K_e)}$.

An additional comment is necessary for the definition of the normal to both faces and vertices presented in Fig. 3.2b. The normal to a face $\vec{s}_f$ is uniquely defined by the normal to the edge (or surface in a 3-D case) created by the nodes as shown. Each normal to the edge $\vec{s}_f$ is additionally scaled by the length of the edge. The expression of the normal to each vertex inside a primary cell is hence given by,

$$\vec{s}_k = \sum_{f\in k} -\frac{n_d}{n_v^f}\vec{s}_f \tag{3.2}$$

where n_v^f is the number of vertices on an edge.

3.1.2 Residual calculation

The residual is computed for each primary element using an integration rule on the surrounding faces. Rewriting Eq. (2.11) and transforming it using the Green-Gauss theorem,

$$R_{K_e} = \frac{1}{V_e} \int_{\partial K_e} \vec{F} \cdot \vec{n} dS. \tag{3.3}$$

Using the notation described in Sec. 3.1.1, Eq. (3.3) can be expressed as

$$R_{K_e} = -\frac{1}{n_d V_e} \sum_k \vec{F}_k \cdot \vec{s}_k. \tag{3.4}$$

Once the cell residuals are calculated, one can obtain the nodal residual at node j as the volume average of the cell residuals,

$$R_j = \frac{1}{V_j} \sum_{k|j \in K_e} D_{j|K_e} V_{K_e} R_{K_e} \tag{3.5}$$

where $D_{j|K_e}$ is a distribution matrix from the primary cells K_e to the dual cells j that is conservative if $\sum_{k|k \in K_e} D_{k|K_e} = I$. Then the time advancement must be performed, that is

$$\frac{dU_j}{dt} = -R_j. \tag{3.6}$$

This section provides the foundation of all cell-vertex schemes and associated operations present in the AVBP codes. Different schemes however exist, their derivation and link to the above discussed steps are the subject of the following sections.

3.2 Convection schemes in AVBP

AVBP uses a cell-vertex approach and different spatial discretizations, either FV or FE, depending on the scheme used. The main schemes used in AVBP are the second-order Lax-Wendroff and the Taylor-Galerkin (TG) family. Both the LW and the TTG family are based on a Taylor expansion in time of the solution vector function,

$$U^{n+1} = U^n + \Delta t \left(\frac{\partial U}{\partial t}\right)^n + \frac{1}{2}\Delta t^2 \left(\frac{\partial^2 U}{\partial t^2}\right)^n + \frac{1}{6}\Delta t^3 \left(\frac{\partial^3 U}{\partial t^3}\right)^n + \mathrm{O}(\Delta t^4), \tag{3.7}$$

but have different truncation errors. Each term of type $\frac{\partial^n U}{\partial t^n}$ is solved using diverse flux expressions and is then substituted into the general continuity equation.

3.2.1 Lax-Wendroff scheme

The first scheme to be presented is the second-order Lax-Wendroff (LW) scheme [104] and serves as an example to introduce the main concepts. The LW scheme uses Eq. (3.7) keeping the terms up to Δt^2. The idea behind the Lax-Wendroff scheme is to substitute the temporal derivatives with spatial derivatives using the continuity equation (Eq. (3.8)),

$$\frac{\partial U}{\partial t} = -\nabla \cdot \vec{F}, \tag{3.8}$$

and,

$$\frac{\partial^2 U}{\partial t^2} = \frac{\partial}{\partial t}\left(-\nabla \cdot \vec{F}\right) = -\nabla \cdot \frac{\partial \vec{F}}{\partial t}. \tag{3.9}$$

Once this point is reached, it is necessary to introduce an additional operator as the fluxes' temporal derivative cf. Eq. (3.9) is unknown. To do this, the idea of Ni [130] was to use the Jacobian matrix defined as $\vec{A} = \frac{\partial \vec{F}}{\partial U}$ so the temporal derivative of the fluxes is rewritten as $\frac{\partial \vec{F}}{\partial t} = \vec{A} \cdot \frac{\partial U}{\partial t}$ since spatial and temporal derivatives can be interchanged. The second order derivative can hence be expressed as,

$$\frac{\partial^2 U}{\partial t^2} = -\nabla \cdot \left[\vec{A} \cdot \left(\frac{\partial U}{\partial t}\right)\right] = \nabla \left[\vec{A} \cdot \left(\nabla \cdot \vec{F}\right)\right] \tag{3.10}$$

The LW scheme is finally obtained and reads,

$$U^{n+1} = U^n - \Delta t \left\{ \underbrace{\left(\nabla \cdot \vec{F}\right)^n}_{\mathrm{L}} - \underbrace{\frac{1}{2}\Delta t \, \nabla \cdot \left[\vec{A} \cdot \left(\nabla \cdot \vec{F}\right)^n\right]}_{\mathrm{LL}} \right\}. \tag{3.11}$$

Two terms are to be noted on the RHS of Eq. (3.11). The second term factor of Δt is here on defined as L while the third term factor of Δt^2 will be named LL. For this scheme, as the implementation done is based on a FV approach (although the FE is also possible), all cells are treated in the same way not distinguishing between linear and bi or tri-linear elements (see Sec. 3.1.1). The first term of the scheme is obtained for a cell using a local volume integral re-expressed using the Green theorem,

$$L = \int_{K_e} \nabla \cdot \vec{F} dV = \sum_{\partial K_e} \vec{F}_f \cdot \vec{s}_f \tag{3.12}$$

where the fluxes and surface normals are given at the faces. The fluxes are defined at the primary cell vertices which define the faces where a linear variation is assumed along the edges so that,

$$\vec{F}_f = \sum_k^{n_v^f} \frac{\vec{F}_k}{n_v^f}, \tag{3.13}$$

where n_v^f represents the number of vertices on an edge or face.

The residual contribution from the L term corresponds to the first order temporal derivatives of the original problem and is calculated at a primary cell level using,

$$R^L_{K_e} = -\frac{1}{n_d V_{K_e}} \sum_{k|k\in K_e} \vec{F}_k \cdot \vec{s}_k. \tag{3.14}$$

Once this residual is calculated, it can be redistributed to the nodes using the distribution matrix previously noted in Eq. (3.5).

The second term LL of Eq. (3.11) is calculated directly at the vertex of each primary cell using Eq. (3.10). The Green-Gauss theorem is once again used to go from a volume to a surface integral leading for each subcell $K_e \cap C_j$,

$$LL_{j|K_e} = \frac{1}{2}\Delta t \iiint_{K_e\cap\mathcal{C}_j} \nabla\cdot\left[\vec{A}\left(\nabla\cdot\vec{F}\right)\right] \mathrm{d}V = \frac{1}{2}\Delta t \iint_{\partial\mathcal{C}_j} \left[\vec{A}\left(\nabla\cdot\vec{F}\right)\right]\vec{n}\; dS. \tag{3.15}$$

This term is then discretized to read,

$$LL_{j|K_e} = \frac{1}{2V_j n_d}\Delta t \sum_{e\in\sum C_j} \left[\vec{A}_{K_e}\left(\nabla\cdot\vec{F}\right)_{K_e}\right]\vec{s}_{j|K_e}. \tag{3.16}$$

where $j|K_e$ refers to the node contribution to a certain primary cell.

Although the residual associated to this LL term only has sense from a dual cell point of view, the primary cell residuals previously calculated are used in this step too. The loop performed in Eq. (3.16) is done for all subcells $\sum K_e \cap C_j$ and the terms that correspond to $\left(\nabla\cdot\vec{F}\right)_{K_e}$ are precisely the first order residual of each intersection cell. The Jacobian matrix is evaluated using this residual. The assumption made here is to assume a constant Jacobian for each K_e.

Applying the assumption of a constant Jacobian over each primary cell to Eq. (3.16) requires then only to substitute the values obtained by the Jacobian matrix, the residuals of the primary cell and the normals of the corresponding node. Composing both first and second order derivatives it is possible to construct the global distribution matrix as,

$$D_{j|K_e} = V_{j|K_e}\left(I - \frac{\Delta t}{2n_d}\frac{n_{v(K_e)}}{V_{K_e}}\vec{A}_{K_e}\cdot S_{j|K_e}\right). \tag{3.17}$$

3.2.2 TTG numerical schemes

The Taylor-Galerkin family of schemes first appeared with Donea [52] and consisted in developing the same Taylor expansion as done for the LW scheme but performing a Finite Element discretization in space using the Galerkin discretization method. Due to the cell-vertex nature, no great difference is present in terms of discretization whenever compared to a Finite Volume approach. Indeed, residuals are calculated at the primary cell and redistributed to vertices while

for a Finite Element case these are directly calculated at the vertices. However, introducing the Finite Element discretization implies the apparition of a consistent mass-matrix that greatly improves the dispersion error [54] but also increases the cost of the update. The acronym that gives name to the section is Two-Step Taylor-Galerkin and relates to an improved version of the one-step scheme presented by Donea et al. [54] to extend the stability domain of the scheme, especially for a multi-dimensional problem. The extension to multi-step schemes (order higher than two) was provided in Safjan and Oden [155] but is only applicable in the context of h-p type elements. For AVBP only *P1* type elements (elements whose shape functions use only the vertices of each edge) are considered which limits the improvement of the schemes but at the same time limits the cost of the different operations.

The one-step family is first presented to show the disadvantages and justify the extension to the two-step method. The one-step family is not unique and depends on the time-integration order of the scheme. As presented in [37], the most popular time integrator is the Euler integration method. Ultimately, the difference with the LW scheme is that the truncation order of the Taylor expansion is of order three instead of second order.

Starting back with Eq. (3.7), the idea behind the first and second temporal derivatives introduced by the LW scheme is conserved Ni [130]. The treatment of the third order temporal derivative can not however be equivalent to the second order derivative. Instead it is dealt with using a simple Euler equation so,

$$\frac{\partial^3 U}{\partial t^3} = \frac{\partial}{\partial t}\left(\nabla\left[\vec{A}\left(\nabla\cdot\vec{F}\right)\right]\right), \tag{3.18}$$

or by commutation of temporal and spatial derivatives,

$$\frac{\partial^3 U}{\partial t^3} = \left(\nabla\left[\vec{A}\left(\nabla\cdot\frac{\partial}{\partial t}\vec{F}\right)\right]\right), \tag{3.19}$$

where $\frac{\partial F}{\partial t}$ is approximated by $\frac{F^{n+1}-F^n}{\Delta t}$ which renders the method implicit. The development done by Donea [52] used only the simple advection equation to treat more easily this Euler time integration method ending up with only a modified mass matrix. The stability limits of these schemes (shown in [52]) have led however to their disuse.

The development by Quartapelle and Selmin [146] of the two-step corresponding schemes eliminated issues. The coefficients used for their schemes can be generalized as done by Colin et al. [37] to present the whole family of schemes as detailed in Eqs. (3.20) & (3.21) where both steps are expanded,

$$\tilde{U}^n = U^n - \alpha\Delta t\vec{\nabla}\cdot\vec{F}^n + \beta\Delta t^2\vec{\nabla}\cdot\left(\vec{A}\,\vec{\nabla}\cdot\vec{F}^n\right), \tag{3.20}$$

$$U^{n+1} = U^n - \Delta t\vec{\nabla}\cdot\left(\theta_1\vec{F}^n + \theta_2\tilde{\vec{F}}^n\right) + \Delta t^2\left(\epsilon_1\vec{\nabla}\cdot\left(\vec{A}\,\vec{\nabla}\cdot\vec{F}^n\right) + \epsilon_2\vec{\nabla}\cdot\left(\vec{A}\,\vec{\nabla}\cdot\tilde{\vec{F}}^n\right)\right), \tag{3.21}$$

	TTGC	TTG4A
α	0.49	$\frac{1}{3}$
β	$\frac{1}{6}$	$\frac{1}{12}$
θ_1	0	1
θ_2	1	0
ϵ_1	0.01	0
ϵ_2	0	$\frac{1}{2}$

Table 3.1: Coefficients for the Two-Step Taylor Galerkin schemes implemented in AVBP.

where ˜ stands for the intermediate step variables.

If substituting Eq. (3.20) into Eq. (3.21) the expression resembles a Taylor expansion up to the fourth order. This meaning for example that to obtain a first order scheme $\theta_1 + \theta_2 = 1$ is required, and so on for higher order schemes. The choice of the coefficients is not trivial, as it could be desirable to have a lower order scheme to try to enforce other desired proprieties. In the original document [146] the choice was to develop two fourth-order schemes, notably *TTG4A* that is a scheme used in AVBP. However, for LES it is a good approach to try to have the lowest dissipation possible for a large range of wavenumbers which led to the developments of Colin et al. [37]. The coefficients used for these two schemes are presented in Table 3.1.

Before discussing the differences between schemes which is left for the next chapter where properties are tested, the Galerkin spatial discretization is introduced. By multiplying Eqs. (3.20) & (3.21) by the test functions ϕ_j leads to the weak formulation of the problem. There are three main operators that intervene for each step of the update, the two derivatives as for the LW scheme and the additional mass matrix inversion. The two derivatives are the *RHS* terms while the matrix operation is kept in the *LHS* term,

$$\underbrace{\int_{\Omega_j} \tilde{R}^n \phi_j dV}_{\text{LHS}} = \underbrace{-\alpha L_j(U^n, \phi_j) - \beta \Delta t L L_j(U^n, \phi_j)}_{\text{RHS}} \tag{3.22}$$

$$\int_{\Omega_j} R^{n+1} \phi_j dV = -L_j(\tilde{U}^n, \phi_j) - \gamma \Delta t L L_j(U^n, \phi_j), \tag{3.23}$$

remembering that U and R represent the conservative variables and the residual update respectively,

$$\begin{aligned} \tilde{R}^n &= \frac{\tilde{U}^n - U^n}{\Delta t} \\ R^{n+1} &= \frac{U^{n+1} - U^n}{\Delta t}. \end{aligned} \tag{3.24}$$

Note that in the above expression similar terms and identifications as for the LW description are retained. Notations are hence equivalent, only the field dependency differ: i.e. either $\tilde{U}^n$ or U^n. Functions are furthermore dependent on the shape function ϕ_j contrarily to the LW scheme as presented in Sec. 3.2.1. Similarly the *RHS* terms of Eq. (3.22) can be written as,

$$L_j(U^n, \phi_j) = \int_\Omega \nabla \cdot \vec{F}(U^n)\phi_j dV, \tag{3.25}$$

$$LL_j(U^n, \phi_j) = \int_\Omega \nabla \cdot \left(\vec{A}\left(\nabla \cdot \vec{F}(U^n)\right)\right)\phi_j dV. \tag{3.26}$$

This second term is decomposed using integration by parts to decompose the interior and boundary terms in a suitable way as will be shown later,

$$LL_j(U^n, \phi_j) = -\underbrace{\int_\Omega \vec{A}\left(\nabla \cdot \vec{F}(U^n)\right)\nabla\phi_j dV}_{LL_j^0(U^n,\phi_j)} + \underbrace{\int_{\partial\Omega} \phi_j \vec{A}\left(\nabla \cdot \vec{F}(U^n)\right)\vec{n}dS}_{BT_j(U^n,\phi_j)}. \tag{3.27}$$

The term noted as LL_j^0 is integrated over the whole domain as it is a volume integral while the second BT_j is different from zero only at boundaries. The difficulty concerning this second term is that additional boundary conditions must be provided. These BCs are discussed in Sec. 3.6. The final step is to apply the Galerkin method, taking the shape functions ϕ_k equal to the test functions previously noted ϕ_j. With this *LHS* are expressed as,

$$R^n = \sum_k R_k^n \phi_k, \tag{3.28}$$

$$\nabla \cdot \vec{F} = \sum_k F_k \nabla\phi_k, \tag{3.29}$$

$$\int_\Omega \tilde{R}^n \phi_j dV = \sum_k \left(\int_\Omega \phi_j\phi_k dV\right)\tilde{R}_k^n = \sum_k M_{jk}\tilde{R}_k^n, \tag{3.30}$$

where M_{jk} is the mass-matrix that must be inverted. The *RHS* terms of Eq. (3.22) are hence expressed similarly,

$$L_j(U^n, \phi_j) = \sum_{k|j\in K_e} L_k(U^n, \phi_j)_{K_e} \tag{3.31}$$

$$LL_j(U^n, \phi_j) = \sum_{k|j\in K_e} LL_k(U^n, \phi_j)_{K_e} \tag{3.32}$$

so only the neighbour primary cells contribute to the nodal residual. The development of the L term for a primary cell leads to,

$$L_j(U^n, \phi_j)_{K_e} = \sum_{k|k\in K_e} F_k^n \int_{K_e} \phi_j \nabla\phi_k dV, \tag{3.33}$$

and for the LL term,

$$LL_j(U^n, \phi_j)_{K_e} = A^n_{K_e} \sum_{k|k\in K_e} F_k^n \int_{K_e} \nabla\phi_j \cdot \nabla\phi_k dV - A^n_{K_e} \sum_{k|k\in K_e\cap\partial K_e} F_k^n \int_{\partial K_e\cap\partial\Omega} \phi_j \nabla\phi_k \vec{n} dS. \tag{3.34}$$

Various points must be noted before continuing. The first important assumption is the one taken to write Eq. (3.29). The Galerkin approach discretizes the conservative variables using certain test functions. If the fluxes were taken to be linear, this would not present any inconsistency, but this is not the case when dealing with the Navier Stokes equations where non-linearities are clearly present. This hypothesis has been addressed by Fletcher [65] who named this latter context of work group finite elements and stated two conditions for the well-posedness of the equations. The first one deals with the way the NS equations are written which must be in a conservative form. This presents no problem as equations are indeed solved using this formalism. The second condition is that only one type of interpolation is used for the group of terms it discretizes, meaning that the test functions are the same independently of the equation it is applied to. Thus, terms such as u^2, uv or v^2 must use the same test functions, e.g. $u^2 = \sum_k u_j^2 \phi_k$. This formulation allows a much simpler differentiation. In [65], various examples show that an improved behaviour with such recommendations is found if large discontinuities are encountered while maintaining a good accuracy at a much lower cost than classical Finite Element approaches.

Another hypothesis of importance is used when writing Eq. (3.34). The Jacobian is assumed constant inside the cell, which is true for linear type elements such as triangles and tetrahedra. This is not the case for bilinear type elements like quadrilaterals, although as stated in Colin et al. [37] it is only used for the second derivative terms.

Differences are nonetheless seen for this scheme for bi-linear or tri-linear elements such as quads, pyramids, prisms and hexahedra. If triangles or tetrahedra are used, the spatial discretization resembles that of Finite Volumes. This can easily be shown as in Auffray [9]: i.e.,

$$\nabla\phi_k = -\frac{\vec{s}_k}{n_d V_{K_e}}, \tag{3.35}$$

$$\int_{K_e} \phi_k dV = \frac{V_{K_e}}{n_v(K_e)} \qquad \forall k \in K_e. \tag{3.36}$$

It is then simple to show that Eqs. (3.33) & (3.34), neglecting the border contribution in the LL term, take the form,

$$L_j(U^n, \phi_j)_{K_e} = \sum_{k|k\in K_e} F_k^n \nabla\phi_k \int_{K_e} \phi_j dV = (\nabla\cdot\vec{F}^n)_{K_e} \int_{K_e} \phi_i dV = R^n_{K_e} \frac{V_{K_e}}{n_v(K_e)} \tag{3.37}$$

$$LL_j(U^n,\phi_j)_{K_e} = A^n_{K_e}\sum_{k|k\in K_e} F^n_k \nabla\phi_k \cdot \int_{K_e} \nabla\phi_j dV = -\frac{1}{n_d}(A^n_{K_e}R^n_{K_e})\cdot\vec{s}_{j|K_e} \tag{3.38}$$

which are exactly the expressions obtained previously for the LW scheme once the redistribution is done. Of course difficulties arise when the gradient can not be considered constant inside the cell. In this case, the approach followed in Colin et al. [37] is to add a correction to the bi-linear and tri-linear elements as simple quadrature leads to oscillatory profiles. The correction proposed by Colin et al. [37] consists in splitting the $\Theta_{j,k}$ matrix in Eq. (3.39) into two parts $\Theta^0_{j,k} + \Theta^1_{j,k}$ where,

$$L_j\left(U^n,\phi_j\right)|_c = \sum_{k\in K_e} F_k \Theta_{j,k}|_c, \tag{3.39}$$

and

$$\Theta_{j,k}|_c = \int_{K_e} \phi_j \nabla\phi_k dV, \tag{3.40}$$

$$\Theta^0_{j,k}\Big|_c = \int_{K_e} \phi_j \overline{\nabla\phi_k} dV, \tag{3.41}$$

$$\Theta^1_{j,k}\Big|_c = \int_{K_e} \phi_j \left(\phi_k - \overline{\nabla\phi_k}\right) dV. \tag{3.42}$$

In the case of regular elements,

$$\overline{\nabla\phi_k} = {\nabla\phi_k}^{FV}, \tag{3.43}$$

which is equivalent to

$${\nabla\phi_k}^{FV} = -\frac{\vec{s}_k}{n_d\ V_{K_e}}. \tag{3.44}$$

This last formulation is adequate but as soon as the element is deformed a transformation matrix T is needed to map the original element onto the canonical reference element as shown in Fig. 3.3. The definition of this matrix is given as $T = |P|\left(P^T\right)^{-1}$ where $P = \frac{\partial x}{\partial \tilde{x}}$ is the Jacobian geometrical matrix and $\tilde{x}$ corresponds to the canonical coordinate system. This mapping is taken to be constant for each element which implies it is treated as if it were a regular element and hence evaluated at the barycentre of the cell. This implies that only the average distortion is taken into account comparatively to the real deformation and thus does not take into account the exact metrics.

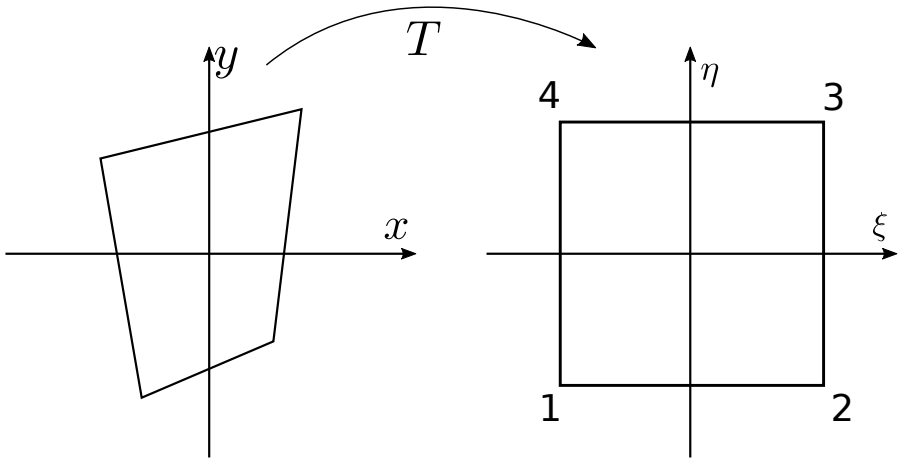

Figure 3.3: Detail of mesh dual cell.

The missing step concerns the *LHS* terms of Eqs. 3.22 and the inversion of the mass matrix. Following [36] there are alternatives to the exact inversion of the whole matrix containing all the degrees of freedom of the system, which can be memory intensive when large numbers of degrees of freedom are used and the problem is to be parallelized. These methods are iterative methods and locally invert the matrix as described below. One of the most popular methods is the Jacobi method, which in very few iterations allows to converge towards the solution accurately. The process can be summarized in the following:

- Copy initial residual $\tilde{R}_j^n$, Eq. (3.45), to new variable,
- Scale initial residual with D^{-1}, (cf Eq.3.47), where D represents the diagonal of the lumped mass matrix M,
- Multiply (M-D) matrix by scaled residual, Eq. (3.47),
- Add copy of residual,
- Scale result by D^{-1} if final iteration is not reached.

Mathematically, this could be represented by the following operations,

$$\tilde{R}_j^n = -\alpha \frac{1}{V_j} \sum \frac{1}{n_{v(K_e)}} V_{K_e} R_{K_e} + \beta \frac{\Delta t}{2 n_d V_j} \sum \left(\vec{A}_{K_e} \cdot R_{K_e} \right) \cdot \vec{S}_{j|K_e}, \tag{3.45}$$

$$\int R_j^n \phi_j dV = \sum_j \left(\int \phi_k \phi_j dV \right) R_k^n = \sum_j M_{jk} R_j^n, \tag{3.46}$$

$$\left(\tilde{R}^n \right)^i = \left(\tilde{R}^n \right)^0 - D^{-1} \left(M - D \right) \left(\tilde{R}^n \right)^{i-1}, \tag{3.47}$$

$$\left(\tilde{R}^n\right)^0 = D^{-1}\tilde{R}_j^n. \tag{3.48}$$

This specific iterative method has been verified to tend to the exact solution when inverting exactly the matrix using a bi-periodic mesh. The stencil is affected by the number of inversion steps performed and is larger when the number of Jacobi iterations increases. This is logical as each Jacobi step affects locally the neighbour cells and hence nodes, of the initial set of degrees of freedom. Of course, it is necessary to define the number of iterations to be performed in the Jacobi method to assure a sufficient accuracy while guaranteeing no excessive cost. Tests performed in [36] show that for academic cases when the number of iterations is equal or larger than two, the errors between the iterative and the exact approaches are sufficiently small to be considered acceptable.

3.3 Diffusion schemes in AVBP

Diffusive fluxes require additional considerations for their discretization. The additional requirements are due to the presence of the gradients in the diffusive fluxes defined in App. A. The literature is vast on this matter, so the following focuses only on unstructured multi-element meshes that are of interest for this thesis. In a cell-vertex context and using unstructured meshes as in AVBP, constructing an operator becomes even more cumbersome due to the duality of the meshes already seen and because the stencil connectivity is harder to access. The type of dual cell is of type median dual as in [13] so the cell nodes are at the centroids of each cell but also at the center of the edges of the intersected faces as seen in Fig. 3.2a. The cell-vertex approximation is also known to be much better when compared to a cell-center approach as the number of operations scales with the number of edges while the cell centered approach scales with the number of elements. In 2D this does not imply a much larger cost but it does largely increase in 3D. Depending on the metrics, more specifically the type of elements, it has been shown by Barth [11] that triangular and tetrahedral type elements are conservative and additionally, the gradient is constant over the element. The objective behind such operators are also in Barth [11] and summarized in Puigt et al. [145]. The operator should indeed satisfy the following criteria to be efficient:

- Consistent,
- Conservative,
- Monotonic,
- Second-order accurate,
- Insensitive to mesh quality,
- and rely on a compact stencil.

In AVBP there exist two operators, the FV 4Δ operator and the FE 2Δ operator. Using the previous criteria these two operators are compared in terms of performance. Consistency is guaranteed for the FV 4Δ in all cases but this is not the case for the FE 2Δ operator for certain connectivity as defined in Colin [35]. This however does not affect the quality of the results as shown in the same document. Both operators are built to be fully conservative and second-order accurate in all cases for regular meshes but neither of them is monotonic. This means that the appearance of chequerboard modes is expected. However, due to the Finite Element formulation and the more compact stencil, the FE 2Δ allows to diffuse the chequerboard modes contrarily to the FV 4Δ. This FE 2Δ operator was purposely developed to dissipate these chequerboard modes and is today the standard option for AVBP simulations. Both of these operators are detailed hereafter. It is important to note that for this section and to differentiate the notation from previous sections, the superscript V is used to denote the viscous part of the problem.

3.3.1 FV 4Δ operator

The spatial discretization is evidently the same as for the convection schemes so the same hypotheses are taken into account when dealing with non-linear elements. The first operation to be performed is the obtention of the gradient at each node. To do this, the gradient is calculated in all primary cells represented in Fig. 3.4 using,

$$\vec{\nabla} U_{K_e} = \frac{1}{n_d \, V_{K_e}} \sum_k U_k \vec{s}_k, \tag{3.49}$$

and redistributed to the nodes so that,

$$\vec{\nabla} U|_j = \frac{1}{V_j} \sum_k \frac{V_{K_e}}{n_{v(K_e)}} \vec{\nabla} U_{K_e}. \tag{3.50}$$

Once the gradients are obtained at all neighbour nodes to j, the diffusive fluxes are recalculated using both the conservative variables and the gradients previously calculated in the cells shaded in Fig. 3.4

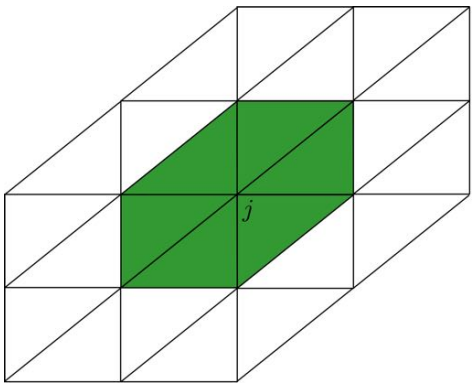

Figure 3.4: Complete connectivity around node j for FV 4Δ. Gradients are required in all the primary cells and the divergence operator is applied only to the shaded cell.

$$R^V_{K_e} = -\frac{1}{n_d V_{K_e}} \sum_{k \in K_e} \vec{F}^V_k \cdot \vec{s}_k, \tag{3.51}$$

and redistributed once again using Eq. (3.50).

3.3.2 FE 2Δ operator

The passage to the 2Δ stencil is necessary to dissipate unwanted modes. The introduction of the Finite Element method instead of the Finite Volume approach that would be cheaper and easier to implement, is justified by the need to filter any diagonal modes that could appear [35]. Note that for triangular elements however the method degenerates into a Finite Volume scheme.

Instead of extending the stencil to the $n+2$ neighbours as for the FV 4Δ, only the $n+1$ neighbours are used as for the median dual cell. The calculation of the gradients is analogous to the one calculated for the fluxes for the family of convective TTG family schemes. These gradients are corrected for the non-linear elements for the set of primitive variables necessary to construct the viscous fluxes using the same operators. The divergence is then calculated around the dual cell of node j,

$$\vec{\nabla} \cdot \vec{F}^V = \frac{1}{n_d V_j} \sum_{j \in \Omega} \vec{F}^V_{j|K_e} \vec{s}_{j|K_e}. \tag{3.52}$$

This operator provides the necessary ingredients to avoid the apparition of diagonal modes, in no case excluding the appearance of other type of oscillations that are common in these simulations.

At this point, all of the operations either linked to the spatial or temporal operators have been detailed. Although most of the discussion has focused on the LW or TTG schemes that are mainly used for LES, other schemes are also implemented in AVBP. An important property that clearly differentiate all these numerical schemes relates to their stability limits.

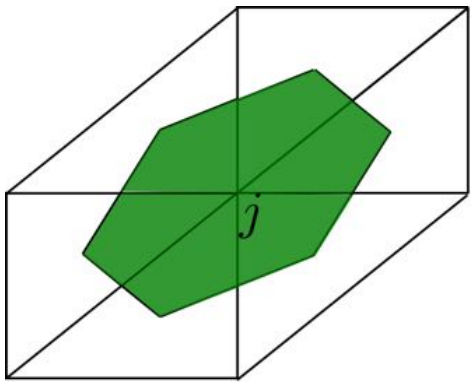

Figure 3.5: Complete connectivity around node j for FE 2Δ. Gradients are required in all the primary cells and the divergence operator is applied only to the shaded cell.

3.4 Numerical scheme stability constraints

The update of the global variables at the end of the iteration requires a time advancement. This advancement impacts the temporal accuracy of the scheme as well as impacts its overall characteristics. In the end, the main problem resides in calculating the time advancement step Δt to be used so as to ensure a stable scheme while keeping under control its main spectral properties.

There are two parameters that account for the stability limits in a non-reactive flow, one due to the convective advancement (CFL) and one due to the diffusion limit (Fourier number). The definition of the CFL already provided reads $CFL = \frac{(u+c)\Delta t}{\Delta x}$ where u and c are the convective velocity and sound speed. In schemes present in AVBP the maximum value should be of order $\mathcal{O}(1)$ considering it uses an explicit time advancement. The Fourier number is defined as $F = \frac{D\Delta t}{\Delta x^2}$ where D is the diffusion coefficient and limits diffusion dominated problems.

3.4.1 CFL number

Using the definition given of the CFL, the stable value the CFL can take depends on the scheme used and logically, the highest limit possible is searched. In the case of a one-dimensional scheme Δx is uniquely defined, not being always the case for higher-order dimension problems, especially if the elements are deformed. In this case, the information might propagate in a direction different to the main directions and so, the characteristic distance requires to be defined in another way. The choice is to use the *L2-norm* of the velocity propagation in each cell, which for a 2-D case reads,

$$norm_{K_e} = \frac{1}{2}\sqrt{\sum_{k\in K_e} \left(|u\cdot s_1 + v\cdot s_2| + dsc_k\cdot\vec{c}\right)^2}, \tag{3.53}$$

where dsc_k is the geometrical norm defined by $dsc_k = \left(\vec{s}_1^2 + \vec{s}_2^2\right)^{0.5}$ and normals s_1 and s_2 are vertex based norms in global coordinates respectively. Then the Δt for temporal integration of the scheme is the minimal value over the whole domain Ω reading,

$$\Delta t = min_\Omega \left(CFL \frac{V_{K_e}}{norm_{K_e}} \right). \tag{3.54}$$

3.4.2 Fourier number

The Fourier number is the equivalent for the diffusion fluxes to the CFL values. In this case, the difficulty resides again in estimating the characteristic length scale which is calculated through the following relation in AVBP,

$$\Delta x^2 = \frac{2V_{K_e}}{\sum_{k\in K_e} s_k^2/n_d^2}. \tag{3.55}$$

Once again, it is necessary to search for the minimal value in the whole domain to set the limit. In general, or at least for all tests performed in the following, this parameter does not represent a constraint whenever compared to the CFL number.

The compliance of these constraints leads, in theory, to stable schemes. In practice however, issues such as strong physical discontinuities or the existence of non-regular metrics affect negatively the accuracy of the different operators, in occasions, being at the origin of oscillations. This has led many authors to develop a framework where a dissipation operator is added to minimize the presence of such output without it being too dissipative, a desired property when performing LES.

3.5 Artificial viscosity (AV)

Convective schemes in AVBP are spatially centered which is known to present oscillations in regions where the fields vary abruptly. The effect of chequerboard spurious modes should be minimized and this requires the addition of a carefully chosen dissipation operator to deal with these oscillations. The Artificial Viscosity (AV) does not only eliminate these high-frequency oscillations but improves the convergence of the scheme being highly dependent on the amount of viscosity added [154]. A high value of artificial viscosity however is inconvenient for LES purposes as it artificially modifies the Reynolds number of the flow so a balance must be found which is also different depending on the configuration and the flow topology. In cases of strong discontinuities such as shocks it is also applied to mitigate its effects. The application of the artificial viscosity in a simulation falls upon two main steps: to detect the need to apply the AV, done with a *sensor* and the correction applied through an *operator*.

3.5.1 The operators

There are two AV operators in AVBP, a second-order pseudo Laplacian sharp sensor and a fourth-order pseudo bi-Laplacian operator. The order of each operator and how to obtain them is detailed in Jameson et al. [84]. They have the following properties:

- Second Order operator

  The second order operator introduces viscosity in the same way diffusion terms do. It is thus applied locally and exclusively in regions where very strong gradients are encountered. Some approaches use it exclusively in regions where shocks are encountered to smooth variables such as pressure or density, but may of course be active in regions of strong physical gradients. Others such as Stringer and Morton [176] however indicate that this operator should be inactive in regions where shocks are present since resulting in a thickening that is incorrectly predicted. The former approach is however the one adopted in AVBP.

- Fourth Order operator

  It is as a bi-Laplacian operator used to suppress the spurious high-frequency modes. It has been shown to be effective to treat both chequerboards and washboards that are related to the errors committed in the residual estimation while the latter are associated

to errors in the redistribution matrices [176]. Improvements are available by increasing even further the order of the operator (up to 6^{th} order) towards the same end, which is reducing the spurious oscillations.

The way they are combined is determined both by the sensor and by user-defined parameters. Both operator contributions are first computed on each cell vertex, and are then scattered back to nodes.

3.5.2 Sensors

The sensor is either active or not in a boolean sense, meaning the sensor is active when there are steep gradients present in the flow (higher than a certain predefined value). The stencil and the fields that intervene in the detection differentiate each model. Depending on the sensitivity of the sensor each one will determine different activation locations depending on the field studied. Various types of sensors are available in AVBP, the main ones being the Jameson-sensor [84] and the Colin-sensor [34].

3.5.2.1 The Jameson sensor

The variable it is based on for the activation is denoted as S in the following section, usually being pressure. The sensor is calculated at the vertices and is active when:

$$\zeta_k^J = \frac{|\Delta_1^k - \Delta_2^k|}{|\Delta_1^k| + |\Delta_2^k| + |S_k|}. \tag{3.56}$$

Δ_1^k and Δ_2^k being functions that are written as,

$$\Delta_1^k = S_{\Omega_j} - S_k, \qquad \Delta_2^k = (\vec{\nabla} S)_k.(\vec{x}_{\Omega_j} - \vec{x}_k), \tag{3.57}$$

where Ω_j is the subscript for cell-averaged values and $\vec{x}$ represents the coordinates. Δ_1^k measures the variation of S inside each cell Ω_j. Δ_2^k is an estimation of the same variation but on a wider stencil (using all the neighbouring cell of the node). The operator is proportional to the second derivative of S, which is zero in the linear case and different from zero when the gradient of S varies rapidly.

3.5.2.2 The Colin sensor

The Jameson sensor, used mainly in the framework of steady-state computations, is too dissipative in most unsteady turbulent simulations. The necessity to develop a more sensitive operator to capture the small gradients but also able of applying large dissipation values in the presence of shocks for example, led to the development of the Colin sensor.

The properties of the sensor can be resumed in,

- It is very small when both Δ_1^k and Δ_2^k are small compared to S_{Ω_j}. This corresponds to low amplitude numerical errors (when Δ_1^k and Δ_2^k have opposite signs) or smooth gradients that are well resolved by the scheme (when Δ_1^k and Δ_2^k have the same sign).

- It is small when Δ_1^k and Δ_2^k have the same sign and the same order of magnitude, even if they are quite large. This corresponds to stiff gradients well resolved by the scheme.
- It is big when Δ_1^k and Δ_2^k have opposite signs and one of the two term is large compared to the other. This corresponds to a high-amplitude numerical oscillation.
- It is big when either Δ_1^k or Δ_2^k is of the same order of magnitude as S_{Ω_j}. This corresponds to a non-physical situation that originates from a numerical problem.

The previous artificial viscosity algorithms are necessary for the numerical stability of the cell-vertex schemes that is to say, from a purely numerical point of view. From a mathematical point of view however, the problem has not been properly closed yet because it requires to impose the boundary conditions. These are important from the physical point of view of the problem as they determine the flow, the mathematical closure of the system to correctly solve the equations and the numerical stability of the scheme which can be affected by their imposition.

3.6 Boundary conditions (BC)

Literature is rich about the number of physical variables to be set at each boundary to close the mathematical problem [175]. In terms of physics, there are two possible conditions of interest to be imposed in a fluid problem.

- **Physical boundary conditions**

  The physical boundary conditions are those imposed to solve the PDE. The distinction between both BCs is made because one targets the physical variable and the other type imposes the spatial derivative of a physical value.

  Dirichlet BCs

  Dirichlet boundary conditions are conditions to be set directly onto the solution variable. An example of this type is the velocity at the wall. Indeed, an impermeability condition must be set for a wall so the fluid may not cross the solid boundary. Hence, the normal velocity to the wall must be zero. Likewise for a non moving wall, the tangential velocity of the fluid should be zero:

$$\vec{u} \cdot \vec{t} = 0, \tag{3.58}$$

  where $\vec{t}$ represents the tangential vector.

  Neumman boundary conditions

  Boundary condition applied to the first spatial derivative. Using again the example of the wall, in the case of an adiabatic wall where, by definition, the heat exchange is zero. This is represented by

$$\vec{\nabla} T \cdot \vec{n} = 0, \tag{3.59}$$

where $\vec{n}$ is the normal vector to the surface.

The choice of well-suited BCs for LES presents further difficulties. Additionally to the physical interactions that must be respected, imposing either the Dirichlet or the Neumann BCs in a *hard* way can induce different types of numerical errors. A common error is found in the prediction of waves impacting a wall and the consequent inaccurate reflection. It can be shown [185] that discontinuities in the flow (either physical caused by a boundary limit or numerical due to an abrupt change of mesh cell size) *always* leads to a dispersion error of the waves reflected by the wall (see Chap. 4). This effect must be minimized to have a good LES. The characteristic boundary conditions [138] provide a path to comply with the physics by relaxing the solution predicted by the scheme towards the target value.

- **Characteristic BC's**

  This kind of approach was first introduced by Thompson [181] to account for the interaction between waves at boundaries using the Euler equations. The validity of these conditions was limited to the inviscid flow and was extended to the viscous flow by Poinsot and Lele [138]. The principle consists in providing a solution at the boundary from the balance between incoming and outgoing waves. The outgoing waves of the domain contain physical information as they are calculated from the interior domain. The incoming waves however, have no physical sense as it would require outside information that is not available. The conditions are then appropriately set as ingoing/outgoing, in a wave sense, which will be transformed back in the original variables performing matrix operations. The whole set of equations is extensive and may be found in [181, 200].

  With these approaches, the main problem resides in the correct estimation of the waves. Great advancements in the amplitude estimation of waves in the Euler equations formalism were done by Nicoud [131], who took into account the importance of the three-dimensional effects of the boundary layer as well as the effect of developing the partial differentials in a spatial or a temporal space. The method was extended to the Navier-Stokes equations by Prosser [144]. One of the main problems when doing a study of wave interaction is that only the partial derivatives are considered, which may lead to drifts as no hard condition is imposed. A solution proposed by Yoo and Im [199] consists in introducing a relaxation factor to suppress spurious oscillations. This method works quite well but is too dissipative for higher frequencies and must be handled with care in LES or DNS simulations. Lamarque et al. [101] showed the difference between the use of normal Dirichlet boundary conditions and characteristic conditions, demonstrating the slightly more dissipative behaviour of the characteristic conditions but suppressing many output errors. Other studies have extended the formulation originally provided by [138] including additional terms as in Yoo et al. [200] or extending it to a broader range of

boundary conditions as done by Lodato et al. [110].

Imposing BCs in a hard or a weak way is not the only issue for certain numerical schemes such as for those used in AVBP. Additional problems appear because the development of high-order schemes, that require higher order derivatives [139], results in the need for additional boundary conditions. The increase in order, as done when using a Taylor expansion to increase the temporal order (see Sec. 3.2) thus requires high-order derivatives to close the problem at the boundaries. The problem resides in the fact that *no available physical boundary conditions exist to satisfy the mathematical needs*. This has led to name these conditions as numerical BCs. For example, when developing Eq. (3.27) in Sec. 3.2.2, a surface integral appears during the derivation. But why isn't there a physical condition? For a convective scheme it would require to impose a condition for the spatial derivative as a BC. There are two ways to treat these terms in AVBP which are studied in detail in the following. The *USOT* formulation which consists in setting the $BT_j(U^n, \phi_j)$ term to zero. The second possibility is the *CSOT* formalism which sets the $LL_j(U^n, \phi_j)$ term to zero at the boundary nodes. Again, these terms do not have any physical meaning and are dealt with specifically in Sec. 7.2.

In this chapter the AVBP code and the subtleties related to numerical schemes have been approached. The cell-vertex formalism has been detailed as it is the method AVBP is based on. The convection operator is detailed for both low-order and high-order schemes. The truncation error is clearly superior for high-order schemes and the mass-matrix that appears from the FE context notably improves the spatial order. In that respect high-order schemes are expected to behave more accurately in any type of configuration, something that is questioned in Chap. 7. This is however confirmed and detailed analyses discussed in the next chapter or later on highlight the importance of knowing what is behind each numerical scheme, its virtues and its defects. The next chapter is dedicated to the 1D and 2D spectral analysis of the schemes in AVBP. The objective behind this is to understand and illustrate their behaviour at both high and low resolution.

Chapter 4

Spectral properties of the AVBP schemes

Contents

It has been observed that CFD numerical solvers have a recurrent appearance of oscillations near discontinuities or at interfaces between different elements, physical gradients, i.e. shock waves, or geometry boundaries [187]. Such issues have also been reported in numerical simulations in other fields of study as in seismic imaging, see Scales [157]. The nature of these oscillations can be due in some cases to an insufficient mesh resolution. In other cases, they might be due to numerical issues inferred by a numerical boundary treatment for example. It is these numerical issues that will be studied during a great part of the present work as they are important in two aspects. The first one is how it influences the physical field itself and its sensitivity to perturbations. The second one is to actually simulate a problem robustly without a crash of the algorithm due to bad quality grids for example.

Numerical oscillations are one of the hardest problems today in CFD. Most of these problems arise from the fact that there is a physical under-resolved effect that is not captured by the scheme for the present mesh. When this happens, the most usual output is the feared 'wiggles'. Various approaches are possible to deal with these numerical artifacts. Eliminating such oscillations is justifiable as they may spatially grow and convect (while remaining bounded and causing no stability issue for the scheme and simulation) inducing an interaction with physical scales and thus modifying the flow prediction. Others like Gresho and Lee [73] have the opinion that an attempt to eliminate these oscillations is not the optimal path. It is necessary to understand the reasons that cause their appearance and correct the cause and not the output, by adapting the local grid resolution for example. The most commonly accepted diagnostic is that these oscillations must remain 'bounded' so that they will not lead to the crash of a simulation nor affect the small scales encountered. For fluid flows, unresolved physics are most common in complex physical regions such as near-wall flows where not only the physics is to be captured

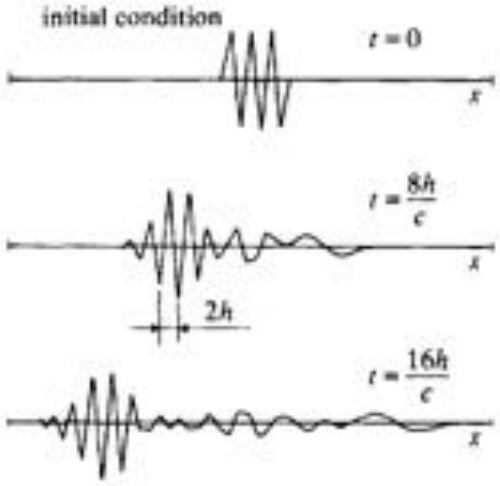

Figure 4.1: Group velocity as shown by Vichnevetsky and Bowles [187]. Three snapshots of a spatially evolving signal highlights the dispersion it undergoes.

by the solver but it is also a region where the numerical scheme is usually adapted to allow the treatment of the imposed boundary condition. This is a difficult situation as various problems are possible and may even coexist. The boundary condition applied and how it is implemented in the scheme is not a trivial nor straightforward process. Boundary conditions are associated to domain limits where the discretization is distorted as a result of the lack of points in the proximity of a wall for example.

Boundary conditions previously presented in Chapter 3 are sufficient to account for the physical interactions and for certain cases, represent a well-posed system following Gustafsson and Sundstrøm [74]. This however might not be enough in terms of numerical boundary conditions. The most common output which can be observed is the existence of node-to-node oscillations, also known as wiggles. These oscillations can be explained by the non-uniqueness of the solution to the associated numerical problem in the wavenumber spectra: i.e. non-monotonic curves [187], see Fig. 4.1. A great number of numerical schemes are analyzed in this document to determine the stability using a Fourier analysis. One of the most important findings in [187] was that an increasing spurious behaviour, even for almost hyperbolic equations, is found when low-order degree of accuracy is used for the spatial discretization near boundaries. This critical observation assures that independently of the scheme used (except for spectral methods), a wave impacting a boundary can generate additional numerical waves and that chain of reaction will be worse if low-order discretizations are used! A later study done also by Vichnevetsky [186] for finite element scheme boundaries showed the effect of treating upwind and downwind boundaries and how this can affect the reflection of non-physical waves (q-type) as well as energy conservation to try to improve the behaviour. Conclusion is then that the degradation of the scheme is to be held responsible for spurious effects near boundaries and thus their appearance is inevitable.

This additional problem of scheme degradation is common to all schemes as a result of the

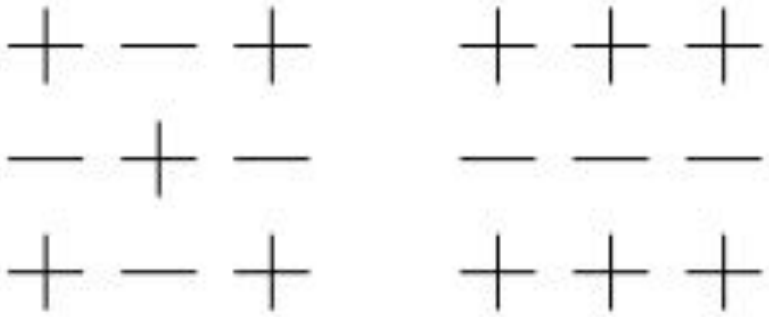

Figure 4.2: Chequerboard mode and washboard modes on left and right respectively.

existence of a set of cells which do not have a neighbour that inevitably decreases the order for any type of discretization. It is natural to study if additionally to the apparition of these unwanted waves this could affect both the robustness and accuracy of the simulation leading to a decrease of the global scheme order. Kreiss and Gustafsson et al. [98, 75] have shown, using different approximation methods for both inviscid and viscous flows, that the decrease in order due to the lack of neighboring nodes will not affect the global scheme if there is a loss of no more than one order of accuracy at the boundary $\mathcal{O}\left(\Delta x^{global-1}\right)$.

Assuming the previous condition is respected, these non-physical waves can also be related to the way the boundary conditions are imposed in a strong (imposing directly the condition on the boundary) or a weak way (relaxing the value towards the target) [1]. Weak solutions have been seen to be more accurate and less oscillatory on coarse meshes compared to imposing the strong solution which is more accurate in a sufficiently refined mesh. To try to relax the appearance of spurious oscillations, remembering we are in a fully compressible context, characteristic type boundary conditions are preferred to impose boundary conditions in terms of ingoing and outgoing waves.

The presence of oscillations in the near wall-region is not new for the cell-vertex used in AVBP and is thus even expected if no specific care or treatments are added. From the first applications to the NS equations in Crumpton et al. [45] it was seen that artificial viscosity was a necessary step to dissipate not only the spurious waves already mentioned but also to treat additional problems related to the cell-vertex method, notably chequerboard and washboard modes. Of course, at first instance it is difficult to discern what type of oscillation is present in the simulation and only numerical experiments may lead to the real origin of oscillations that are, if not noted until now, case dependent.

Most numerical tests in the literature are performed on perfectly isotropic regular meshes [99]. However, this is not the case in most of the real applications done today where very different cell volumes are encountered in the same mesh. This is certainly the first analysis to be performed, especially when more complex metrics are present, see Chap. 7. One might then be tempted to analyze the effect not only of distorted meshes but also on meshes with high

aspect ratios. It is thus necessary to ask in which situations this might be an issue because an error is being introduced. It is known that redistributing the residual calculated at a dual cell and assigning it to the node instead can introduce a discretization error [21]. This is why upwind discretizations are commonly introduced to try to control possible errors that arise from this additional dissipative step [67]. If no upwinding is explicitly done however, the errors can be large when this difference is important. In general, for all LES schemes it is desired that the dissipation be minimal to retain the original signal while being transported at the correct speed. A good balance must hence be found.

The following chapter introduces the necessary concepts and notation used for the present chapter which will be also used in Chap. 7. A short description of the consistency of the AVBP schemes is given, proof being found in [99]. Then, a von Neumann analysis is accomplished in 1-D and 2-D. At first, the approach taken is to perform a classical Fourier analysis of the schemes implemented in the solver to evidence specificities of each scheme and go beyond the respective CFL criterion. The 1-D case provides useful information but only represents the behaviour in one direction and is limited as the multi-dimensional will be shown to be very different. A 2D Fourier analysis has then been performed for bilinear elements such as the one done in Donea et al. [54]. Doing so allows to have a deeper understanding of the main errors which are then studied numerically; i.e. dissipation by analyzing the modulus and dispersion by studying the phase error of the amplification factor. In whole, the final goal to be achieved is to track the possible sources of instabilities and to understand their apparition at first instance.

4.1 Concepts and definitions

Numerical schemes are required to obtain an approximate solution to the continuous Partial Differential Equation (PDE). It is then natural to ask what degree of accuracy is to be expected from seemingly very different schemes. With such an objective in mind, it is necessary to establish certain criteria to evaluate and compare the different approaches. The criteria taken to do this are *consistency*, *stability* and *convergence* and stem from the work of mathematicians whenever confronted to such issues and the derivation of schemes.

- Consistency

  A numerical scheme is said to be consistent if the truncation error between the discretized and continuous PDE tends to zero when the spatial and temporal steps also go to zero. This implies that in the limit where $\Delta x \to 0$ and $\Delta t \to 0$ the equation being resolved is indeed the original continuous equation.

- Stability

  A scheme is defined as stable for finite values of Δx and Δt if the error between the exact solution of the scheme and the numerical approximation remain bounded. This means that since it is impossible to take values of $\Delta x = 0$ and $\Delta t = 0$ to resolve the exact continuous equation, there will always exist a numerical approximation. This approximation has to be the same as the exact discretized equation, or to have an error that does not

increase as the number of time steps increases. Defining ϵ_i as the error (can be due to various reasons, i.e.; round-off errors), the following should hold

$$\lim_{n\to\infty} \mid \epsilon^n \mid < C, \tag{4.1}$$

i.e. the error must be bounded as the number of iterations tends to infinity, C being a real number.

- Convergence

  The numerical solution obtained with a numerical scheme must converge to the exact solution of the continuous PDE when $\Delta x \to 0$ and $\Delta t \to 0$. This may seem to be the same condition as for consistency, the difference being that in this case it is the numerical solution that must tend to the exact solution.

All three criteria are clearly not independent relations and led to the equivalence theorem of Lax that states that for a well-posed initial value problem that is consistent, the scheme is convergent if and only if the stability condition is verified. So,

$$Consistency \ + \ Stability \ = \ Convergence. \tag{4.2}$$

Effectively, investigation of the consistency of a scheme resides in identifying the truncation error both spatially and temporally to evaluate its order of accuracy $\epsilon_{truncation} = \mathcal{O}\left(\Delta x^p, \Delta t^q\right)$. Developing the numerical scheme in a Taylor expansion, it is possible to eliminate the lower order errors to obtain what is known as the modified equation as described by Warming and Hyett [191]. Applying this method it is possible to discern the lowest order error performed and in turn determines the order of the scheme. In terms of stability however, there is a wider range of problems to be studied as there is a clear influence of the steps taken for time advancement (related to the spatial step through the CFL value) as well as the inclusion of the boundary conditions in the problem or not. Many methods exist and are explained in the following section.

For what remains in this document, the consistency of the scheme will be assumed in agreement with the results demonstrated by Lamarque [99], results being shown in Sec. 4.2 but no demonstration will be provided for the specific schemes of AVBP. The stability is then analyzed using a standard von Neumann approach for a convection problem where the phase speed c is assumed to be constant, first in a 1D context and then moving to a 2D context where the properties are shown to differ. It will be shown that the properties of the schemes are determined by the CFL value associated to each scheme and will justify the use of high-order schemes (TTG family) which perform better when compared to simple second-order schemes (LW).

4.2 Consistency results

To further understand the dispersion properties of the high-order schemes, a modified equation analysis was shown in Lamarque [99] to define the order of the scheme. The modified phase

velocity (Ω) of the schemes previously presented, which can all be seen to be fully consistent, and whose stability is going to be studied are,

$$\Omega_{LW} = kc - \frac{c\Delta x^2}{6}\nu k^3 - i\frac{c\Delta x^3}{8}\nu\left(1-\nu^2\right)k^4 + \mathcal{O}\left(\Delta x^4\right) \tag{4.3}$$

$$\Omega_{TTGC} = kc - i\frac{c\Delta x^3}{24}\nu k^4 - \frac{c\Delta x^4}{360}\left(3\nu^4 - 10\nu^2 + 2\right)k^5 + \mathcal{O}\left(\Delta x^5\right) \tag{4.4}$$

$$\Omega_{TTG4A} = kc - i\frac{c\Delta x^3}{24}\nu\left(\nu^2 - 0.02\right)k^4 + \frac{c\Delta x^4}{360}\left(12\nu^4 - 4.7\nu^2 - 2\right)k^5 + \mathcal{O}\left(\Delta x^5\right) \tag{4.5}$$

where the error is determined by the lowest order of Δx, k is the wavenumber denoted by $\frac{2\pi}{\lambda}$ and λ varies between $2\Delta x$ and ∞, c is the phase velocity and ν is the CFL value. The low-order LW method scales with Δx^2 while the other two scale with Δx^3. The term not present in the higher-order schemes can be shown to be directly related to the dispersion properties and is thus the reason why TTGC and TTG4A perform better on this specific property usually desired for any LES.

4.3 von Neumann stability analysis

The most widely used method to study the stability of a scheme is the **von Neumann analysis** which was developed by Crank and Nicolson and documented by von Neumann and Richtmeyer [43, 188]. The method is based on the expansion of the numerical solution in a finite Taylor series which is analogous to the finite difference method. This expansion is then decomposed into Fourier modes (normal spatial and temporal modes). A crucial point that is implied in the development of the Fourier series is the linearity of the solution. The solution is only true if each mode is independent from the others which is important to note especially when applying it to a set of non-linear equations such as NS. The condition for this method to be applicable also requires the solution to be defined over the real axis, meaning that 2π periodic conditions are assumed at all boundaries. Clearly, the applicability of the method when other type of boundary conditions of interest such as walls, is greatly limited and it is necessary to evaluate the error performed when assuming such a specific context. Another requirement is that the solution must also be square integrable [53]. More importantly, the method requires the uniformity of the discretization as it needs each node to be fully discretized by the same equations. To study the stability, it is possible to either study the computed solution and therefore the error, as it is also a solution to the discretized equations,

$$u_i = \bar{u}_i + \epsilon_i, \tag{4.6}$$

where u_i is the exact solution to the discretized equation which is decomposed into the solution obtained with the truncated scheme $\bar{u}_i$ and the associated round-off error ϵ_i. Note that the

numerical solution decomposition includes the truncation error and can only be a solution of the original PDE if the scheme is consistent and is thus a pre-requisite to be confirmed.

The decomposition in Fourier modes allows the separation of temporal and spatial domains. As the interest in the method resides in the growth or decay of the solution over time to determine the stability of the scheme, it is commonly the error which is studied as it has the same behaviour. The amplitude V_j^n of the k_j Fourier mode contains the temporal contribution while the exponential part contains the space dependency,

$$u_i^n = \sum_{j=-N}^{N} V_j^n e^{-\imath k_j \Delta x}. \tag{4.7}$$

The condition for stability can then be expressed as in von Neumann and Richtmeyer 'the amplitude of any harmonic must not grow indefinitely in time when n tends to infinity'. This leads to the definition of the complex number called amplification factor,

$$G_j = \frac{V_j^{n+1}}{V_j^n} = \mid G_j \mid e^{\imath\Phi}, \tag{4.8}$$

where $\Phi = kc\Delta t$ which relates the amplitude of a given harmonic at two consecutive time steps and is defined as stable when for any $j \mid G_j \mid < 1$. No indications will be given on how to perform a stability analysis as the literature is rich in this sense [124], nor their application to classical time-stepping schemes [54] different from those used in the **AVBP** solver. By performing this stability analysis however, additional information may be extracted. By introducing concepts such as *dissipation* or *dispersion*:

- Dissipation: Error in amplitude between the numerical scheme prediction and the exact signal. This dissipation error ϵ_{Dissip} measured by,

$$\epsilon_{Dissip} = \mid G \mid. \tag{4.9}$$

  This error is usually measured from one temporal step n to another $n+1$ leading to $\epsilon_{Dissip} = \frac{|V^{n+1}|}{|V^n|}$. Note that this definition is the same as the previous amplification factor. From a stability point of view, the *amplification factor* or the *spectral radius* of G is used to determine if the scheme dissipates or amplifies the amplitude to define a scheme as stable or unstable. The difference between definitions is that when talking about *dissipation*, the scheme is assumed to be stable and the difference between amplitudes is quantified.

- Dispersion: Dispersion relates to error committed by the numerical scheme in the prediction of the phase speed with respect to the exact speed. In the same way dissipation was defined, dispersion can be written as the cocient between the predicted phase speed and the exact value,

$$\epsilon_\Phi = \frac{\mid \Phi \mid}{\mid \Phi_{exact} \mid}. \tag{4.10}$$

Just as a reminder, a non-dimensional wavenumber defined as $\phi = k\Delta x$ is used. Outside the context of spectral methods it is hence only possible to have wavenumber values between $[0, \pi]$. The relative phase speed respect to the exact phase speed at which the waves propagate is defined by $\frac{c^*}{c_{exact}}$. This expression is an indicator of the dispersion error,

$$\frac{c^*(\phi)}{c_{exact}} = \frac{arg\,(G)}{\phi\nu}, \tag{4.11}$$

where $arg\,(G)$ is the argument of G. This parameter is widely used in the following sections.

Results are provided for the schemes in the AVBP solver to study the following:

- The scheme properties in multi-dimensional problems.
- The impact of a numerical treatment on the above mentioned scheme to deal with the application of a boundary condition.

4.3.1 1D analysis

To ease the interpretation of the figures present in this section, a short explanation is provided in the context of regular meshes. Recall first that high wavenumbers are representative of the smallest wavelengths and thus correspond to low resolution waves. On the other hand, the lowest wavenumbers are representative of waves that have a large number of points to discretize them and are thus expected to have better dispersion properties in the low wavenumber range as more points are available to discretize a wave.

Figure 4.3 shows the non-dimensional modulus and phase velocity of each scheme for a certain CFL value. As can be seen, all schemes show low dissipation because the numerical solution must converge towards the physical solution when reducing both spatial and time discretization steps. Thus, a smaller time step should always lead to a lower dissipation for all wavenumbers. Between the different schemes, it can be observed that the high-order TTG4A scheme seems to have a higher dissipation when compared to the second-order LW. Although true for the highest wavenumbers, plotting the error, $\mid 1 - G \mid$ instead shows that this is not the case for most of the spectrum as seen in Fig. 4.4a. TTGC is clearly the less dissipative scheme followed by TTG4A except for the highest wavenumbers and finally LW. Concerning the dispersion however, it can be seen that the two-step schemes, TTGC and TTG4A, show a much lower dispersion error compared to LW through most of the wavenumbers Fig. 4.3. Once again, by analyzing the error done for each scheme for the whole spectrum as in Fig. 4.5a, TTGC can be seen to be slighly more dispersive for the largest wavenumbers. This statement

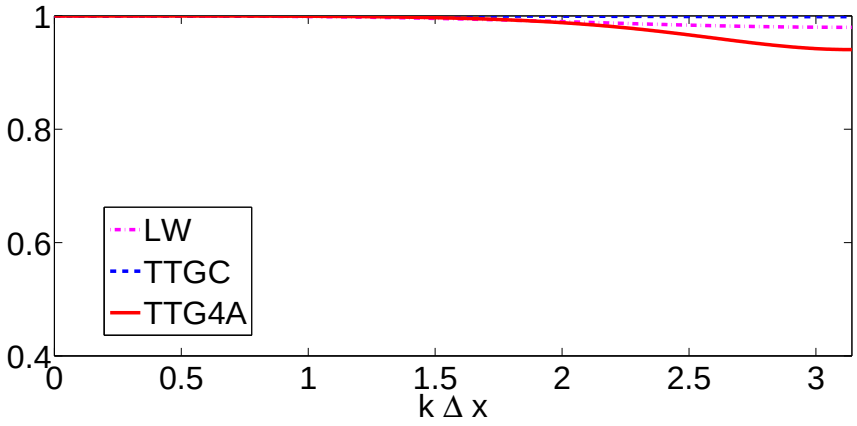

(a) Modulus

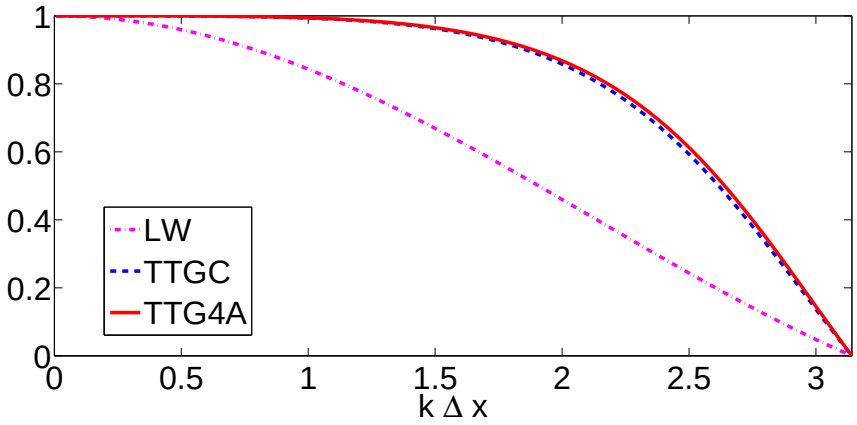

(b) Phase velocity

Figure 4.3: Amplification factor of various schemes for CFL=0.1.

holds when zooming in, Fig. 4.5b. Note that the choice of the abscissa value limit for Figs. 4.4b, 4.5b is not arbitrary. It is chosen such that for a regular mesh all the waves in the wavenumber range are represented by at least 10 points which is a good estimate of the minimum number of points to properly capture a wave [10] when comparing to the schemes addressed.

When increasing the CFL number, notable changes are observed in Fig. 4.6. The same behaviour can be found with the difference that between the high-order schemes, dissipation is much higher for the high wavenumbers for TTG4A while dispersion is better for this same range when comparing to TTGC. Although not shown, dissipation and dispersion properties have the same tendency for the smaller wavenumbers, TTGC presenting the best properties in terms of dissipation and TTG4A for dispersion. For a CFL value of 0.5 as in Fig. 4.7, a different behaviour can be seen for TTG4A concerning its dispersion properties. Note that dissipation curves may never be higher than one or it would be an unstable scheme. Dispersion relations however may be higher than one in which case a phase velocity higher than that of the original wave, yielding a wave that is transported at a higher speed than the exact one. TTG4A provides the highest levels of dissipation for these values of CFL and LW can be seen

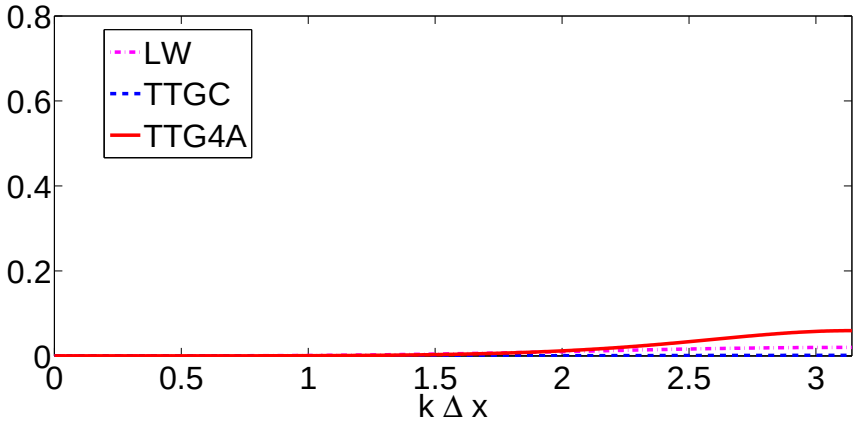

(a) Main view.

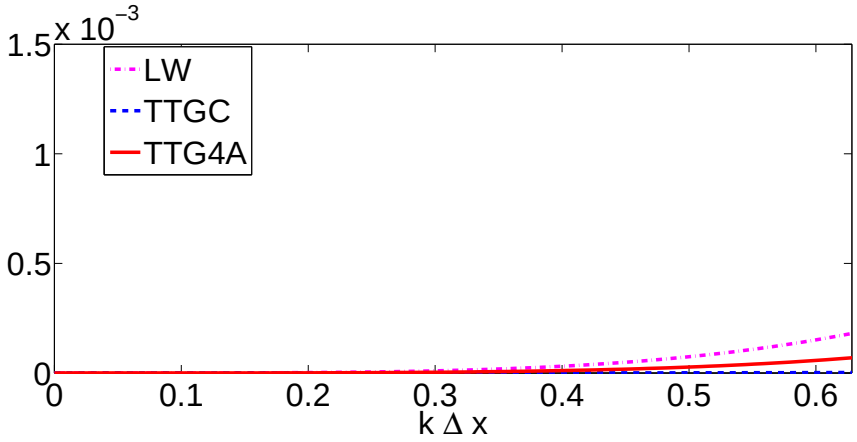

(b) Zoomed in view in the range of $0 - \pi/5$ wavenumbers.

Figure 4.4: Dissipation error using the amplification factor of various schemes for CFL=0.1.

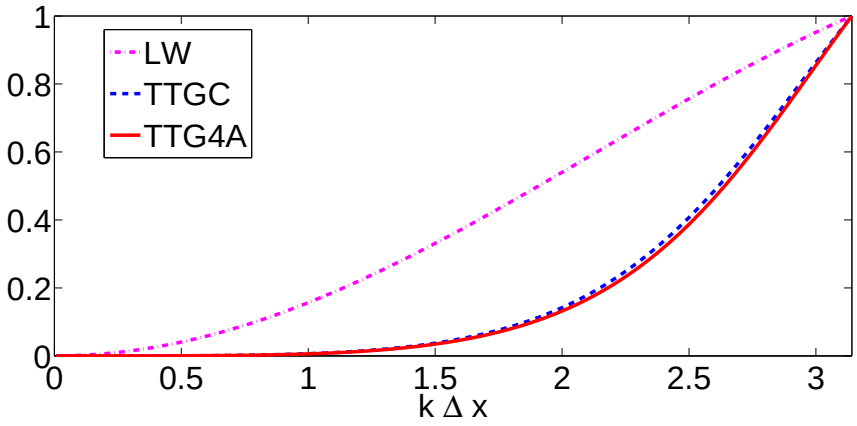

(a) Main view.

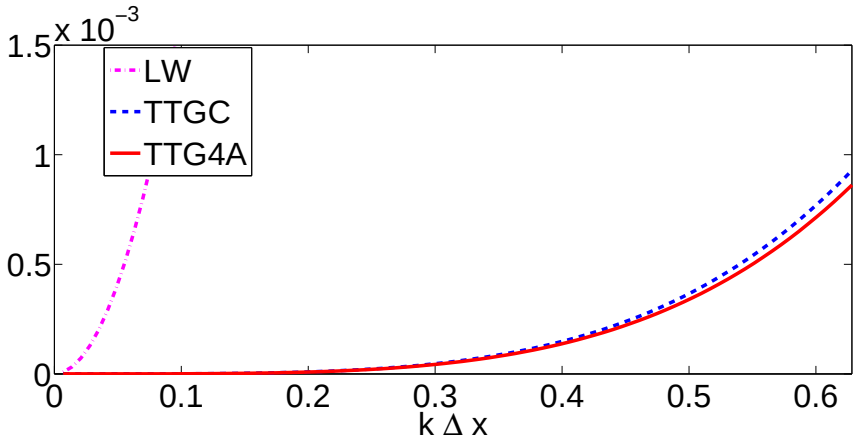

(b) Zoomed in view in the range of $0 - \pi/5$ wavenumbers.

Figure 4.5: Dispersion error using the amplification factor of various schemes for CFL=0.1.

to be much too dispersive at nearly all wavenumbers. Confirmation of this can be found for even higher CFL values as seen in Fig. 4.8. Once again waves are propagated at a higher speed when using the TTG4A scheme.

When analyzing these results, the first conclusions are that TTGC seems the best suited for LES as it has the lowest dissipation for all wavenumbers [36]. This is an interesting feature for 1D analysis but that will be pursued in 2D. An issue common to all the schemes presented is the existence of the problems associated to the highest wavenumbers. A question that commonly arises is whether if these waves are required to be kept or if, on the contrary, they should be filtered due to their nature. The Nyquist-Shannon theorem states that the minimum points necessary to represent a wave is at least two. Due to this many authors suggest that an explicit filtering is to be performed [10] to remove them from the simulation. This strategy can be further extended to the waves that are seen to propagate with the wrong speed but then the limit is quite arbitrary and strongly dependent on the scheme. For all these reasons, the philosophy adopted here is to look first for the best scheme behaviour.

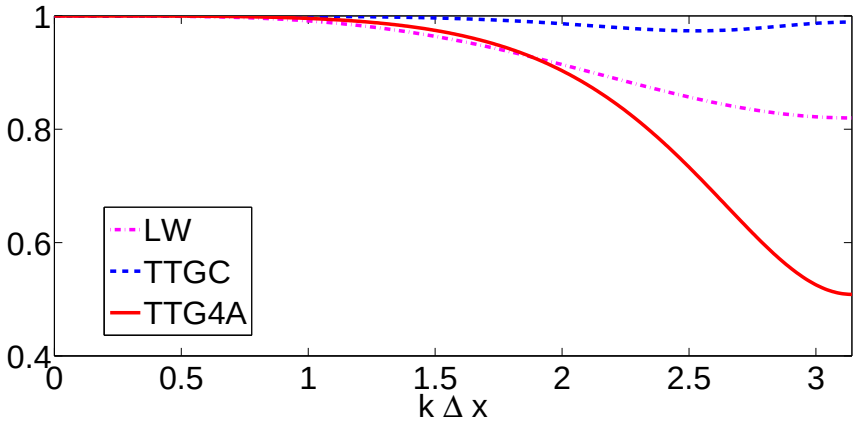

(a) Modulus

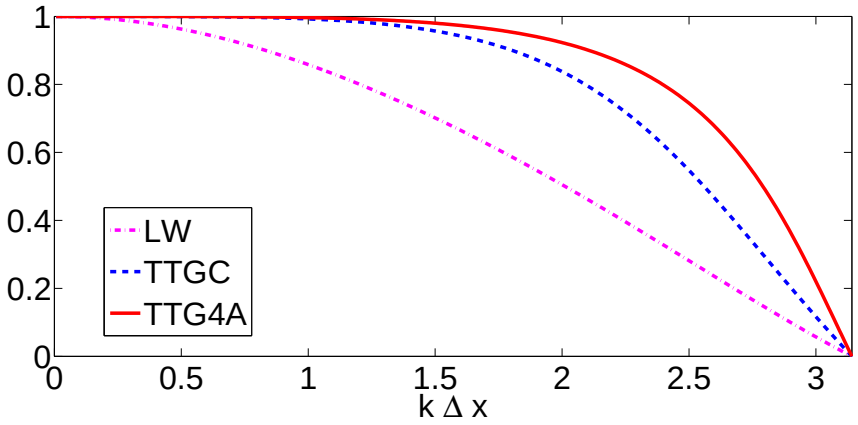

(b) Phase velocity

Figure 4.6: Amplification factor of various schemes for CFL=0.3.

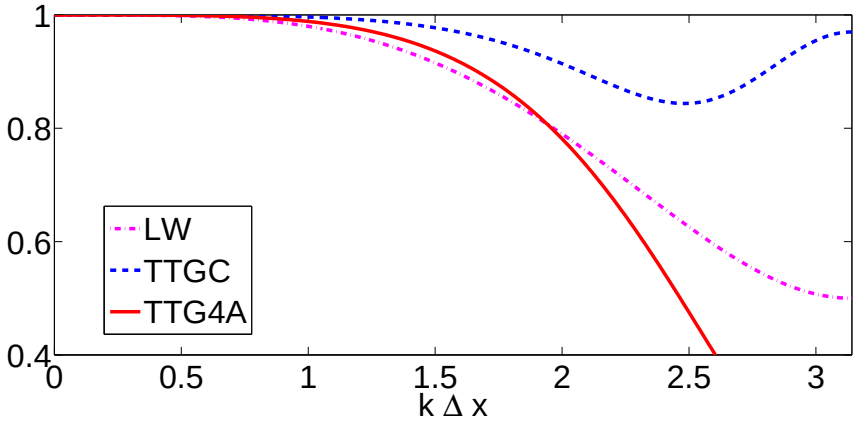

(a) Modulus

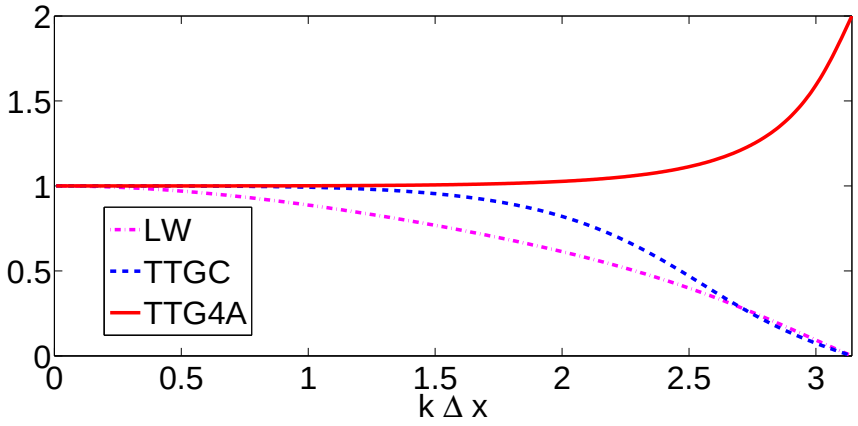

(b) Phase velocity

Figure 4.7: Amplification factor of various schemes for CFL=0.5.

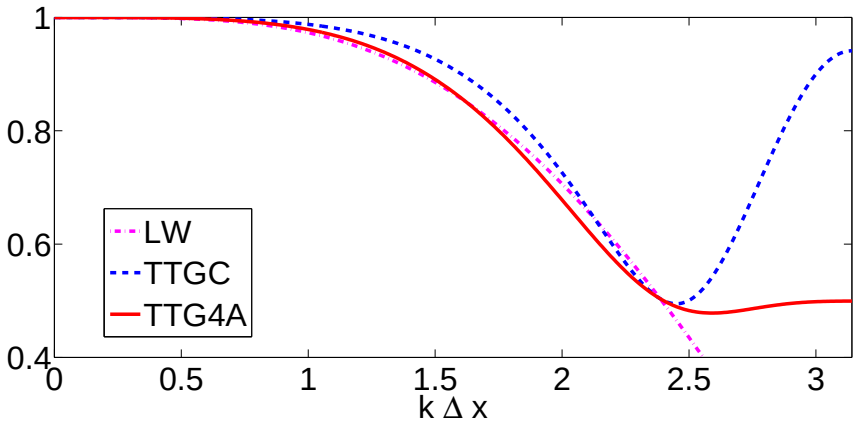

(a) Modulus

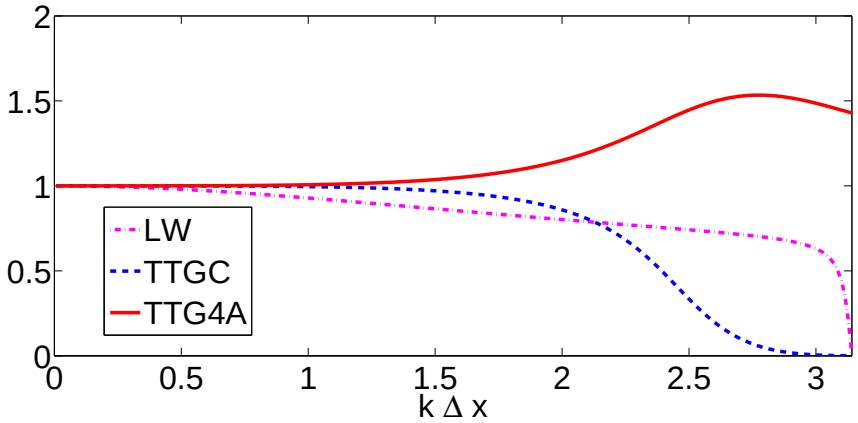

(b) Phase velocity

Figure 4.8: Amplification factor of various schemes for CFL=0.7.

The analysis of the schemes in 2D is also motivated by the need to analyze the behaviour of the schemes when waves are unresolved. The number of points per wavelength has already been shown to be the most important parameter to minimize the dispersion error so the following section performs the scheme analysis for a specific set of wavenumbers. It is important to anticipate when the scheme may present problems, notably oscillations, that are related to the poor dispersion behaviour in such zones. The objective is to have a deeper insight into the wavelength values that bound an acceptable behaviour of a given scheme.

4.3.2 2D analysis

The von Neumann analysis can also be done in 2D, the mesh being limited to regular meshes of characteristic size Δx as done in Vichnevetsky and Bowles [187]. The only constraint is to assume that a wave is moving in a direction $\vec{c}$ colinear to each direction of study.

Following the directives described in Donea et al. [54] for bilinear finite elements it is possible to write the complete equation in the most general case for the family of two-step Taylor-Galerkin,

$$M\left(\tilde{U}-U^n\right) = -\alpha\left(\nu_x\hat{\delta_x}U+\nu_y\hat{\delta_y}\right)U^n+\beta\Delta t\left(\nu_x^2\hat{\delta}_x^2+2\nu_x\nu_y\delta_x\delta_y+\nu_y^2\hat{\delta}_y^2\right)U^n, \tag{4.12}$$

$$M\left(U^{n+1}-U^n\right) = -\alpha\left(\nu_x\hat{\delta_x}U+\nu_y\hat{\delta_y}\right)U^n+\beta\Delta t\left(\nu_x^2\hat{\delta}_x^2+2\nu_x\nu_y\delta_x\delta_y+\nu_y^2\hat{\delta}_y^2\right)U^n, \tag{4.13}$$

$$\tag{4.14}$$

where each spatial derivative is represented using centered derivatives,

$$\delta_x U = 0.5\left(U_{j+1,k}-U_{j-1,k}\right), \tag{4.15}$$

$$\delta_y U = 0.5\left(U_{j,k+1}-U_{j,k-1}\right), \tag{4.16}$$

$$\delta_{xy} U = 0.5\left(U_{j+1,k+1}-U_{j-1,k-1}\right), \tag{4.17}$$

$$\delta_{yx} U = 0.5\left(U_{j+1,k-1}-U_{j-1,k+1}\right), \tag{4.18}$$

$$\hat{\delta_x} = \frac{2}{3}\left(\delta_x+\frac{1}{4}\left(\delta_{xy}+\delta_{yx}\right)\right), \tag{4.19}$$

$$\hat{\delta_y} = \frac{2}{3}\left(\delta_y+\frac{1}{4}\left(\delta_{xy}-\delta_{yx}\right)\right). \tag{4.20}$$

Following the same approach for the second order derivatives,

$$\delta_x^2 U = (U_{j+1,k} + U_{j-1,k} - 2U_{j,k}), \tag{4.21}$$
$$\delta_y^2 U = (U_{j,k+1} + U_{j,k-1} - 2U_{j,k}), \tag{4.22}$$
$$\delta_{xy}^2 U = (U_{j+1,k+1} + U_{j-1,k-1} - 2U_{j,k}), \tag{4.23}$$
$$\delta_{yx}^2 U = (U_{j+1,k-1} + U_{j-1,k+1} - 2U_{j,k}), \tag{4.24}$$
$$\hat{\delta}_x^2 = \frac{2}{3}\delta_x^2 - \frac{1}{3}\delta_y^2 + \frac{1}{6}\left(\delta_{xy}^2 + \delta_{yx}^2\right), \tag{4.25}$$
$$\hat{\delta}_y^2 = \frac{2}{3}\delta_y^2 - \frac{1}{3}\delta_y^2 + \frac{1}{6}\left(\delta_{xy}^2 + \delta_{yx}^2\right). \tag{4.26}$$

The consistent mass matrix can then be re-expressed using these operators

$$M = 1 + \frac{1}{9}\left(\delta_x^2 + \delta_y^2 + \frac{1}{4}\delta_{xy}^2 + \frac{1}{4}\delta_{yx}^2\right). \tag{4.27}$$

Similarly to what was done in 1D, the equivalent transfer function may be found in 2D to determine the dissipation and dispersion properties for each scheme. In the same way for the 1D analysis, a short explanation and interpretation of the obtained curves is given. The plots for the 1D section present the behaviour of the scheme for a wavenumber range in $[0, \pi]$. For the 2D case, the polar plots represent not the wavenumber but the physical direction of propagation, namely in cartesian coordinates, x and y. These coordinates are the main directions of the scheme and present the same behaviour in both directions. This implies that all figures shown from here on, although represented in the range of $[0, 2\pi]$ could be presented in $[0, \pi/2]$ and be then rotated. It is difficult to present a whole range of wavenumbers due to visualization effects so certain wavelength values have been chosen to be specifically represented, namely $[2h, 3h, 4h, 8h]$. Each coefficient that accompanies the studied wavelengths indicates the number of points used to discretize a whole wavelength. Starting from the lowest value which corresponds to 2 and moving outwards shows the effect resolution has. Of course, it would be possible to analyze higher values but as more points are added, waves are better represented and errors decrease. Note that theoretically, the non-dimensional exact values of both dissipation and dispersion for pure convection should have a value equal to 1, meaning that ideally the values should be located on the circle of radius equal to one.

To show the different behaviour, for the same wavenumber values, different schemes are compared in Figs. 4.9-4.19. Starting from the lowest wavenumbers addressed, which correspond to the $8h$ wavelengths, it can be seen that for all schemes the errors are low. The only apparent error is seen in the dispersion behaviour of the second-order scheme, LW which is to be expected as it requires more points to resolve a wave. It is necessary to study the error performed as seen in Figs. 4.11a and 4.11b. In all cases dissipation exists but remains acceptable $\epsilon < 1\%$, and is lower in most directions for TTGC. For a CFL value of 0.3, TTG4A always performs better than LW. Increasing the CFL number shows however directions where TTG4A is less dissipative than TTGC, mainly in the diagonal directions but TTGC remains more homogeneous through the whole spectrum. In all cases there is however an oscillatory behaviour being always more dissipative in the main directions.

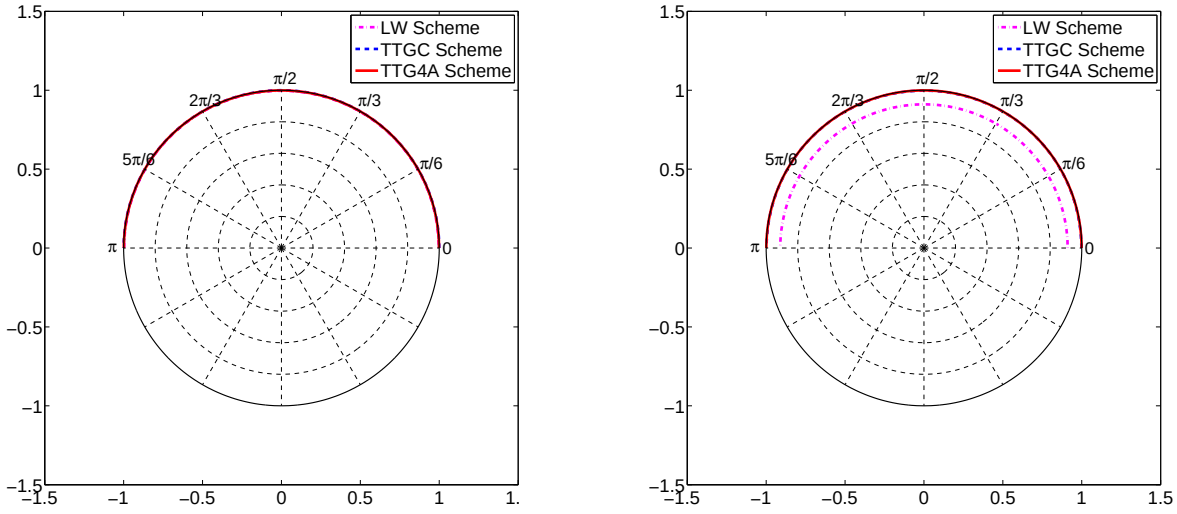

(a) Modulus (b) Phase velocity

Figure 4.9: Amplification factor of various schemes for CFL=0.3 at $8h$ wavelengths.

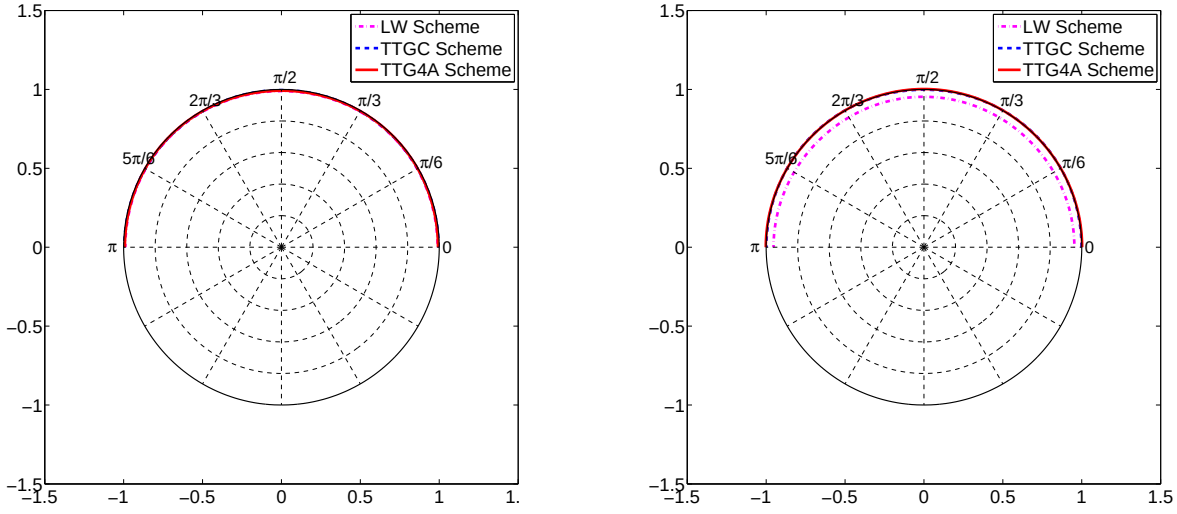

(a) Modulus (b) Phase velocity

Figure 4.10: Amplification factor of various schemes for CFL=0.7 at $8h$ wavelengths.

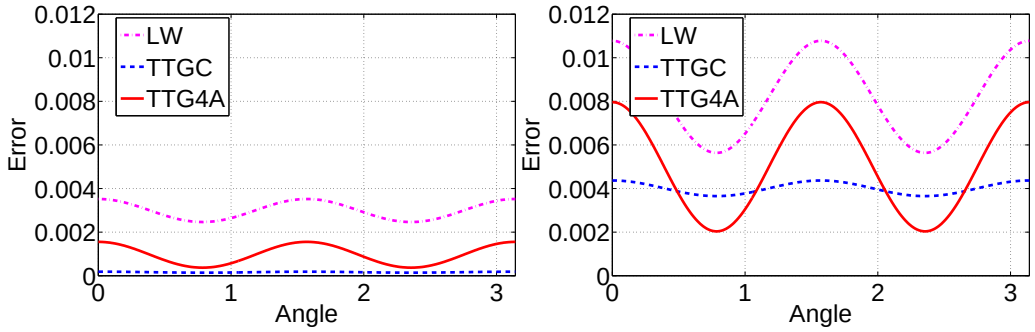

(a) CFL = 0.3 (b) CFL = 0.7

Figure 4.11: Dissipation errors $8h$ wavelengths.

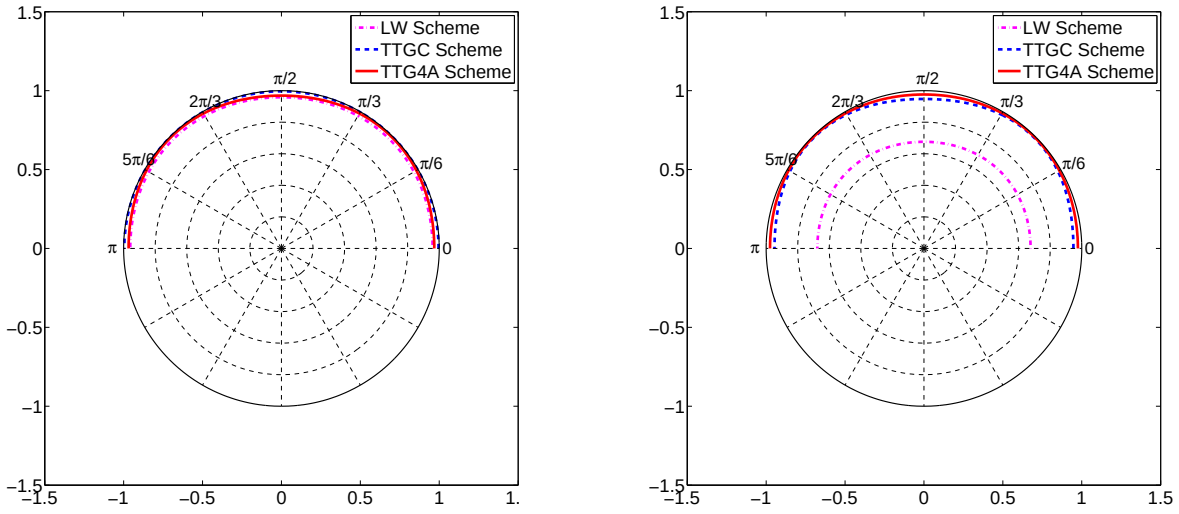

(a) Modulus (b) Phase velocity

Figure 4.12: Amplification factor of various schemes for CFL=0.3 at $4h$ wavelengths.

When using less points to discretize the waves as in Figs. 4.12 & 4.13 where four points are used and for various CFL values, the general behaviour of the curves is modified and differences are observed in terms of dissipation but also dispersion. Once again the dispersion for LW is clearly the most noticeable issue but high-order schemes are also affected, especially for the higher CFL value. Once again, the schemes become more dissipative (see Fig. 4.12) and dispersion increases, see Fig. 4.13. The same holds for both Figs. 4.16 & 4.17. Note that for larger wavenumbers and high CFL values, the dispersion error is negative for TTG4A. This means that the phase speed is larger than the real value and thus the wave is transported at a higher speed.

For the smallest wavelengths, due to the lack of points, it was seen for the 1D case that the error done in terms of dispersion is large, meaning that these waves are not transported at the correct speed. When comparing Figs. 4.18b & 4.19b, both show a fairer behaviour in the diagonal directions contrarily to the main axes. For CFL of 0.7 shown in Fig. 4.19a, certain

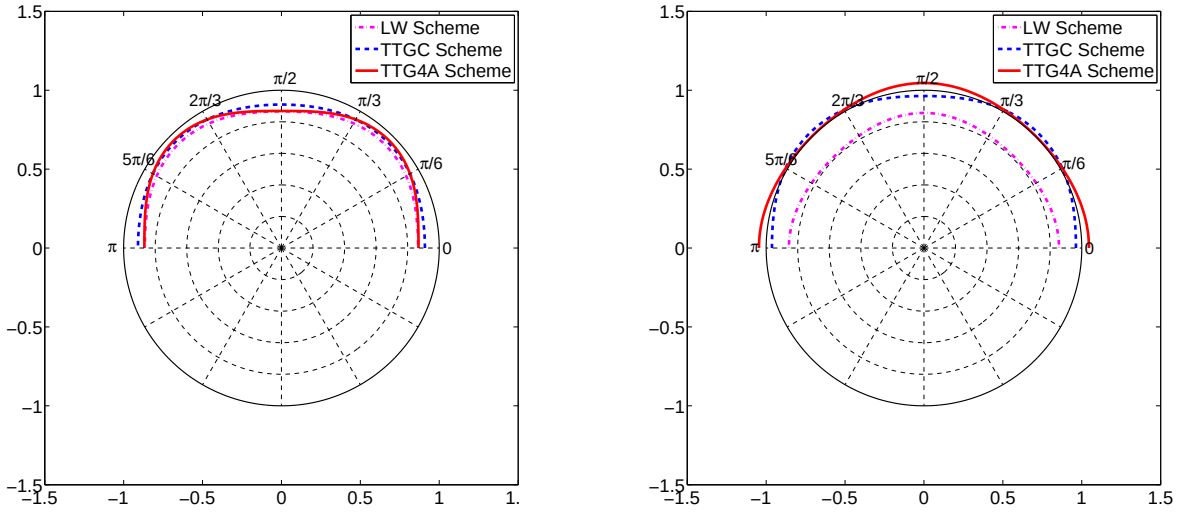

(a) Modulus (b) Phase velocity

Figure 4.13: Amplification factor of various schemes for CFL=0.7 at $4h$ wavelengths.

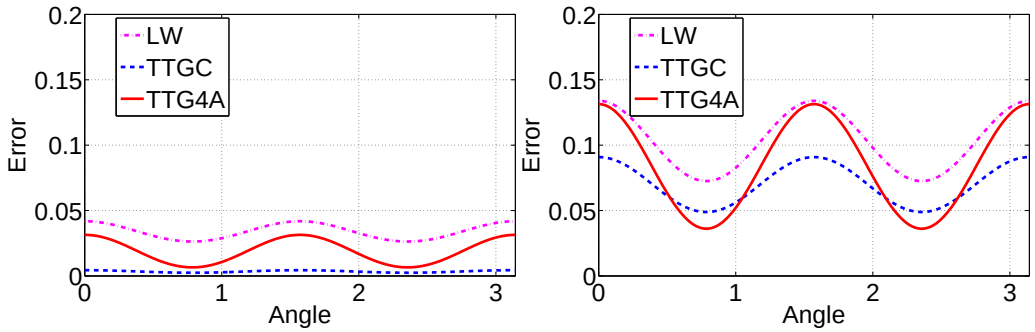

(a) CFL = 0.3 (b) CFL = 0.7

Figure 4.14: Dissipation errors $4h$ wavelengths.

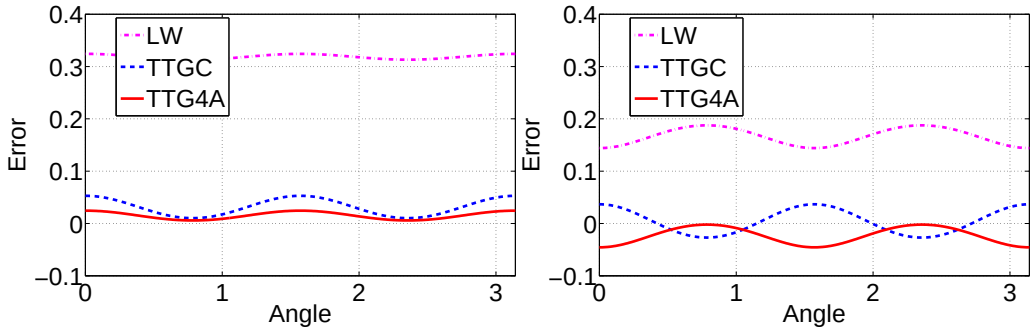

(a) CFL = 0.3 (b) CFL = 0.7

Figure 4.15: Dispersion errors $4h$ wavelengths.

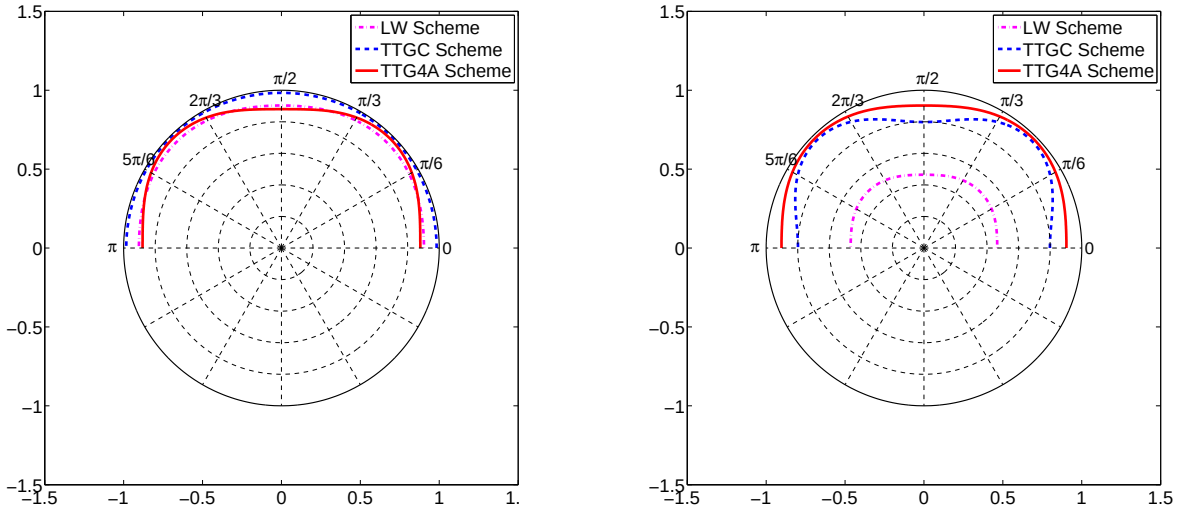

(a) Modulus (b) Phase velocity

Figure 4.16: Amplification factor of various schemes for CFL=0.3 at $= 3h$ wavelengths.

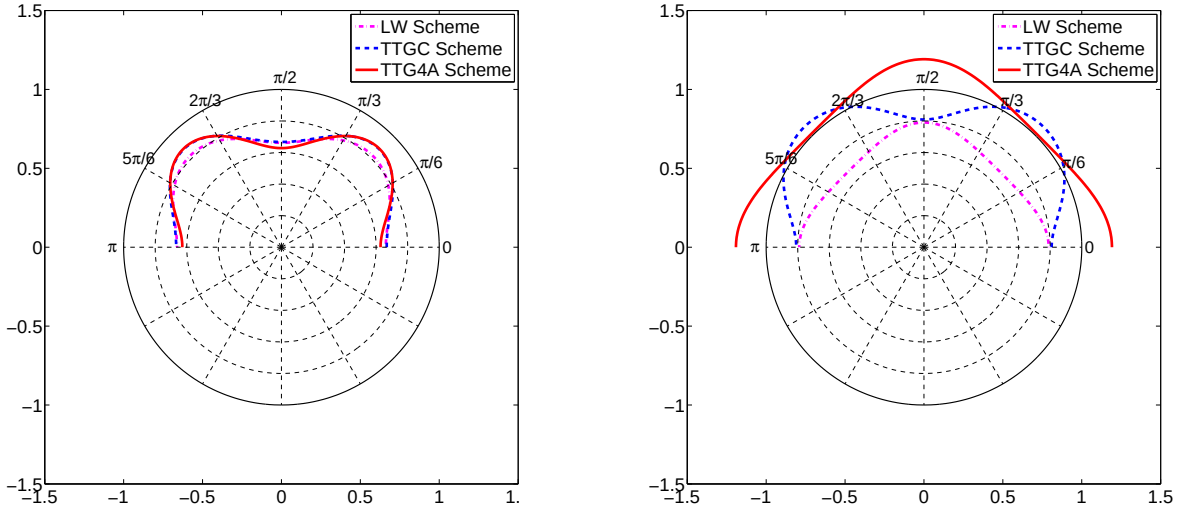

(a) Modulus (b) Phase velocity

Figure 4.17: Amplification factor of various schemes for CFL=0.7 at $3h$ wavelengths.

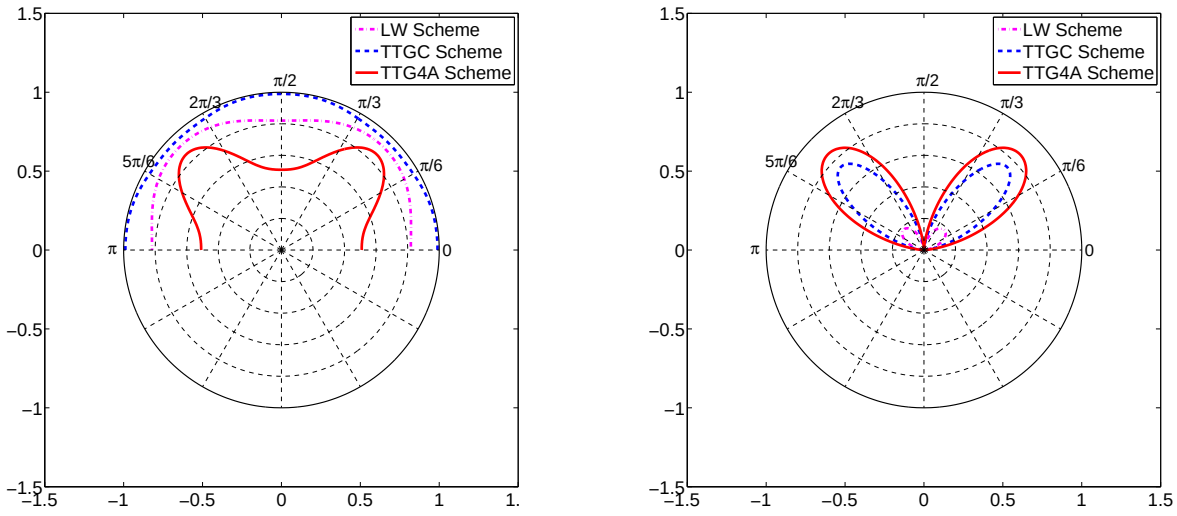

(a) Modulus

(b) Phase velocity

Figure 4.18: Amplification factor of various schemes for CFL=0.3 at $2h$ wavelengths.

schemes even do not dissipate the smallest waves, notably TTGC in the main directions. In 2D, this specific behaviour is clearly not homogeneous and is highly dissipative in the diagonal directions. LW and TTG4A are observed to dissipate waves in all directions. For lower CFL values as in Fig. 4.19a, TTGC recovers its homogeneity in terms of direction of propagation while LW is less directional.

The conclusions to be extracted from this analysis are that errors are large when transporting low-resolved waves for all schemes. These cannot be expected to be correctly transported and observed behaviour will be strong direction dependent. To include boundary condition effect and implementation of such waves, the von Neumann analysis previously presented is not an option. Another method must be used to estimate the stability of the scheme near the boundaries to evaluate its influence on the resulting predictions. It has been proven that the effect of boundary conditions can indeed hinder the accuracy of the general scheme [75]. Taking into account the boundary conditions is imperative when performing such an analysis as it aims at evaluating the stability in more standard circumstances. This will be done in Sec. 7.1 where differences become evident.

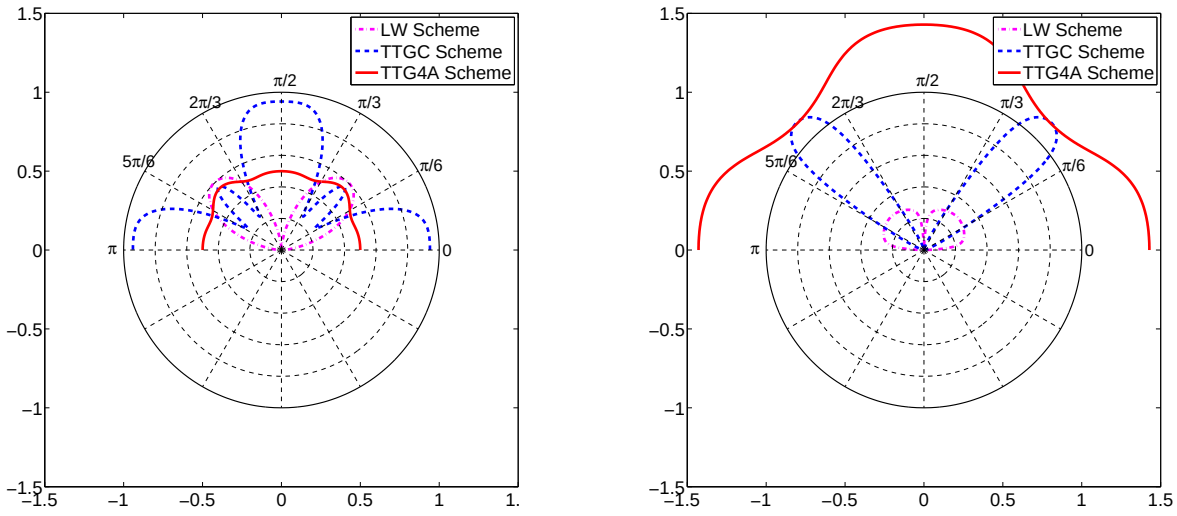

(a) Modulus

(b) Phase velocity

Figure 4.19: Amplification factor of various schemes for CFL=0.7 at $2h$ wavelengths.

At the end of Part I, you have a better idea of what to expect from different free-stream modelling approaches and how to model the near-wall region (if it exists) in a simulation. The first question to tackle is if the simulation to perform is going to be RANS, LES or DNS. Can you pay it and is it worth the extra cost? The answer to these questions is, as in most cases, it depends. If the simulation is unsteady, RANS may be discarded quickly. An average behaviour of the flow is in most cases insufficient, e.g. flashback effects in a combustion chamber. Say then you move on to evaluate the pros and the cons of LES and DNS. It is true that some wall-bounded flows require a highly refined grid so LES will not scale that far from DNS in terms of cost. Performing an accurate simulation will inevitably imply a huge cost and needs to be justified with a deep understanding of the flow physics. This last reason is why you should continue reading Part II where the physics of turbomachinery blades are encountered. A comprehensive analysis of turbulence in the boundary layer included. The modelling is however possible in some simulations if studying the boundary layer is not required (provided a good model accounts for the missing physics), LES being an optimal approach given the computational power today and will continue to be like this for a few years yet.

So, let's summarize. It is important to read carefully the cell-vertex introduction as most of the differences from standard schemes come from this approach. Once this is clear it is possible to move on to the different operators. Convection operators based on the Taylor expansion provide an increase in order using certain cleverness to discretize the spatial operators. However, it was shown that there was an unclosed term that has still not been clarified as well as the boundary conditions that appear as a result of the second-order spatial derivatives (or Hessian). The requirement to impose a BC for this term should certainly be addressed because as mentioned, boundary conditions are responsible for a particular flow to exist. If no boundary condition is provided, the problem is unresolved, and giving an approximative value can be dangerous. Also, the analyses performed have shown the better behaviour of high-order schemes compared to low-order ones in 1D. When the results are extended to 2D the direction properties are seen to change thus showing the limits of the 1D approach. In any case, the high-order schemes show better properties and this is the reason why they are systematically used in the next Part.

Part II

Application to a complex geometry: LS89

Part II of this document concerns the simulations of the complex turbomachinery flows. In the previous part, the necessity to understand the inner workings of a LES solver was described. At this occasion, important points related to LES wall-bounded simulations were also underlined as it is an important aspect for turbomachinery flows. This modelling issue is not new and can rapidly become a major problem to apply LES in an industrial context. Indeed, simulating such flows is expected to be very expensive. In that respect, our initial goal is not necessarily to assess LES for real applications but instead to qualify CERFACS' LES solver on a turbomachinery representative flow. That is: ensure the capacity of the code and associated numerics to address specific flow physics around blades. In this context, to alleviate the weight of the near wall modelling, the simulations performed hereafter are wall-resolved.

In this document, the targeted configuration is the LS89 vane [7]. Literature is rich for this configuration but certain operating points are not properly captured even when performing a priori good quality type simulations either using the RANS, URANS or LES and DNS formalisms. The present study is divided in three parts, each corresponding to a different chapter. The first chapter addresses the physics encountered in turbomachines, and more specifically linked to the presence of near walls that are known to condition the boundary layer physics. An introduction to the test case and the possible sources of existing discrepancies between simulations and experiments are discussed. The second chapter corresponds to the simulation of two operating points. The first operating point is used to validate the LES solver under simple physics. The second point represents the complex physics that are normally encountered in high-pressure turbines. This second case leads to a series of simulations that try to explain the exact physical behaviour of the flow and why the numerical simulations have problems to match the experiments. The third chapter discusses the numerical artifacts that may be at the origin of certain flow prediction behaviours. A thorough discussion on how to deal with the different issues is provided. These discussions concern mainly the boundary term closures seen in Part I, an alternative Fourier analysis being done for the existing closures. A promising new methodology to treat the closure terms are at this occasion detailed.

Chapter 5

Introduction to LS89 simulations

Contents

5.1 Application and validation of LES for a complex turbomachinery flow

Turbomachinery applications have traditionally been studied numerically using Reynolds Averaged Navier-Stokes (RANS) or Unsteady Reynolds Averaged Navier-Stokes (URANS) turbulence modelling approaches. RANS benefits from a large experience acquired during the years and is still of great use in the design phase of an industrial project, Large Eddy Simulations (LES) and Direct Numerical Simulations (DNS) being too expensive for this goal. This explains why active research is still being done in this direction [71, 127]. However, LES allows to resolve, at a more reasonable cost when compared to DNS, the larger energy-containing wavelengths of the turbulence spectrum in unsteady flows. This is not the case for the RANS or URANS approaches, which are not capable of predicting many unsteady turbulent effects such as transition or flow separation. These limitations have motivated turbomachinery studies using LES to try to capture effects that are missed with approaches that require more modelling.

The first unsteady simulations of LES and DNS type were the fully resolved turbomachinery simulations performed by Wu and Durbin [196] for a low-pressure turbine. The low Reynolds and low Mach numbers of the configuration addressed permitted such a study at the time. In

recent years, the number of publications of LES in turbomachinery has increased exponentially in both compressor, McMullan and Page [121], and turbines, Wheeler et al. [192]. A large review of different configurations and simulations performed in the context of LES can be found in Tucker [183] and the future use of LES in aeroengines in Tyacke and Tucker [184]. It is thus possible today to perform LES of turbomachine components in research institutions. The main limitation in this context is of course the cost, one that can difficultly be overcome for cases with rich physics that are normally present in wall-bounded flows.

The rich physics near the wall are the main problem encountered in turbomachinery flows because in most cases, unsteady transitional flows are encountered. When fully developed turbulent boundary layers (BLs) are present there are models that account for most physics and are capable of producing good results. The problem however is that most boundary layers are initially in a laminar state and undergo a transitional process. The simulation of the necessary flow dynamics to capture transition and the accurate prediction of the position where this process happens is the most difficult aspect of turbulence around blades. The position where this process takes place is especially critical in the design of the blade profile to determine its loading or performance, and is thus of upmost importance. In order to understand the process of transition, it is first necessary to study the features that define a BL as turbulent as well as the possible sources that may trigger this transition. The details and knowledge about this specific fundamental fluid mechanics problem are briefly covered in the following paragraphs.

Boundary layer physics

A turbulent boundary layer may be divided into different sublayers as shown in Fig. 5.1. The near-wall region is dominated by viscous effects, the intermediate region named 'buffer layer' requires to take into account both viscous and inertial effects followed by the logarithmic region and wake where inertial effects are dominant. By describing the structures that exist in the BL, starting from the wall towards the outer part of the boundary layer, the main wall-signatures can be explained. The nearest layer to the wall is the viscous sublayer, region that is dominated by 'streaks' [94]. The generation of streaks, which are low and high-velocity fluctuating regions, are an effect of both the high shear strain [105] induced by the wall in most cases and the velocity normal to the surface. The normal velocity in this region makes low momentum fluid initially located at the wall move into higher momentum regions leading to long streamwise zones of negative fluctuation velocities. It seems clear now that this normal velocity necessary for streak generation is induced by the set of counter rotating streamwise vortices that are present in the viscous sublayer and buffer regions [19]. It is an accepted process that streamwise vortices generate streaks but how the streamwise vortices are generated remains unclear. Inflectional instability mechanisms of streaks seem to be at the origin but they are not responsible for the energy necessary for vortices to form [85]. What is known is that streaks are three-dimensional structures that are responsible for the bursting processes described by Kim et al. [91]. These longitudinal fluctuating structures (a fancier way of naming the streaks) may enter the buffer layer and under different instability processes, breakdown to local turbulent structures. For this specific process, two main instabilities are found to coexist: the varicose mode, related to wall-normal inflectional profiles, and the sinuous mode which is related to spanwise inflectional

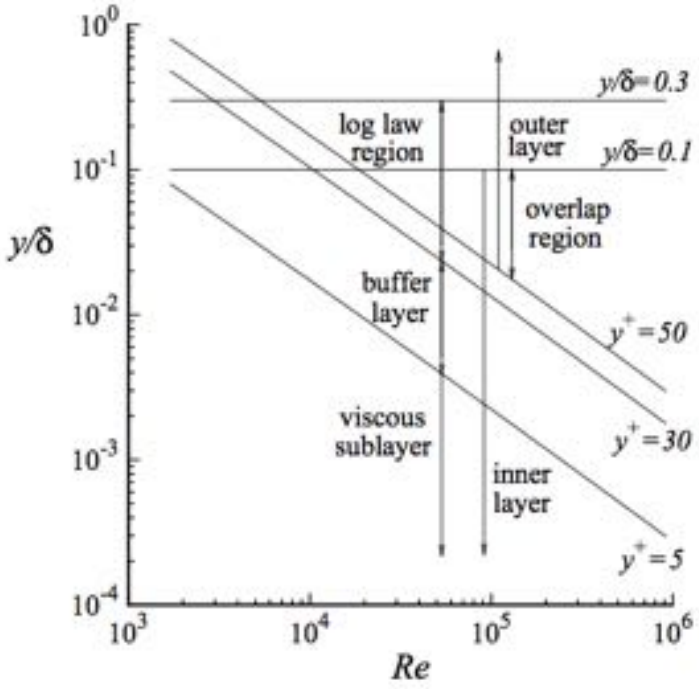

Figure 5.1: Boundary layer distribution in terms of Reynolds number [140].

modes, the latter being seen to be more unstable [158, 90]. Once these sources of turbulence are generated, they may expand in the streamwise and spanwise directions as detailed in Fig. 5.2 once again leading to fully turbulent fields.

All the previous near wall features are accompanied in a turbulent boundary layer by coherent turbulent structures seen for example in the DNS of Wu and Moin [197]. These structures and their relation between inner and outer structures and their importance in the regeneration mechanism of near-wall turbulence remain an issue of controversy. These coherent structures are fundamentally organized into the known 'hairpin' vortices. Originally introduced by Theodorsen [180] they have been hypothesised to be a composition of the streamwise vortices dominant in the buffer layer and the spanwise arch-like vortices seen in the outer wake [151]. They are mainly related to the existence of varicose modes and to wall-normal instabilities of the streaks nearest to the wall. These hairpin vortices are however not always observed in DNS [158] as one unique structure, e.g. the streamwise vortex, can exist without the spanwise vortex leading to new definitions such as one-legged hairpin or cane and arch vortices. Although no specific analysis concerning instabilities is performed, it is useful to recognise the patterns expected to visually examine the turbulence organisation near the wall. What is important is to recognise the sources of instabilities that lead to a turbulent boundary layer as this is one of the mechanisms potentially present in turbomachinery flows studied in this document.

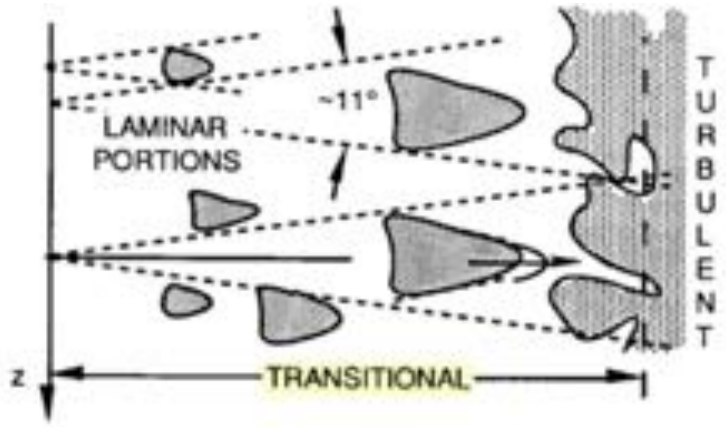

Figure 5.2: Formation and evolution of turbulent spots [120].

5.1.1 Boundary layer transition

For all existing flows, it has been very early known that there is a value of the Reynolds number that triggers the transition to a turbulent state. This has led many authors to study the stability of laminar flows and the need to identify the perturbations that could give rise to this transition [160]. However, it is important to underline the fact that it is still impossible today to determine the path taken by the flow once it has undergone the transition process. Indeed, turbulence is merely an observation that occurs at high Reynolds number as described in White [193]. It is a fact however that the transition process happens, and it is the various mechanisms responsible for it that are of interest and are described in the following.

Natural transition

In the absence of pressure gradients and external perturbations, for a laminar BL on a flat plate configuration for example, the mechanism that drives the instability is widely accepted and known as natural transition. The first step in the global process shown in Fig. 5.3 is the generation of the instability waves known as Tollmien-Schlichting waves, thoroughly described in hydrodynamic stability documents [55]. The mechanism that generates these waves is known as receptivity of the flow to external disturbances that can be of various natures, e.g. acoustics, and was first noted in Morkovin [125]. Linear stability analysis can explain this feature using only 2D theories and provides the growth and amplification of these unstable waves. It has also been shown that these waves undergo a non-linear phase when the amplitude of the waves is of the order of $1-2\%$ of the free-stream velocity resulting in the wave break down. Various types of regimes can lead to this boundary layer breakdown such as the K-regime [93] which always develops a three-dimensional flow. An additional process was observed by Emmons [61] prior to a fully turbulent flow. Emmons observed the appearance of turbulent patches that he baptised 'spots'. These spots are nothing other than the local apparition of turbulent regions where the disturbances 'break' and expand spatially until all spots overlap, situation where the flow is then said to be fully turbulent. Although this process is important for fundamental studies, note that small perturbations present in the free-stream will affect the path towards a

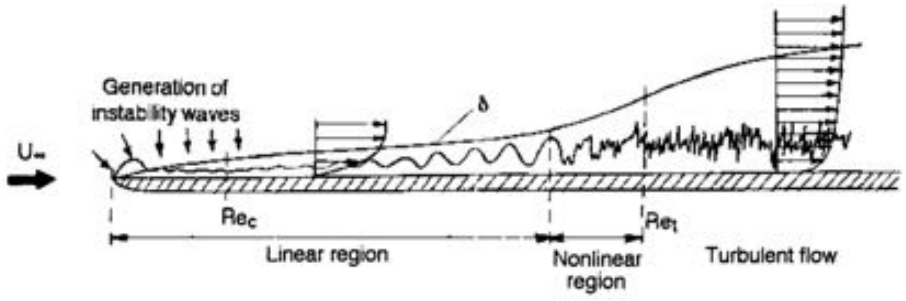

Figure 5.3: Instability process in natural transition as described in [89].

turbulent flow. Such alternative paths towards fully turbulent BLs are detailed hereafter.

By-pass transition

The first processes of receptivity, wave amplification and breakdown can be by-passed obtaining directly turbulent spots in the laminar BL without any of the former. The origin of the perturbations that overcome the first steps of natural transition need therefore to be explained. Such mechanisms are relevant to turbomachinery applications because strong turbulent fields are usually present in the main stream flow around blades and transition is often of by-pass type.

Free-stream turbulence

Experiments done by Schubauer and Skramstad [162] for a flat plate subject to a moderate free-stream turbulence were the first to show the influence of free-stream turbulence on the onset of transition. Matsubara and Alfredsson [117] showed by performing flow visualizations that the free-stream turbulence induced spanwise variations of the streamwise velocity near the wall. These structres are the dominant longitudinal streaks found in the viscous sublayer that are the same wall-signatures first seen by Kline et al. [94]. They have been shown to be a crucial part of the dynamics of turbulent boundary layers and the absence of these would lead to a relaminarization of the flow [86].

Free-stream turbulence provides also the necessary fluctuations for the coupling within the boundary layer. Important contributions from Jacobs and Durbin [81] confirmed by other DNS such as Brandt et al. [26] indicated the apparition of negative (and positive) streamwise fluctuating structures under external free-stream turbulence in the laminar boundary layer and positioned prior to the spot apparitions that were termed 'backward' jets. These jets induce a low-frequency flow region that couple to turbulent eddies from the free-stream turbulence, something that is normally avoided thanks to the natural shear induced by the boundary layer. Requirements in terms of necessary turbulent intensity and integral length scale to produce these effects are discussed in Nagarajan et al. [128].

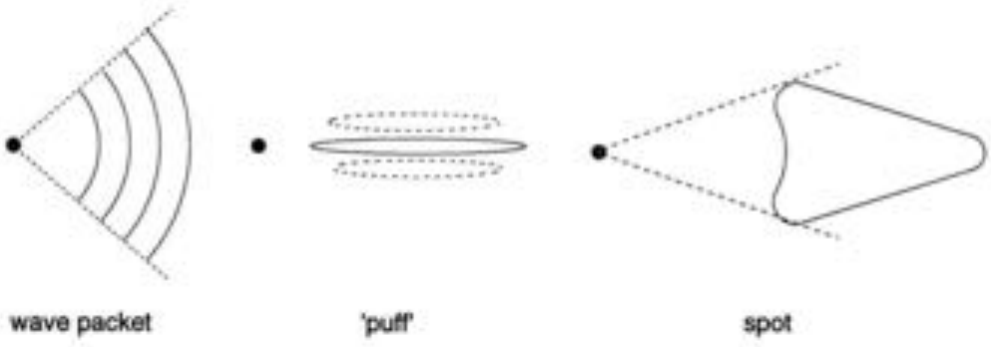

Figure 5.4: Sources of streak generation in boundary layers [120].

Wake-induced transition

Wake interactions normally happen between different stages of compressors or turbines such as rotor-stator as shown in Wu et al. [198]. Although sometimes considered separately, the wake induced transition generates perturbations that have the same effect as the free-stream turbulence induced by-pass transition mechanism. The main difference is that the disturbances generated by the wake evolve in what are termed as puffs shown in Fig. 5.4. These are then stretched downstream and evolve into the same streaky structures generally observed in turbulent boundary layers.

Separation induced transition

In the presence of strong adverse pressure gradients the flow may separate. This causes the flow to locally transition but it may reattach further downstream due to the high mixing. When this happens, the formation of a bubble in the laminar flow at a streamwise position that moves in time induces a reverse flow. The mechanism is thoroughly described in Simpson [166] involving many secondary instabilities. This separation process has many origins such as geometry discontinuities, curvature effects or shocks and is present in many turbomachinery flows. Independently of the reattachment or not of the flow, it is important to capture the bubble and thus the separation as it has a critical effect on the global performance of the blade. This type of process is also largely influenced by free-stream turbulence which determines in many cases the bursting or not of the separation bubble and the rapidity of the transition, Fig. 5.5.

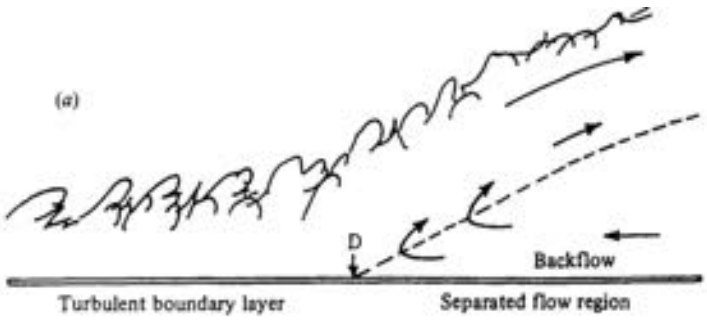

Figure 5.5: Separation mechanism instability in a boundary layer [120].

Reverse transition

Reverse transition, as indicated by its name, is the inverse process by which a flow 'relaminarizes'. Contrarily to the processes described until now, a flow that is initially turbulent can become laminar. The streamwise vortices present in the viscous sublayer are subject to strong viscous forces. As these vortices move downstream while the mean flow accelerates, the wall acts as a sink of momentum and stretches the vortices until finally dissipating these structures. From studies such as Jiménez and Pinelli [86] the filtering of such structures disrupts the turbulence cycle and laminar flows are encountered shortly after this interruption. Mayle [120] showed comprehensively the non-negligible frequency at which this process happens in turbomachinery flows reminding it is a process largely underestimated.

A first conclusion from the above discussion is that there are many different paths that can lead to a turbulent flow. Different sources of instability are potentially present and will be more important depending on aspects such as pressure gradients, curvature or Reynolds number. The difficulty to capture transition is thus due essentially to the capacity to take into account all these effects accurately and reaffirms the fact that only wall-resolved LES simulations can trace all the small structures that contribute to such a potential transitions. In most cases, transition in complex geometry high Reynolds number flows will be of by-pass type although recent studies have shown the presence in some cases of the *a priori* less probable natural transition process. Indeed in specific cases, the flow around blades may become laminar and can separate. The difficulty to capture transition even today limits the quantity of information obtained through numerical simulations and questions may be posed on how these results have been obtained. This is why experiments have been until now much more reliable and one of the main goals at VKI when performing the LS89 test case. Numerical studies usually try to compare their predictions against experiments, which in turbomachinery are generally accepted as being the exact solution, one of the reasons being that CFD lacks of correct models or computational power to prove the contrary. With the advent of HPC facilities, LES has appeared as an appropriate tool to provide good comparison and understanding of experiments. Indeed outside the specific problem of flows around blades, it can go further helping the understanding of the flow. LES predictions in specific circumstances are a complement to circumvent possible deficiencies or uncertainties that come with any experiment. The conviction that numerical studies today are not accurate enough on configurations such as the LS89 is mainly due to the

lack of a comprehensive understanding of the loading mechanisms present in this specific test case. As a result, numerical simulation inabilities to reproduce the entire spectrum of test cases of this database can have many different origins: grid used, boundary conditions and numerical schemes. The following is in that respect primarily oriented in the identification of the need for AVBP to provide the "right" prediction. With this in mind the following gives first a literature review of the different numerical simulations performed after the initial experimental setup was published. The problems encountered as a result of the lack of information for values such as the integral length scale as well as the conclusion that the geometrical profile was unsuitable for CFD simulations is further explained. The operating points selected for this study are presented and the numerical grids and parameters are noted for the following chapter where the simulations are actually analyzed. Finally, a short section provides the criteria used to conclude when a convergent state is reached as well as the total cost required to do this.

5.2 LS89: Experiments and literature review

The blade cascade LS89 turbine vane configuration tested in the experimental facility at the Von Karman Institute, see Fig. 5.6. This configuration consists of a set of highly loaded transonic nozzle guide vanes in a linear configuration [7]. The vane profile was especially designed for this experiment and consists of a 2D extruded profile. More details related to the original geometry provided are given in Fig. 5.7 and Table 5.1. Although it is an academic configuration, the values encountered could easily be found in current aeroengines today and it represents the most valued database available for numerical comparisons in turbomachinery due to the reduced data provided by industrial partners. This has led to the thorough study already performed numerically by a large number of authors as Bhaskaran and Lele [18], Gourdain et al. [72], Wheeler et al. [192] or Collado Morata et al. [38].

The first simulations that used this configuration were of RANS type like in Smirnov and Smirnovsky [168], requiring complex turbulence models to capture transition and other phenomena. Results when compared to experimental data had hence an improvement margin and LES showed its capabilities to capture unsteady effects that RANS can not. The increase in numerical power as well as the large number of operating points, has led in the last years to an increase in the number of publications concerning this test case. RANS as in Emory et al. [62] for Uncertainty Quantification analyses but also DNS studies in Wheeler et al. [192] have been performed nearly simultaneously, showing that there are many ways to approach the problem. Focus is set on different parameters such as the certainty in low-cost simulations or the effect of high resolution are reported of crucial importance for simulation assessment. This exemplifies the fact that a simplified 2D extruded profile vane still represents a challenge in terms of numerical reproduction due to the complex physics it entails and that different methodologies are still today possible towards the resolution of this problem.

Although experiments available for comparison have been available for a few decades already, numerical simulations and finer aspects of them such as sensitivity to boundary conditions, shock capturing techniques have not been evaluated thoroughly in a LES context. This can be explained by the lack of computational power available until recent years. Latest publications show that one of the most critical issues points towards the evaluation of free-stream

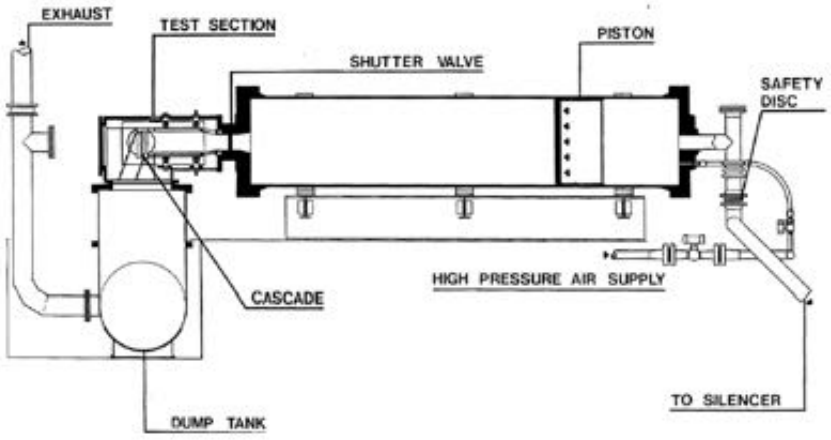

Figure 5.6: Isentropic Light Piston Compression Tube facility at VKI facilities.

c	67.674 mm
c_{ax}	38.81 mm
g/c	0.85
γ	55.0 deg
o/g	0.2597
$r_{LE/c}$	0.061
$r_{TE/c}$	0.0105

Table 5.1: Geometrical parameters characterizing LS89 geometry.

turbulence and the parameters that characterize it. Turbulence characterization requires both intensity measurements but also correlations to estimate for example, the integral length scale which in turn, will influence the dissipation rate and the turbulence evolution. This type of information is not provided in Arts et al. [7] and has been a problem towards characterizing the real conditions that the blade encounters. Studies in Consigny and Richards [40] give estimations but these have proven to be insufficient. Recent experimental tests on the same test bench at VKI have provided complementary and valuable information concerning these missing parameters [66].

Many of the first simulations performed show large differences. The most notable of them all is the heat transfer field which represents the most challenging task as it requires to correctly solve all phenomena (thermal and aerodynamic) involved. This has been improved during the last few years due partly to an increased quality in the geometry description. Indeed, based on the original data available to describe the blade geometry, one of the concerns when first performing the simulations was the existence of high-frequency oscillations around the profiles when investigating heat transfer or shear stress fields from the predictions. This problem has also been reported by Wheeler et al. [192], stating that the geometry provided by the original authors [7], although accurate, is not adapted to high fidelity CFD simulations. By taking a set

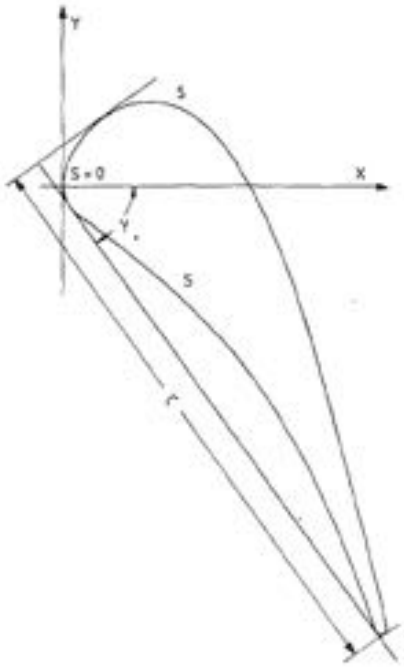

Figure 5.7: Geometrical detail of the LS89 blade.

of coordinates of the contour of the vane under manufacturing tolerance, it is possible to obtain a curvature that avoids the observed "bumps" and renders a geometrical profile adapted to such numerical simulations. For this study, the geometry was provided by the CENAERO group under the same constraints leading to an appropriate curvature profile. Note that with the original geometry, numerical oscillations were observed whenever diagnosing the LES predictions obtained with AVBP, and these were always found at the same position on the curvilinear abscissa. This led to a study of the curvature around the vane, which even under eye inspection can be found to be uneven confirming previous conclusions.

To summarize; difficulties are known to exist to predict the heat transfer coefficient profile around the blade or more generally the overall aerodynamics. This specific field can hence serve to evaluate the quality of the simulation since it is easily accessible experimentally. Different experimental observations on this specific field will then be associated to different boundary layer states or flows around the blade profile. Indeed, the dynamics present in the near-wall region is the most probable reason for these differences as they affect both the momentum and the thermal boundary layers. One of the sources of fluctuations in these boundary layers are due to the free-stream turbulence in the mainstream. This value is fixed experimentally but different turbulent intensities and integral length scales are tested to check its impact and importance. From a numerical point of view, turbulence has to be created and different methods to generate this turbulence may lead to different results, this point is further investigated. Finally, different LES predictions when modifying the turbulent parameters require a mesh convergence analysis. Once the grid effect is assessed and the flow prediction is considered of good quality, a more detailed analysis of the boundary layer statistics is performed to discriminate the findings and

gain insight on the transition mechanism of the LS89 test case.

5.3 LS89: Operating points

The LS89 configuration presented in section 5.1 has been thoroughly studied, as mentioned already. The computational domain retained for the LES to be discussed hereafter is presented in Fig. 5.8. Out of the great extent of the experimental operating points provided, **MUR129** and **MUR235** are two of the existing points of the database and are detailed in Table 5.2. These points have been chosen because the flow presents many interesting aspects such as shock waves, skin vortices or wave interaction and they are similar in terms of pressure ratio between inlet and outlet, as well as Reynolds number. To underline the effect of free-stream turbulence, both points have been retained as the weak turbulence injected in the **MUR129** case is considered negligible. The importance to study these specific points comes from the following interrogations: can the current code provide a satisfactory result in conditions such as those of the **MUR129**? If so, is this still the case once the physics becomes more realistic and thus, more complex? These two operating points are also the most realistic in terms of equivalence with industrial turbines. Finally, comparisons to previous numerical simulations are possible.

	MUR129	MUR235
P_{01} (bar)	1.849	1.828
T_{01} (K)	409.2	413.3
P_{s2}/P_{01}	0.63	0.57
T_w	297.75	301.15
Mach number at outlet	0.84	0.927
Reynolds outlet	$1.1352\ 10^6$	$1.15\ 10^6$
Inlet turbulent intensity (%)	1	6

Table 5.2: Operation point conditions.

For all the coming simulations, the computational domain retained relies on the view given in Fig. 5.8 unless specifically mentioned. The position of the inlet of the domain is located at approximately 0.82 blade chords upstream of the blade which is the same location as the hot wire probe present in the experiments and used for turbulent intensity measurements. The outlet region of the domain is chosen far enough for the wake to develop and for acoustic waves to exit the domain with no reflection. Note that such an objective also requires the use of non-reflecting boundary conditions [200]. In terms of specifications, the blade behaves as an uncooled isothermal surface and periodicity is enforced in the pitch and span wise directions. For the simulation, two aspects must be analyzed: the spanwise boundary conditions and the domain extent in this direction. Likewise, a comprehensive analysis concerning the inlet boundary conditions is to be performed and is presented in Section 5.5.1.

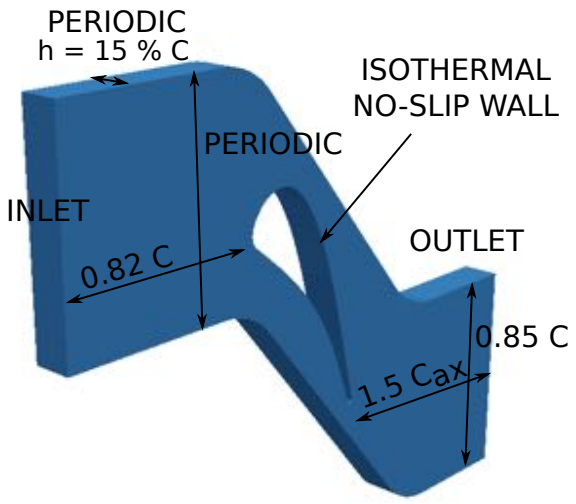

Figure 5.8: Computational domain used for the simulation of the LS89 configuration.

The periodicity condition enforced in the spanwise direction is valid due to the the fact that measurements have been taken on the central part of the blade. In this context, oil flow visualizations show that the tip and hub walls induce corner vortices. Two other types of vortices are also observed thanks to this analysis and correspond to passage and horseshoe vortices. Such secondary flows are absent only for a short portion of the blade corresponding to 17% of the total height of the blade. It is in this range that the probes were located so a spanwise periodicity condition would seem appropriate. The question remains however about the possible influence these secondary flows may actually have going downstream since these structures will necessarily evolve while going through the passage.

A second question relates to the spanwise domain *extent*. Requirements for the turbulence injection in terms of integral length scales are that these must not be affected by the numerics or lateral boundaries. Note that numerically the largest eddy the domain can reproduce is limited by the smallest dimension of the computational domain. For eddy interaction to occur, a best-practice is to take a length scale value that does not surpass half the smallest distance of the domain, to be confirmed by correlations obtained from the simulations. This specific point and numerical difficulty should be validated a posteriori in CFD. Note that most numerical studies take a spanwise extent of the computational domain of approximately 10 mm, which should be sufficient for the turbulence not to be constrained in this direction if an integral length scale of 3.5 mm is used. It is important to notice however that this value does not correspond to any measured values from the original experimental database.

Through the course of this study, new information was communicated to CERFACS' industrial partner. Indeed, Fontaneto [66] explicitly characterized the missing information about the integral length scales on the same workbench. The turbulence generated is of grid type, the grid being a set of horizontal cylinders that cover the duct inlet. The position of the hot-wire probe used to measure the turbulent intensity is at a fixed position in all cases and it is the grid that is displaced to modify the level of turbulence for the different operating positions. The turbulence intensity is thus determined by the distance of the grid to the probe identified

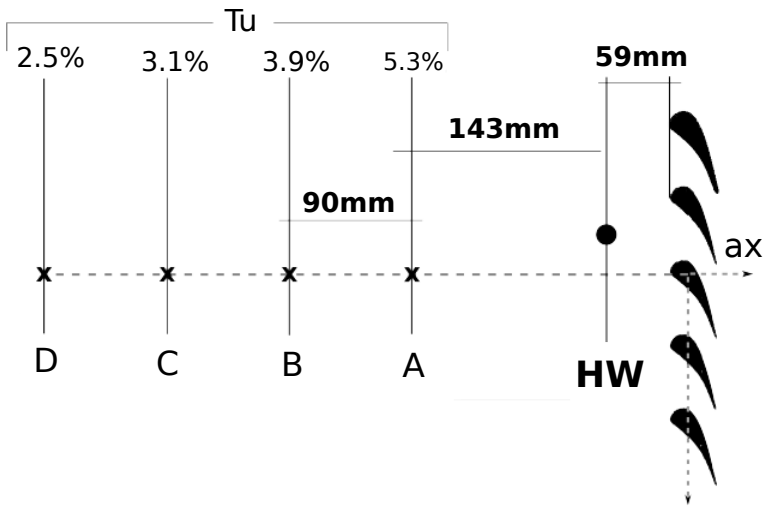

Figure 5.9: Measured turbulence intensity dependency on the grid position. Positions A-D correspond to different grid locations.

in Fig. 5.9. In the case detailed in Fontaneto [66] and contrarily to the original experiment, a signal was recorded at the hot-wire position. The autocorrelation of this signal is then obtained, producing an integral time scale transformed to an integral length scale applying Taylor's hypothesis [179]. Based on these new findings, a 30 mm spanwise domain has also been simulated to take into account the value of the integral length scale since the 10 mm domain is insufficient for the newly reported value. Indeed such changes in integral length scale specifications: i.e. presumed 3.5 mm against newly reported values of 7.6 mm will affect both the spatial decay of the turbulent kinetic energy since the turbulence dissipation rate ϵ is known to be proportional to the inverse of the integral length scale, $L_{ii} \; \alpha \; \frac{1}{\epsilon}$. It also impacts how the free-stream eddies will interact with the boundary layer and therefore the predicted transitioning mechanism. Of course, this boundary layer must be sufficiently refined to reproduce the smaller scales present and so, mesh resolution must be discussed and evaluated first, especially if a wall resolved LES is thought.

5.4 Mesh resolution

Three meshes are used for the simulations of the operating points shown in Figs. 5.10-5.12 for which specific parameters are given in Table 5.3. All meshes are hybrid and consist of tetrahedra except for the first layers of elements adjacent to the blade surface which consist of prisms as seen in Fig. 5.11. This specific meshing approach allows stretching the elements in the wall-normal direction without degrading the mesh quality excessively. In Fig. 5.10 the inlet region is seen to be coarser for M1 and more refined for M3 which allows to reproduce the smallest scales of the free-stream turbulence. The trailing edge region is also shown in Fig. 5.12. M1 has no specific refinement around the trailing edge while M2 and M3 do. The transition between the wake region and the free-stream region for M2 is seen to be more abrupt than

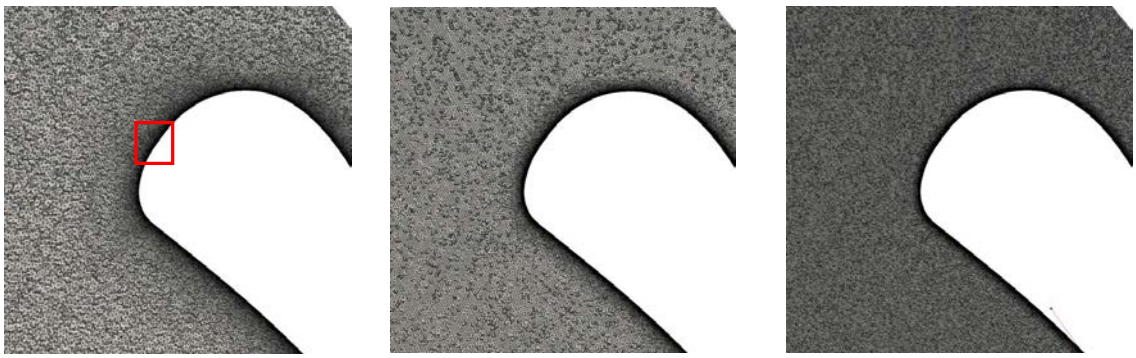

(a) (b) (c)

Figure 5.10: LS89 mesh at inlet for (a) M1 mesh (b) M2 mesh (c) M3 mesh.

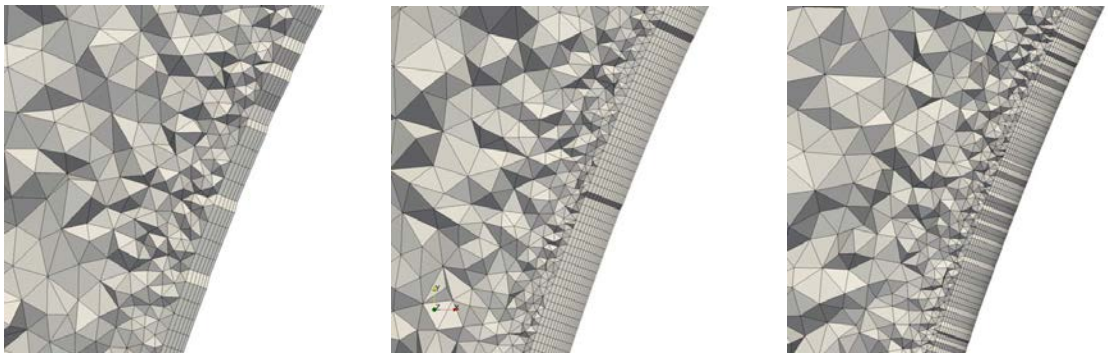

(a) (b) (c)

Figure 5.11: LS89 mesh in near-wall region as highlighted by the box represented on Fig. 5.10a (a) M1 mesh (b) M2 mesh (c) M3 mesh.

for M3. This could explain differences seen later on when comparing predictions issued by the use of the three meshes for the **MUR235** case. Note that the influence of mesh resolution for the **MUR129** operating point was seen to be negligible. Only small differences were observed between M1 and M2 so the finest and most expensive simulation issued by the use of M3 was not performed for **MUR129**.

	M1 mesh	M2 mesh	M3 mesh
Total number of cells	65M	213M	587M
Total number of prisms	8M	89M	269M
Prims layers	5	25	15
Total number of nodes	14.4M	67.6M	193M

Table 5.3: Mesh parameters for three meshes simulated.

(a) (b) (c)

Figure 5.12: LS89 mesh at trailing edge for (a) M1 mesh (b) M2 mesh (c) M3 mesh.

5.5 Numerics and modelling

The convective scheme used in this specific study is a Finite Element high-order scheme (3rd-order in space, 4th order in time) [146] unless otherwise specified. The mean y^+ corresponding to the three meshes is approximately 5, 3 and 1.5 over the whole blade with corresponding $\Delta x^+ = \Delta z^+ \approx 6y^+$, so these are wall-resolved simulations. The sub-grid scale model used is the WALE model [132], various sub-grid scale models (WALE, SIGMA, Dynamic Smagorinsky) being tested for the M1 mesh without large differences. In the current simulations, no shock capturing technique is used and the correct representation of the shock relies solely on the use of artificial viscosity.

In terms of boundary conditions, the following boundary conditions are used:

- Inlet boundary where total pressure and total temperature are imposed. Depending on the operating point, a fluctuating turbulent field is superimposed.
- Outlet where pressure is imposed.
- Isothermal wall for the blade surface.
- Translational periodicity in the pitchwise and spanwise directions.

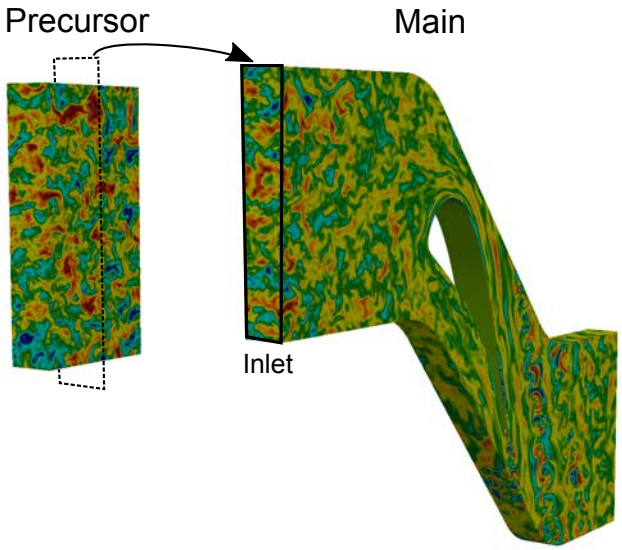

Figure 5.13: Global process of the precursor technique; fluctuations extracted from the precursor domain are transferred to the inlet of the main domain.

All conditions aside from the periodicity condition are imposed in a characteristic way meaning a relax parameter is used to avoid strong unphysical wave reflections. Values imposed on each surface are provided in Table 5.2.

5.5.1 Turbulence injection

Although the integral length scale imposed at the inlet remains an open question, the quality of the turbulence is to be accounted for. Classical synthetic type injection methods [96] require some adaptation distance to develop a physical energy spectrum. Such modeling strategies add onto the difficulty of having an adequate boundary condition implementation and adequate grid resolution as well as numerical schemes. As such, different methods and LES codes will inevitably produce different inflows or turbulent fields prior to the blade and hence responses of the flow. A comprehensive review of the different turbulent injection methods is given by Dhamankar et al. [50] where aside from the synthetic methods previously mentioned, details about the rescaling or precursor methods [113] are also discussed.

To discriminate the importance of the initial spectra and move away from synthetic turbulent spectrum that does not give physical solutions: i.e. solution of Navier-Stokes, a pre-computed turbulence approach is also used here to provide information to the boundary conditions. To do so, a precursor simulation performed using the same code, represented in Fig. 5.13, is coupled to the inlet domain to overcome any issue related to the adaptation of the unphysical inflow. For this specific case, only modeling and grid resolution are expected to play a role and can be compared to the synthetic turbulence injection methodology previously mentioned. Details about these specific developments and the difference with synthetic turbulence injection are available in Appendix C.

5.6 Characteristic flow time, convergence and simulation cost

To assure the simulation is statistically converged it is necessary to determine two things; first, a temporal value sufficiently large to guarantee that the results are independent of the data collection; second, the field used to determine this convergence measure. The most constraining quantity is probably the profile of heat transfer around the blade which additionally, is part of the experimental data provided for each operating point. This field is thus chosen to decide if the convergence of the simulation has been reached. The characteristic time used is based on the time it takes for a particle with a certain velocity to travel a distance, calculated as $t_{characteristic} = \frac{c}{u_0}$, where u_0 is an average of the inlet and outlet mean velocities and c is the chord of the blade. Once this non-dimensional value is obtained, it is possible to talk of the number of *flowthrough times* necessary. It must be noted for the following that spanwise averaging is done to help convergence, hence reducing the cost of the simulation. Note also that spatial averaging was also performed in the experiments. These definitions are used and quantitative results are provided in App. D, different proofs of convergence being given. The cost in term of CPU hours is necessarily an issue and orders of magnitudes are provided hereafter to underline the computational effort needed.

All simulations have been run on different machines with different architectures, details are provided in Table 5.4. All cases presented are for the **MUR235** conducted with synthetic turbulence, which requires the random data generation and implies an additional cost. All machines have been extensively used, having received a GENCI allocation x20162a6074 for access to the CINES machine.

Name	Affiliation	Max. nb. processors	Year	Architecture
NEMO	CERFACS	360	2015	Intel Haswell, 2.5 GHz
OCCIGEN	CINES	6720	2014	Intel Haswell, 2.6 GHz
BEAUFIX	Meteo-France	3840	2013	Intel Ivy Bridge, 2.7 GHz

Table 5.4: Machine architecture description.

The most important parameter to study is the CPU cost per flowthrough time which gives the total cost on a particular machine. These times may be decomposed into the various pre-processing and post-processing steps and other additional parameters of interest.

Name	Nemo	OCCIGEN	BEAUFIX
Cells (million)	65	65	195
Iterations/T_{conv} (x10^3)	55	55	55
CPU time pre-processing (s)	17.94	16.2	21.3
CPU time/T_{conv}	6133	4400	20750
CPU time writing	10.4	6.61	13.2
Nb. processes	360	1200	1600
Time/(nb. it * nb. cells) (x10^{-6} s)	5.78	6.5	6.67
Max. memory/core (Mb)	153.79	44.35	103.89

Table 5.5: CPU detailed for various simulations.

The following chapter shows the results of the simulations done for the various operating points addressed. The first simulations as can be intuited give similar results to those found in literature. A sensitivity analysis was however performed to test the influence of mesh refinement, turbulence injection parameters at the inlet and domain size effects. When possible, a comparison to the experiments is given, normally in terms of heat flux coefficient. Once the LES has been validated, an analysis concerning the transition mechanisms is sought to explain the results here obtained.

Chapter 6

LES predictions of MUR129 and MUR235

Contents

It is now time to evaluate the predictions given by AVBP for the chosen configuration. For the following, the two operating points selected are the **MUR129** and **MUR235**. The former case will be used as a reference test case. No turbulence is present and previous simulations from the literature are usually seen to be capable of correctly predicting the heat transfer coefficient. This operating condition therefore evaluates how well AVBP and associated numerical schemes compare to other codes that also match the experimental results. The results obtained when studying the **MUR129** case are then used as a preliminary step before addressing the more complex **MUR235** operating point. For this second operating point, the level of heat transfer coefficient is quite accurately predicted over the whole blade profile, accuracy depending on the mesh refinement used. Sensitivity to the grid is in particular seen to be locally crucial on the suction side. This particular region is targeted in the following steps to understand the driving parameter that allows to attain the levels reported in the experimental data.

6.1 MUR129 predictions

The first case considered is **MUR129**. This operating point reports a 1% turbulence intensity at the inflow, which corresponds to an absolute *rms* value of 0.61 m/s. Tests have been performed to quantify the influence of this parameter compared to a no turbulence simulation on fields such as heat transfer or shear stress. Although the mean heat transfer is the only data available in Arts et al. [7], no noticeable difference can be observed on this field nor on others such as the isentropic Mach number. The effect of introducing small values (equal or lower

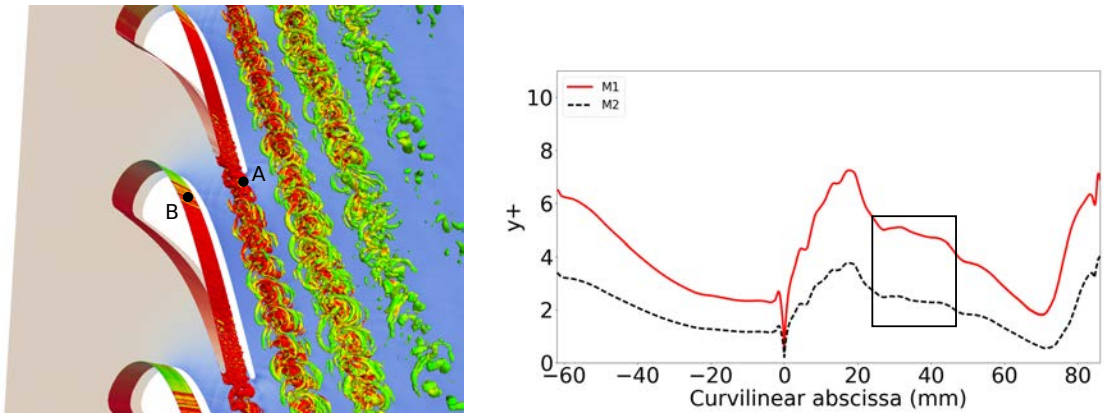

(a) (b)

Figure 6.1: **MUR129** operating point. a) Q-criterion coloured by vorticity. Background plane represents the $\frac{|\nabla\rho|}{\rho}$ b) y^+ distribution along curvilinear abscissa for M1. Box indicates region where neighbour acoustic waves impact the blade surface.

than 1 %) are therefore assumed to be negligible for the rest of the section.

When analyzing the instantaneous flows issued by the LES prediction based on the M1 mesh, the Q-criterion represented in Fig. 6.1a shows that the only coherent structures present in the simulation locate in the wake of the blade. These are the result of the vortex shedding that issues from the trailing edge and will be shown to be a strong source of noise. This can be observed on the background plane where the density gradient is shown. The acoustic waves that are issued from the wake impact the contiguous vane perturbing locally the boundary layer. This generates a pattern visible on fields such as the y^+ profile of Fig. 6.1b and marks even the averaged profiles. To check that this is indeed the effect of the acoustic waves, two probes are used in the simulation to register the flow activity in the wake, Probe A, and on the surface of the blade where these waves impact, Probe B. By tracing the FFT of the pressure evolution of both signals, a clear correlation is found and confirms the source of the waves as depicted by Fig. 6.2. To verify the frequency at which the flow sheds is effective, its corresponding Strouhal number is evaluated as this non-dimensional number is widely used in literature to study if, for the Reynolds number of the flow, the shedding is indeed physical. It is defined by $St = \frac{Lf}{U}$ where L is a characteristic length (taken as double the radius of the trailing edge), f is the shedding frequency and U is the mean velocity in the wake. It is also known that for $Re \approx 10^6$, its value should range between $0.2 \sim 0.24$. Based on the present simulation, $St = 0.1988$ which confirms that these waves are indeed physical although slightly too coherent; i.e. below 0.2.

In any case and despite this unsteady activity, the boundary layer predicted by the simulation is observed as attached on both pressure and suction sides. Some vortices may be found locally on the suction side in the region where contiguous waves emanating from the wake impact the suction side. However, the intermittency and weakness of their appearance may be considered negligible. On the pressure side, it is not until the flow reaches the trailing edge that the flow detaches. Note that boundary layer velocity profiles will be presented and compared to cases where free-stream turbulence is present in later sections.

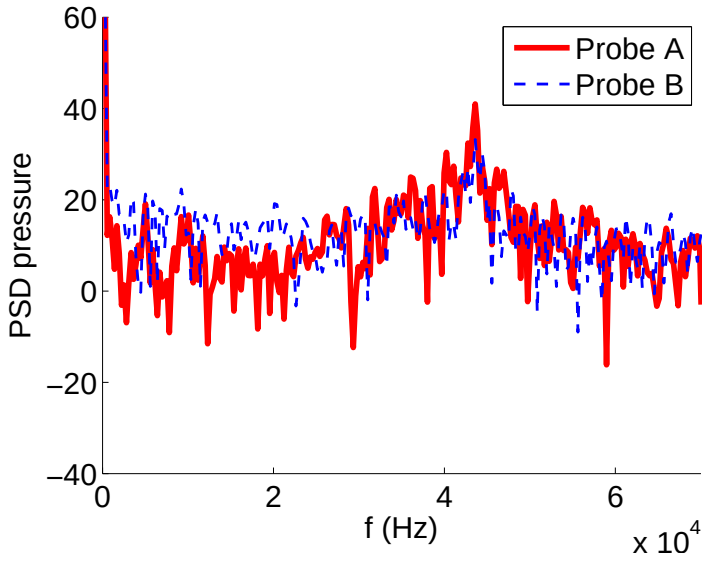

Figure 6.2: Spectral composition of the pressure signal at probes A and B.

The heat transfer coefficient is retrieved from the simulation following the expression $h = \frac{q_n}{T_{0,1}-T_w}$, where q_n is the heat flux, $T_{0,1}$ is the total temperature at the inlet and T_w is the wall temperature. Shown on Fig. 6.3 along the blade, its prediction is found to be in excellent agreement with the available experimental data. The level of the profile on the pressure side is slightly underestimated, the shape of the curve being well captured. On the suction side, the simulation captures very well the experimental profile. The M1 mesh is hence found to be sufficient for the prediction of the heat flux although the slope on the suction side near the trailing edge could require a better refinement such as the one provided by M2. Whenever comparing these predictions to the one obtained by Collado Morata et al. [38], a slightly different transition offset position is found: i.e. sudden h increase near the blade trailing edge. It must however be stated that although the value of y^+ has been kept the same, a better mesh quality has been used here complemented by the use of twice the original number of degrees of freedom in the case of the M1 mesh. For this operating point it is hence concluded that LES predicts the flow independently of the mesh used. This is also observed to be independent of the numerical scheme employed: TTG and LW giving similar results on the M1 and M2 meshes (not shown).

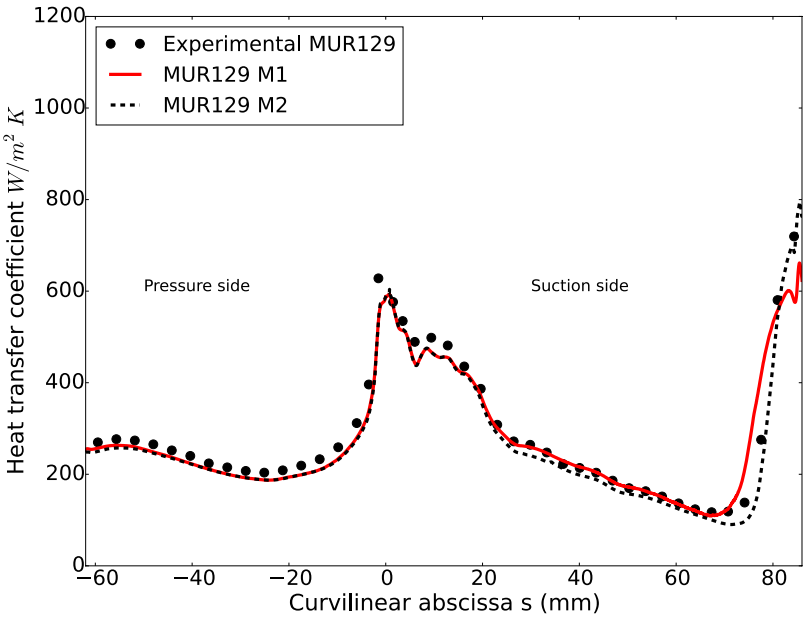

Figure 6.3: Heat transfer coefficient of **MUR129**.

6.2 MUR235 predictions

This operating point is richer in terms of physics than the previous **MUR129**. The different physics that happen for this particular operating point can be observed in Fig. 6.4. The key that differentiates **MUR235** from **MUR129** is the turbulence present in the incoming inflow. In the former case, free-stream turbulence convects from the inlet before interacting with the blade boundary layer resulting in a completely different flow field. On the suction side of the blade the presence of acoustic waves generated by the wake of the neighbour blade are seen provided the adequate mesh resolution just like for the **MUR129** case. The shock wave present here on the suction side of the vane is furthermore seen to interact with the wake issued by the trailing edge of the upper vane and migrates upstream compared to **MUR129**. The shear stress that is shown on the blade surface on Fig. 6.4 shows localized high-shear stress regions upstream from the shock wave indicating the appearance of turbulent regions that may develop as discussed in the following sections depending on the simulation. The pressure side boundary layer remains laminar although free-stream vortices are seen to impact the surface and deform due to the imposed near wall shear stress. Finally, a Karman vortex street develops downstream from the trailing edge generating acoustic waves similarly to the **MUR129** case.

From a CFD point of view, the difficulty concerning this operating point with higher free-stream intensity is the clear inability of current codes to correctly predict the heat transfer coefficient of the experimental results. In light of the multiple physical interactions, various modelling parameters are tested and a sensitivity analysis is performed to discriminate the seemingly more important interactions. First, inlet turbulence parameters are modified to check the influence they have on the heat transfer curves and other flow profiles. The influence of a higher intensity as well as various values of the integral length scale are tested, the

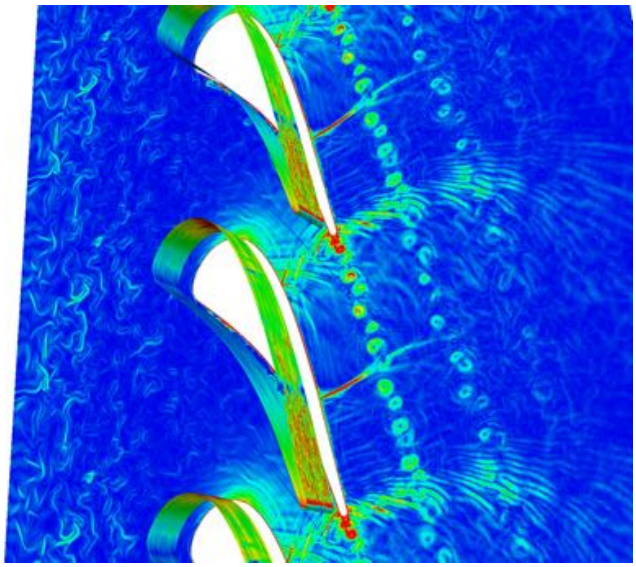

Figure 6.4: Shear stress field on blade surface. Background plane represents the $\frac{|\nabla\rho|}{\rho}$.

latter being addressed in light of the recent experimental findings [66]. The spectrum used to inject turbulent structures at the inlet is then qualified, a comparison being made between classical synthetic turbulence injection and the precursor turbulence injection method detailed in App. C. Mesh convergence is finally addressed in this chapter to determine the importance of resolution. To finish, a detailed analysis of turbulence statistics in view of the previous tests is also performed based on the best prediction in an attempt to evidence the mechanism responsible for the boundary layer transition. Note that whenever possible, results provided by Arts et al. [7] are compared to the simulations.

6.2.1 M1 mesh predictions using synthetic turbulence injection

The first simulation detailed here was obtained using the M1 grid and turbulent inflow conditions specified in [7] with a 6% turbulence intensity, injecting a synthetic turbulent spectrum and a characteristic integral length scale of 3.5 mm. This test is done to check how a validated code behaves using literature parameters. Experimental values are set when available but values from literature are used to see how well AVBP behaves compared to other codes.

First, a visualization of the flow prediction is done focusing on the inlet passage region upstream the blade as well as around the leading edge of the blade. The structures generated at the inlet are seen to arrive to the vane in Fig. 6.5a contrarily to the **MUR129** case. These vortices are then stretched around the leading edge as seen in Fig. 6.5b and are no longer isotropic. Note that from now on and when necessary to ease the representation, a blade representation is added alongside the Q-criterion as shown in Fig. 6.5b to show the camera position from which the blade is being viewed.

The existence of such structures around the leading edge requires to validate the hypothesis

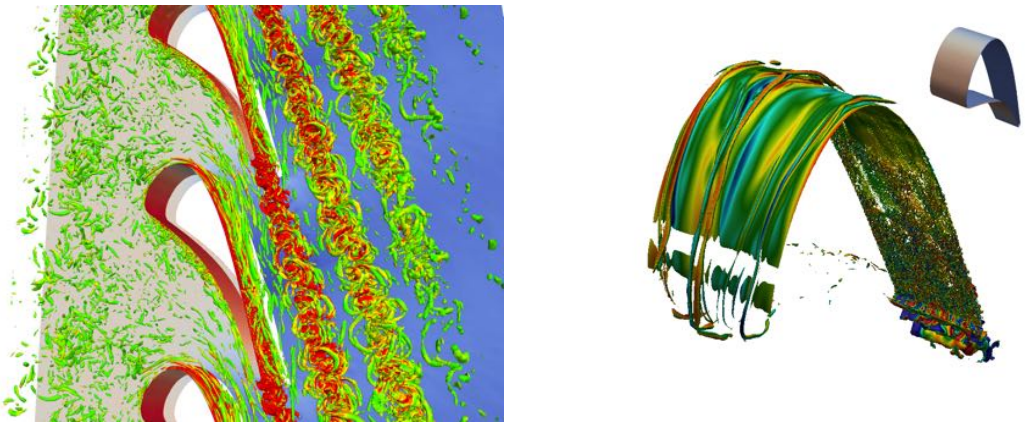

(a) (b)

Figure 6.5: **MUR235** operating point. a) Q-criterion coloured by vorticity. Background plane represents the $\frac{|\nabla\rho|}{\rho}$ b) Stretched vortices around leading edge of the blade represented by Q-criterion coloured by spanwise velocity.

described in Sec. 5.3 concerning the spanwise domain extent. Indeed, the domain was said to possibly constrain the injected turbulence requiring an a posteriori validation as the turbulent structures could be affected by the spanwise BCs. For verifications, spatial correlations are studied at a position upstream from the blade at $s/c = -0.2$ ($s \approx -15$ mm) where c is the chord value presented in the previous chapter. The two-point correlation shows how correlated the structures are along the stagnation point height (y axis). The criterium assumed is that structures are not correlated if the absolute value of the correlation is lower than 0.3. It can be observed in Fig. 6.6 that this value is much lower than this threshold value and so, the periodicity does not seem to constrain the free-stream turbulence. Other positions were tested confirming our conclusion for the main stream flow.

In Fig. 6.7, it can be observed that the heat flux coefficient h retrieved from the M1 prediction, remains almost at the same level as the **MUR 129** predictions on most of the suction side, and is hence, far from the corresponding experimental data. The position of the shock wave present at approximately $s \approx 60$ mm is nonetheless predicted quite accurately, position at which a large increase in heat flux coefficient is seen although the level of the jump is not well captured if compared to the experiment. This could indicate either that the shock is not sufficiently resolved or that the physics may be different upstream this point. Compared to **MUR129**, an increase in h appears on the suction side in the proximity of the leading edge $s = 0 - 20$ mm in coherence with experimental findings in this region. The Q-criterion structures seen in Fig. 6.5b when free-stream turbulence is present have not been recovered in the simulations with low turbulence levels, which confirms that the source of the increase in heat transfer around the leading edge is indeed due to the turbulence upstream from the blade. The pressure side is also seen to have much larger h values compared to a case with no turbulence. It also confirms that free-stream turbulence does play an important role in the prediction of the heat transfer coefficient for this flow. To test the sensitivity of the prediction to this parameter, simulations at different turbulence intensity levels are compared. Additionally, a realistic spectrum is also injected to have a broader view on the impact of the injection models.

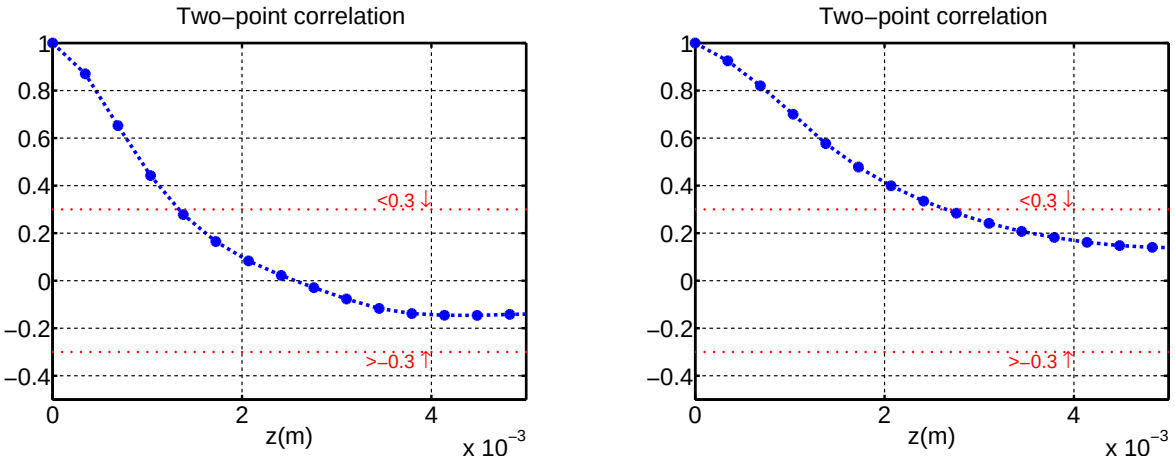

(a) Axial velocity (b) Spanwise velocity

Figure 6.6: Axial and spanwise velocity correlations in spanwise direction.

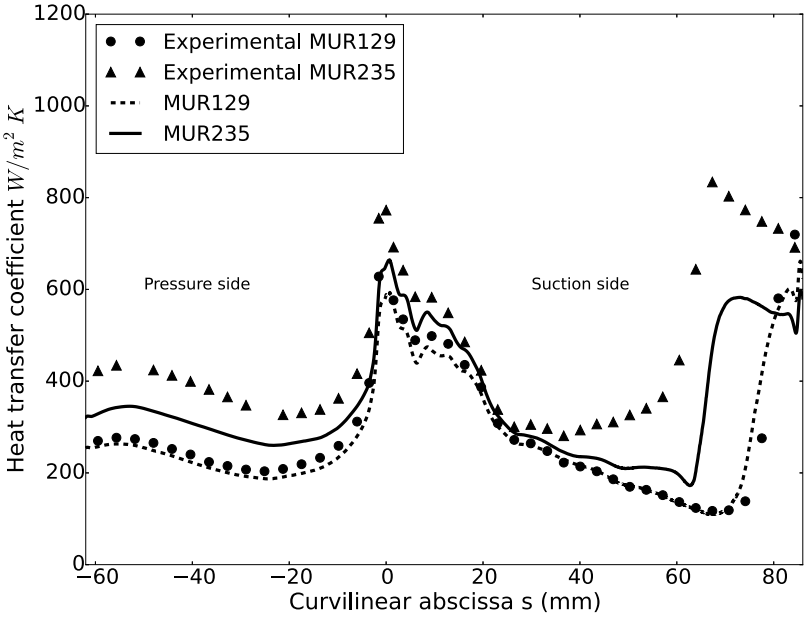

Figure 6.7: Heat flux comparison of **MUR129** and **MUR235** operating points using synthetic injection methods when required.

Turbulence injection model effects

The first modelling aspect to be studied is the turbulence intensity as well as the approach employed to determine the inflow turbulent signal. Indeed, the impact of the turbulence evolution from the inlet channel is different depending on the methodology used (cf. App. C for validations and illustration of such models). There are various parameters that are known to influence the turbulence evolution in a LES simulation: the turbulent intensity level, the turbulent length scale, the spectrum of turbulence injected and the mesh refinement. Note that all tests in this section are conducted using the M1 mesh and a fixed integral length scale set to 3.5 mm.

The first point that must be addressed is the flow evolution in the passage region upstream the blade. The difference in the turbulence intensity decay is illustrated on Fig. 6.8 for different turbulent inflow signals and intensities. Decay is plotted on streamlines that go from the inlet up to the stagnation point on the leading edge of the blade. At this specific location, care must be taken since when the flow approaches the blade, it will stretch inducing anisotropy in the turbulence. This means the turbulent intensity can no longer be studied using the homogeneous turbulence injection expressions. When comparing the simulations using the same inlet intensities, it can be noted that the decaying slopes do not agree and depend on the methodology used to create the inflow field. The precursor simulation has been shown to have a physical spectrum at the inlet, (i.e. solution of NS equations) which is not the case for the synthetic method. To explain the differences, it should be noted that at the inlet, the most energetic length scale of the synthetic method is large with no dissipative length-scales (PP spectrum). Most of the energy at the inlet for the synthetic injection is distributed in large spots. During the streamwise advection however, energy is naturally distributed to the whole spectrum. This process modifies the integral length scale and in turn determines the turbulence rate of decay. When this happens it is difficult to correctly estimate the decay of Turbulent Kinetic Energy (TKE) since the perturbations introduced at the inflow do not initially comply with the NS equations. It requires an undefined axial distance for the length scales to attain a physical behaviour. This problem is not an issue with the precursor as the spectrum injected is generated by solving the NS equations and the TKE rate of decay is correct from the inlet. It is thus expected that curves don't have the same slope for the same turbulent injection level. It can also be noted that the TKE at position $x = -55$ mm is not exactly the one prescribed retrieving neither 6% nor 18% at the inlet. In the precursor case, to obtain the correct turbulence properties (intensity level, length scale) a momentum source term is added in the precursor simulation. This source term is not trivial to obtain [136] and it is difficult to impose the exact values and comply with all the turbulent inputs. A small tolerance is thus accepted. For the synthetic case, the previous non-physical behaviour at the inlet may be blamed.

The effects the turbulence level and the spectrum have on the aerodynamics are overall observed to be negligible with mesh M1. The control parameter for this conclusion is the isentropic Mach number profile shown on Fig. 6.9. Furthermore and for all cases, inlet to outlet pressure ratios are correctly estimated and losses are also of the same order for all injection methods which implies that the isentropic Mach number does not show large differences. Given the global performance of the flow compared in Table 6.1, Fig. 6.9 shows the expected agreement, small differences are only seen in the abscissa of the oscillating shock.

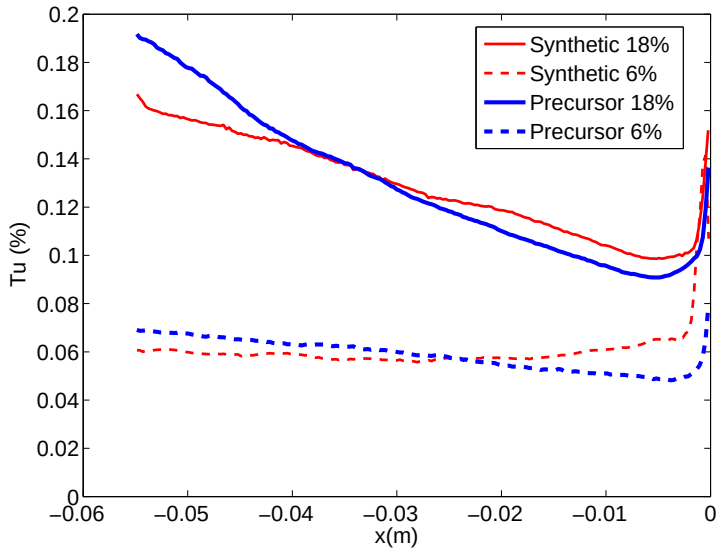

Figure 6.8: Turbulent intensity decay at inlet channel upstream from blade.

	Synthetic turbulence		Precursor	
Tu	6%	18%	6%	18%
P_{s2}/P_{01}	0.57345	0.57372	0.57341	0.57348
$(P_{01} - P_{02})/P_{02}$	0.018208	0.018180	0.017669	0.017836

Table 6.1: Global performance for each value of turbulent intensity and spectrum injected.

Fields such as the shear stress values represented in Fig. 6.10 are observed to be more prone to differences as the boundary layers can be excited differently by the different turbulent surrounding fields. From Fig. 6.10 which compares all cases, the pressure side boundary layer remains laminar so the shear stress is not modified for this part of the blade. The same can be said for the leading edge region around the suction side: i.e. between $s = 0 - 20$ mm where it was previously seen that the heat flux was enhanced by turbulence compared to MUR129. Here this response seems however independent of the turbulent field at least with the level and models tested here. Moving downstream on the suction side, the plateau between $s = 30 - 60$ mm shows the largest differences between the four simulations. The mean shear stress is notably higher for the larger values of turbulence intensity (18%) and are always slightly lower for the precursor case. This observation corresponds to the same findings when analyzing the previous TKE decay in Fig. 6.8. The highest turbulence intensity levels near the blade correspond to the 18% inlet level and the synthetic is always slightly higher than the precursor. The connection between free-stream turbulence and the profiles around the blade seems to also be important in the region $s = 30 - 60$ mm. An effect should thus be seen on the heat transfer profile.

Heat coefficient profiles are given in Fig. 6.11 and show that both turbulence injection methods predict a similar heat transfer coefficient over the whole blade. Increasing the inflow

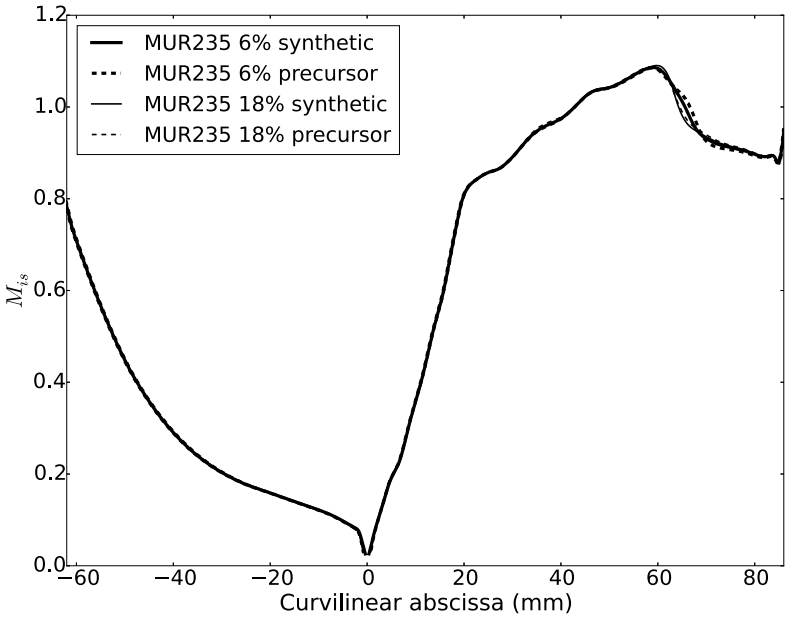

Figure 6.9: Isentropic Mach number comparison of turbulence injection methods for **MUR235** operating point for M1 grid.

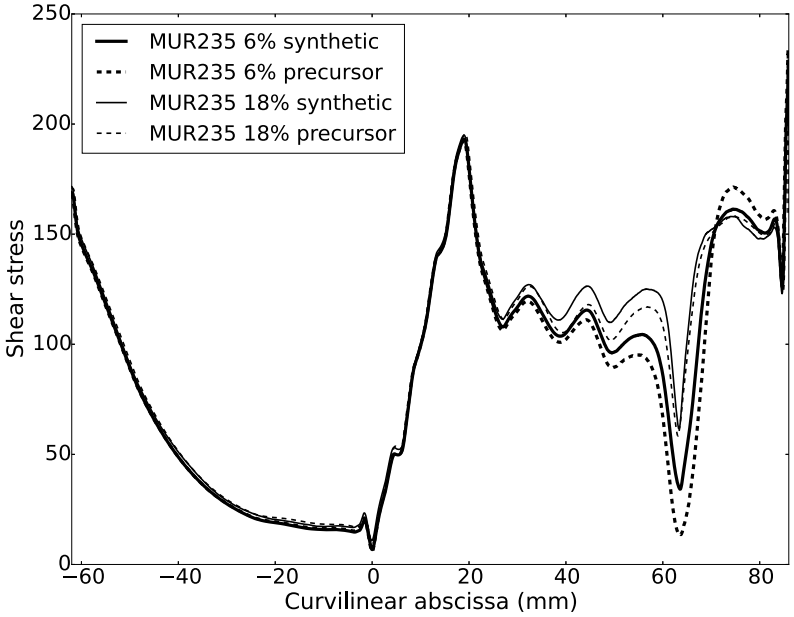

Figure 6.10: Shear stress comparison of turbulence injection methods for **MUR235** operating point for M1 grid.

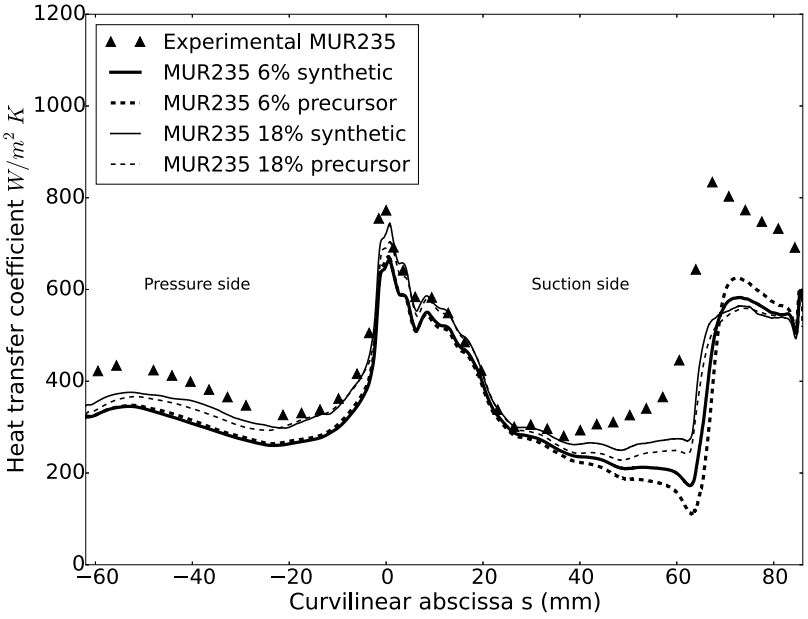

Figure 6.11: Heat flux comparison of turbulence injection methods for **MUR235** operating point for M1 grid.

turbulent intensity shows an improved agreement around the leading edge region, complemented by an improvement on the pressure side region. The suction side downstream from the location of impact of the neighbour acoustic waves $s/c \approx 0.3$ ($s \approx 20$ mm) remains however the most challenging. The importance of free-stream turbulence for the prediction of the heat flux plateau between $s/c \approx 0.4 - 0.9$ ($s \approx 27 - 61$ mm) is observed once again. Finally, at $s/c = 1.1$ ($s \approx 74$ mm) and locations downstream the shock, the flow is fully turbulent and independent of the level of turbulence imposed at the inlet.

The turbulent intensity level has been seen to have a great impact on the different profiles such as the shear stress and the heat transfer around the blade. A much better agreement in terms of heat transfer is found for higher levels of turbulent intensity while the spectrum injected does not seem to be critical for these simulations. These findings are only the output of changes in the mean flow and a more detailed analysis of the physical interactions is required. Visual and instantaneous field inspections are now proposed to see how different inflow turbulent fields may affect the heat transfer. For this investigation, the blade will be divided in two different parts. First, the suction section that goes from $s \approx 20\ mm$ to the trailing edge will be analyzed. This section is of particular interest as it is seen to be the most sensitive region to the different turbulent parameters. The second part is the pressure side and leading edge of the blade which seems to be directly driven by the level of turbulence at the inlet. Complementary mean statistical fields are also detailed hereafter to ease the analysis whenever needed.

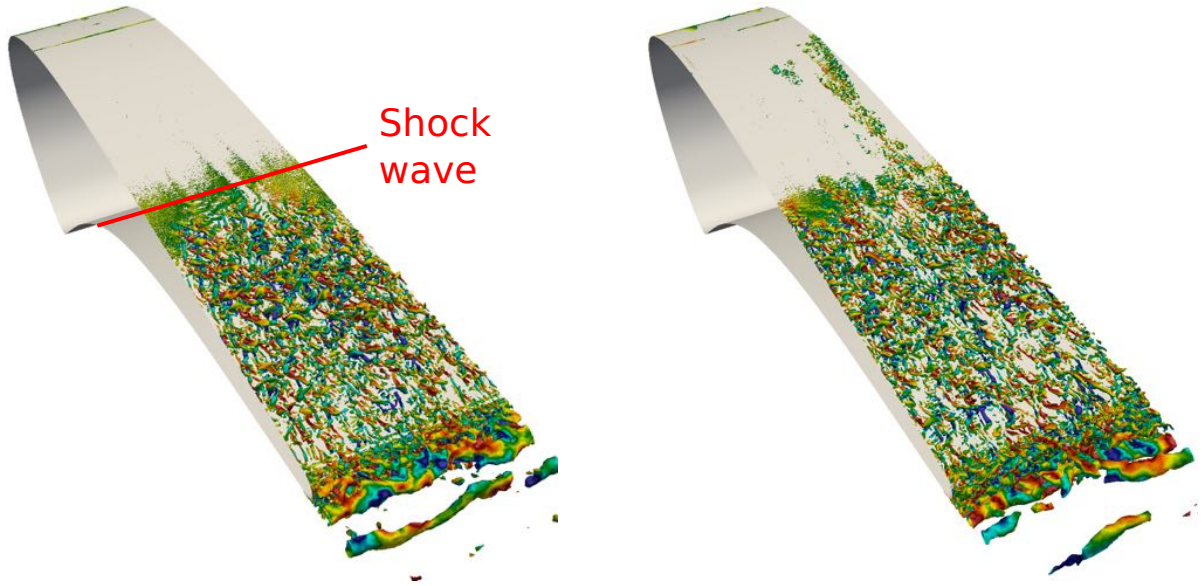

(a) (b)

Figure 6.12: Coherent structures representation for a) 6% b) 18% turbulent intensity at the inlet using M1.

Flow dynamics

Visualization of the instantaneous flow helps to understand the mean flow behaviour and more precisely, the local dynamics that takes place and its imprint on the mean fields. Differences between 6% and 18% fields are first sought by doing a visualization of the Q-criterion and comparing them in Fig. 6.12. The main differences between the two predictions are found in the region upstream the shock wave where turbulent structures are found for the 18% level that are named 'spots' in literature. This indicates that the main differences between simulations in the range of $s/c = 0.4 - 0.9$ ($s \approx 27 - 61$ mm) are due to a pre-transition region found when injecting the higher turbulence intensity. In other words, the higher free-stream turbulence level acts as a source of instability leading the boundary layer to locally transition. This specific process seems to be absent for the 6% case.

In Fig. 6.13 an instantaneous contour of Q-criterion based on the 18% case shows how turbulent structures develop inhomogeneously in the spanwise direction prior to the shock wave on the suction side. As seen on this specific view, turbulent patches are found when large structures from the free-stream turbulence are near the wall for interactions to occur. Such free-stream vortices are believed to be responsible for the spots found upstream of the shock wave. As seen on this figure further downstream, these structures tend to redistribute along the whole span due to the strong shock and give place to more coherent structures.

To confirm this transitioning effect the shape factor has been extracted along the abscissa comprised between $s/c = 0 - 1.1$ ($s \approx 0 - 74$ mm) for both 6% and 18% synthetic turbulence at the inlet. The shape factor is an indicator of the state of the boundary layer [120, 165] and

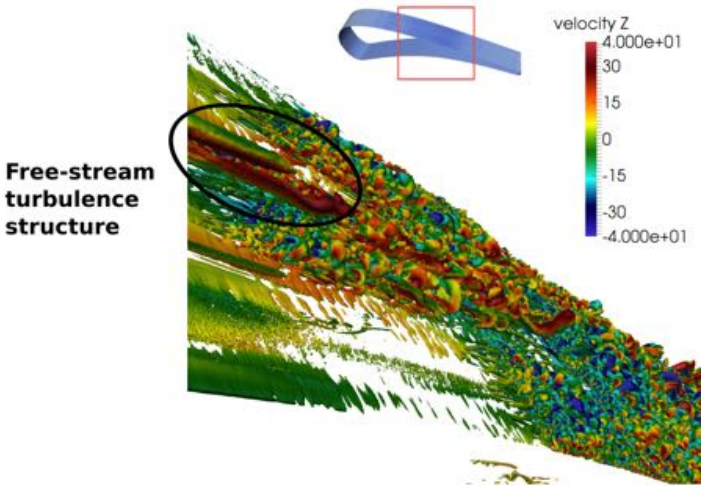

Figure 6.13: Interaction between free-stream vortices and wall structures.

serves to evaluate if the boundary layer remains laminar or if it is turbulent. This factor is defined by $H = \delta^*/\theta$, where δ^* and θ are the displacement and momentum thicknesses [160] written as,

$$\delta^* = \int_0^\infty \left(1 - \frac{\rho(y)U_s(y)}{\rho_0 U_{s,0}}\right) dy, \tag{6.1}$$

$$\theta = \int_0^\infty \frac{\rho(y)U_s(y)}{\rho_0 U_{s,0}} \left(1 - \frac{U_s(y)}{U_{s,0}}\right) dy. \tag{6.2}$$

Their streamwise evolution along the blade is shown in Fig. 6.14. The displacement thicknesses are seen to be very similar implying that the streamwise velocity profiles do not show large differences. However, the momentum thickness value is larger for the higher injected turbulence case in the pre-transitioning region. This is expected as the existence of turbulent spots increases locally the momentum exchange in the boundary layer which moves the momentum thickness limit further away from the wall. As a consequence, an increases in the shear stress is found as anticipated in Fig. 6.10.

These two variables are now used to calculate the shape factor. From Sieverding [165], it can be said that transition region is attained when values range between $1.3 - 1.7$ which is not far from the retrieved values for both intensity levels when $s/c > 0.9$ ($s \approx 61$ mm). Further upstream, current predictions clearly produce initially laminar boundary layers. The existence of turbulent spots tends to decrease the shape factor until it fully transitions after the shock at $s/c \approx 0.92$. This effect is only seen when injecting the 18% turbulence intensity at the inlet. This corroborates the transitioning effect seen visually but does not contribute to explaining the mechanism responsible for transition as the same type of behaviour can be found for natural

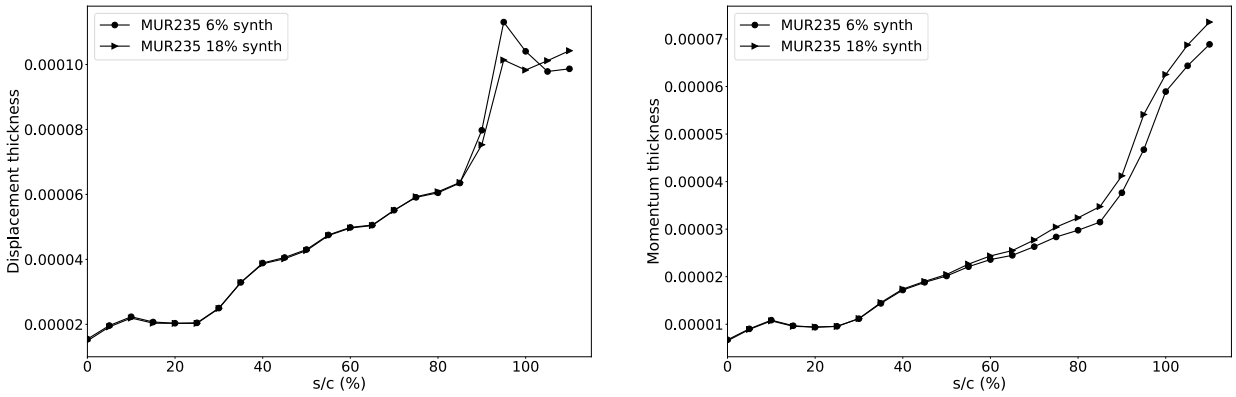

(a) (b)

Figure 6.14: Displacement and momentum thickness along the suction side of the blade for M1 mesh.

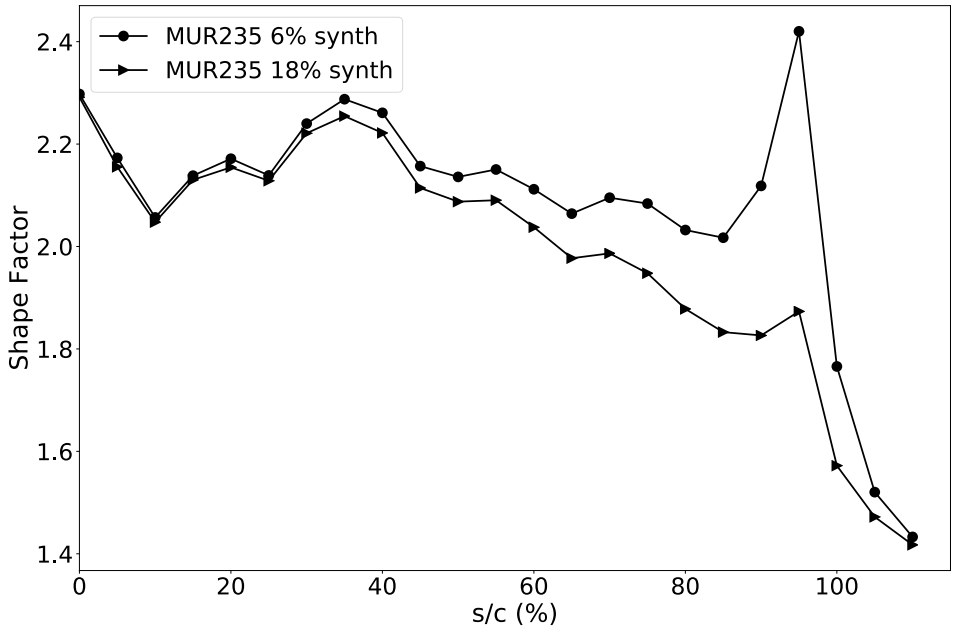

Figure 6.15: Shape factor on suction side at different abscissas in the transitioning region.

transition mechanisms as shown by Abu-Ghannam and Shaw [4] when by-pass transition is suspected for the configuration studied in this document. A more detailed analysis on this specific point is provided in Sec. 6.3. In any case, the existence of spots can be suspected to be related to the increase in heat transfer seen previously in the simulations and in the experiment. It is also reasonable to question if the appearance of these spots which occur at an undefined frequency and the increase in heat transfer can be related to the statistical time duration used to extract the profile. A short study was conducted to answer this question and confirms that the period taken to extract the discussed profiles was sufficient to satisfy convergence, c.f. App. D.

Such events however can explain the observed differences in the boundary layer profiles of streamwise velocity shown at three different positions of interest. The first position is located upstream the position where incoming acoustic waves from the contiguous blade impact the blade at $s/c = 0.3$ ($s \approx 20$ mm). The second at $s/c = 0.7$ ($s \approx 47$ mm) is representative of the pre-transition region before the shock wave while the third position represents the fully-developed transition region after the shock wave $s/c = 1.1$ ($s \approx 74$ mm). The streamwise velocity profiles as a function of the local normal distance from the blade wall are compared at the cited positions between the 0% and 6% inlet turbulence cases in Fig. 6.16. Streamwise velocity comparisons between higher intensity levels of turbulence and spectrum are not shown here because profiles are very similar. The **MUR129** case, where no turbulence is injected is added for comparison and is seen to be very similar to the turbulent case at $s/c = 0.3$ ($s \approx 20$ mm) in Fig. 6.16a. At this position the boundary layer is still laminar in all cases and the acceleration around the leading edge dominates the mean velocity. The impact of the external turbulent flow is quasi-null and seen to introduce only a weak unsteady component. At the second position however, Fig. 6.16b shows that the streamwise velocity starts to differ. The shape of the profiles are similar but the absolute value is larger for the **MUR235** case due to a reduced effective section for the flow to go through the passage. At $s/c = 1.1$ ($s \approx 74$ mm), a fully developed velocity profile appears for the turbulent case while the **MUR129** velocity evolution approaches a laminar shape, remaining in this state up to the trailing edge where a sudden transition takes place.

More information about the BL state is accessible by studying the profiles for the Turbulent Kinetic Energy (TKE) at the same positions. TKE indeed gives insight into the turbulent activity in the boundary layer. Additionally to the previous profiles studied in Fig. 6.16, the different levels of turbulence intensity injected and the two spectrums are compared. The additional curves were previously neglected because the streamwise velocity curves did not show appreciable differences as mentioned earlier. At the first position $s = 0.3\ c$, profiles of TKE are seen to be larger for higher levels of turbulent intensity, Fig. 6.17a. On the outer region of the boundary layer, TKE values differ being in agreement with each inflow specification: i.e. 6% and 18%. However, in terms of spectrum injected the precursor injection leads to lower turbulent fluctuations in the boundary layer. In all cases, the maximum values are obtained at a value of $y^+ \approx 30$. At the second position $s = 0.7\ c$, higher values of TKE are found in all cases which means there is indeed a development of the boundary layer becoming more energetic. Different methodologies to inject turbulence lead however to very distinct boundary layer profiles. It can be noted that the effective TKE level between the 6% synthetic and 18% precursor simulations are nearly the same. From Figs. 6.8 & 6.11 which show the turbulence

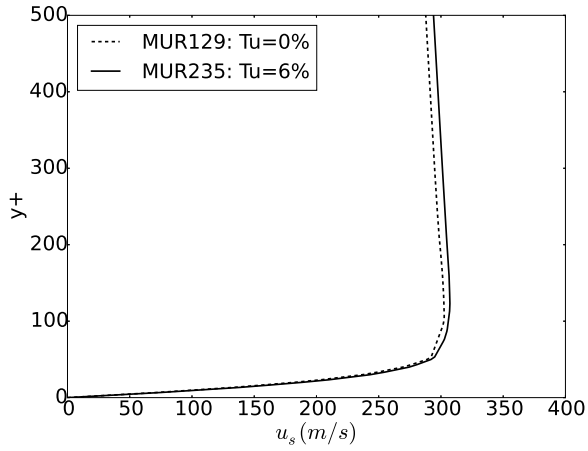

(a) 30%

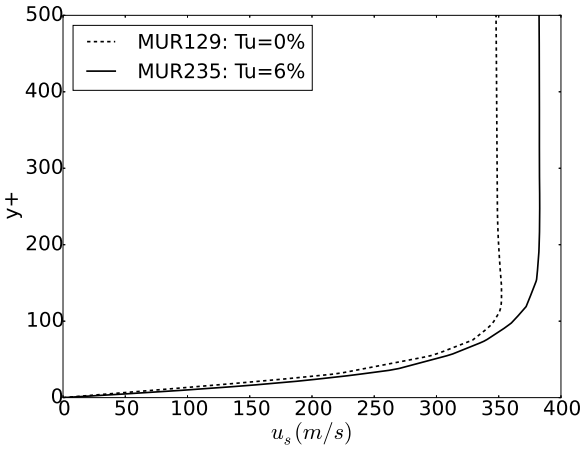

(b) 70%

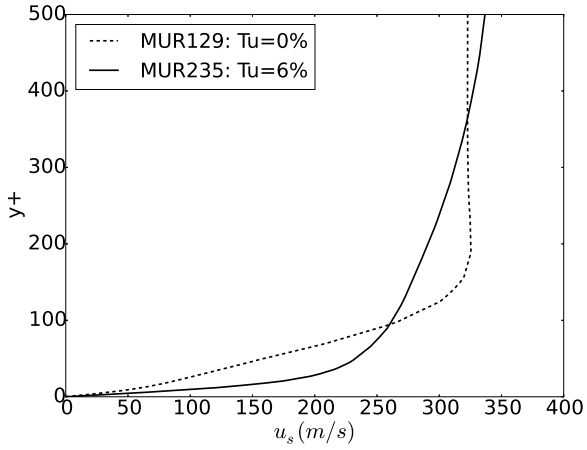

(c) 110%

Figure 6.16: Tangential velocity profiles on suction side at different s/c.

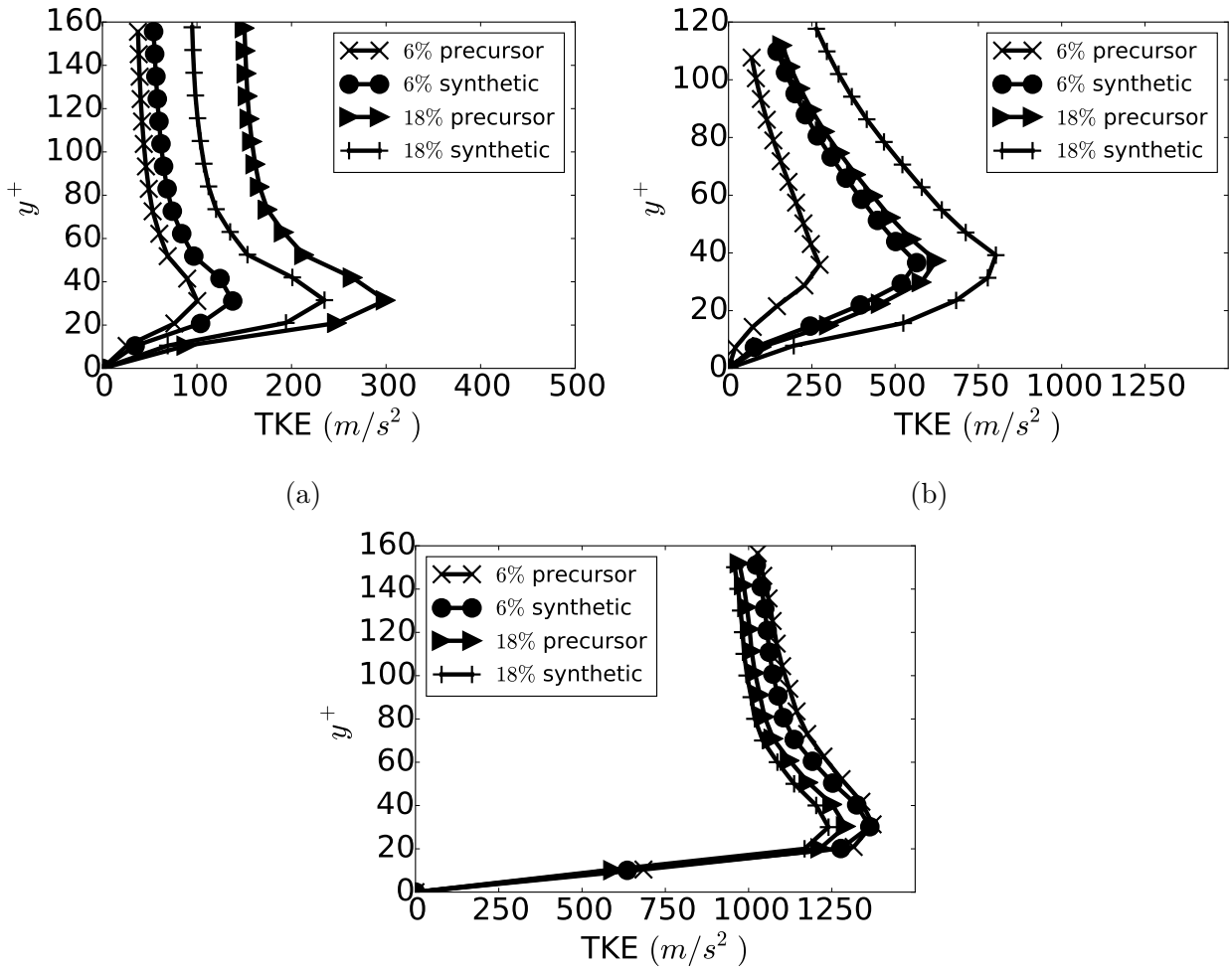

Figure 6.17: Turbulent Kinetic Energy profiles along different stations on the suction side a) s/c = 0.3 b) s/c = 0.7 c) s/c = 1.1.

decay in the channel and the heat flux on the blade, it is clearly seen that at this position both simulations show a very similar prediction. The reasons for this behaviour remains to be investigated. Finally, at $s/c = 1.1$ ($s \approx 74$ mm) all TKE profiles show a fully developed turbulent boundary layer which is expected downstream the shock. It must be stated that only the resolved part of the turbulent kinetic energy is represented in the previous and following figures. Using a subgrid-scale model that complies with the asymptotic relation $\overline{u'v'} \sim y^3$ [30], it is possible to assume that the contribution of unresolved terms is indeed negligible.

Having analyzed the transitional region of the suction side we now move to the remainder regions of the blade. The pressure side and the leading edge of the blade require investigation of other fields as fewer structures are seen using the Q-criterion compared to the transitional zone on the suction side. When studying instantaneous snapshots at a value of $y^+ \approx 20$ normal to the blade surface, temperature contours in the near blade wall flow give insight to the flow as seen in Fig. 6.18. Streaky regions are observed in cases where turbulence is injected in agreement

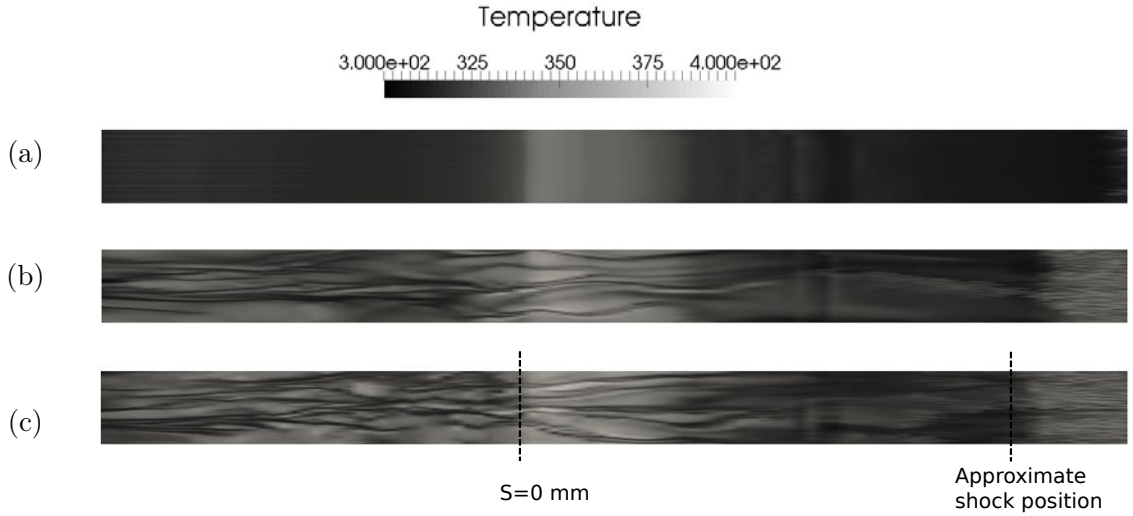

Figure 6.18: Instantaneous temperature field a) **MUR129**, b) **MUR235** u=6%, c) **MUR235** u=18%.

with Jacobs and Durbin [81]. Although the turbulent intensity at the inlet is notably different in the three cases, no large visual difference is seen around the leading edge when comparing the two simulations with turbulence injection. The stretching of vortices observed in Fig. 6.5b are indeed seen for both cases to mark the temperature field as evidenced on cases b) and c) of Fig. 6.18. This highlights the effect induced by the free-stream turbulence on the heat transfer profile near the leading edge. This effect extends to the pressure side of the blade where the temperature field is also highly marked by elongated structures which induce a higher heat flux transfer coefficient. The existence of free-stream turbulence and its intensity are directly related to the heat transfer coefficient recovered thanks to the temperature fluctuations observed in the BL.

The higher turbulence intensity case of the previous section proves that there is a boundary condition that provides the necessary physical conditions to match the experimental values. Various reasons might be pointed out. First, the size of the integral length scale could be responsible for the free-stream turbulence and the consequent interaction with the boundary layer of the blade. It is well-known that only certain frequencies are capable of trespassing the shielding effect the shear stress induces [81] and these modes will therefore be capable of perturbing this layer to create an instability in the boundary layer. The effect of the integral length scale could be important if this process is of first order and pilots the transition. Along this same line, another possible interaction that may be missed is the unresolved turbulence structures. The sub-grid scale model should correctly account for the missing energy but not for the interactions of the smaller vortices and therefore their interaction with the boundary layer flow. In that respect, a fine mesh will be important for the near-wall resolution but also to convect the free stream vortices and represent adequately a larger part of the spectrum. These paths are explored in the following.

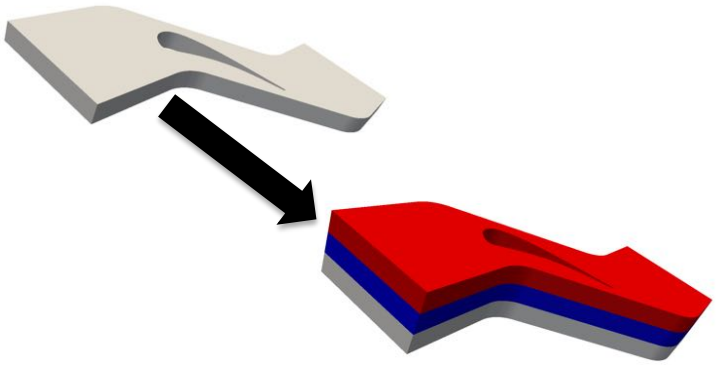

Figure 6.19: Modified geometry with three times initial spanwise domain.

Integral length scale effect

As already discussed, in the original experiments the information concerning the integral length scale of the upstream free-stream turbulence has only been a recent point of study. Due to the incapability of codes to reproduce the pre-transitioning region on the suction side of the vane, but also to capture the missing level on the pressure side of the vane, it has long been suggested that this parameter could be the origin of the errors. The study performed by Fontaneto [66] provided a value of approximately 7.6 mm, which is not far from usual values of the domain in the span wise direction (here taken to be 10 mm). For adequate modelling, this means that it is necessary to increase the limits in this direction. To do so while measuring the impact it may have on the predictions, a 30 mm thick domain is constructed. For this purpose, the M1 mesh generated previously is twice duplicated in the span wise direction leading to the final 30 mm mesh, approximately four times the integral length scale to be imposed as represented in Fig. 6.19.

To analyze if there is indeed a length scale effect, two different simulations corresponding to an inflow turbulent integral length scale prescribed at 3.5 mm and 7.6 mm are compared in terms of heat transfer coefficient in Fig. 6.20. For both predictions, a 6% turbulent intensity Passot-Pouquet spectrum is used as no clear effect was reported earlier. Although the turbulence intensity decay rate is smaller in the passage previous to the blade due to the larger initial integral length scale imposed, simulations show a similar behaviour for the larger 7.6 mm length scale. Results show an even worse agreement for the 7.6 mm length scale. This might indicate, as found by Collado Morata et al. [38], that only the smaller structures are able to penetrate the boundary layer and so, it is by decreasing the size of the integral length scale that the heat transfer profile increases to be in better agreement with the experiments. Of course and for fixed intensity, smaller length scales will make the turbulence decay rate larger and the forcing induced by the free-stream would be weaker when reaching the blade further downstream. In fact it is suspected that for the smaller values of the integral length scale, resulting structures may require a mesh refinement effort, a subject that is studied in Sec. 6.2.2.

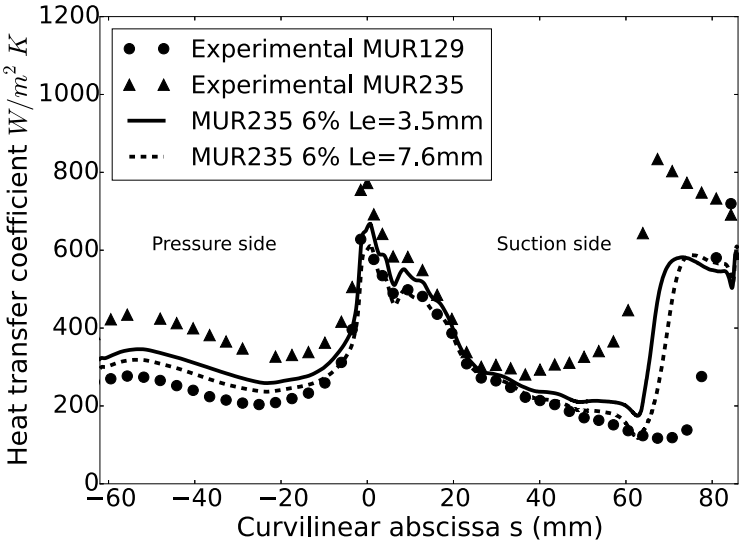

Figure 6.20: Heat transfer coefficient comparison for different length scales.

6.2.2 Grid resolution impact

In this section, only synthetic turbulence method is used for the two intensity levels previously seen in Sec. 6.2.1 since in LES, one of the most important effect relates to the mesh resolution. For the **MUR235** case it is naturally expected to play a key role. By refining the mesh, the increase in resolution will allow smaller structures to arrive to the leading edge. Such a behaviour is confirmed by looking at instantaneous views issued from the use of meshes M1 and M2, Figs. 6.21a & 6.21b. Smaller turbulent structures can clearly be observed with the finer mesh. The other most noticeable effect of the grid resolution concerns the effect it has on the acoustic waves emanating from the vortex shedding from the trailing edge, see Fig. 6.21a. The strong acoustic waves that are emitted from the blade are seen to be much less intense with the refined mesh as observed in Fig. 6.21b.

To further investigate the differences issued by the use of M1 or M2 grids, local probes A and B are placed in the wake and on the blade surface for both simulations as shown in Figs. 6.21a and Fig. 6.23a. Recall that for **MUR129**, Fig. 6.2 represented the pressure spectra recorded at the same probes A and B. Spectrum at probe B clearly highlighted a tonal peak corresponding to the vortex shedding frequency at 43 kHz. A peak at the exact same frequency was found for probe A on the wall and which is also found when analyzing the M1 grid **MUR235** simulation. However, performing the simulation with the M2 mesh, Fig. 6.22, a peak is no longer clearly visible in the pressure spectrum recorded in the wake at probe A nor at probe B. The reason for this is found by doing a visual comparison between the wakes for M1 and M2 grids, Fig. 6.23. The wakes issued by the two simulations are very different if looking at shear zones and coherent vortices. The M1 mesh shows a shorter shear zone accompanied by some very coherent vortices. On the other hand, the M2 mesh has a longer shear zone and the vortices

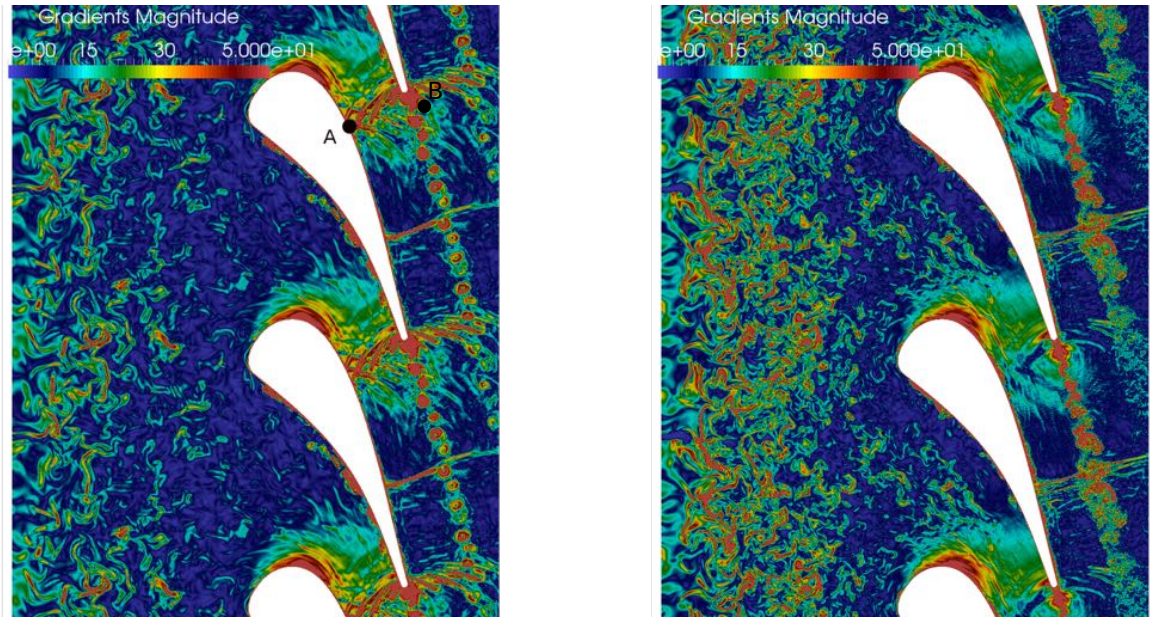

(a) M1 mesh density gradient

(b) M2 mesh density gradient

Figure 6.21: Density gradient comparison for 18% turbulent intensity at inlet.

are less coherent. As a consequence the spectrum recorded at probe A for M2 contains many less tonal frequencies than the M1 grid.

The presence or absence of these waves can however have a direct impact on the boundary layer and thus affect the heat transfer as shown in Fig. 6.24. Indeed, the boundary layer evolution of the M1 mesh shows a higher heat transfer upstream when compared to the fine mesh observed between $s \approx 25 - 40$ mm. Figure 6.24 also shows that the fine mesh predicts more accurately the level of heat flux downstream from the shock if compared to the M1 mesh, confirming it is a mesh refinement effect. It is reasonable to ask then if one of the meshes (or both) might not be adequate for the capture of these waves or that the waves are generated due to the way the domain was meshed. It seems logical thus to generate a third more refined mesh M3.

The first aspect to consider is the existence of these waves for the new M3 mesh. For this new mesh, acoustic waves are seen to reappear similarly to the M1 grid which suggests that the M2 mesh is not adequate for the capture of the correct trailing edge physics and thus the acoustic waves issued. The effect on fields such as the isentropic Mach number is shown in Fig. 6.25b. Small differences may be seen for the pressure side of the leading edge. The same conclusions are extracted on the suction side between $s \approx 0 - 25$ mm which corresponds to the leading edge region. Up to $s \approx 40$ mm, it is the impacting acoustic waves that dominate the flow, and so, the absence of acoustic waves in M2 shows differences compared to M1 and M3. Downstream from this position, M1 and M2 have a great resemblance while M3 departs from the previous one due to differences in flow physics.

Shear stress profiles show larger differences between meshes. On the pressure side, a slight increase in shear stress is found thanks to a better transport of turbulent structures in the pas-

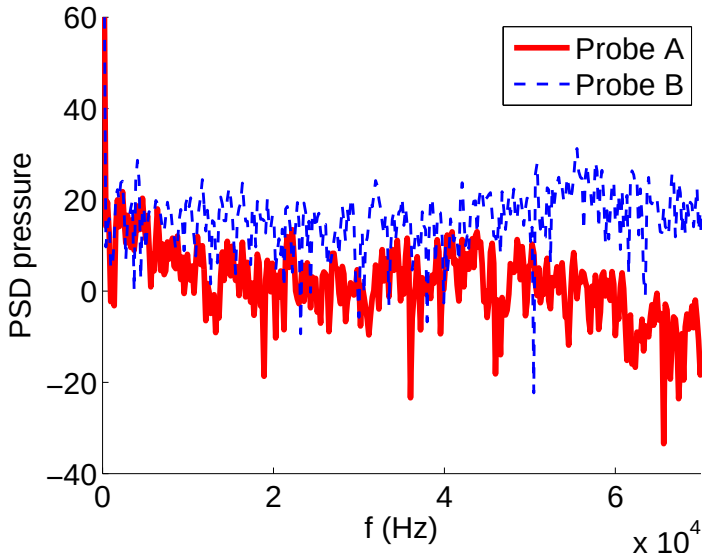

Figure 6.22: Spectral composition of the pressure signal at probes A and B.

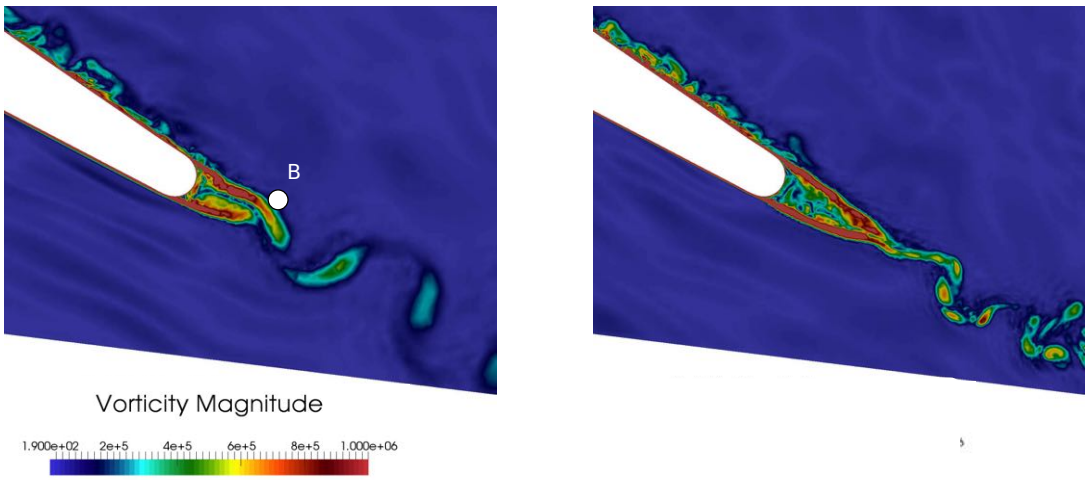

(a) M1

(b) M2

Figure 6.23: Trailing edge vorticity comparison between different meshes.

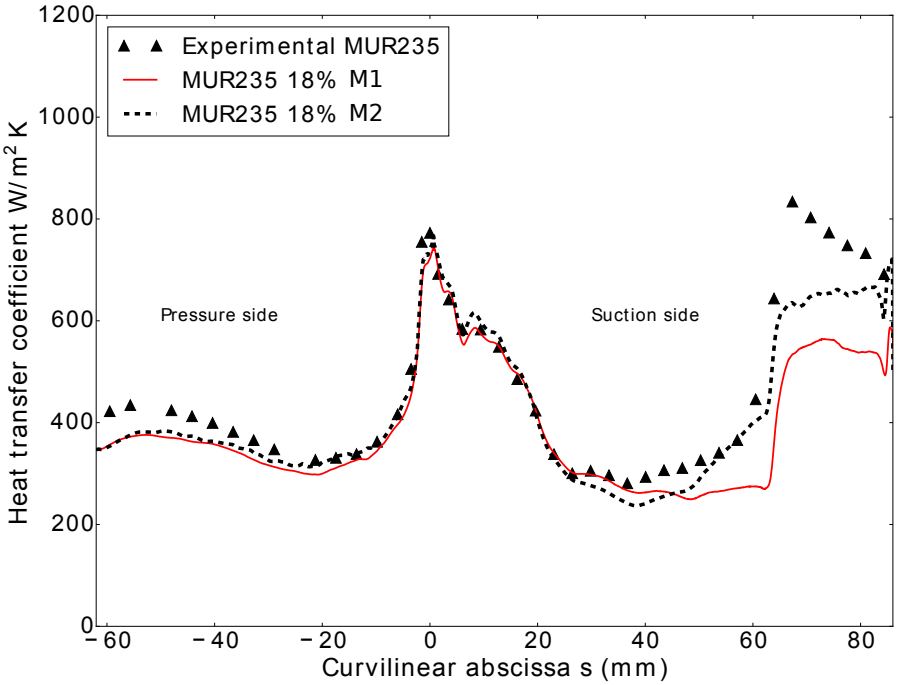

Figure 6.24: Heat flux comparison of **MUR235** with fine mesh.

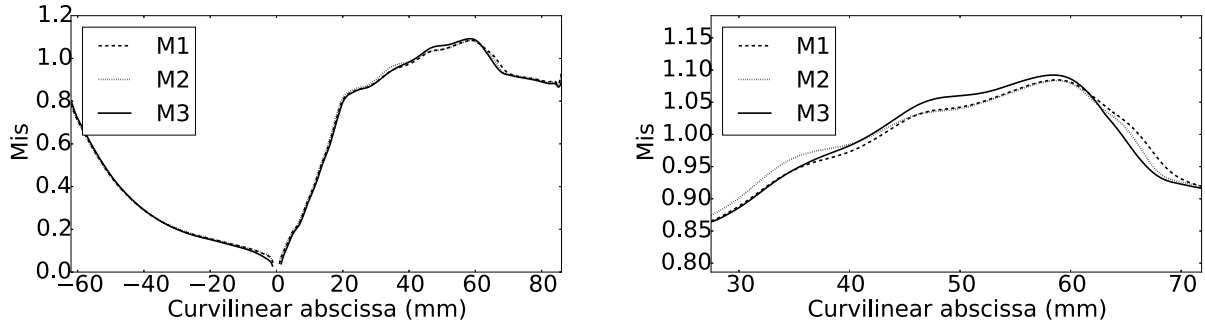

(a) (b)

Figure 6.25: Isentropic Mach number comparison of **MUR235** with three meshes and 6% turbulent intensity at inlet.

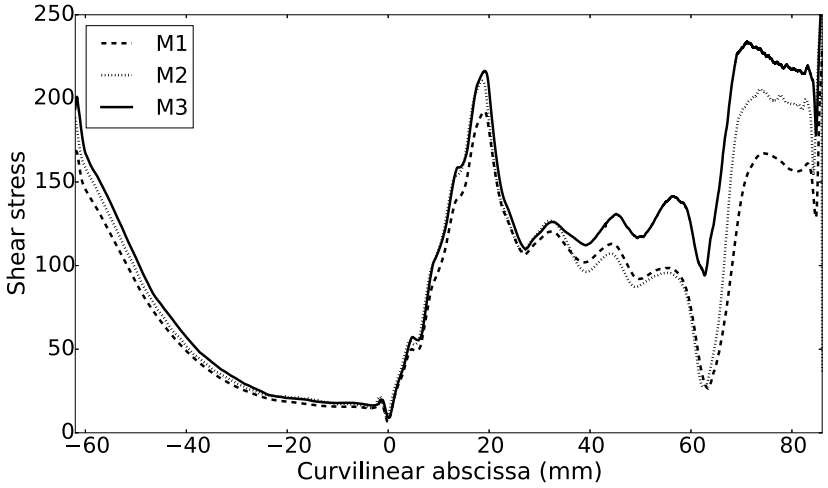

Figure 6.26: Shear stress comparison of **MUR235** with three meshes and 6% turbulent intensity at inlet.

sage upstream the blade as well as a better refinement in the near-wall region. This conclusion extends to the profile around the leading edge of the blade which is also better captured. The influence of the free-stream turbulence on these two regions was shown in Sec. 6.2.1 so it is not surprising that a more resolved free-stream leads to better results. The largest differences are seen however in the transitional area on the suction side. Both M1 and M2 meshes remain practically at the same level while the M3 mesh predicts a shear stress that is up to 50% higher at the abscissa before the shock wave. This tendency is similar to the already observed effect when increasing the turbulence at the inlet for a coarser grid (M1) seen in Fig. 6.10. It was demonstrated that this effect was due to the existence of turbulent spots along the suction side.

Figure 6.27 shows the heat flux predictions obtained with the three meshes for the level of free stream turbulence indicated in the experiments, 6%. This turbulence level seems to have a different impact on heat flux for M3 if compared to the two coarser meshes. Both M2 and M3 show a better prediction on the pressure side of the blade, probably only due to refinement both at inlet and in the wall region. On the suction side, in the pre-transitioning region, the heat flux is notably different between the finer mesh M3 and the other two. The surface heat transfer after the shock is captured much more accurately for increasing the refinement even if the isentropic Mach number distributions are very similar as in Fig. 6.25a.

For all cases, an increase in shear stress is accompanied by an increase of heat flux at every curvilinear abscissa position. Both shear stress and heat transfer together suggest that the simulation with the M3 grid and a 6% turbulence at the inlet does present turbulent patches on the blade surface. The Q-criterion presented in Sec. 6.3 of this M3 grid confirms this aspect, turbulent spots appearing very early on within the flow BL: i.e. way upstream the shock around $s/c \approx 0.7$ ($s \approx 47$ mm).

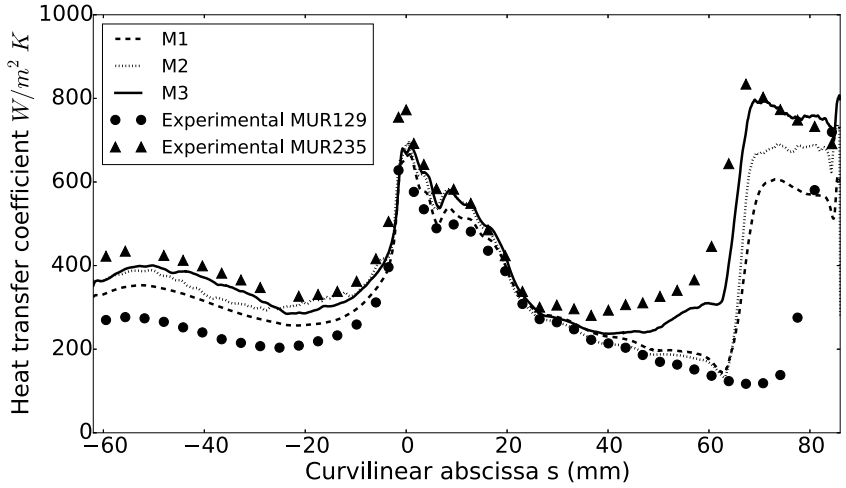

Figure 6.27: Heat flux comparison of **MUR235** with three meshes and 6% turbulent intensity at inlet.

6.2.3 Preliminar conclusions from the parametric study

From this parametric study, various conclusions are extracted:

- Boundary conditions based on experimental values on an insufficiently refined mesh (although acceptable) do not provide the adequate prediction of the flow.
- The increase of turbulence intensity level at the inlet allows a better agreement with the experiment and seems to be the most important factor towards recovering the correct heat flux.
- The injected turbulent spectrum is not important to obtain a physical solution at the leading edge of the blade because it has enough distance to develop for the present configuration. It does however affect the decay rate of TKE.
- Integral length scale effects are negligible in the tests here conducted.
- A very refined mesh is capable of predicting the heat flux plateau on the suction side of the blade when using experimental data as boundary conditions. These results are, to the authors knowledge, the results that agree the most up-to-date and within all available predictions to the experimental data of Arts et al. [7] for this operating point.

The question is now why this mesh behaves differently than the other two M1 and M2. It is well-known that small structures feed on the mean flow [112], and that higher Reynolds values decrease the threshold limit of turbulent intensity required to produce turbulent spots at higher intermittency as shown by Mayle [120]. The effective Reynolds number of the simulation (modified by the SGS viscosity added to the simulation) indeed increases as a result of an increased resolution. Likewise, numerical scheme properties will be affected by grid quality and resolution as discussed in Chapter 7. All of these contributions as discussed in Sec. 3.5

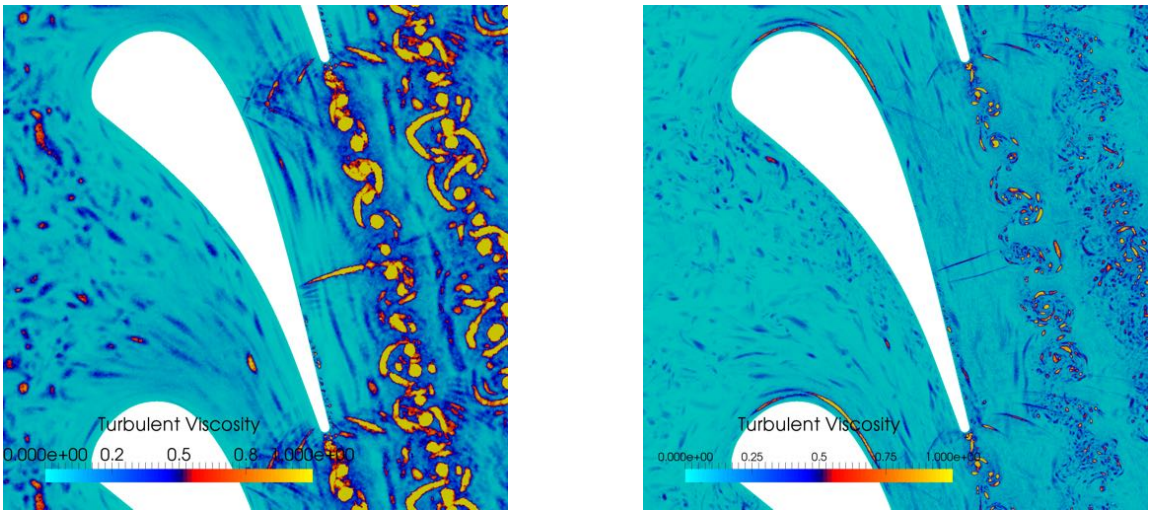

(a) (b)

Figure 6.28: Turbulent viscosity comparison between a) M1 and b) M3 grids.

will thereby decrease artificially the numerical effective Reynolds number and a need for higher intensity fluctuating levels to generate more frequent spots.

This however is only a supposition. Certainly, the better prediction of the heat transfer goes along with an increase in shear stress. Accompanied by the instantaneous visualizations of the Q-criterion on the surface blade, it certainly seems as though the turbulent spots are at the origin of this change of behaviour on the suction side of the blade. The first aspect to confirm is that turbulence features are indeed retrieved. To do so, skewness of the velocity fluctuations, ejection and sweep events as well as turbulence anisotropy are all addressed to check their agreement to literature values on the basis of the M3 predictions. Then, comparisons can be made to other grid simulations to identify the differences and thus, the reason why one simulation transitions (M3) and why the others do not (M1, M2).

6.3 Temporal evolution of near-wall turbulence

The turbulence encountered in the near-wall region is analyzed on the basis of the best LES prediction reported previously for the MUR235 case, i.e.: the M3 grid except when noted differently. The objective is to study the near-wall structures that are from our analysis seen to play an important role towards the heat transfer prediction as shown in fundamental papers like Hadziabdic and Hanjalic [76]. Before going into the details of the signals and statistics, some instantaneous visualizations are shown for this specific simulation in terms of flow and structures encountered notably on the suction side of the blade. Then, temporal data and statistics extracted from the signals are analyzed and compared to experimental findings. Although it might seem trivial, the first check that must be done is to confirm that the structures seen are indeed turbulent events. The Q-criterion is useful from a visualization point of view but nowadays it is thought that both visual and statistical data are required for the analysis

of a turbulent boundary layer. Furthermore, depending on the value chosen for the Q-criterion to plot the contours, different conclusions can be extracted. This is why statistics are also searched, something not so usual in turbomachinery flows and much more commonly encountered in channel flows.

Instantaneous visualizations

The visualization of coherent structures on the suction side of the blade shows the typical structures found in the transition process as in Adrian [5]. Indeed, Fig. 6.29 evidences the existence of hairpin vortices and canes coloured by the saturated spanwise local velocity values. The Λ vortices indicated at position A are the union of two streamwise vortices that have alternatively positive and negative spanwise velocities indicating they are counter rotating vortices. These are the near-wall streamwise vortices that are responsible for the streak generation mechanism. From the literature, these vortices may undergo lift-up and develop arch-type vortices connecting the streamwise rolls as those indicated at position B. Finally, one-legged vortices or canes may exist independently and are observed at position C.

The previously mentioned streamwise vortices along with the streamwise velocity fluctuating component are shown in Fig. 6.30 on a plane formed by the normal to the blade surface (n) and spanwise directions (z). The normal direction to the n-z plane just described is the streamwise direction (s). Various counter rotating vortices are seen in the cross-wise plane (n-z) shown by the arrows that represent the normal and spanwise velocities. These are the vortices responsible for the negative streamwise velocity fluctuations (with respect to the temporal and spatially spanwise averaged velocity) represented by the negative (blue light areas) coloured field on the plane. The streamwise vortices 'lift-up' fluid from the wall which has lower momentum creating streaks of lower fluctuating velocity. The dark red zones represent on the contrary positive fluctuations of velocity. This same n-z plane in Fig. 6.30 is now shown accompanied by two s-z planes at distances of y^+ equal to 5 and 20 respectively in Fig. 6.31. This allows to study the longitudinal characteristics of the streaks that have been lifted. The longitudinal behaviour of these streaks shows a certain waviness and streaks are separated by a distance of the order of $z^+ \approx 100$. The value here obtained corresponds to the mean value of spacing between streaks found in literature [151]. The presence of streaks at the two distances (5 and 20) is however not always encountered as they are characteristic of the viscous sublayer. The longitudinal traces found in Fig. 6.31b implies they have penetrated into the buffer layer and so may eventually be a source of transition to turbulence further downstream [8].

Although the previous views give sufficient evidence for the existence of turbulence on the suction side of the blade where the corresponding structures are seen, a statistical analysis of the signals recorded is put in place in the following.

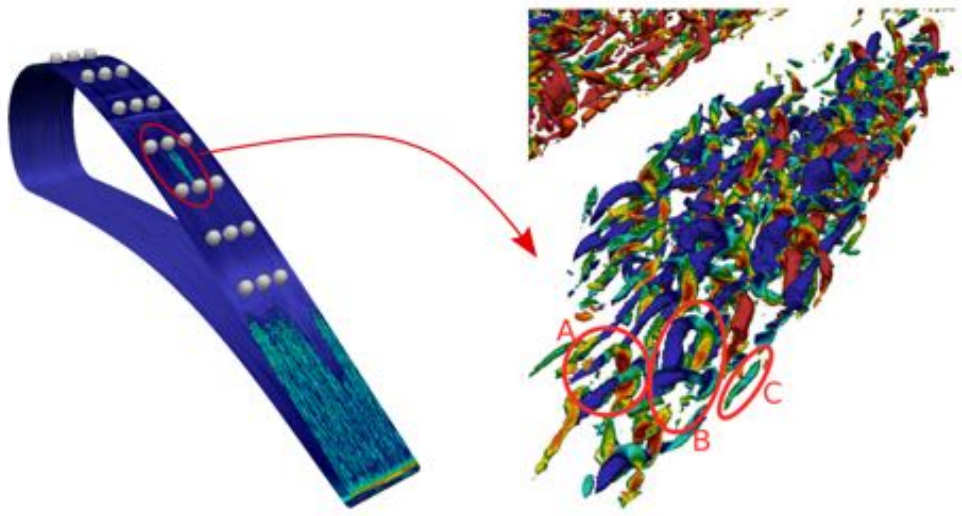

Figure 6.29: Shear stress field shown on the blade surface where each sphere corresponds to locations where probes were located. The region highlighted on the blade surface shows turbulent structures represented to the right of the figure.

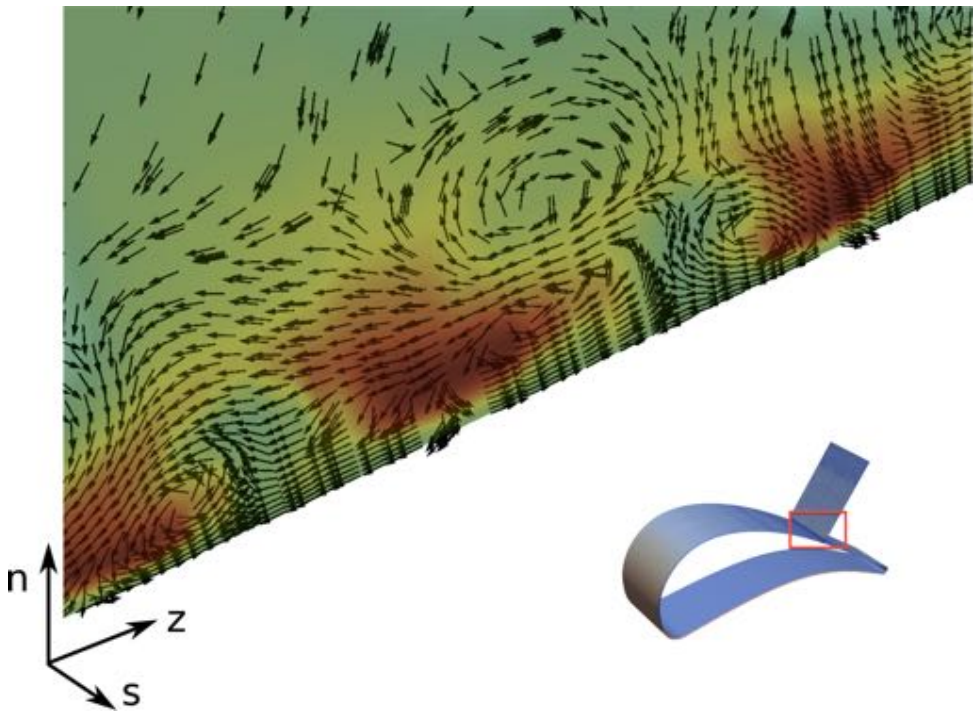

Figure 6.30: Coloured field shows cross-stream (n-z) instantaneous distribution of streamwise velocity fluctuations at $s/c = 0.8$. Arrows show normal (n) and spanwise (z) velocity vectors.

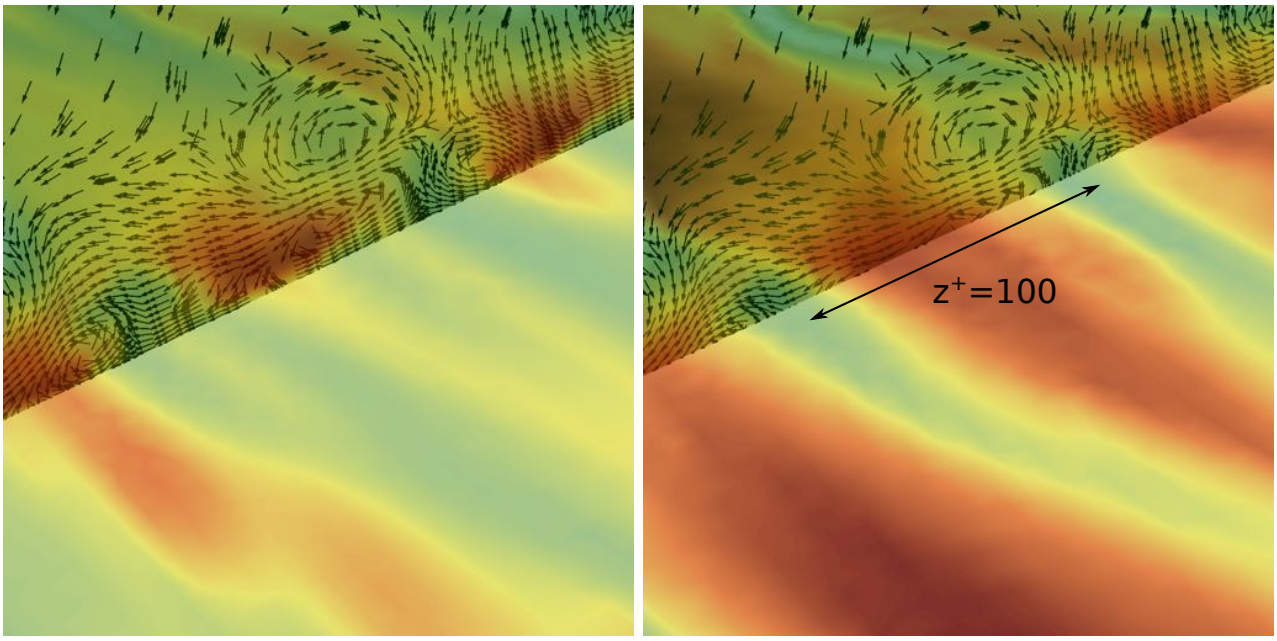

(a) (b)

Figure 6.31: Coloured field shows streamwise (s-z) instantaneous distribution of streamwise velocity fluctuations at $s/c = 0.8$ at a) $y^+ = 5$ b) $y^+ = 20$. Arrows show normal and spanwise velocity vectors.

Signals and statistical data of the boundary layer

The temporal signals recorded at different positions along the streamwise direction of the blade and at different distances normal to the surface are analyzed. An example of recording is shown in Fig. 6.32 which only shows random temporal events of strong fluctuations. An additional step is used to discriminate time periods where a turbulent event is taking place at the probe location, in other words, to take into account the intermittency effect. The definition of intermittency given by Narasimha [129] is of course applicable so classical distributions where the intermittency factor is 0 for laminar flows and 1 for fully turbulent regions holds true. However, it must be stressed that the probes measuring the signals are static and do not follow the streamwise evolution of the spots. This means that in a certain temporal range, the flow may be turbulent because a convected spot is detected by the sensor. To discriminate turbulent from laminar events, various sensors are provided in the literature namely for experimental collections such as described in Antonia et al. or Cousteix [6, 42]. The evaluation used in the following is based on the latter that has also been used by Blair [20] and relies on criteria based on $\left(\frac{du_s}{dt}^2\right)$ or $\left(\frac{du_s u_n}{dt}^2\right)$ to determine the intermittency factor. If the value of this parameter surpasses a case-dependent value, the period is taken to be turbulent. An example of event detection is shown in Fig. 6.33. Recall that Fig. 6.29 shows the different locations at which the probes are placed, the physical normal distance to the blade of each probe being given in Table. 6.2. Once the signals have been correctly processed to obtain the fluctuating components, these signals can be analyzed in detail.

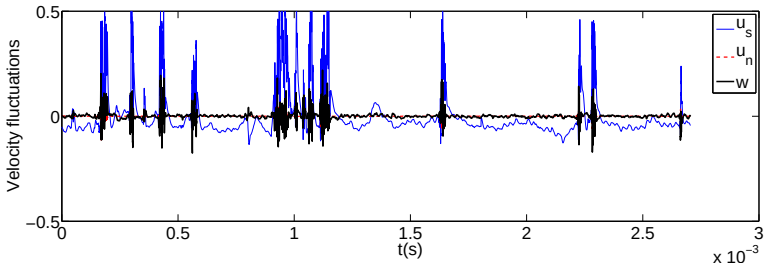

Figure 6.32: Temporal evolution of streamwise, normal and spanwise velocities at $s/c = 0.7$ and $y^+ = 10$.

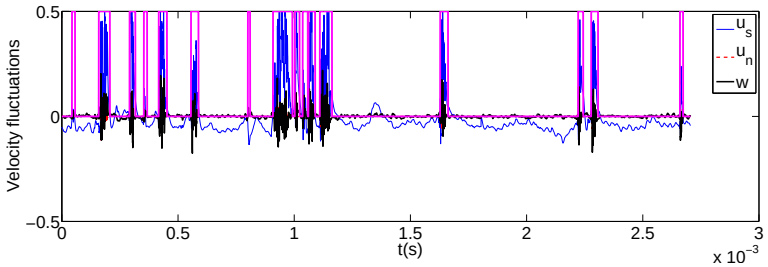

Figure 6.33: Temporal evolution of velocity fluctuations. Boxes show where the sensor is active and records the signal to be used.

Streamwise velocity fluctuations in the boundary layer are known to be highly skewed as a result of the coupling between the turbulence in the outer- and inner-regions of a BL. In the proximity of a wall, the skewness of streamwise velocity fluctuations is always positive as evidenced by Kim et al. [92], values that increase with growing Re_t (turbulent Reynolds number) as shown by Metzger and Klewicki [123]. High streamwise velocity fluctuations may be induced by the 'inactive' large scale structures [24] in the outer part of the boundary layer that interact with the free-stream intensity without altering the mean flow. These fluctuations undergo a 'modulation' process and couple to the smaller structures near the wall [170]. Recent studies such as Mathis et al. or Dróżdż [116, 57] have tried to relate pressure gradients to the skewness of streamwise velocity components. Following Mathis et al. [116], the skewness can be represented in terms of y^+ and Reynolds number which is shown in Fig. 6.34 for only the Reynolds number of the present flow. The retrieved curved shape is qualitatively in excellent agreement with the skewness data provided in previous citations showing that it is indeed the free-stream turbulence that is at the origin of the turbulent events seen. The inner motion in the boundary layer is characterized by positive streamwise fluctuations because the modulation with the free-stream turbulence, which has higher momentum, amplifies the wall fluctuations in the streamwise direction.

It is questionable at this stage to know if these streamwise fluctuations u_s and corresponding normal to the surface fluctuations u_n contribute to the production of turbulence. The Reynolds stresses which are related to the turbulence production terms through $\mathcal{P} = -\langle u_s u_n \rangle \frac{\partial U_s}{\partial x_n}$ [140]

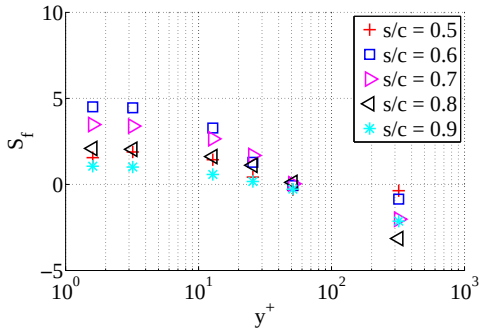

Figure 6.34: Skewness of streamwise velocity fluctuations at various positions normal to the surface.

Position 1	2 μm
Position 2	4 μm
Position 3	16 μm
Position 4	32 μm
Position 5	64 μm
Position 6	400 μm

Table 6.2: Position of local probes in normal to blade direction.

are indeed responsible for the generation of turbulent kinetic energy (TKE). The production of turbulence is here a viscous process that takes place mainly in the BL and the position at which the production peaks usually happens approximately at $y^+ \approx 15$, position located in the buffer region (for realistic Reynolds numbers). To evaluate the qualitative behaviour of the Reynolds stresses, various 2D plots representing normal u_n against streamwise u_s velocity fluctuations are given and considered sufficient to measure the turbulence generation as the production terms are proportional to $\overline{u_s u_n}$. This furthermore holds true because in the proximity of a wall the mean shear component is always positive. The production of turbulence can further be separated using a quadrant analysis [111]. In this case, two main events presented in Fig. 6.35 contribute to the turbulence production terms. Sweep events, which correspond to $u_s > 0$ and $u_n < 0$ correspond to high-speed exterior fluid entering the low-speed internal region. The second mechanism is due to ejection events $u_s < 0$ and $u_n > 0$ corresponding to low-speed fluid ejected from the internal boundary layer.

The first position analyzed is the location where acoustic waves impact the suction side of the blade: i.e. $s/c = 0.5$ ($s \approx 34$ mm) for M1 and M3 (cf. Fig. 6.29). The temporal evolution of fluctuating components of velocity are represented in Fig. 6.36 and the streamwise against normal velocities at various perpendicular positions to the blade in Fig. 6.37. Figure 6.36 shows a periodic peak of both u_s and u_n components, confirmed if performing a FFT of the raw signal and yielding a peak value around 42 kHz. This effect is related to the acoustics issued from the contiguous blade which is independent of the mesh used. This frequency is furthermore

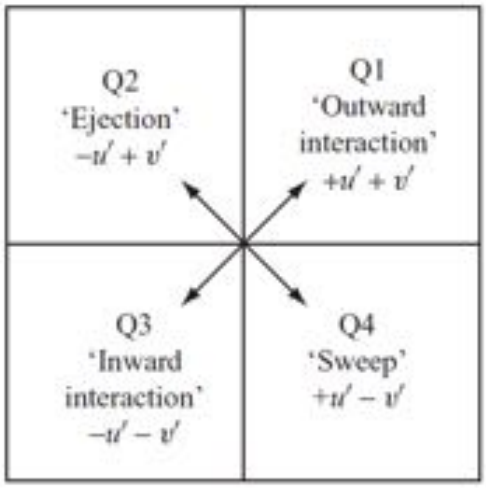

Figure 6.35: Quadrant analysis of boundary layer interactions [134].

evidenced independently of the distance to the blade surface, Fig. 6.37, and has been found to have a linear relationship between velocity components $u_n \approx -0.5u_s$. It seems therefore legitimate to conclude that the effect of acoustic waves impacting the blade surfaces is to excite the boundary layer and potentially contribute to the apparition of a flow instability and/or the production of turbulence.

Further downstream, at $s/c = 0.6$ ($s \approx 40$ mm) the behaviour is notably different from what is observed in Fig. 6.38. For visualization reasons, the different normal positions are separated for each distance from the blade as the statistical behaviour can not be condensed as previously. At near-wall positions $y^+ = 1.24$ and $y^+ = 2.48$, the streamwise fluctuations are mostly positive, the first position having a negligible normal velocity component, that is slightly higher at the second position. In the viscous sublayer, it is the sweep events that dominate. A part of this entering fluid leaves the near-wall region corresponding to positive streamwise fluctuations $u_s > 0$ and positive normal components $u_n > 0$. Moving away from the wall, in the buffer region, normal velocities start to have larger absolute values as well as more important contributions of negative streamwise velocity components. However, these negative streamwise velocities also coincide with low normal velocities and so, turbulent production terms are mainly due to sweep events. For increasing y^+, ejection events become more important in terms of contribution to the production of turbulent kinetic energy. This data is consistent with channel flow observations such as those presented by Kim et al. [92]. When comparing to a position even further downstream, at $s/c = 0.8$ ($s \approx 54$ mm) in Fig. 6.39, except for distances very close to the wall as in Fig. 6.39a, streamwise velocity fluctuations are approximately of the same order as for position $s/c = 0.6$ ($s \approx 40$ mm) but much larger normal velocity fluctuations are seen. This means that moving further downstream, the streaks have had the time to breakdown and ejection events are more probable.

A more detailed analysis of the importance of turbulent events is given in Fig. 6.40. Reynolds stress contributions from streamwise and normal velocities are decomposed into four groups

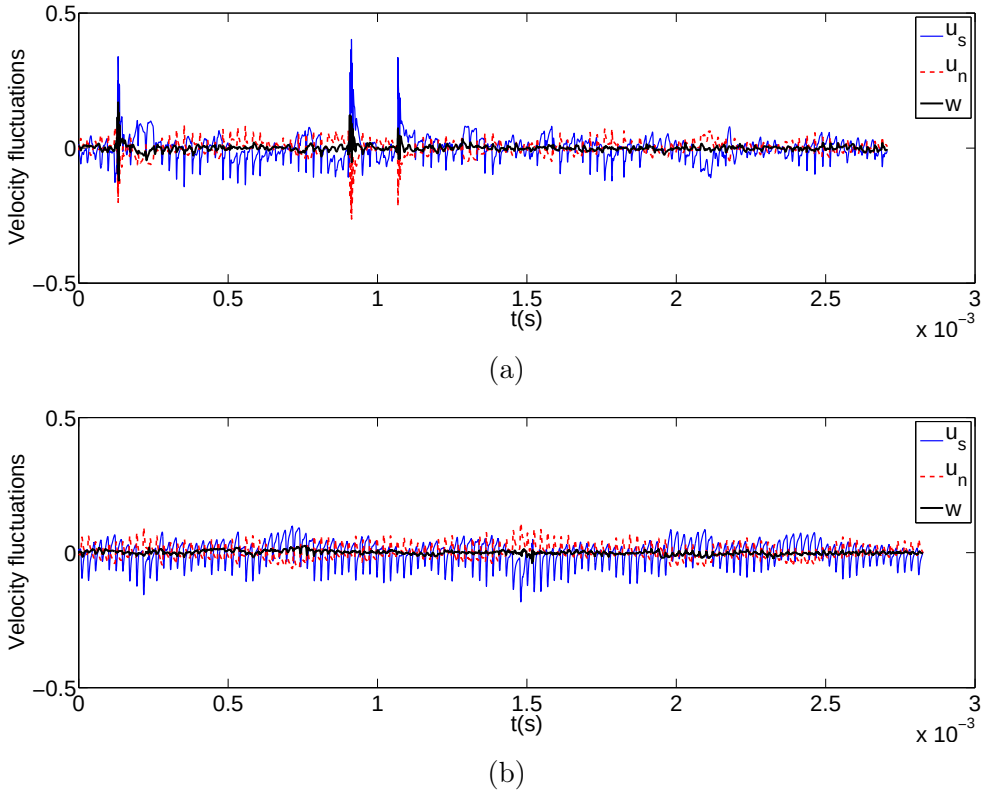

Figure 6.36: Velocity fluctuations at Position 4 of the a) M3 and b) M1 meshes.

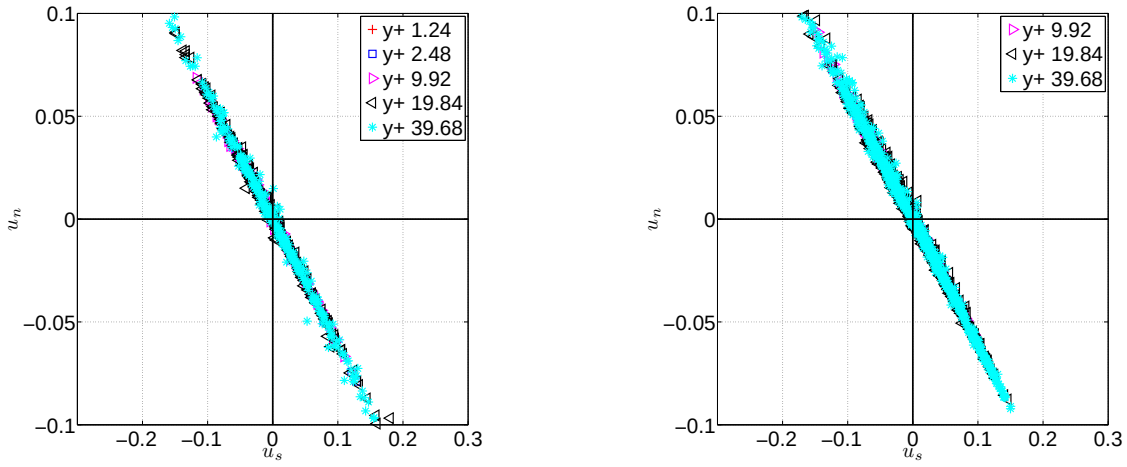

Figure 6.37: Evolution at $s/c = 0.5$ of normal against streamwise fluctuation map for a) M3 b) M1 mesh.

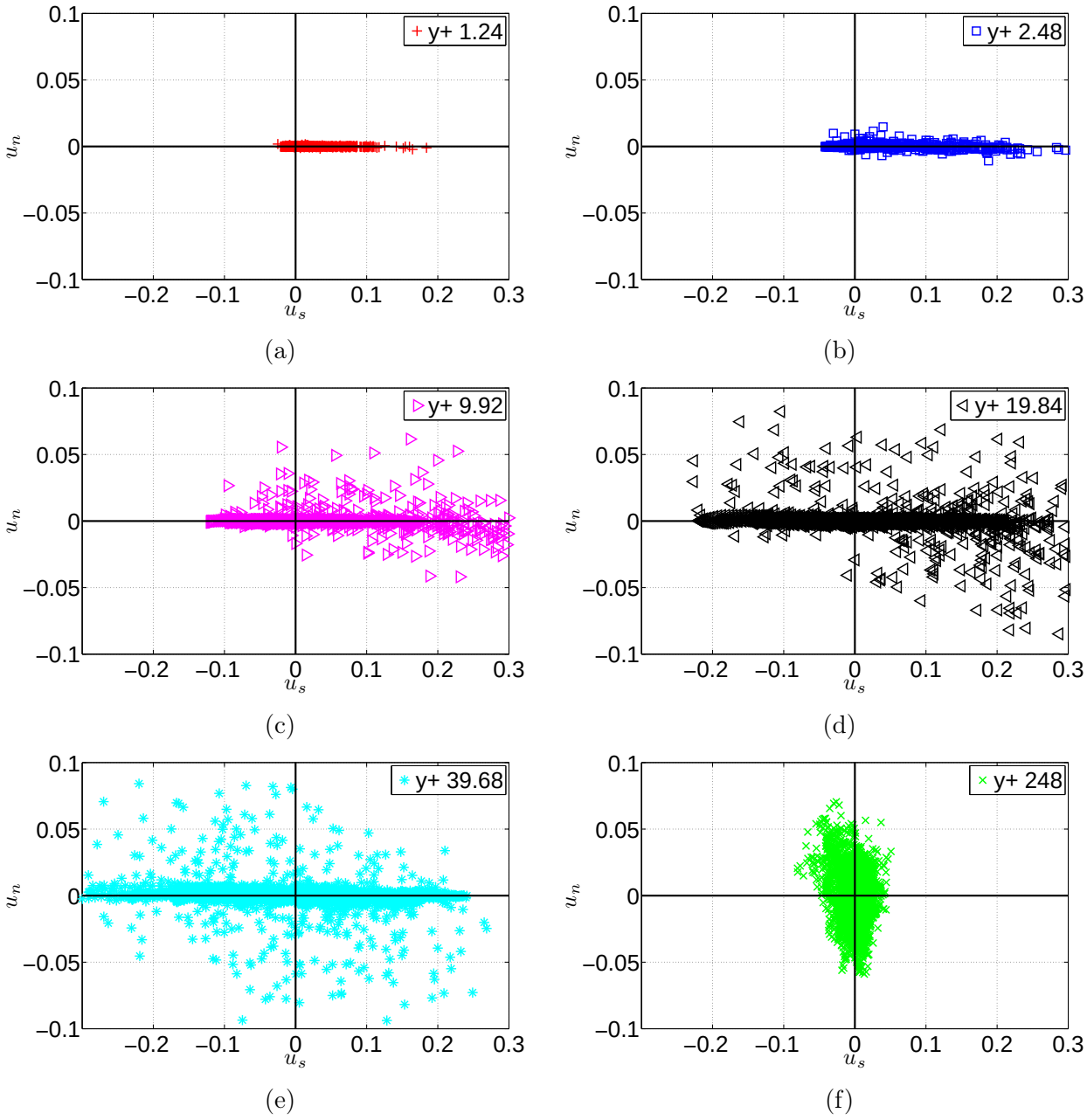

Figure 6.38: Streamwise agains normal velocity fluctuations at various positions normal to the blade at $s/c = 0.6$ using M3 grid.

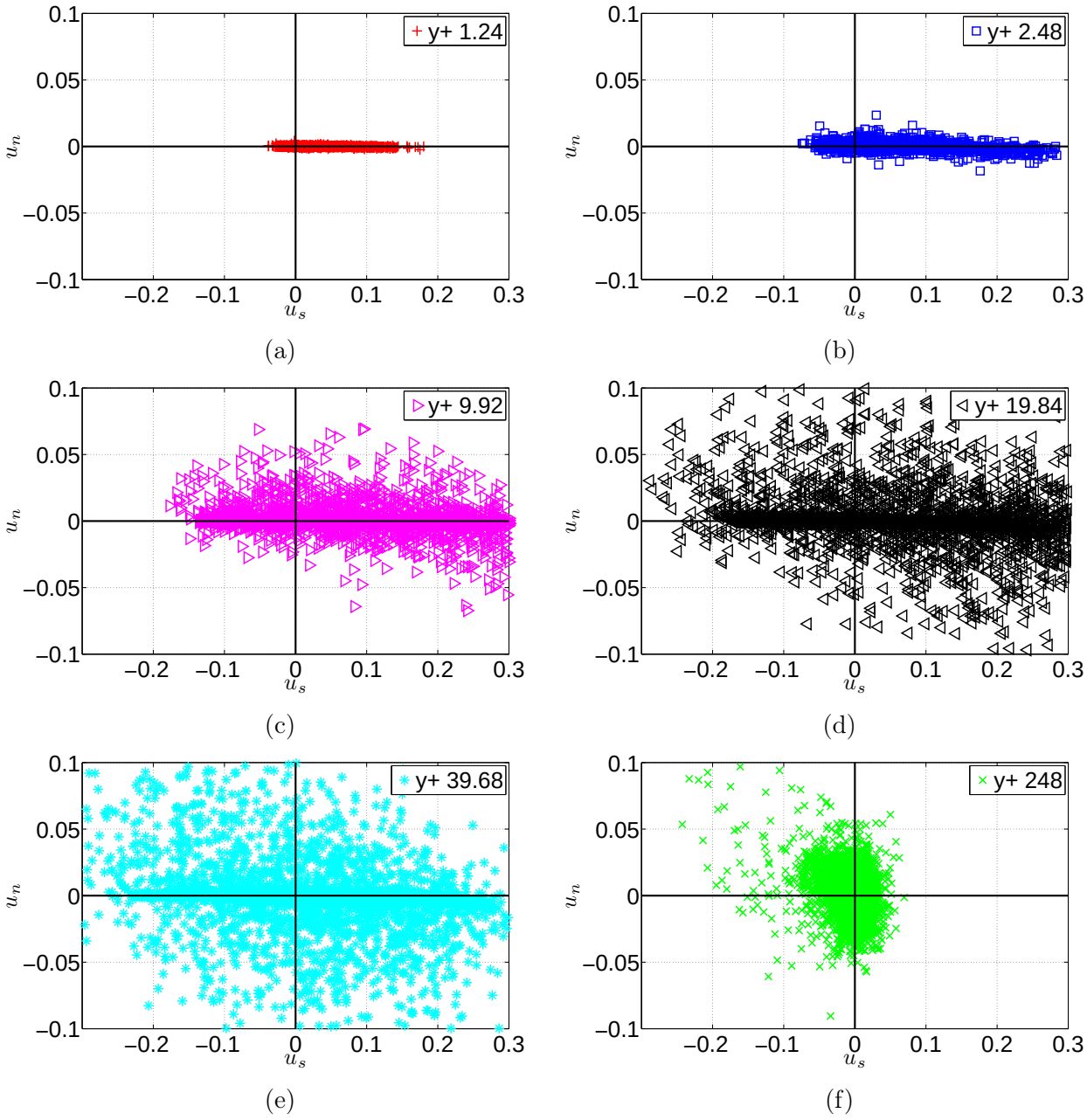

Figure 6.39: Streamwise agains normal velocity fluctuations at various positions normal to the blade at $s/c = 0.8$ using M3 grid.

depending on the quadrant at the different positions provided in Table. 6.2 and for various streamwise positions as done by Lu and Willmarth [111]. At $s/c = 0.4$ ($s \approx 27$ mm) and $s/c = 0.5$ ($s \approx 34$ mm) which are shown in Figs. 6.40a & 6.40b, the locations are under the influence of impacting acoustic waves and the behaviour is slightly different compared to the downstream probes. Ejection events can be seen to be of the same order of importance at all distances. Downstream, the fourth quadrant events are more important near the wall where it peaks between $y^+ = 10$ and $y^+ = 20$ while ejection events are found mainly at distances between $y^+ = 20$ and $y^+ = 40$. In terms of amplitude, Reynolds stresses have large values at $s/c = 0.5$ ($s \approx 34$ mm) but decrease abruptly at $s/c = 0.6$ ($s \approx 40$ mm). Downstream of this last position, they increase back monotonically. This implies that although the impacting acoustic waves on the suction side of the blade contribute to the production of TKE, it is rapidly dissipated downstream.

Another interesting point is the nature of the turbulence and its potential anisotropy. Such effects are exposed by use of the turbulence triangle [112] of the resolved components of the velocity (sub-grid scale components are neglected due to the SGS model used, WALE, although methods exist that take into account these contributions [159]). The turbulence triangle is defined as in Choi and Lumley [32], a variation of the original Lumley triangle for a better visualization of trajectories for the return to isotropy. The Reynolds stress anisotropy tensor is defined as $a_{ij} = \frac{\overline{u_i u_j}}{k} - \frac{\delta_{ij}}{3}$ where $k = \frac{\overline{u_k u_k}}{2}$. It is possible to construct an invariant map that leads to the classical Lumley triangle,

$$II = \frac{a_{ij}a_{ji}}{2};\ III = \frac{a_{ij}a_{jn}a_{ni}}{3}, \tag{6.3}$$

but an additional transformation is used here to give the turbulence triangle,

$$\xi^3 = \frac{III}{2};\ \eta^2 = \frac{II}{3}. \tag{6.4}$$

When analyzing Fig. 6.41 that contains information about the turbulence triangle, it can be seen that at all positions the evolution of turbulence is very similar. Note in Fig. 6.41a the markers found correspond to near-wall values moving outwards from the wall at the positions presented in Table. 6.2. For earlier positions as $s/c = 0.5$ ($s \approx 34$ mm), turbulence is mainly one-dimensional for probes located in the range $y^+ \approx 1 - 40$ which implies that the streamwise component is much larger than the other two. The strong sweeping events generate large streamwise velocity fluctuations that are seen near the wall and concentrate most of the points near the one-component region of the turbulence triangle. When moving downstream near the shock-wave, Fig. 6.41e, the invariant map shows a behaviour similar to turbulent channels where near to the wall the viscous sublayer shows a two-component behaviour, moving upwards towards a one dimensional component for $y^+ \approx 10$. Well away from the wall, turbulence moves towards an isotropic state through the axisymmetric expansion path where one component fluctuations, in this case the streamwise, are larger than the other two. Except for the last curvilinear abscissa position, the anisotropy is the same as upstream and thus result in higher heat flux levels. Note that here turbulent events are only related to the amplitude fluctuations

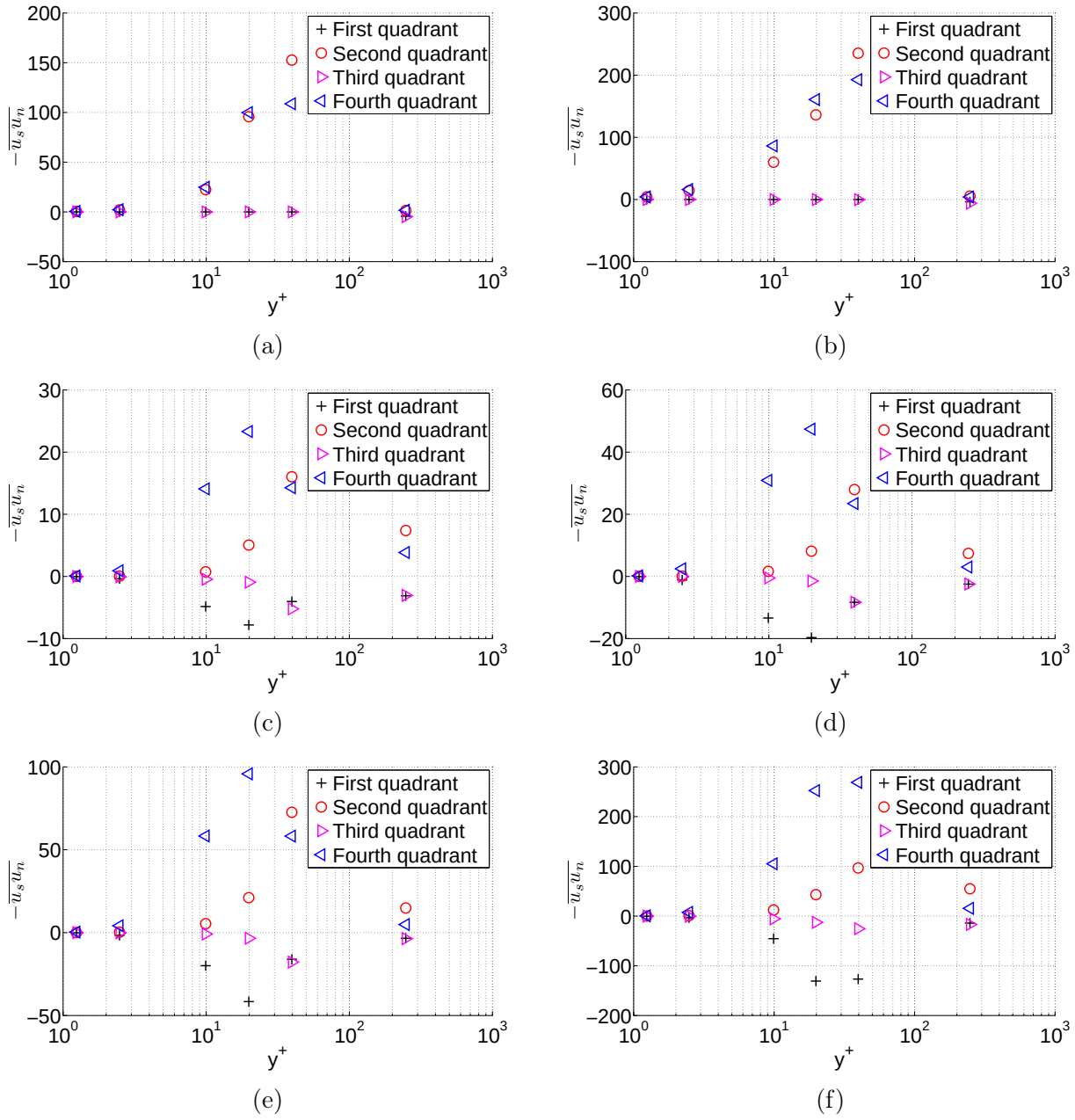

Figure 6.40: Reynolds stresses separated in quadrants plotted as a function to the wall distance. The streamwise position on the suction side corresponds to a) $s/c = 0.4$ b) $s/c = 0.5$ c) $s/c = 0.6$ d) $s/c = 0.7$ e) $s/c = 0.8$ f) $s/c = 0.9$.

and time between events.

The finer aspects of turbulence have shown that the behaviour is that expected for a transitional flow. The initial growth is due to an instability, probably of two types as hairpin vortices are observed but strong spanwise oscillations too, which then develop further downstream. The Reynolds stresses along the normal to the wall distance confirm this observation. These have been separated and as expected, positive streamwise velocity fluctuations dominate the inner-region of the boundary layer but are overcome by ejection events further away from the wall. Finally, the anisotropy of turbulence is similar to that encountered in channel flows and no large difference is seen depending on the streamwise position. Also, the wake effects that were pointed out as being a possible precursor to transition have been seen to have destabilising effect on the simulated boundary layer. Nonetheless, their existence does not seem to be the main reason for turbulent spots to appear. This conclusion is reached because further downstream, Reynolds stresses seem to be smaller compared to the region where acoustic waves impact the blade surface and are also found in simulations where transition does not occur.

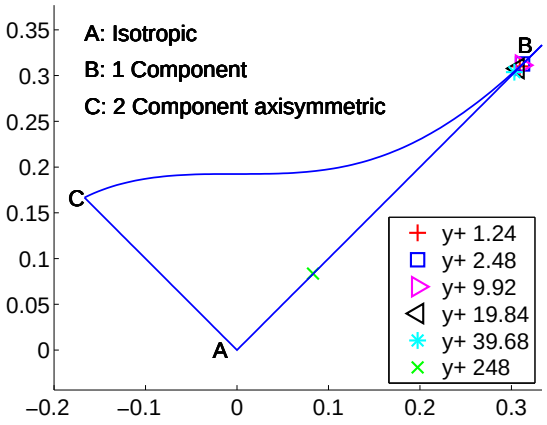

(a) $s/c = 0.5$

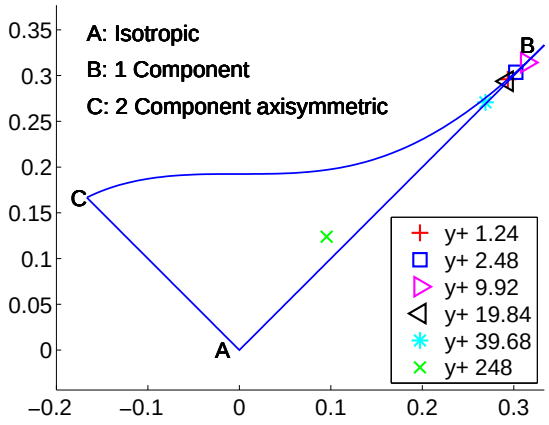

(b) $s/c = 0.6$

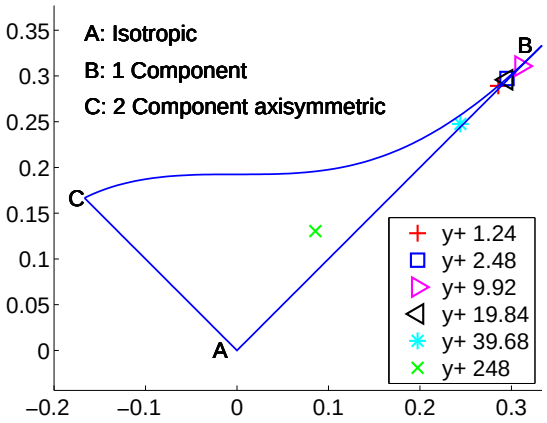

(c) $s/c = 0.7$

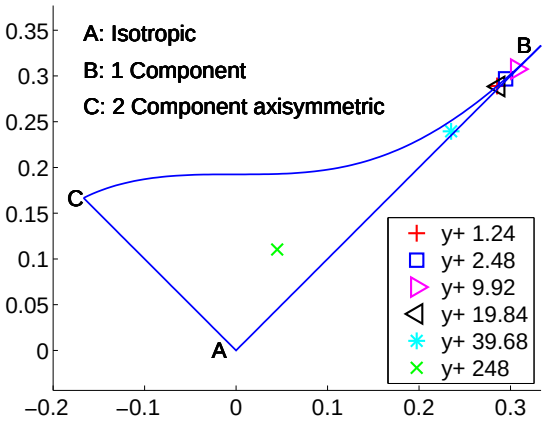

(d) $s/c = 0.8$

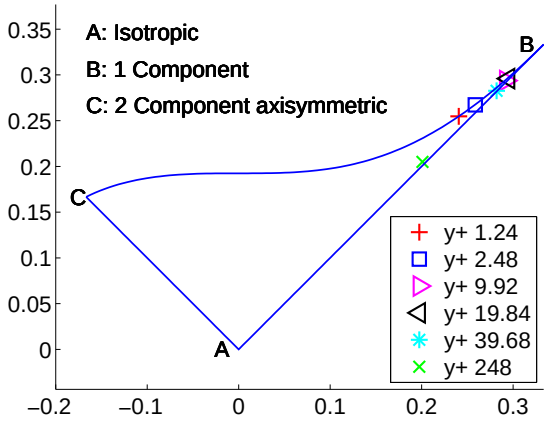

(e) $s/c = 0.9$

Figure 6.41: Turbulence triangles at various locations normal to the blade and different curvilinear abscissa positions for M3 mesh.

6.4 Conclusions

The analysis performed of the LS89 test case developed by the VKI has proven to be enriching. Two cases have been studied. The first case, **MUR129** has no turbulence injection. Assuming the heat flux coefficient field remains the most challenging field to predict, profiles compare adequately to those obtained experimentally. It is thus concluded that in the absence of larger turbulent intensities the flow is precisely reproduced due to the simpler physics encountered. For higher levels of turbulence combined with larger Mach number values at the exit, literature shows that operating points such as **MUR235** represent a more difficult case. Turbulence injection introduces a level of uncertainty due to the influence of different length scales and effective intensity.

The sensitivity of the simulations to different parameters and spectrum has been investigated. The turbulent intensity level at the inlet seems to be the most important parameter and the level of heat transfer is better captured when imposing a 18% level instead of the measured 6%. Certain uncertainties may be present due to the natural turbulence introduced by the experimental facility, however, values required for adequate predictions are too large so other parameters have been investigated [153]. The use of a larger integral length scale at the inlet, which corresponds to the one indicated by Fontaneto, did not show an improvement of the prediction in the simulation performed. Although the level of turbulent intensity that arrives to the blade leading edge is higher, this does not seem to be sufficient to trigger the transition. From the simulations performed here, this does not seem to be the dominant parameter although simulating the finest mesh with the latter integral length scale could lead to different conclusions. A grid resolution study points to important differences in the predictions. The coarser M1 mesh remains far when compared to other meshes, both on the suction and pressure sides. A first refinement shows a closer agreement on the pressure side but does not capture the plateau on the suction side. This objective is partly attained with the M3 mesh that adds sufficient points in the boundary layer to have a more accurate value of heat fluxes while reducing the contribution of the SGS turbulent viscosity. A detailed analysis of the temporal evolution and statistics extracted from temporal recordings give evidence of the importance of transition to adequately capture the heat transfer field. Contiguous acoustic waves are also seen to destabilize the flow but it is only responsible locally for an increase of heat transfer. Downstream, TKE decreases immediately after the impact of these waves and increases back towards the position of the shock wave. The critical bypass transition seems to be determined by the mesh refinement exclusively.

All these findings may be termed as 'physical', meaning they are the output of a sensitivity analysis of physical variables. The only effect that has not been shown is the behaviour and importance of the numerical scheme. The following chapter opens with an analysis of their influence on the prediction of the flow. A numerical analysis is then detailed to try to explain the behaviour observed and ways to improve existing methods are proposed when possible. Note that the sensitivity analysis developed in Sec. 6.2.1 has been used as a starting point for a UQ analysis detailed in App. F.

Chapter 7

LS89 Numerical Aspects and associated analyses

Contents

The properties of the numerical schemes in AVBP were studied in the previous Part but the sensitivity of the complex geometry to these parameters has not been shown yet. Different results may be expected when performing a simulation with low-order or high-order schemes, especially if a mesh convergence analysis such as the one performed in Sec. 6.2.2 shows differences. Just as a reminder, the objective of increasing the order of a scheme is to reduce the number of degrees of freedom necessary to capture the correct physics. The two numerical schemes compared are the high-order Two-Step Taylor Galerkin (TTG) family of schemes and a second-order Lax-Wendroff (LW) for the M1 mesh and 6% turbulent intensity level at the inlet.

During the course of the simulations, it was observed that numerical oscillations appeared in the proximity of mesh element transitions such as the one between prism layers in the BL and tetrahedra in the rest of the domain, Fig. 7.1. In Fig. 7.1 the noise is seen to be more intense between the last layer of prisms and the tetrahedra for the LW scheme, observation confirmed using the crinkled view in Fig. 7.1c. The high-order schemes are not free from these oscillations as it may seem however. In Fig. 7.2 the surface pressure field is shown on the suction side downstream the shock wave. This field shows that when dealing with small turbulent

(a) (b) (c)

Figure 7.1: Pressure field in wall region at an arbitrary position on the suction side of the blade for a) LW scheme b) TTG scheme c) crinkled slice of pressure field for LW.

structures near the wall the pressure field is affected by the numerics. The influence these small oscillations observed on the surface is assumed to be small in wall-resolved simulations but can be important for coarser meshes.

This leads to the question if the analyses done for simple cases where meshes are perfectly uniform and the physics are not as complex as encountered in industrial configurations are sufficient. Indeed, the numerical schemes used in AVBP were analyzed in Chap. 4 in terms of consistency and stability, and thus convergence, concluding that although all schemes complied with the requirements to be used in the context of LES, some were better adapted for those simple cases. These properties were however obtained under two important circumstances, the lack of boundary conditions (BCs) and using perfectly regular meshes. In literature, similar tests to those already presented in Chap. 4 are normally performed to determine the dispersion and dissipation properties [146]. The orders of convergence of the scheme are also shown in general on a variety of meshes that include non-regular elements, but do not take into account in most cases the influence of the boundary conditions. For the following, the cases shown will be performed using simple physics but will include other uncertain aspects such as metrics and BCs.

Boundary conditions can be taken into account using the well-known amplification matrix method [78]. This method is a brute-force method that has been used previously [39] but due to the lack of computational power has not been exploited to its extent. The matrix method is applied to two different configurations and the boundary closure terms presented in Chap. 3 are tested. This method can deal with any type of configuration for any scheme and all BCs without an additional large human effort. The prediction of the stability or instability of each scheme is consistent with conclusions obtained in Lamarque et al. [101] who performed an analytical analysis of a particular scheme coupled to a certain boundary condition. These closure terms are then studied in the context of the test case they were originally validated with. An explanation on why these closure terms were successful in providing a satisfactory solution is given and a new closure is presented to take into account the correct BCs.

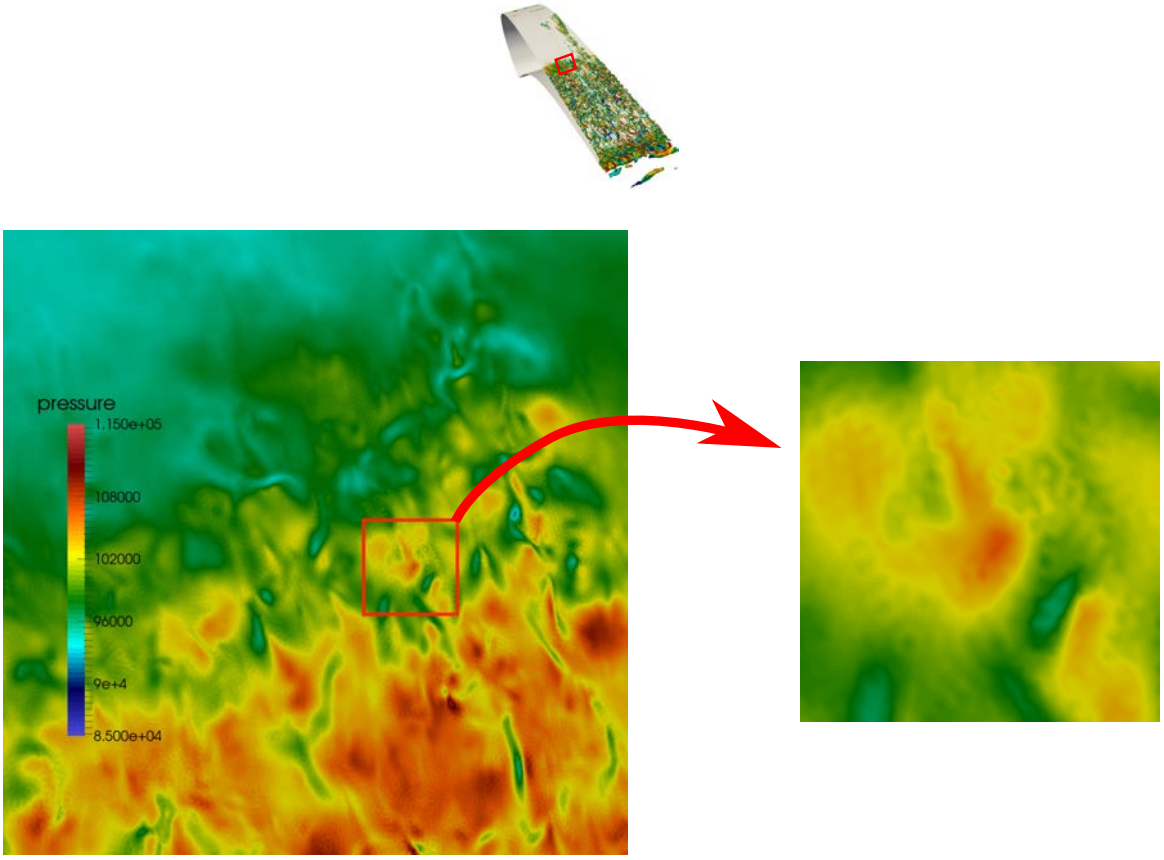

(a)

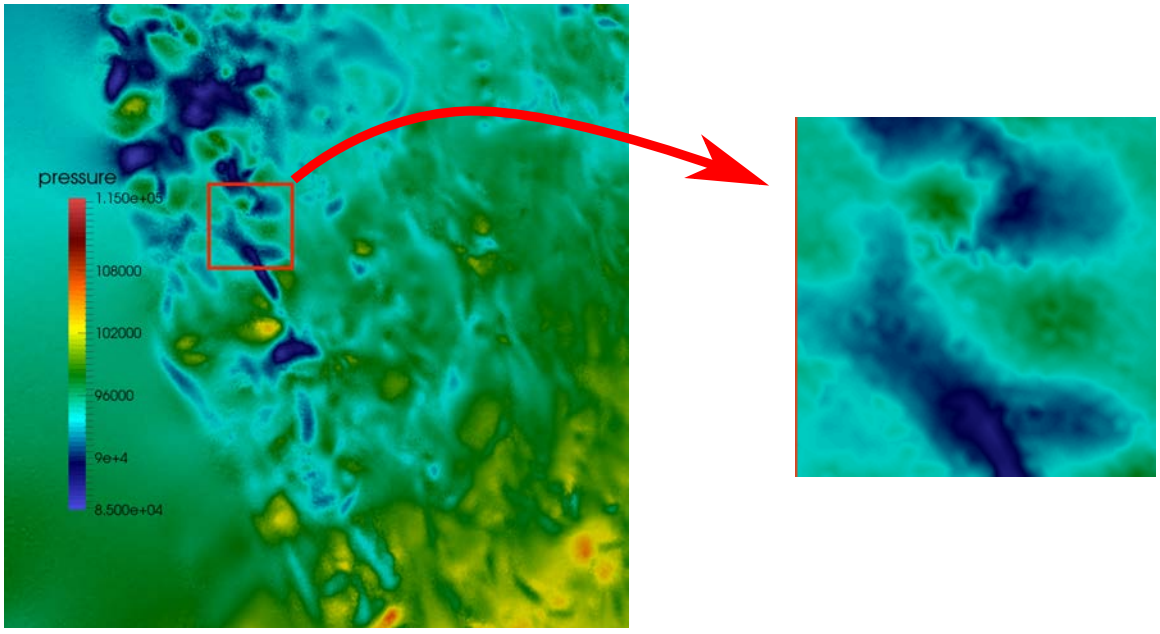

(b)

Figure 7.2: Instantaneous surface pressure field on the suction side of the blade downstream the shock for a) TTGC scheme b) TTG4A scheme.

For the mesh effects, simple test cases where oscillatory profiles appeared were analyzed and similarities between them were sought. It initially seemed that the preponderant location for the apparition of these profiles was any location in the proximity of a boundary condition. Nonetheless, when perturbing slightly the mesh regularity in the absence of BCs, similar problems appeared as shown at the interface region between hybrid elements in Chapter 6. This indicates that as well as possible issues in the coupling of the scheme and BCs, there is an improvement margin for the actual scheme and its implementation. The origin of this unexpected oscillatory behaviour in the absence of BCs comes from the metrics themselves when using a cell-vertex method. It was seen in Chap. 3 that cell-vertex algorithms introduce the concept of cell duality for each node of the mesh as well as the redistribution matrix. This redistribution matrix however does not take into account the relative position between the centroid of the dual cell and the position of the node. Tests done in this chapter show the importance of this relation.

The following chapter is divided into three distinct parts:

1. Stability analysis using the matrix method coupled to BCs.
2. Analysis of Second Order Terms that appear in the AVBP schemes. Existing closures and new developments are studied in a simple test case used for validation.
3. Metrics importance for non-regular meshes with a cell-vertex algorithm.

Global conclusions to the three parts are given. Although all three points are studied independently, they are not uncorrelated and so, a reminder of what is done for the second-order term for the TTG family is first illustrated as it is targeted as being a potential source of problems.

Second-order Temporal Terms and Current Treatment

As shown in Chap. 3, all AVBP schemes based on a Taylor expansion in time include a second order temporal derivative or higher that is transformed into a spatial derivative which calls for a contribution that is due to the boundaries. This was not the case for first order derivatives where it is necessary to comply with the Dirichlet conditions that are naturally imposed. For the case of second order derivatives however, it is necessary to impose additional conditions. Although documents as Donea and Huerta [53] suggest that the second order derivative must be seen as a mean to increase the order of the scheme, in nature it introduces a second order spatial derivative that is responsible for a diffusive effect. This modifies the nature of the equation requiring a diffusion type boundary condition for a convection scheme. It is thus an artificial boundary condition that has already been discussed in this same context [143, 100].

The additional term that appears is shown again in Eq. (7.1),

$$LL_j\left(U^n,\phi_j\right)=\underbrace{\Delta t\oint_{\partial\Omega}\phi_j\left(\vec{A}\vec{\nabla}\cdot\vec{F}\right)^n\cdot\vec{n}dS}_{BT_j(U^n)}-\underbrace{\Delta t\int_{\Omega}\left(\vec{A}\vec{\nabla}\cdot\vec{F}\right)^n\cdot\vec{\nabla}\phi_j dV}_{LL_j^0(U^n)}, \tag{7.1}$$

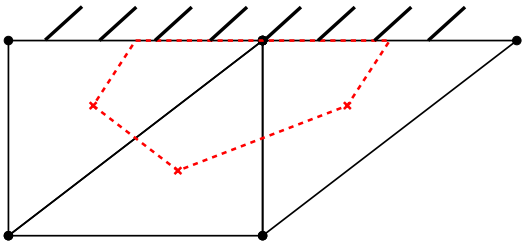

Figure 7.3: Border cell indicating primary and dual cells (discontinuous line).

where the boundary term is, assuming a constant Jacobian in the primary cell,

$$BT_j(U^n, \phi_j) = \Delta t A^n_{K_e} \sum_{k|k\in\partial K_e\cap\partial\Omega} F^n_k \nabla\phi_k \int_{\partial K_e\cap\partial\Omega} \phi_j dS = \Delta t \frac{1}{n^{bf}_v} (A^n_{K_e} R^n_{K_e}) \cdot S^{bf}_{j|K_e}, \qquad (7.2)$$

where $S^{bf}_{j|K_e}$ is the normal to the boundary and n^{bf}_v the number of vertices on the boundary. From a geometrical point of view one might recognize the requirement to close this cell too in Fig. 7.3. It is important to note that the apparition of this last equation is independent of the boundary condition to be imposed, either if it is a Dirichlet or a characteristic condition.

Previously, closure propositions classically accessible in AVBP for these terms are:

- Uncancelled Second Order Term (USOT)

  The volume term LL^0_j is calculated in the whole domain but the boundary term $BT_j(U^n)$ is set to zero. This approach, in the absence of information, in first instance would seem logical but does not close the boundary terms.

- Cancelled Second Order Term (CSOT)

  The surface term $BT_j(U^n)$ is set to a value such that the contribution of volume and surface terms is zero over the boundary nodes.

Their contribution to the stability of the scheme in particular cases will be seen in the following section and an alternative to these two approaches is proposed in the section after.

7.1 Advanced stability analysis of AVBP

The most general method to perform a stability analysis is the so-called linear matrix method [79]. The method consists in building a linear matrix that relates a set of conservative variables at instant *n* to the same variables at instant *n+1*. Once the method has been explained, the matrix *A* obtained can be analyzed. The most common approach is to perform an eigenvalue and eigenvector analysis of the matrix to link the absolute value of the eigenvalues to the stability. The difficulty of this method resides in the obtention of the eigenvalues and eigenvectors

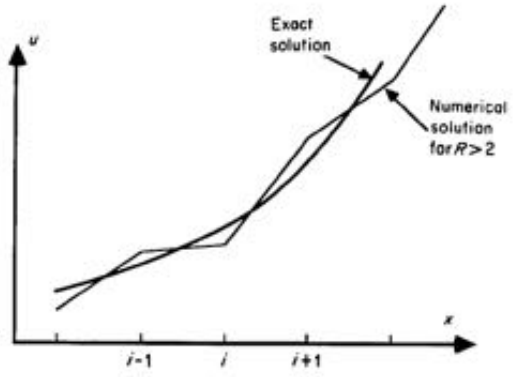

Figure 7.4: Oscillations originated by round-off error example [79].

that are nearly impossible to obtain analytically for a convection-diffusion problem. The matrix method is nonetheless much more expensive and to perform it correctly, the directives from Mitchell and Griffiths [124] must be followed.

The matrix method compared to the traditional von Neumann analysis allows also to take into account implementation effects. Indeed numerical implementation of schemes may vary with codes and as an example, the border terms and the discretization done at these points may be different, specifically for AVBP which gives access to two types of boundary closure terms. This effect may be studied using the amplification matrix method which therefore provides a deeper insight into the nature of the different closures.

Another method to study the effect of boundary conditions on the stability of the scheme is the normal mode decomposition. This is the method used by Gustafsson et al. [75] which consists in searching for a localized power-law solution where the coefficients are determined by the boundary conditions. This method is also applicable to a convection-diffusion type problem. Once again, the main drawback of this approach is the complexity of the algebraic solution. This however, is compensated by the prediction of the potential oscillatory behavior of the solution. An example in Hirsch [79], shows the round-off error on a set of nodes as in Fig. 7.4.

In any case, there does not seem to be a perfect method towards the analysis of the schemes for a general configuration and this document, tests have been carried out using the amplification matrix through an automatic tool. The more general application of the matrix method was the reason to pursue this path and not try the power-law solution. It allows to provide the stability curves in terms of amplification factors and gives insight into the stability matrix for specific grids, schemes and BCs. The steps required for this analysis are provided in the following.

7.1.1 Amplification matrix

The method retained to build the matrix resides in the idea of introducing perturbations onto a steady or reference flow. This assumption allows the linearization and differentiation of the

mean field evolution from the perturbated field. It furthermore allows to represent the perturbated system evolution in time by use of a linear application represented by a matrix around an operating point for which,

$$w^{n+1} = A \cdot w^n. \tag{7.3}$$

Note that exceptionally for this section, the conservative variable vector previously denoted as U will be redefined as vector w to avoid confusion with other variables. In Eq.(7.3), the vector w represents the vector of conservative variables and A is the linear matrix that includes both information of the scheme and the flow. This matrix contains both temporal and spatial information related to the influence on neighbour nodes and between time steps. In the code used, AVBP, this vector is composed of the following in 2D,

$$w = \begin{pmatrix} \rho \\ \rho u \\ \rho v \\ \rho E \end{pmatrix}, \tag{7.4}$$

where ρ for example, is a vector containing the density value at each mesh point x_n,

$$\rho = \begin{pmatrix} \rho\left(x_1\right) \\ \rho\left(x_2\right) \\ \vdots \end{pmatrix}. \tag{7.5}$$

If Eq. (7.3) holds, a perturbation δ can be added to the solution at instant n so,

$$w_p^n = w^n + \delta e_j^n \ , \delta e_1^n = \begin{pmatrix} \delta \\ 0 \\ \vdots \\ 0 \end{pmatrix}, \tag{7.6}$$

and,

$$w_p^{n+1} = A \cdot w_p^n. \tag{7.7}$$

The value of the perturbation to be added can not be trivial and this will be discussed later on. For the moment the assumption of small perturbations is accepted to be correct. The field of interest will be composed of the conservative variables presented in Eq. (7.4) and will have as many degrees of freedom as nodes times the number of equations in the problem (excluding certain boundary conditions, i.e. periodicities which will have extra constraints). The whole vector containing information is hence written as,

$$w_n = \begin{pmatrix} \rho_1^n \\ \vdots \\ \rho_N^n \\ \rho u_1^n \\ \vdots \\ \rho u_N^n \\ \rho v_1^n \\ \vdots \\ \rho v_N^n \\ \rho E_1^n \\ \vdots \\ \rho E_N^n \end{pmatrix}, \tag{7.8}$$

where N is the total number of nodes.

An issue that has not yet been addressed is *how* this perturbation is added and how it can help to construct the matrix representative of the full scheme integration. The key to building the matrix consists in adding the perturbation to only one node and one variable at a time to build a column of matrix A. Then, substracting Eq. (7.7) from Eq. (7.3) leads to,

$$w_p^{n+1} - w^{n+1} = A \cdot \left(w_p^n - w^n\right) = A \cdot \delta e_j^n. \tag{7.9}$$

It can easily be seen that the addition of each perturbation will lead to the construction of each column j where the perturbation has been added,

$$\begin{pmatrix} \rho_{1p}^{n+1} - \rho_1^{n+1} \\ \vdots \\ \rho_{Np}^{n+1} - \rho_N^{n+1} \\ \rho u_{1p}^{n+1} - \rho u_1^{n+1} \\ \vdots \\ \rho E_{Np}^{n+1} - \rho E_N^{n+1} \end{pmatrix} = \begin{pmatrix} a_{1,1} & \cdots \\ \vdots & \vdots \\ a_{N,1} & \cdots \\ a_{N+1,1} & \cdots \\ \vdots & \vdots \\ a_{4N,1} & \cdots \end{pmatrix} \begin{pmatrix} \delta \\ \vdots \\ 0 \\ \vdots \\ 0 \end{pmatrix}, \tag{7.10}$$

$$a_{i,1} = \frac{w_{ip}^{n+1} - w_i^{n+1}}{\delta}, \tag{7.11}$$

which explains the cost and the limitations encountered by Colonius [39] that are much more acceptable nowadays.

A final note must be added which will help to validate the method. If the initial solution w^n is indeed a stable solution in the sense that it is a stationary converged state, it is then

possible to say that applying the matrix to this field will not induce any change of the field at instant $n+1$. Being this the case, the following must be true,

$$Aw^n - w^n = \begin{pmatrix} 0 \\ 0 \\ \vdots \end{pmatrix}. \tag{7.12}$$

Equation (7.12) will however not always be true if careful attention is not paid to the magnitude of the perturbation added to the problem in Eq. (7.9). Two reasons can explain such a behaviour: error propagation and round-off error can be held responsible as well as the fact that it is a non-linear system of equations. A certain tolerance must hence be chosen.

The relation that must be verified to guarantee the stability can be expressed by the limits of the amplification factor, defined as,

$$G_j = \frac{{w_j}^{n+1}}{{w_j}^n} = \mid G_j \mid e^{\imath\phi}. \tag{7.13}$$

If the perturbation added is amplified A will have eigenvalues larger than one and the system will be unstable, while if $\mid G \mid$ is less than 1 the perturbation will be damped. This relation coincides with the von Neumann condition for stability,

$$\mid G_j \mid < 1. \tag{7.14}$$

Obtaining the eigenvalues of A and plotting their real and imaginary parts, it can be compared to the unitary circle. If the eigenvalues are located outside the circle, the numerical system will be unstable as seen in Fig. 7.5.

The method described above must be validated and the tool must prove robust to the different test cases. The first step is thus to obtain this matrix A for a simple case, moving on then to modify the boundary conditions and the different schemes to study their stability.

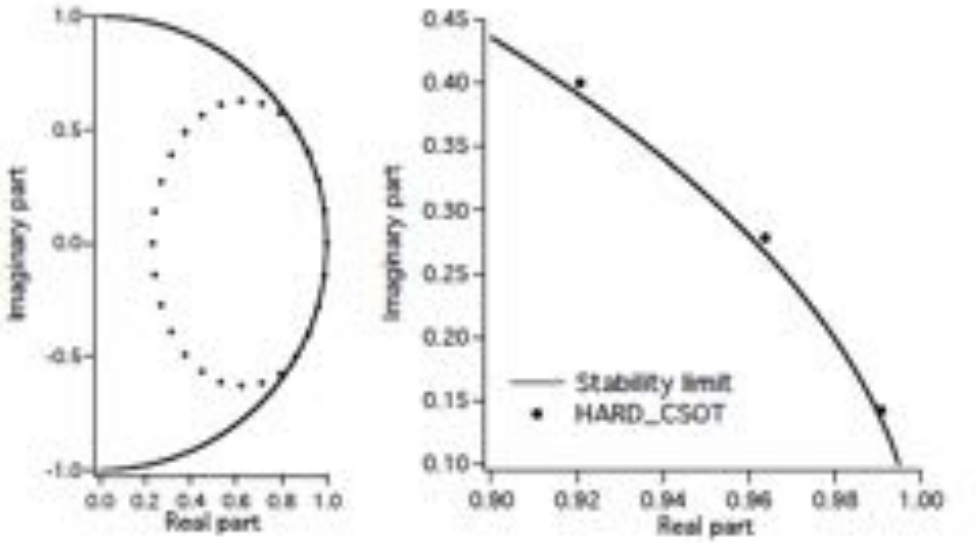

Figure 7.5: Eigenvalues spectra obtained using the amplification matrix, [99].

7.1.2 1D cavity eigenmode

The configuration consists of an acoustic wave moving between two adiabatic walls on the left and right sides with Dirichlet type conditions in Fig. 7.6. Top and bottom conditions are set to be periodic as the flow should remain 1D. The wave is then advected until it impacts the wall and 'rebounds'. The Euler equations are preferred to simplify the study for which an analytical expression can be found. A CFL value of approximately 0.4 was used in this case although various values were tested and for which the same conclusions can be extracted. In the simulations, the wave is expected to dissipate due to the natural numerical dissipation terms of the scheme and it is never expected to be unstable for an adequate numerical scheme. This is why two numerical schemes are tested, LW and TTGC. Also, this test can be compared to the results found in previous works of Lamarque and Poinsot [100].

Figures 7.7-7.9 show the comparison between two different analyses and for different schemes. The first one is the method explained above concerning the matrix method while the second

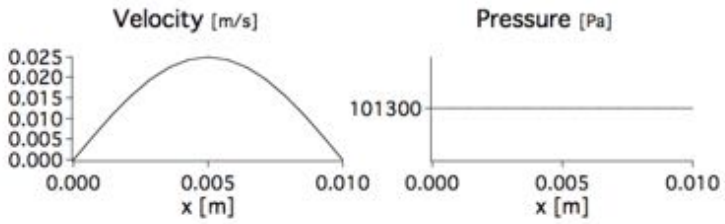

Figure 7.6: Initialization of the wave for the 1D cavity.

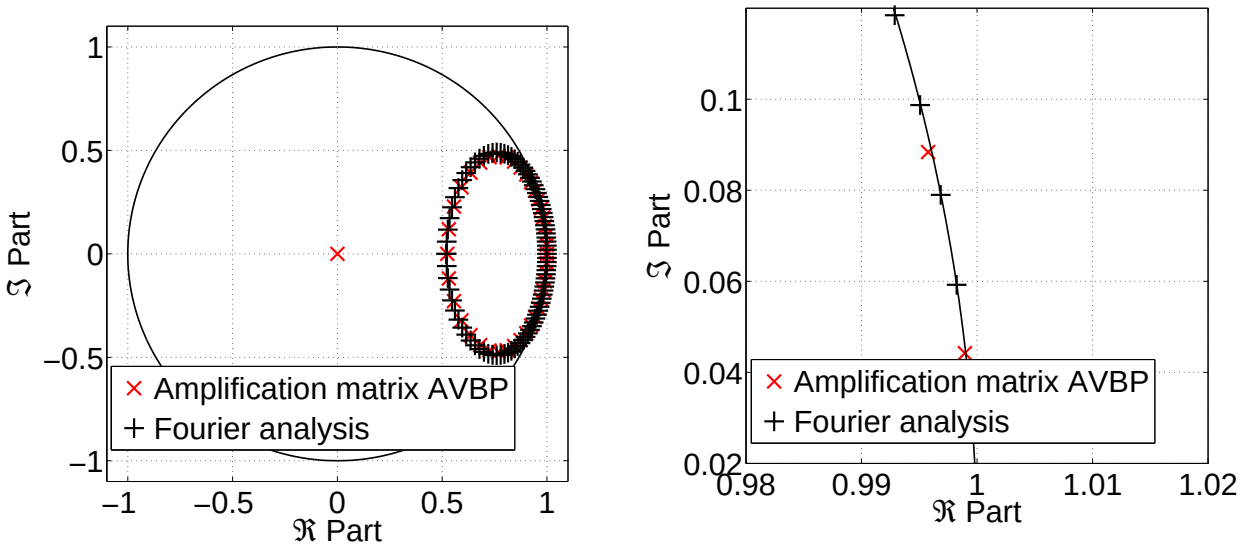

(a) Global view of the spectrum.

(b) Zoomed in view of the spectrum to the most critical eigenvalues.

Figure 7.7: Eigenvalue distribution of LW USOT amplification matrix applied to a 1D cavity eigenmode.

method is the Fourier analysis which will not take into account the boundary condition effects. The first comment concerns the matrix amplification method and the eigenvalues located at the origin. These eigenvalues exist because at the walls, a perturbation is being added artificially in a no penetration direction. The influence this perturbation has on the actual stability has however not been quantified as it is a numerical bias, a pre-processing step was done to set to zero the matrix rows and columns correspondingly. The figures show how the Fourier analysis gives results that do not agree with the other approach that does take into account the boundary conditions. In Figs. 7.7 & 7.8 the comparison is being done between the different schemes in a *USOT* (Uncancelled Second Order Term) context. By plotting the eigenvalues it is possible to discern the dissipation properties as the scheme will be less dissipative the nearer it is to the unit circle. As seen in Fig. 7.7a the eigenvalues are distributed in an oval form, the lowest eigenvalue being of the order of ~ 0.5. In Fig. 7.8a however the eigenvalues are seen to be very close to the unit circle through the whole spectrum. These differences between the *LW* and *TTGC* schemes are consistent with results obtained in previous chapters. The further the eigenvalues are from the unit circle, the more dissipative the scheme is and so, *TTGC* is better adapted to LES. However, introducing the *CSOT* (Cancelled Second Order Term) context combined with Dirichlet type boundary conditions in Fig. 7.9 the scheme is found to be unstable. The *CSOT* formalism in an inviscid case leads to a numerical divergence [101] due to the presence of eigenvalues outside the unit circle, see Fig. 7.9b. This proves the prediction power of the tool that would not be accomplished using exclusively a Fourier analysis that predicts a stable behaviour and confirms the observations of Lamarque et al. [101].

It seems clear from the previous problem that an issue arises for the correct closure of the scheme boundary terms. Indeed, for a simple wave transported inside a channel the *CSOT*

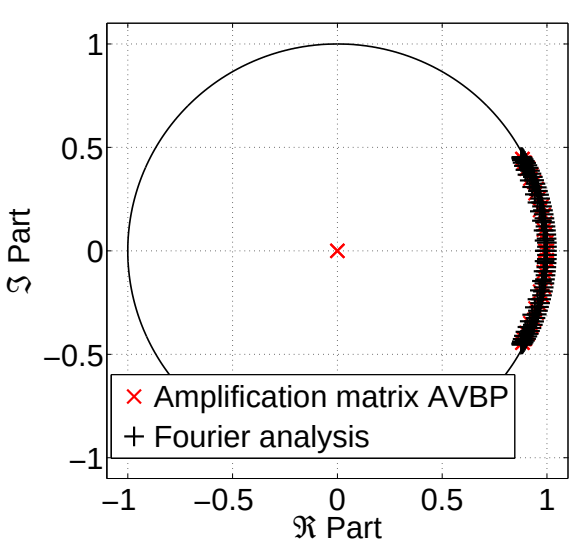

(a) Global view of the spectrum.

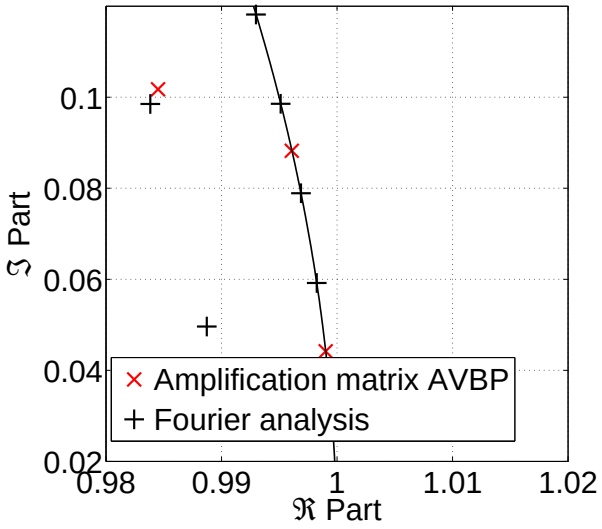

(b) Zoomed in view of the spectrum to the most critical eigenvalues.

Figure 7.8: Eigenvalue distribution of TTGC USOT amplification matrix applied to a 1D cavity eigenmode.

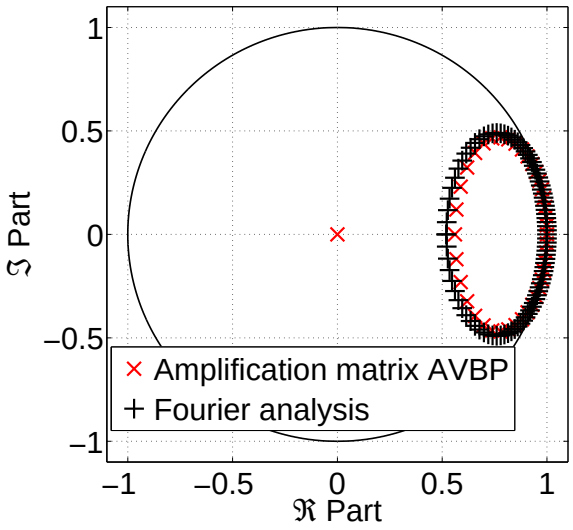

(a) Global view of the spectrum.

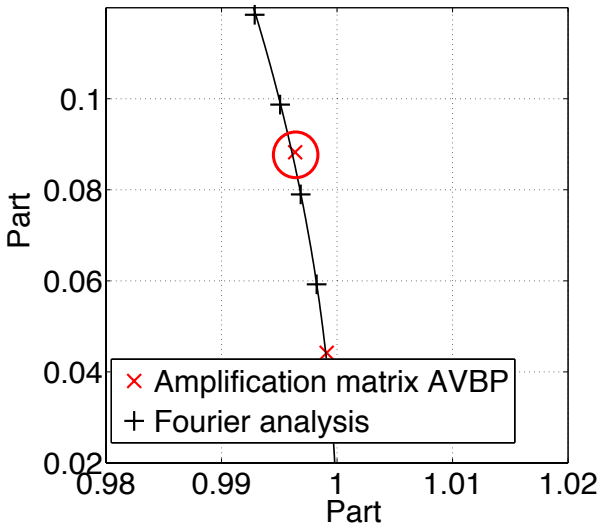

(b) Zoomed in view of the spectrum to the most critical eigenvalues.

Figure 7.9: Eigenvalue distribution of LW CSOT amplification matrix applied to a 1D cavity eigenmode. The red circle highlights an eigenvalue located outside the unit circle which indicates an unstable mode.

formulation is seen to be slightly unstable which for the Euler equations is problematic. The question that remains is how such issues behave in a case where diffusion exists to determine if the scheme remains unstable. A Poiseuille flow is hence addressed below.

7.1.3 Application to a Poiseuille flow

A typical Poiseuille flow is adopted for this test. The conditions demanded for this case are essentially to have a Reynolds number sufficiently small for the flow to remain perfectly laminar. As the test intends to be a purely numerical test case, a value of $Re = 1000$ is taken so no physical interactions may be held responsible for any eventual instability. The mesh used to simulate the converged Poiseuille flow is 2D, Fig. 7.10 and is composed of 7x21 nodes. The boundary conditions are periodic on the left and right sides of the computational domain in the direction of the flow. Isothermal no-slip Dirichlet boundary conditions are set on both top and bottom limits and a source term is added to the system of equations to account for the pressure drop. The CFL value used in this case is a realistic CFL=0.7 value and only the TTGC scheme is tested. The flow is converged until residuals are of the order of machine precision before applying the method. Results obtained with the evaluated matrix issued by the previous flow prediction are compared with a convective Fourier analysis of the scheme.

Analyzing Figs. 7.11 & 7.12 it can be seen that both schemes are stable. Differences may be seen in the shape of the curve due to the different CFL value compared to the previous section. In any case, similarities between the Fourier analysis that includes only the convective terms and the amplification matrix method are clear. Although it is a diffusion dominated problem, the effect of introducing a perturbation in the flow is seen. The physical diffusion seems to be sufficient to render stable the slightly unstable convective *CSOT* formulation. It must also be noted that the use of artificial viscosity, which is not used here, is common for realistic simulations in a cell-vertex method which would add an additional source of dissipation. It seems therefore clear that both closures may be used without worrying about stability issues. The conclusion then is that although the closure terms definitely influence the stability properties of the scheme, any type of fluctuation that may cause spurious oscillations remains bounded and will never appear in a stability analysis even when boundary conditions are taken into account. This poses a problem towards the analysis of these modes as any stability analysis will not detect them as they do not represent an unstable state.

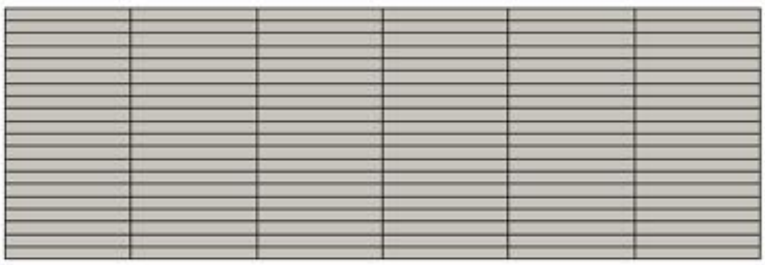

Figure 7.10: Mesh used for amplification matrix test.

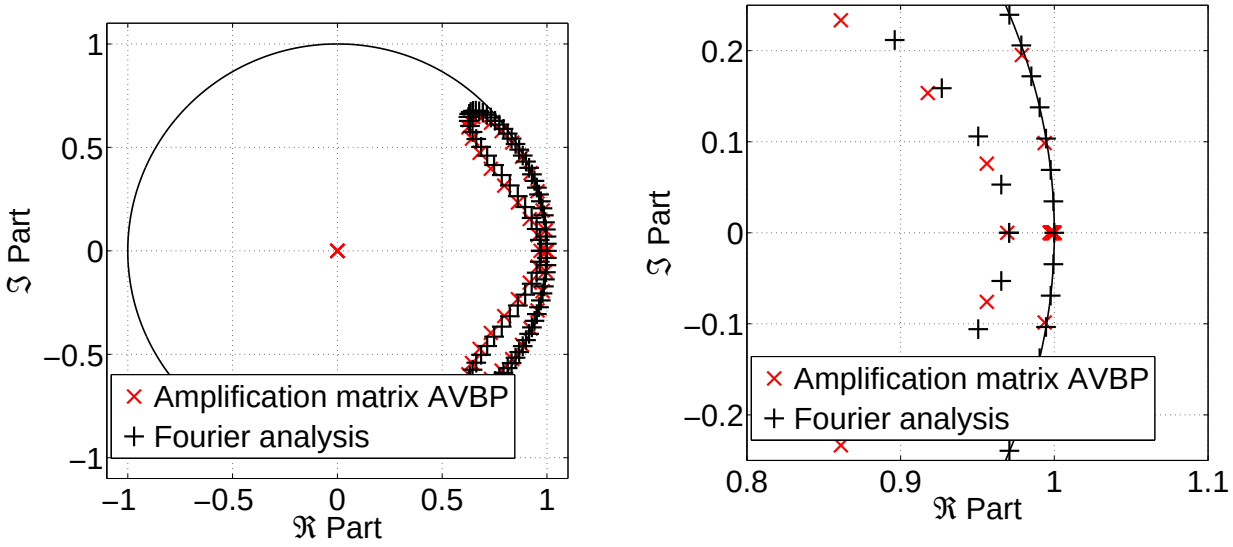

(a) Global view of the spectrum.

(b) Zoomed in view of the spectrum to the most critical eigenvalues.

Figure 7.11: Eigenvalue distribution of USOT amplification matrix applied to a Poiseuille flow.

The previous stability analyses are useful for various reasons. The analysis is performed directly on the implemented schemes and not only on a theoretical analysis. The main advantage is that the effect of the different numerical closures can be detected between, one resulting in a stable behaviour while the other yields an unstable solution that would end up blowing up. Although not shown, this last conclusion is confirmed when running the corresponding simulation and in which the pressure amplitude of the signal increases in time. In the following chapter the issue of oscillations and their treatment will be discussed. Closure terms will receive special attention concluding with a metric analysis typically found for an unstructured solver.

From here on, two different problems are addressed. The first section treats the recurrent apparition of boundary closure terms and how to mathematically impose the missing information. The two existing formalisms are examined and a new method is proposed which is consistent with the scheme. The second section discusses the effect of the metrics on the relation with non-physical oscillations. It will be shown that the existing shift between nodes and associated dual cell centroids seen in Chap. 3 plays a significant role in the development of oscillations when meshes are not perfectly regular.

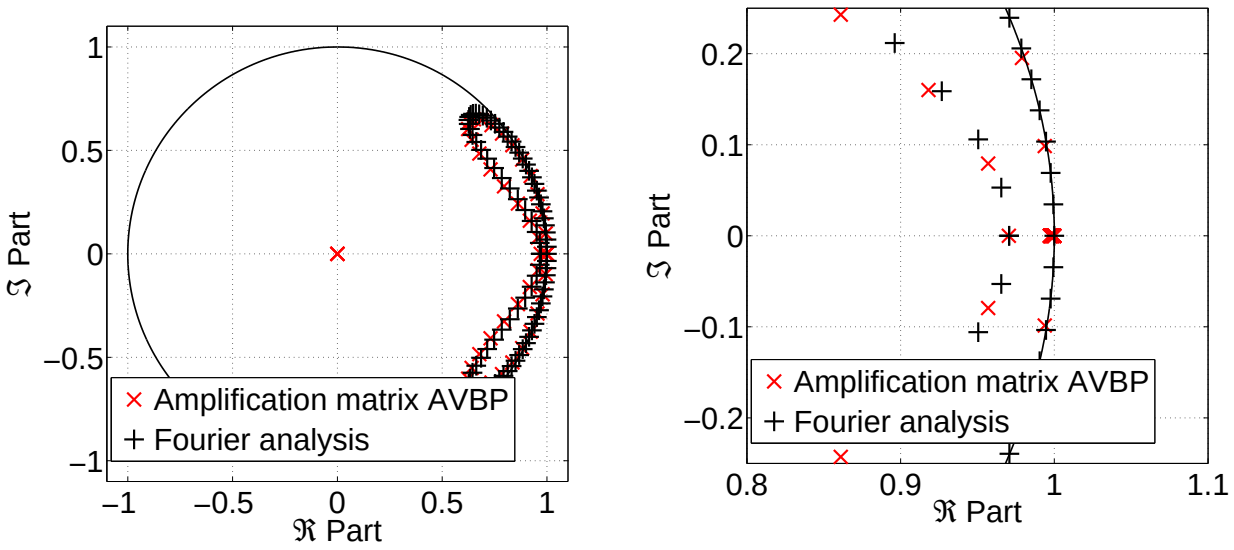

(a) Global view of the spectrum.

(b) Zoomed in view of the spectrum to the most critical eigenvalues.

Figure 7.12: Eigenvalue distribution of CSOT amplification matrix applied to a Poiseuille flow.

7.2 Development of a new numerical closure

The two closures currently implemented in the AVBP code have been previously detailed. To illustrate mathematically the impact of these two methods, the simple advection equation is used as a mathematical toy case to discuss the difficulty of the problem. By substituting $u_t = -cu_x$ in the Lax-Wendroff scheme,

$$\frac{u^{n+1}-u^n}{\Delta t} = u_t^n + \frac{\Delta t}{2}u_{tt}^n + \mathcal{O}\left(\Delta t^2\right) = -cu_x + \frac{\Delta t}{2}c^2 u_{xx} \tag{7.15}$$

the second order term represents the Hessian operator, which implies the calculation of a second order spatial derivative. The difficulty resides in providing a boundary condition to this operator that has no physical sense. Not providing any information to this operator as in the *USOT* case provides a degree of freedom and the system is thus mathematically undetermined. The value of the operator will then be that predicted by the volumetric term with no surface term contribution. For the case of *CSOT*, it implies setting the second order derivative contribution to zero. This is only true if the Hessian is indeed zero at the border of the domain implying that the volumetric term is equal to the boundary term always. However, when any other type of profile is encountered the value imposed will not be in agreement with the physics. The system requires imposing the exact profile which is not the case when setting the operator to zero. Note finally that although potentially modified, the equations must still verify the conservative properties of the scheme which in the end and depending on the choice adopted between the

two operators available today, may not be guaranteed.

As it has proven difficult to obtain additional information from a spatial formulation, thoroughly discussed in the next section, tests have been performed to complement boundary condition information through the temporal derivatives. In Eq. (7.1), the surface term contains the term $\vec{\nabla} \cdot \vec{F}$ which is taken to be the value of the residual predicted by the scheme without the imposition of boundary conditions associated to the physics. To alleviate the problem, it is however possible to estimate the value of $\frac{\partial U}{\partial t}$, related through the expression $\frac{\partial U}{\partial t} = -\vec{\nabla} \cdot \vec{F}$. The idea is to reconstruct this term using backward information from previous iterations. Mathematically this is done through a Taylor expansion as shown in Eq. (7.19). The first derivative can be estimated using a backward reconstruction that although not exact, provides a better estimation of the exact derivative,

$$\frac{\partial U^n}{\partial t} = \frac{1}{\Delta t} \sum_{i=0}^{i_{max}} \alpha_i * U^{n-i} \tag{7.16}$$

where n is the current time step, α_i correspond to the coefficients of the development and i_{max} is the maximum number of time steps stored. This new closure will be denoted here onwards as *TSOT* (Temporal Second Order Term). This formulation has been put into place and a test case originally done by Porta [143] is performed to illustrate the advantages of the *TSOT* formalism and to show the reasons why the other two will only work in specific cases.

7.2.1 1D profile between walls

The test case used to test the accuracy of the closure terms in AVBP is an artificial one. It relies on the work of Porta [143] and solves using only the Euler equations. Inside a cavity such as the one represented in Fig. 7.13 composed of triangles (although a quadrilateral mesh has also been tested with the same conclusions) using 21x21 nodes, the simulation is initialized with the profiles seen in Fig. 7.14. The linear profile respects the boundary conditions at the limits (x=0 and x=0.01 m with walls) and remains very simple. In particular, this saw-tooth shape is useful for the prediction of incoming and outgoing waves as can be intuited from Eq. (7.17),

$$\mathcal{L}_- = \lambda_- \left(\frac{\partial p}{\partial n} - \rho c \frac{\partial u}{\partial n} \right), \tag{7.17}$$

which represents the outgoing acoustic wave amplitude as done in Poinsot and Veynante [139].

By imposing a constant pressure profile, the first RHS term of Eq. (7.17) will be zero. The outgoing acoustic wave can then be written as $\mathcal{L}_- = \rho c^2$ given $\lambda_- = u - c$. Using the notation in [29] the notion of strength of the wave can be determined using the following expression,

$$strength = -\frac{\mathcal{L}_- \Delta t}{\rho c} = c \Delta t, \tag{7.18}$$

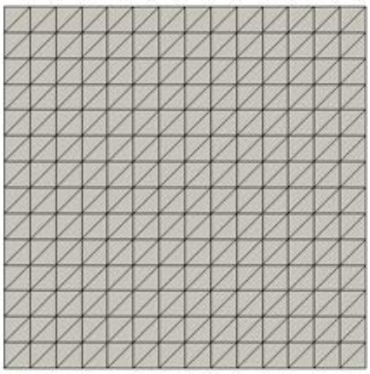

Figure 7.13: Mesh used to impose the 1D acoustic profile sufficient to neglect possible border effects.

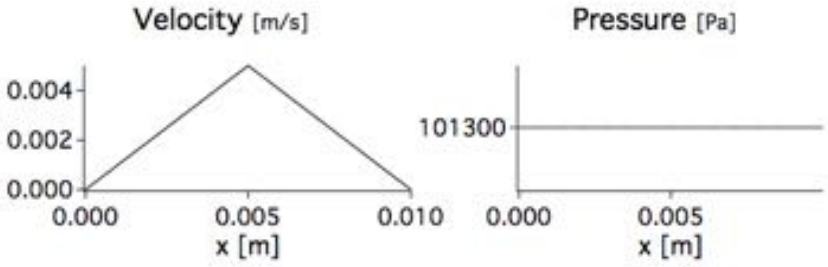

Figure 7.14: 1D acoustic profile of the initial solution.

Analytical	USOT	CSOT
$-3.7299 \cdot 10^{-4}$	$-5.677 \cdot 10^{-4}$	$-3.7296 \cdot 10^{-4}$

Table 7.1: Wave strength values obtained by Porta [143].

	Analytical	TSOT	$\mid Error \mid$
$\Delta t = 1.039 \cdot 10^{-6}$	$-3.669 \cdot 10^{-4}$	$-1.307 \cdot 10^{-4}$	64%
$\Delta t = 1.039 \cdot 10^{-7}$	$-3.669 \cdot 10^{-5}$	$-3.655 \cdot 10^{-5}$	0.4%
$\Delta t = 1.039 \cdot 10^{-8}$	$-3.669 \cdot 10^{-6}$	$-3.670 \cdot 10^{-6}$	0.02%

Table 7.2: TSOT closure terms using different time steps for the same order approximation.

and can easily be compared with the value provided by the code.

For the test case, the value of the sound speed is $c = 353.212$ m/s and the value of the time step will be varied. The proof given in Porta, and Lamarque and Poinsot [143, 100] is that the *USOT* formalism does not predict the correct strengths compared to the *CSOT* that provides them in an exact way when performing a one-iteration test. Of course, imposing a Hessian operator equal to zero which is true only if a linear profile is used, the solution complies with this condition and *CSOT* is exact for this case. However, this is not true in other more general cases where the profile isn't linear. Providing a null value of the Hessian is not an option either as can be seen in this simple test case comparing the results shown in Table. 7.1.

The new formulation developed in this section, from here on denoted as *TSOT* for Temporal Second-Order Term, is applied to this same test case. The first issue encountered for the application of this closure is the initialization as no previous iteration information is available. Once the term corresponding to $\frac{\partial U}{\partial t}$ is reconstructed using previous values of the conservative variables of previous iterations, the method is straightforward. The first test performed is to reconstruct the term using only a first order approximation, so,

$$\frac{\partial U}{\partial t} = \frac{1}{\Delta t}\left(U^n - U^{n-1}\right). \tag{7.19}$$

Only two iterations are then necessary, the first one to obtain the $\frac{\partial U}{\partial t}$ used in the second iteration. Table. 7.2 shows the results for various time steps to illustrate the effect of the first iteration. The effect of having an erroneous first iteration is much more important when the time step is larger as the flow will evolve differently and there will be other contributions to be taken into account. Furthermore, the space-time consistency holds only for small time steps meaning that using the temporal discretization of Eq. (7.19) is valid only for a certain range. This could hence also be held responsible for the differences observed. However, when small time steps are taken the value tends to the analytical one.

Using the intermediate time step value of $\Delta t = 1.039 \cdot 10^{-7}$, ten iterations are done for

	TSOT	$\mid Error \mid$
First order	$-3.6553 \cdot 10^{-4}$	0.1%
Second order	$-3.6553 \cdot 10^{-5}$	0.1%
Third order	$-3.6654 \cdot 10^{-6}$	0.095%

Table 7.3: TSOT closure terms using a constant time step for different order approximation.

different order of approximations of the $\frac{\partial U}{\partial t}$ term. Three different tests using first, second and third order approximations for the first derivative are used and are shown in Table. 7.3. For the current time step used, the increase in order does not present any advantage which does not mean it is true for other time steps. The same conclusions can be extracted for other schemes (such as TTGC) except that the error is of the order of 0.005%. For the *USOT* formulation after 10 iterations the error is of the order of 4% which means that the reduced time step is not the only important point for the accurate prediction of the outgoing wave. Using a mathematically obtained relation using backward derivatives in time therefore provides the correct estimation of the strengths in this case. Note that ideally, this should be done using a spatial discretization as the temporal discretization is only a 'trick' that holds as long as the time step used remains small. The next section explains the reasons why the spatial discretization was not possible with the current implementation.

7.3 Node and dual cell centroid conundrum

The majority of tests dedicated to stability or consistency studies are done on regular meshes. This is not the case of many complex simulations however where high aspect ratio meshes exist or when the scheme is degenerated near the border of the domain. Considering a border cell such as shown in Fig. 7.15, geometrical differences that exist between the nodes and the centroid of the dual cell are evidenced. In the previous figure, the center of gravity of each primary cell is represented by the red crosses while the centroid of the median dual cell (CMDC) is represented by the blue plus sign. The first thing to note is the large difference present between the CMDC and the node. Clearly borders are a flagrant example of the distance from the CMDC to the node which differs in almost half the size of the dual cell. Just as a reminder, this problem is related to cell-vertex formulations as cell-centered formulations store the information at the same location it is calculated for second order schemes. When higher order schemes are used it requires additional operations [135]. This redistribution process can lead to the washboard modes noted by Stringer and Morton [176]. Errors associated to the washboard modes are a result of using an imprecise distribution matrix effect as noted by Blazek [21] that leads to a nodal residual convergence (of the order of machine precision values) but rendering a seemingly 'oscillatory profile' that does not move in time. The scheme consistently approximates the residual value at the CMDC but is then erroneously sent to the node. The gradients associated to the calculation of the residual have therefore a small error that may be especially critical for boundary conditions.

An interpolation step may be added to correct this distribution matrix using a linear gradient

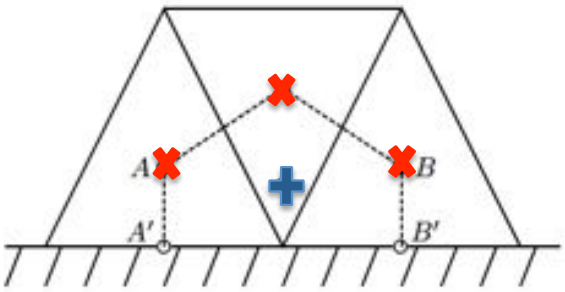

Figure 7.15: Dual cell of a border schemes indicating the centroid of primary cells with red crosses and the CMDC by the blue plus sign.

reconstruction as done by Mavriplis [119] where,

$$U_{node} = U_{CG} + \vec{\nabla} U_{CG} \cdot \vec{r}_{CG-node}. \tag{7.20}$$

The problem of this formulation is the difficulty in unstructured meshes to reconstruct high-order gradients necessary to comply with the order of the scheme. If the solution of a scheme is said to be of order n the gradients must be at least of order $n-1$. This difficulty has been addressed in the literature by Ollivier-Gooch and Van Altena [135] and more recently by Jalali and Ollivier-Gooch [82] to provide the necessary order by using least-square reconstruction. The objective of the following tests is exclusively to point out the problem in a simple configuration and link it to the metrics.

7.3.1 1D convection of an acoustic wave

The following test case was done to evaluate exclusively the behaviour of convection schemes using the Euler equations. More specifically, the behaviour of the schemes is tested when deformed meshes are encountered. The test case therefore consists of a simple 2D domain box as shown in Fig. 7.16 with three layers of cells in the y direction and fifty in the x direction and in which an acoustic wave is convected. The convection distance domain is kept constant but the transverse direction will vary for reasons explained later on. Periodicity boundary conditions are enforced in the top-bottom and left-right limits on various meshes as shown; Fig. 7.17. The idea behind this test case is to evaluate the effect of introducing a deviation between the node position, defined by the degrees of freedom of the grid, and the centroid of the median dual cell (CMDC) implicitly defined. Profiles are traced in both directions in a multi-dimensional context for a problem that should remain 1D. Different schemes are also tested to discriminate the influence of the L and LL terms described in Chapter 3.

The first simulation is conducted on a standard isotropic mesh, Fig. 7.17a, and for which all elements are the same and the connectivity of each node is exactly the same. It is built so that the node position and the center of the dual cell are placed at the same position. The other two meshes however have a deviation as shown in Fig. 7.18. In Fig. 7.17b the domain has been extended in the y direction so the set of middle cells is modified. The third mesh represented

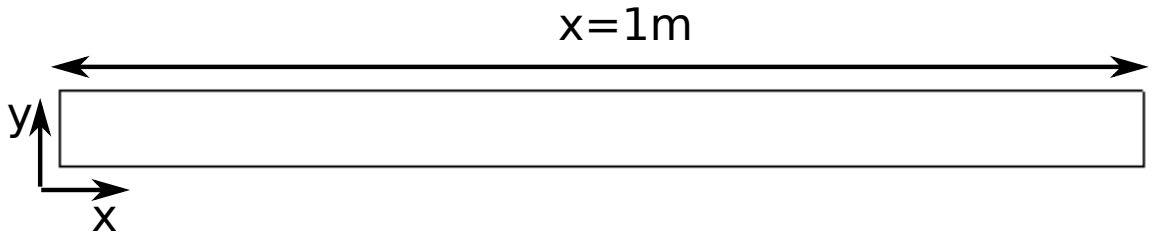

Figure 7.16: Domain used in the 1D convection of an acoustic wave

.

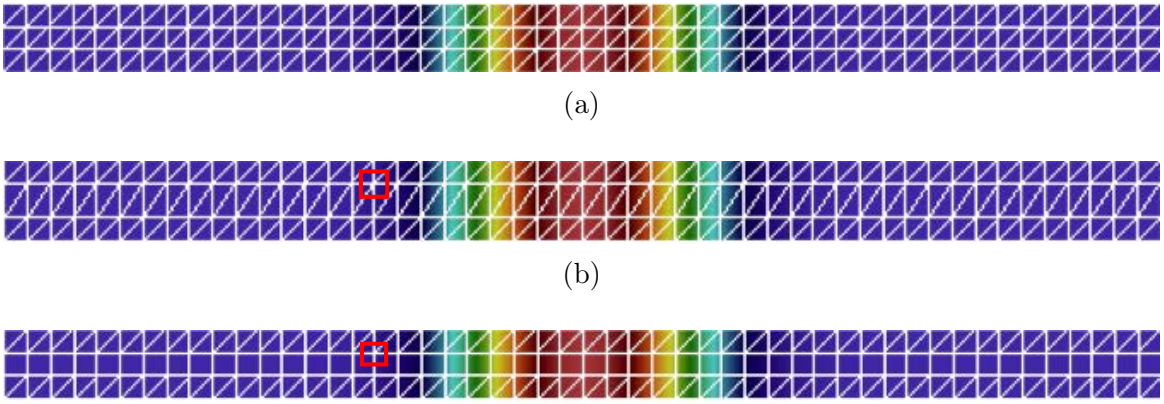

(a)

(b)

(c)

Figure 7.17: Meshes used for the convection of an acoustic wave in a) Isotropic triangles b) Modified triangles c) Hybrid triangle-quad mesh.

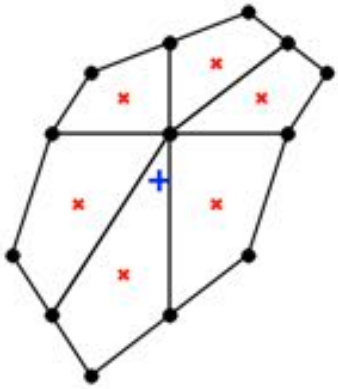

(a) Intersection of primary cells and dual cell in the modified triangle mesh around an arbitrary node.

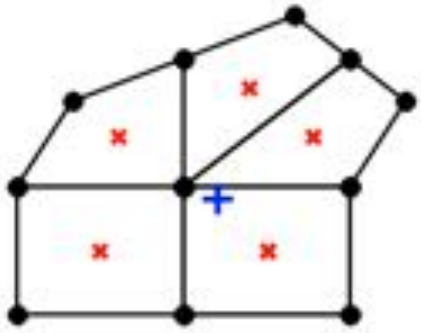

(b) Intersection of primary cells and dual cell in the modified hybrid mesh around an arbitrary node.

Figure 7.18: Representation of a dual cell around node inside box highlighted in a) Fig. 7.17b b) Fig. 7.17c. Red crosses represent the centroid of each intersection of dual cell and primary cell. Deviation of CMDC to node is represented by the blue plus sign.

in Fig. 7.17c substitutes the middle range of triangular cells for quadrilaterals becoming thus a hybrid mesh. To study how this may affect the wave convection only five iterations are necessary.

The profiles in the y direction using the LW and the TTG schemes are presented in Fig. 7.19 after five iterations. It can be seen that for both schemes the pressure is constant at all positions and the flow remains 1D. This however is not the case for the other two meshes. Values at the interior nodes are seen to be displaced with respect to the mean value and are seen to be larger in the hybrid case, in no case negligible after just a few iterations. Additionally, the fluctuations have opposite signs comparing the modified triangle and the hybrid mesh. This would indicate that there could be a scheme-related problem for the calculation of gradients associated to cases where dual cell center and nodes do not coincide.

This problem can be further demonstrated using this same simple test case. If the problem was indeed associated to the gradient calculation it would be possible to modify the mesh in a way that in the convection direction the CMDC were at the same position as the node and modifying the transverse direction only. This can be attained as shown in Fig. 7.20a using quadrilaterals where one of the cells has been stretched in the y direction. This introduces a deformation in the mesh but does not change the mesh in the direction where the gradients are significant. By advancing the same physical time as before, pressure fluctuations are shown in Fig. 7.20b and are seen to be zero indicating that the flow remains 1D.

This simple test case shows that indeed the correct redistribution of residuals is a necessary process and an accurate gradient reconstruction is mandatory to achieve this specific property.

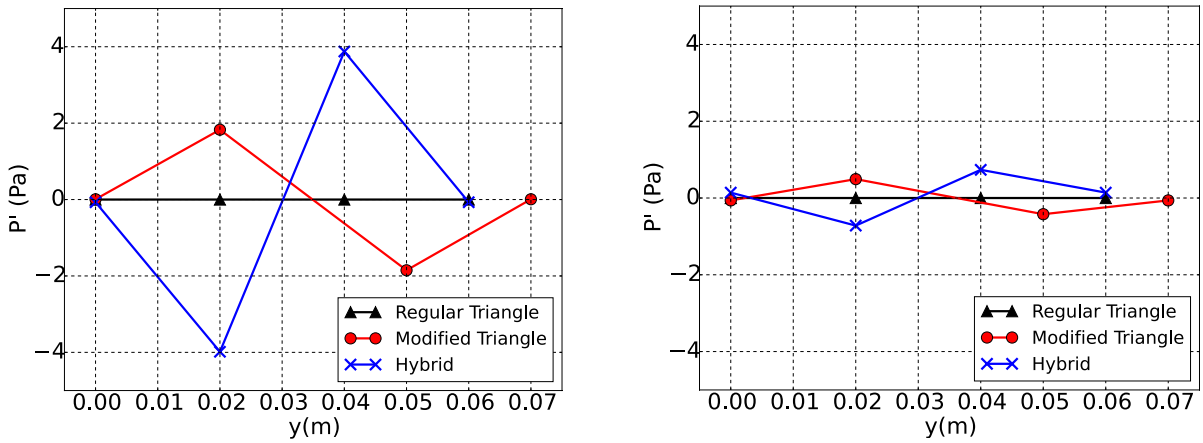

(a) LW (b) TTG

Figure 7.19: Pressure fluctuation profile in y direction at $x = 0.5$ where symbols and their corresponding meshes are: ($\triangle$) Fig. 7.17a; ($\circ$) Fig. 7.17b ; ($\times$) Fig. 7.17c.

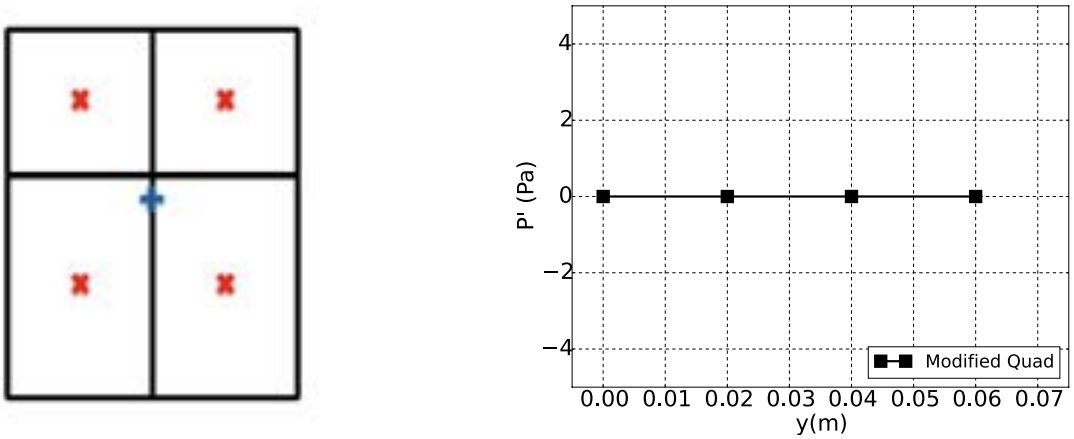

(a) Deformed quadrilateral mesh. (b) Pressure fluctuation profile in y direction at $x = 0.5$.

Figure 7.20: Test performed on alternative mesh where mesh is not stretched in the convection direction.

7.3.2 Perspectives

The implementation of a high-order gradient reconstruction in unstructured meshes such that it remains HPC efficient is not a trivial task. Various methods are available today in a finite volume context such as the MOOD approach [51] or the k-exact formulation [12]. These approaches have been shown to be parallelizable although the gain with respect to other methods such as spectral approaches [185] is still imperfectly addressed in the literature and so remains an issue of controversy. What is clear is that an additional step must be added to account for this grid issue. Various cases are possible:

- Interior nodes

  Currently there are many grid refinement softwares available that require a criteria for mesh adaptation. If the criterion was to minimize the distance between the CMDC and the node positions it would be possible to avoid the gradient calculation for these cells.

- Boundary nodes

  No option but to apply a correction. In no case does the CMDC coincide with the boundary node. Even when applying Dirichlet boundary conditions they are generally applied to velocity fields, i.e.: no-slip walls, but does not impose a condition on density for example. The value estimated by the scheme is thus imposed on the boundary node and corresponds to a value that the conservative variable should take at the centroid of the dual cell.

7.4 Conclusions

Schemes in this part of the thesis have been studied through various types of analyses. The most general one, the von Neumann analysis, predicts a perfect stability and mainly provides information related to the maximum CFL permissible for a simulation not to crash. This is insufficient as no information is given related to boundaries nor their implementation. Tests using the amplification matrix method allow to quantify both of these issues, the influence of such a BC and how it is implemented. Although tests performed are limited to the analysis of AVBP schemes it can be extended to any type of algorithm, a complete description being provided. Despite the effort in this direction, it remains incapable of predicting bounded oscillations that do not render a divergent solution. This is why instead of searching to predict possible instabilities, corrections to potentially problematic aspects of the scheme are sought.

Although nearly always tested on isotropic grids and using tools that do not take into account the influence of boundary conditions and closures, it has been shown that the influence of these two aspects cannot be neglected. The closure terms considered are just another block of a mathematical problem and as such it must be treated. The difficulty of finding numerical conditions for terms that physically have no sense does not exempt from finding a mathematically complying condition. Thus, the two approaches used until now present problems that arise as soon as the test cases are slightly changed. The new temporal formulation presented is not perfect either. The hyperbolicity of the equations allows to describe them either in time or in space but to render the scheme consistent, this approach should be done in space as this

relation only holds when time and space steps tend to zero. This means that errors will grow when the steps are larger, introducing a limitation to the formulation.

The spatial reconstruction of the necessary residual was however unfeasible during this work. Section 7.3 explained at least partially the reasons why problems appeared. The cell-vertex formulation requires a correction to account for the shift between the centroid of a dual cell and the node the residual is redistributed to. If this is not the case, even for very simple test cases as shown in Sec 7.3.1, fields such as pressure or density will suffer from oscillations that are undoubtedly of numerical origin. The interpolation required to correct this represents a complication because it is sensitive to the order of the scheme to be coupled with. Literature does show examples of how to calculate the nodal gradients that are inaccurate in the current implementation. Although costly, they are inevitable if upwinding is to be avoided.

In Part II we have seen the complex simulations done for a HPT linear cascade, the LS89 vane [7]. The experiments provide a large database from which a selection of points are chosen due to their resemblance to realistic operating points in aeroengines. Results in the previous chapters were seen to be highly dependent on all the parameters discussed in Part I: BCs, turbulence models and meshes. Different boundary conditions were tested in Chap. 6 in terms of turbulence injected (intensity level, length scale and spectrum) and conclusions are that only the variation of the intensity level is capable of providing a better agreement to experiments. Mesh refinement does however improve the matching between curves, the effect of turbulence being different depending on the profile region around the blade.

The different numerical signatures encountered during the simulations of this configuration led to a more comprehensive analysis of the already presented schemes in Part I. Although a conclusive solution has not been found to all the problems, the development of a tool capable of predicting the stability of a scheme in a certain configuration is useful for the development of new methods and potential closure solutions. Additional boundary conditions and their implementation may also be studied. The reasons for which current closures in the solver can be improved are shown and a solution is proposed although its applicability is clearly limited. The correct way to approach the issues is to work on the residual interpolations that arise from the cell-vertex algorithm.

General Conclusions and Perspectives

The industrial interest in gas turbines has increased over the past decades. The arrival of new technologies such as electrical or hybrid vehicles are certainly the present of the automotive industry but not yet for the aeronautical industry. The development of this type of technology continues and the current trend is to improve the global behaviour through the use of numerical methods. The objective is to one day be able to couple the different components of the gas turbine by performing massive numerical simulations and obtain the global efficiency of the engine. This objective remains feasible but for the moment unattainable, so each component is studied either separately, or at the very most, coupling is done between two modules of the engine, i.e. combustion chamber-turbine [189]. New approaches completely independent of CFD simulations (such as Deep Learning) appear as an option in the not so distant future. However, these remain to be explored and for the moment the only viable path for the continuous improvement of aeroengines is CFD.

However, these complex studies are still limited and make use of models to be able to afford the simulations. The study here done is specifically related to high-pressure turbines which are still today not perfectly mastered. The correct prediction of such complex configurations requires first a high-fidelity formalism such as LES to grasp the unsteady aspects of the flow. This is not sufficient as it must also be done in a very refined and thus costly simulation nearing DNS in some cases. Two steps are required to perform a quality simulation; first to analyze in detail the solver used, its schemes and its properties in various situations (different size cells, variety of geometries...). Secondly, it must be applied to a test case where complex physics are known to exist. Although problems may be identified in simpler cases, it can be possible that these do not appear until non-linear effects take place: i.e. turbulent structures. The document was divided into two parts:

In Part I the solver used to simulate such a configuration and its specificities is introduced. The numerical developments required for LES and in particular the AVBP schemes are developed including the temporal and spatial discretizations necessary for the resolution of all schemes. Models used for free-stream turbulence modelling are summarized and the limitations for the wall-bounded applications are shown. This leads to the classification of wall-modelled and wall-resolved simulations that represent the hardest barrier for non-reactive simulations today.

In Part II, the simulation of the high-pressure turbine blade LS89 developed by the VKI is performed. The impossibility to obtain the correct heat transfer curves and match the experiments led to the development of new strategies such as modifying the physical boundary

conditions proposed or inferred from experiments and literature. The different boundary conditions are seen to be dominant for the global behaviour so a sensitivity analysis was put in place. The different tests are summarized:

- The turbulent injection level at the inlet patch was the first test performed. Higher turbulent intensity levels could effectively be responsible for the mismatch between profiles of heat flux coefficient. When injecting a level equal to three times the experimental value the resulting heat flux coefficient value is indeed much nearer to the measured one. Differences between the "standard" simulation which injects the experimental values and the modified ones show there are regions of turbulent spots in the latter not present in the low-level turbulence intensity simulation. This effect highlights the importance of turbulence and more importantly, transition on blades.

- Other aspects such as the turbulence spectrum injected did not seem to be as effective as increasing the turbulent intensity. The synthetic turbulence has enough spatial distance to develop a physical spectrum comparable to that provided by a real simulation so no large discrepancies are seen between synthetic and precursor type simulations. Certainly the evolution of the turbulence from the inlet is notably different but no great differences are observed between the outputs of both simulations either for the higher or lower values of turbulence intensity.

- A question concerning the exact value of the integral length scale has existed since the experiments were performed. This value was reported recently for the first time doing new experiments and the agreement with respect to experimental data has not improved when imposing the integral length scale value at the inlet.

The predictions are however in agreement when increasing the mesh resolution in regions identified as important, notably the boundary layer. Transition on the suction side of the blade influences the heat transfer levels and is examined to determine its behaviour. Another aspect that could affect the transition of this boundary layer is a numerical one. Different schemes are seen to provide different results and numerical noise can not be neglected.

The natural consequence is to perform a detailed analysis of the schemes used in the AVBP code and study its interactions with boundary conditions. Stability analyses of larger mathematical difficulty than standard von Neumann tests are done to identify the possible differences between schemes. Various mathematical closures were tested and implemented. Results were shown to be inconclusive in terms of oscillation determination. This led to the study of the metrics and the implications it has for a cell-vertex code.

Several improvements can be envisaged as a result of this dissertation:

- The need for wall-resolved simulations is today necessary due to the inefficient wall models that currently exist for geometries with high curvature and high pressure gradients. The inability to correctly capture the transition position and its impact on the aerodynamic losses does not leave another alternative but to resolve the finer structures. Wall-resolved simulations are not a realistic approach for industrial partners today so better and more robust methods must be found if accurate simulations are to be expected in the short term.

- It is necessary to confirm the results here obtained, either by other groups or using a different solver to conclude that experimental results may indeed be matched if a high-fidelity simulation is performed using a sufficiently refined mesh. Experimental results have long been targeted as being a source of uncertainty that could lead numerical solvers to the incorrect conclusions. Indeed, the boundary layer flow seems to be on the thin edge of the wedge in terms of stability and effects such as the feeble numerical noise observed can contribute to transition.

- The line between the two flows seems to be very fine so features such as wall roughness or geometrical curvature could be targeted. If accurate models were found, it would be interesting to perform a UQ analysis such as the one done in Roy et al. [153]. Determining the influence of the curvature along the blade profile (identified by various groups during the course of this thesis) or the effect of introducing a small perturbation term representative of physical roughness could point to the causes of the turbulent flow appearance.

- Numerical methods are in continuous development but classical methods are still largely used today as evidenced in this document. The improvement of these schemes is necessary and evidenced difficulties must be corrected when identified as they constitute a basis of extensive literature and knowledge. How long classical schemes will be used for is today unknown. New approaches such as Lattice-Boltzmann or Spectral methods seem to provide new paths that seem promising. However, even if classical schemes are no longer used in a HPC context they may at least help to validate new faster algorithms that help to take CFD one step further.

Appendices

Appendix A

General equations

The equations to be solved, written in a conservative form, are

$$\frac{\partial \mathbf{U}}{\partial t} + \vec{\nabla} \cdot \vec{\mathcal{F}} = S, \tag{A.1}$$

where $\mathbf{U}$ corresponds to the vector containing the conservative variables of the solution; $\mathcal{F}$ represents the fluxes and S represents the possible source terms. Such source terms will no longer be considered in this section to simplify the notation.

The conservative variables used are,

$$\mathbf{U} = \left(\rho, \rho u_i \left[i = 1...3\right], \rho E\right). \tag{A.2}$$

each variable corresponding to density, the vector of momentum of size equal to the number of dimensions and total energy.

Fluxes may be separated into two groups, convective and diffusive. This can be justified based on a physical ground but also mathematically. From a mathematical point of view, inviscid fluxes will depend exclusively on the solution $\mathbf{U}$ while the viscous fluxes will also have a dependency on the gradients of $\mathbf{U}$. From a physical point of view, while the convective fluxes can be considered as the directional passive transport of a conserved variable, diffusive fluxes represent a smoothing of the field, a process that is also non-directional. One may note that the non-linearity previously introduced is present in the convective flux. There is no unique way to express the convective fluxes and different formulations led to different truncation and aliasing errors as shown in Kravchenko and Moin [97] in the specific context of LES for example. This is due once again to the non-linear terms and the effects the filter operator has on each set of variables. This non-linearity is not only a problem to model but will also be responsible for possible discontinuities or bifurcations that might appear in the flow (not solely responsible for the known turbulence). The formulation used in **AVBP** is as in Poinsot and Veynante [139] and groups all terms in a divergence form. The inviscid fluxes for this solver are hence, in three-dimensions,

$$\vec{\mathcal{F}} = \begin{pmatrix} \rho u & \rho v & \rho w \\ \rho u^2 + P & \rho uv & \rho uw \\ \rho uv & \rho v^2 + P & \rho vw \\ \rho uw & \rho vw & \rho w^2 + P \\ \rho uH & \rho vH & \rho wH \end{pmatrix} \tag{A.3}$$

where H represents the total specific enthalpy, $H = E + \frac{P}{\rho}$ and for which the perfect gas law is assumed as:

$$P = \rho r T. \tag{A.4}$$

This equation of state is true if one species is used. In the case of a multi-species mixture, it is necessary to take into account each contribution separately. The gas constant will vary then for each species to yield for a mixture

$$r = \frac{R}{W} = \sum_{i=1}^{N} \frac{Y_i R}{W_i} \tag{A.5}$$

where $R = 8.314\ J/mol\ K$ is the universal gas constant, Y_i is the species mass fraction of the mixture and W represents the mean molar mass of the mixture or species, W_i. In this case, the equation of continuity reads,

$$\frac{\partial \rho}{\partial t} + \frac{\partial}{\partial x_j}\left(\rho u_j\right) = 0. \tag{A.6}$$

and additional equations appear for each new species. Of course, it is possible to relate the partial densities to the total density using $\rho_i = \rho Y_i$. One clearly notes that these evolution equations are Euler like equations and represent the hyperbolic part of the problem.

The diffusive part of the NS equations for a unique species is represented by,

$$\vec{\mathcal{F}}_v = \begin{pmatrix} 0 & 0 & 0 \\ \tau_{11} & \tau_{21} & \tau_{31} \\ \tau_{12} & \tau_{22} & \tau_{32} \\ \tau_{13} & \tau_{23} & \tau_{33} \\ u\tau_{11} + v\tau_{12} + w\tau_{13} + \lambda\frac{\partial T}{\partial x} & u\tau_{21} + v\tau_{22} + w\tau_{23} + \lambda\frac{\partial T}{\partial y} & u\tau_{31} + v\tau_{32} + w\tau_{33} + \lambda\frac{\partial T}{\partial z} \end{pmatrix} \tag{A.7}$$

where τ_{ij} are the shear stress components. These can be expressed as,

$$\tau_{ij} = 2\mu\left(S_{ij} - \frac{1}{3}\delta_{ij}S_{kk}\right) \tag{A.8}$$

with $S_{ij} = \frac{1}{2}\left(\frac{\partial u_j}{\partial x_i} + \frac{\partial u_i}{\partial x_j}\right)$. The heat flux term is usually modelled using $-\lambda\frac{\partial T}{\partial x_i}$ where λ is the thermal conductivity defined as $\lambda = \frac{\mu c_p}{Pr}$. In the above viscous terms, μ represents the dynamic viscosity of the fluid, c_p is the heat capacity of the fluid and Pr is the Prandtl number. This Prandtl number is taken constant.

Note that in the case of a multi-species simulation, an additional term appears in the continuity equation which represents the diffusion of species within a mixture, $J_{i,k} = -\rho\left(D_k\frac{W_k}{W}\frac{\partial X_k}{\partial x_i} - Y_k V_i^c\right)$ with X_k representing the molar fraction of species, D_k the diffusion coefficient and V_i^c is a velocity correction to guarantee mass conservation. This diffusion of species does not only affect the continuity equation but also the energy equation as the heat flux is affected by this diffusion process. The modified flux is hence written as,

$$q_i = -\lambda\frac{\partial T}{\partial x_i} - \rho\sum_{k=1}^{N} J_{i,k}h_{s,k}, \tag{A.9}$$

where $h_{s,k}$ is the sensible enthalpy of each species.

A.1 LES governing equations

LES is based on filtered equations, the type of filtering being usually of Favre type [156] introduced on the basis of the following expression,

$$\overline{\rho}\tilde{f}(x) = \int_{-\infty}^{\infty}\rho f(x')\,\mathcal{G}(x-x')\,dx'. \tag{A.10}$$

Note that there is no temporal dependency, the filter being applied in the physical or spectral space the latter being the one retained throughout this document and with AVBP. Note that by construction it is also recommended that the filter function satisfies the condition,

$$\int_{-\infty}^{\infty} G(x)dx = 1. \tag{A.11}$$

This filter acts on the highest wave numbers after a cutoff filter denoted hereafter by Δ. Defining $\overline{f}$ as the resolved field in a numerical simulation (not to be confused with a temporal average), the unresolved part of the physics that is not captured because of the filter, is represented by $f' = f - \overline{f}$ and usually appears through the so-called sub-grid scale terms. The filtered NS equations read,

$$\frac{\partial\overline{\rho}\,\widetilde{u_i}}{\partial t} + \frac{\partial}{\partial x_j}(\overline{\rho}\,\widetilde{u_i}\,\widetilde{u_j}) = -\frac{\partial}{\partial x_j}[\overline{P}\,\delta_{ij} - \overline{\tau_{ij}} - \overline{\tau_{ij}}^t], \tag{A.12}$$

$$\frac{\partial\overline{\rho}\,\widetilde{E}}{\partial t} + \frac{\partial}{\partial x_j}(\overline{\rho}\,\widetilde{E}\,\widetilde{u_j}) = -\frac{\partial}{\partial x_j}[\overline{u_i\,(P\,\delta_{ij} - \tau_{ij})} + \overline{q_j} + \overline{q_j}^t], \tag{A.13}$$

$$\frac{\partial \overline{\rho}\,\widetilde{Y_k}}{\partial t} + \frac{\partial}{\partial x_j}(\overline{\rho}\,\widetilde{Y_k}\,\widetilde{u_j}) = -\frac{\partial}{\partial x_j}[\overline{J_{j,k}} + \overline{J_{j,k}}^t], \tag{A.14}$$

where no summation is indicated for index k (it represents each species present and will add an equation for each additional species used). In the above new system of equations, one recognizes the following,

Inviscid terms:
The three spatial components of the inviscid flux tensor are identical to DNS but now based on the filtered quantities:

$$\begin{pmatrix} \overline{\rho}\widetilde{u_i}\,\widetilde{u_j} + \overline{P}\,\delta_{ij} \\ \overline{\rho}\widetilde{E}\widetilde{u_j} + \overline{P\,u_j}\delta_{ij} \\ \overline{\rho_k}\widetilde{u_j} \end{pmatrix} \tag{A.15}$$

Viscous terms:
The components of the viscous flux tensor take the form:

$$\begin{pmatrix} -\overline{\tau_{ij}} \\ -(\overline{u_i\,\tau_{ij}}) + \overline{q_j} \\ \overline{J_{j,k}} \end{pmatrix} \tag{A.16}$$

where the different terms are:

- the laminar filtered stress tensor $\overline{\tau_{ij}}$, given by the following relations:

$$\begin{aligned} \overline{\tau_{ij}} &= \overline{2\mu(S_{ij} - \tfrac{1}{3}\delta_{ij}S_{ll})}, \\ &\approx 2\overline{\mu}(\widetilde{S}_{ij} - \tfrac{1}{3}\delta_{ij}\widetilde{S}_{ll}), \end{aligned} \tag{A.17}$$

  and the filtered shear stress

$$\widetilde{S}_{ij} = \frac{1}{2}(\frac{\partial \widetilde{u_j}}{\partial x_i} + \frac{\partial \widetilde{u_i}}{\partial x_j}). \tag{A.18}$$

  This term can be explicited for each component,

$$\begin{array}{ll} \overline{\tau_{xx}} \approx \frac{2\overline{\mu}}{3}(2\frac{\partial \widetilde{u}}{\partial x} - \frac{\partial \widetilde{v}}{\partial y} - \frac{\partial \widetilde{w}}{\partial z}), & \overline{\tau_{xy}} \approx \overline{\mu}(\frac{\partial \widetilde{u}}{\partial y} + \frac{\partial \widetilde{v}}{\partial x}) \\ \overline{\tau_{yy}} \approx \frac{2\overline{\mu}}{3}(2\frac{\partial \widetilde{v}}{\partial y} - \frac{\partial \widetilde{u}}{\partial x} - \frac{\partial \widetilde{w}}{\partial z}), & \overline{\tau_{xz}} \approx \overline{\mu}(\frac{\partial \widetilde{u}}{\partial z} + \frac{\partial \widetilde{w}}{\partial x}) \\ \overline{\tau_{zz}} \approx \frac{2\overline{\mu}}{3}(2\frac{\partial \widetilde{w}}{\partial z} - \frac{\partial \widetilde{u}}{\partial x} - \frac{\partial \widetilde{v}}{\partial y}), & \overline{\tau_{yz}} \approx \overline{\mu}(\frac{\partial \widetilde{v}}{\partial z} + \frac{\partial \widetilde{w}}{\partial y}). \end{array} \tag{A.19}$$

- for a multispecies case, the diffusive species flux vector for a non-reacting flow,

$$\begin{aligned} \overline{J_{i,k}} &= -\overline{\rho\left(D_k\frac{W_k}{W}\frac{\partial X_k}{\partial x_i} - Y_k V_i^c\right)} \\ &\approx -\overline{\rho}\left(\overline{D}_k\frac{W_k}{W}\frac{\partial \widetilde{X}_k}{\partial x_i} - \widetilde{Y}_k\widetilde{V}_i^c\right). \end{aligned} \tag{A.20}$$

- the filtered heat flux is,

$$\begin{aligned} \overline{q_i} &= -\overline{\lambda \frac{\partial T}{\partial x_i}} + \sum_{k=1}^{N} \overline{J_{i,k} h_{s,k}} \\ &\approx -\overline{\lambda} \frac{\partial \widetilde{T}}{\partial x_i} + \sum_{k=1}^{N} \overline{J_{i,k}}\, \widetilde{h}_{s,k}. \end{aligned} \tag{A.21}$$

Additional terms appear compared to the original Navier-Stokes equations. These are known as the sub-grid scale components and are detailed in the following.

- Unresolved or sub-grid scale Reynolds stresses: $\overline{\tau_{ij}}^t$
  Reynolds stresses are responsible for many of the properties of a turbulent flow, so capturing their effects is critical. These non-resolved stresses are the result of $\widetilde{u_i u_j} - \widetilde{u}_i \widetilde{u}_j$. These terms have focused the attention of most models, notably those based on an eddy-viscosity model presented in Section B.

- Pressure-velocity term $\frac{\partial}{\partial x_j}\left(\overline{u_i P \delta_{ij}}\right)$
  Responsible for the exchange of momentum between the different velocity components of the momentum vector [140], it is important not to neglect them as it changes the nature of the turbulence. The term is commonly simplified by $\tilde{u}_i \frac{\partial \overline{P}}{\partial x_j}$.

- Unresolved species and enthalpy fluxes
  Similar to the Reynolds stresses, they are unresolved transport terms that are taken into account by the turbulence models presented in the following section.

Appendix B

Sub-grid scale models

The closure terms are a difficulty to be dealt with specifically in LES and RANS. Although equally or even more important for RANS, these models are not detailed and only LES sub-grid scale models are dealt with from here on. There are many sub-grid scale (SGS) models available in the literature for LES most of them being based on the modelling of the Reynolds stress tensor by means of the Boussinesq approximation. The approach used will however affect the physics and a choice must be made. Some desirable properties for such a model are summarized in the following,

- Allow backscatter phenomena
- Should have some local adaptation dependent on the problem

The backscatter phenomena is a process by which small scales in a turbulent flow provide energy to the larger ones. This first affirmation being true, it seems reasonable to allow this physical process and represents the idea behind Germano [68]. This effect is however much more problematic for the Boussinesq assumption based models. In practice, the latter introduces a non-linear viscosity term in front of the laminar viscosity which acts as an additional diffusion term. If the backscatter process was allowed it would mean that the viscosity had taken a negative value, and thus, the term would numerically represent an anti-diffusion term that could affect the stability of the simulation. Also, it can be justified on physical ground, the main argument being that it has to account for the missing energy transfers and these are mainly from large to small scales, the contrary being a second-order effect. This justifies the existence of less physical models such as those proposed by Nicoud et al. [133] who defined a set of additional desirable properties in the context of Boussinesq based models and are summarized in,

- *P0 property.* The value of the turbulent viscosity must not be allowed to take negative values. As explained, for numerical robustness this value is always taken to be positive and is thus a purely diffusive operator.
- *P1 property.* Requires to have a cubic asymptotic behaviour near walls, meaning that this turbulent viscosity must vanish at walls. Due to the physical constraints imposed by walls, such as the no-slip and impermeability conditions, this relation must be of the form $\mathcal{O}(y^3)$ where y represents the normal distance to the wall as done in Chapman and Kuhn [30]. This is especially important when performing wall-resolved LES.

- *P2 property.* The turbulent viscosity value will be zero when the flow is 2D. Indeed, in cases where the flow is 2D like, the evolution of the fluctuating turbulent activity will induce 3D components. It is necessary to deactivate the model in such situations such as pure shear or rotation.
- *P3 property.* The turbulent viscosity must not be active in isotropic or axisymmetric cases. Similarly to the previous *P2* property, these are not associated to phenomena of turbulent nature and as such, must not activate the sub-grid scale models.

In Eq. (B.1) $\overline{\tau_{ij}}^t$ is the SGS tensor to be modelled, ν_t is the SGS turbulent viscosity, $\widetilde{u}_i$ is the Favre filtered velocity vector (compressible flows) and $\widetilde{S}_{ij}$ is the resolved strain rate tensor which must be based on the local resolved velocity fields.

$$\begin{aligned} \overline{\tau_{ij}}^t &= -\overline{\rho}\,(\widetilde{u_i u_j} - \widetilde{u}_i \widetilde{u}_j) \\ &= 2\,\overline{\rho}\,\nu_t\,\widetilde{S}_{ij} - \frac{1}{3}\,\overline{\tau_{ll}}^t\,\delta_{ij}. \end{aligned} \tag{B.1}$$

B.1 Sub-grid models available in AVBP

The models in AVBP only differ through the value of ν_t and the expressions for the most commonly used are given below. A thorough comparison between the different models applied to a high-pressure turbine case can be found in Papadogiannis et al. [137].

B.2 Smagorinsky model

The Smagorinsky model [167] was the first to be developed and is currently still used after undergoing certain modifications [109]. The definition of ν_t is,

$$\nu_t = (C_S \Delta)^2 \sqrt{2\,\widetilde{S}_{ij}\,\widetilde{S}_{ij}}, \tag{B.2}$$

where Δ denotes the filter characteristic length and C_S is the model constant set to 0.18 but can vary between 0.1 and 0.18 depending on the flow configuration. This indicates that there is no flow independent manner of closing the unknown terms and thus, the turbulent viscosity may be added where it is not necessary. Although it is correct for homogeneous isotropic turbulent flows, this is not true in wall-bounded flows as it has a bad scaling in the presence of strong shear. It is known to be too dissipative and its application must be limited [156].

B.3 WALE model

In a wall-resolved context, LES requires to have the adequate scaling when approaching a solid boundary, refer to *Property 1.* The first model presented was the Van Driest damping function [56]. Since then the WALE (Wall-Adapting Local Eddy-viscosity) proposed by Nicoud and

Ducros and Ducros et al. [132, 59] has become more popular. Differently to the Smagorinsky model, the characteristic filtered rate of strain is replaced by a term that detects strong rates of deformation and/or rotation and not shear. Its expression hence reads,

$$s_{ij}^d = \frac{1}{2}\left(\widetilde{g}_{ij}^2 + \widetilde{g}_{ji}^2\right) - \frac{1}{3}\,\widetilde{g}_{kk}^2\,\delta_{ij}, \tag{B.3}$$

$$\nu_t = (C_w\Delta)^2 \frac{(s_{ij}^d s_{ij}^d)^{3/2}}{(\widetilde{S}_{ij}\widetilde{S}_{ij})^{5/2} + (s_{ij}^d s_{ij}^d)^{5/4}}, \tag{B.4}$$

where Δ denotes the filter characteristic length (cubic-root of the cell volume), $C_w = 0.4929$ is the model constant and $\widetilde{g}_{ij}$ denotes the resolved velocity gradient. This expression for ν_t allows for the right scaling of turbulent viscosity when approaching walls: i.e. $\nu_t\ \alpha\,(y^+)^3$ thus complying with both properties **P0** and **P1**.

B.4 Sigma model

Developed also by Nicoud et al. [133], the principle is very similar to that of the WALE model. Instead of using the strain rate tensor, it is based on the singular values of the velocity gradient tensor where,

$$\nu_t = (C_\sigma\Delta)^2 D_\sigma \tag{B.5}$$

where C_σ is a constant equal to 1.5 and

$$D_\sigma = \frac{\sigma_3\,(\sigma_1 - \sigma_2)\,(\sigma_2 - \sigma_3)}{\sigma_1^2}. \tag{B.6}$$

The main advantages of the sigma model in relation to WALE are that no viscosity is applied in pure shear nor for axisymmetric flows, additionally having all the desirable properties defined in the same article. It finally follows the $(y^+)^3$ law when approaching a wall.

It must be noted that although no proof is shown, various sub-grid scale models were tested during this thesis. No large differences were found between the Sigma and the WALE model for the coarsest mesh case. Smagorinsky results were too dissipative as expected.

Appendix C

Precursor methodology

An approach that uses an external simulation to provide information to boundary conditions is not new [50]. As cited in the same publication, turbulence injection requirements are difficult to fulfill in whole. The main features can be summarized in the following points:

- Two-point correlations and spectrum in agreement with physical problem
  Agreement is good when comparing these parameters to known curves such as the Kolmogorov spectrum [80]. More details and comparisons are provided in later sections Sec. C.2.
- No modification required away from the inlet
  Turbulence perturbations are added only through the inlet patch. No modification is required elsewhere.
- No spurious modes introduced through the inlet
  The turbulent fluctuations are introduced through the characteristic conditions, [138]. This approach requires to establish the relax parameters appropriately for the turbulence to be imposed at the inlet but low enough for possible acoustic waves reaching the inlet to leave and not affect the field to be imposed. The implementation done shows that no noise is introduced.
- Instantaneous solutions must be available to reduce the storage
  The coupling is performed on the fly at each iteration. The storage issue is overcome, introducing in contrast the extra cost of an additional simulation running in parallel. Additionally, the interpolation and information exchange between fields must be taken into account.
- No restriction to the type of discretization nor the grid type
  In this particular case, different types of discretizations have been studied, in a purely finite volume context but also using a FE element scheme. In both cases the results obtained were coherent with the initial data and turbulence description only depended on the properties of the schemes. Concerning the type of grid, no constraints have been found as there is an interpolation step between grids, which implies that non-conformal grids are also subjected to this coupling. Of course, the grid size in the main domain will filter any turbulent scales that may be generated in a finer mesh precursor simulation.
- Implementation effort

The difficulty of this methodology, as in most methods, resides in prescribing the correct turbulence parameters in the precursor simulation. The present implementation is performed only for HIT, but may be extended to more complex turbulent fields. The geometrical features of the inlet patch through which turbulence is to be injected however, do represent a constraint towards the general applicability of the method.

- Highly parallelizable
  Tests performed show the interpolation and exchange processes do not compromise the global efficiency of the code. The additional simulation required to generate the turbulence does add a cost that depends on the ratio of degrees of freedom between both simulations.

Periodicity in all directions simplifies the injection as a HIT field can be imposed without the need for cross-correlations as in wall-bounded flows [113].

C.1 Methodology for precursor simulation

The turbulent field to be injected into the main domain is a HIT field, due to the fact that the experimental is of grid-turbulence type. Computationally, it means that it is necessary to keep the turbulent production in the precursor at the desired level. To do so, the methodology described in Paoli and Shariff [136] is adopted. It is based on a stochastically forced source term applied to the momentum and energy equations, corrected to keep the total energy constant. The original idea was proposed in Eswaran and Pope [63].

Note that the precursor simulation is run simultaneously to the main simulation, which adds computational cost due to the exchange time required but reduces the amount of memory necessary for the storage. In terms of boundary conditions specification, the coupling software OpenPALM [58], is used to send the local velocity perturbation field from the precursor simulation to the inflow domain. Note that this operation is done at each time-step and does not require a coincident mesh. The field extracted from the precursor is interpolated onto the inlet and will serve as the reference fluctuating field. The interpolation performed is of order three to comply with the order of the convective scheme.

Finally, it is of note to underline the fact that the precursor field is taken into account by the main domain simulation through characteristic conditions [138]. Indeed, directly superimposing the velocities would lead to the reflection of upstream moving waves which would pollute the inlet channel region. To account for the mean velocity, the Taylor hypothesis is used in this specific application in conjunction with the bulk velocity field of the main simulation [179]. Computationally, this implies that the plane from which the information is extracted in the precursor is not fixed, but moves in the axial direction at the mean bulk velocity of the flow as prescribed by the main domain. Note that such an hypothesis is here relevant since the inlet Mach number is low and fluctuations are of the order of 15% of the mean [106].

To analyze the statistics of the flow, the first points of interest is the evolution of the Turbulent Kinetic Energy (TKE) decay. From the theory of homogeneous isotropic turbulence it is possible to transform the temporal variable into spatial values using the Taylor hypothesis [179]. The general expression that allows to evaluate the TKE is,

$$TKE(x) = \frac{\overline{u'(x)u'(x)}}{2}, \tag{C.1}$$

where u' represents the velocity fluctuations with respect to the mean velocity.

It is important to also check the evolution of the characteristic scales of turbulence in the streamwise direction. These lengthscales can be related to experimental expressions derived in Batchelor and Townsend [15, 16]. It is well known that the evolution of the Taylor and the integral lengthscales is an increasing tendency as turbulence evolves in a free-stream flow. In Batchelor and Townsend [15], a first relation is provided for the growth of the Taylor microscale as,

$$U\frac{d\lambda^2}{dx} = \frac{10\nu}{n}, \tag{C.2}$$

where U represents the mean velocity, ν corresponds to the viscosity and n is a coefficient that was assumed to take a value of 1, a more detailed explanation is provided in the article [15]. However, this relation was not consistent with other contemporaneous data, which led to the study in [16]. New data determined that the slope should be modified according to the $Re_\lambda = \frac{u'\lambda}{\nu}$, where λ is the Taylor microscale, defined as $\lambda = \overline{u_1'^2}/\overline{u_{1,1}'^2}$, where u_1' is the axial velocity fluctuation and $u_{1,1}'$ the axial spatial derivative of the axial velocity fluctuation. Depending on the value of Re_λ, the period of decay is different and so, the tendency of λ. This is logical as Re_λ represents the importance of the inertial terms in the flow.

In Fig. C.1, the evolution of λ^2 is plotted as a function of x/M where M represents the characteristic length of the grid that generates the turbulence in the experiment. The natural question that arises is how to characterize the increase of λ. For inertial terms to be negligible, $R_\lambda << 15$ is commonly established and the decrease rate of R_λ as stated in Batchelor and Townsend [16] is very slow, this meaning that only for very long periods will the final decay period be seen.

An assumption also from [15], is that velocity derivative skewness is independent of the Reynolds number. This value is widely used as proof that a flow is turbulent. Studies such as Tavoularis et al. [178] show a great number of experiments and plot the skewness, changing its sign, as a function of Re_λ, Fig. C.2. For values where $5 < Re_\lambda < 1000$, the skewness value varies between -0.3 and -0.7, which justifies why this value is taken as constant for certain studies.

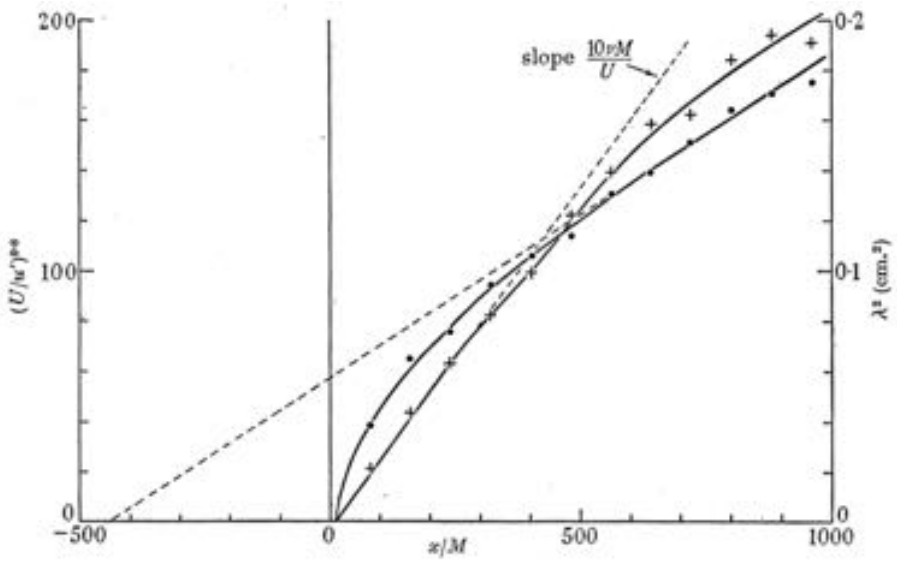

Figure C.1: Spatial evolution of Taylor microscale in experimental study [16]. Marker curves represent various experimental results at different turbulence intensity levels.

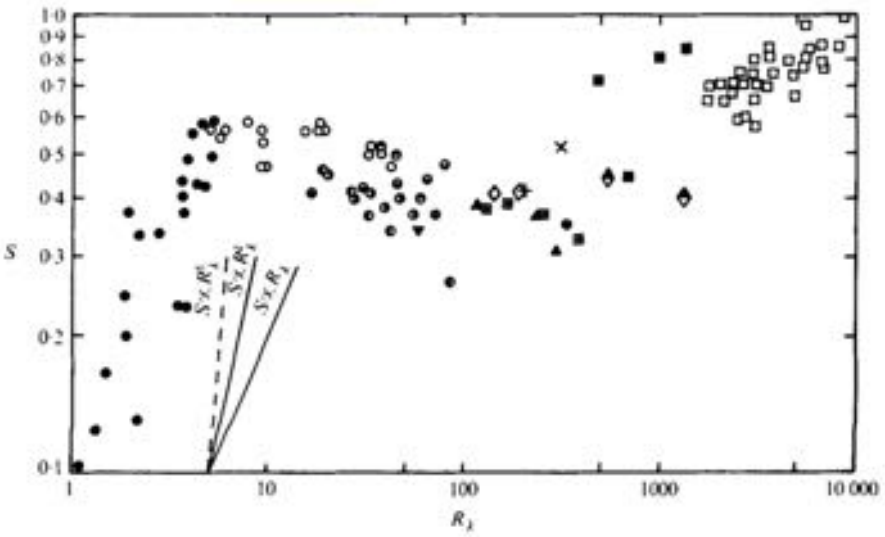

Figure C.2: Skewness of spatial velocity derivative measured experimentally [178].

C.2 Test case: Turbulent channel

This approach has been tested on a quasi DNS configuration. To check the quality of the turbulence injected, two injection type methods are compared in a $4 \times 1 \times 1$ mm channel represented in Fig. C.3. The inlet conditions will vary as shown in Table. C.1, where either the fields imposed correspond to the velocity and temperature, cases 1 and 3, or total pressure and total temperature. At the outlet, static pressure is imposed using characteristic conditions. In the pitchwise and spanwise direction periodicity is prescribed. In all cases, the boundary conditions are set to have a mean velocity field of 100 m/s, a fluctuating velocity of 5 % which corresponds to a Mach number of 0.28. The integral scale is set to 0.13 mm which represents approximately $\frac{L}{2\pi}$, where L is the characteristic length in the periodic directions. The precursor simulation is done on a domain of $3 \times 1 \times 1$ mm and periodicity conditions are imposed on all domain surfaces.

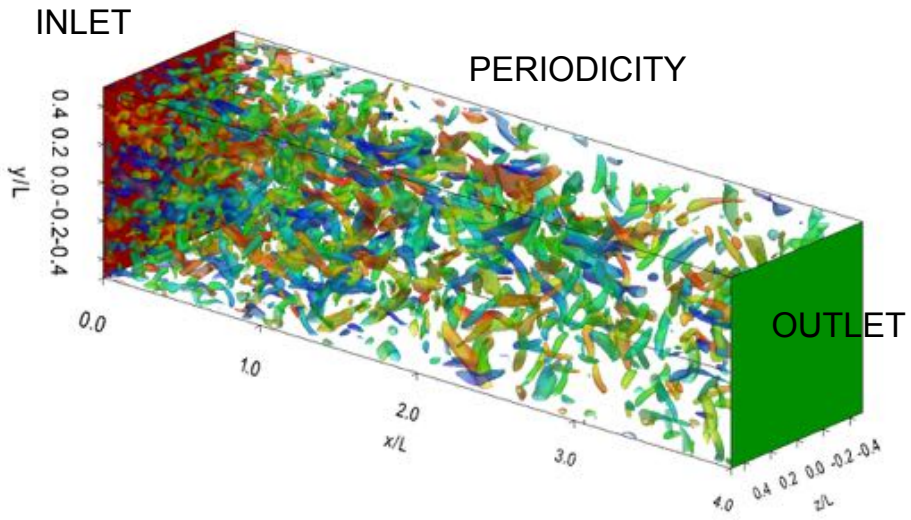

Figure C.3: Channel geometry and boundary conditions.

	Synthetic turbulence		Precursor	
Cases	Case 1	Case 2	Case 3	Case 4
Variables imposed	u,v,w,T	Pt,Tt	u,v,w,T	Pt,Tt

Table C.1: Variables imposed in each precursor simulation.

The different simulations lead in all cases to a fully developed turbulent field as seen in Fig. C.4. Of course the main interest in the use of the precursor is to avoid the region where the spectrum of turbulence does not follow any physical laws. This occurs for all type of synthetic type methods and represents a limitation in terms of domain size as it requires to have a minimum development distance.

The TKE decay is evaluated by the use of probes at different positions along the streamwise direction. In Fig. C.5a, synthetic and precursor methods are compared for **Case 3**. Evolution

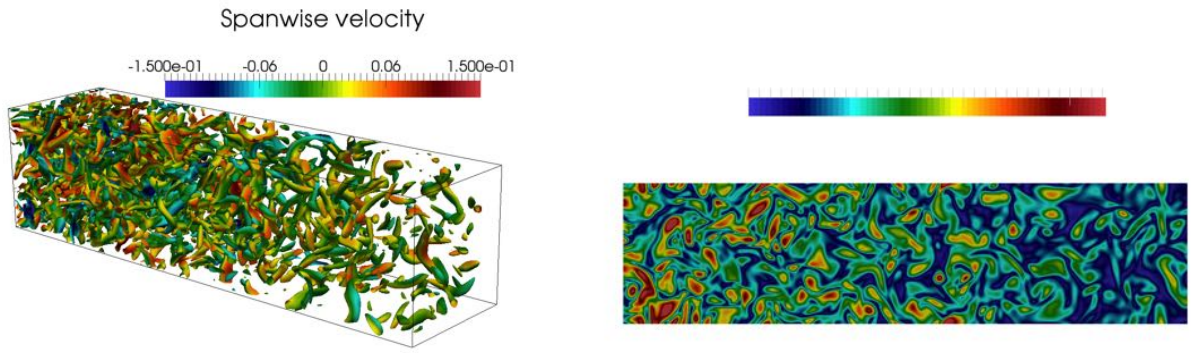

(a) (b)

Figure C.4: Channel test case. a) Q-criterion coloured by vorticity b) Vorticity field on a x-y plane.

of the decaying turbulence shows an excellent agreement with the theoretical approach, while the synthetic turbulence does not follow the exact trend. When comparing the same decay near the boundary conditions using the same characteristic conditions and relax parameters, Fig. C.5b shows the unphysical behaviour for the synthetic injection which is, of course, undesirable.

For this particular case, $R_\lambda \approx 20$, which implies that at least at first the non-linear inertial terms cannot be neglected and the initial decay region which follows the law in Eq. (C.2) should be expected. As seen in Fig. C.6, the precursor follows accurately the $\frac{10\nu x}{U}$ curve except at the limits of the domain where there is a slight shift due to the imposition of the boundary conditions. The initial value at the entrance of the domain can be estimated from the relation,

$$\lambda = l_t 10^{0.5} Re_t^{-0.5}, \tag{C.3}$$

where l_t represents the integral lengthscale and $Re_t = \frac{u' l_t}{\nu}$ is the turbulent Reynolds number. Substituting the values imposed in the simulation gives a value of $\lambda_{theory} = 7.110^{-5}$ m. Although the value in the simulation is of the same order as the estimate, differences may be explained by the low Re_λ which is not representative of fully-sustained turbulence.

As can be observed in Fig. C.7, the value of the velocity derivative skewness along the whole channel for the precursor is found to be between the range found experimentally. Additionally, for the precursor simulation, this value is reached at the inlet of the channel which is not the case for the synthetic turbulence method. This can also be shown when comparing the one-dimensional energy spectrum between both methodologies. While the Kraichnan methodology peaks at a low wavenumber where the energy while Fig. C.8 shows that for the precursor, the spectrum is spread along the whole wavenumber range. Likewise, correlations are also shown to prove the agreement with temporal simulations seen in Figs. C.9 & C.10.

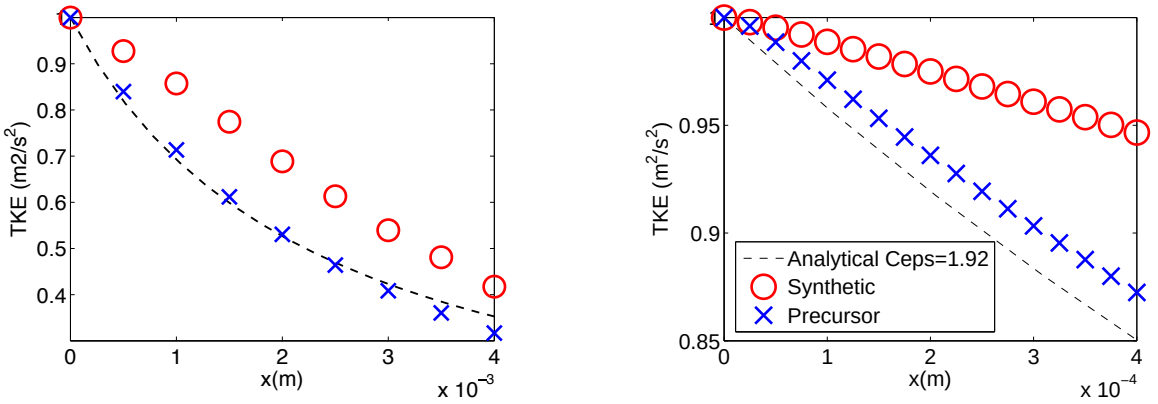

(a) (b)

Figure C.5: Spatial TKE decay comparison. a) TKE decay along axial direction b) View of the 10% inlet channel region.

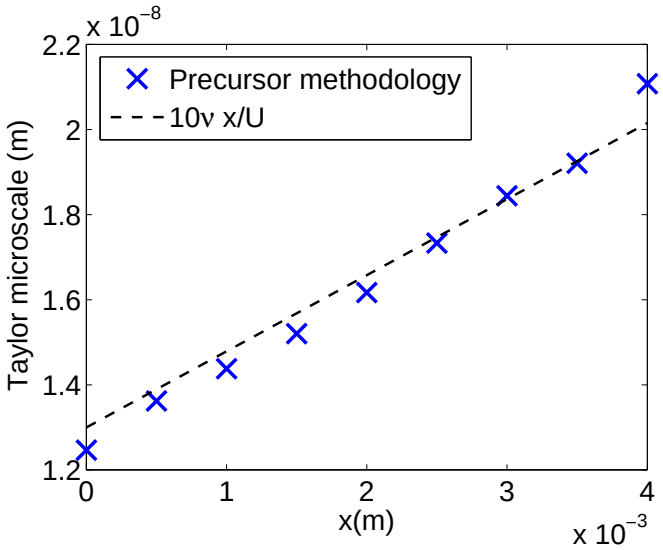

Figure C.6: Spatial evolution comparison of Taylor microscale with numerical simulation.

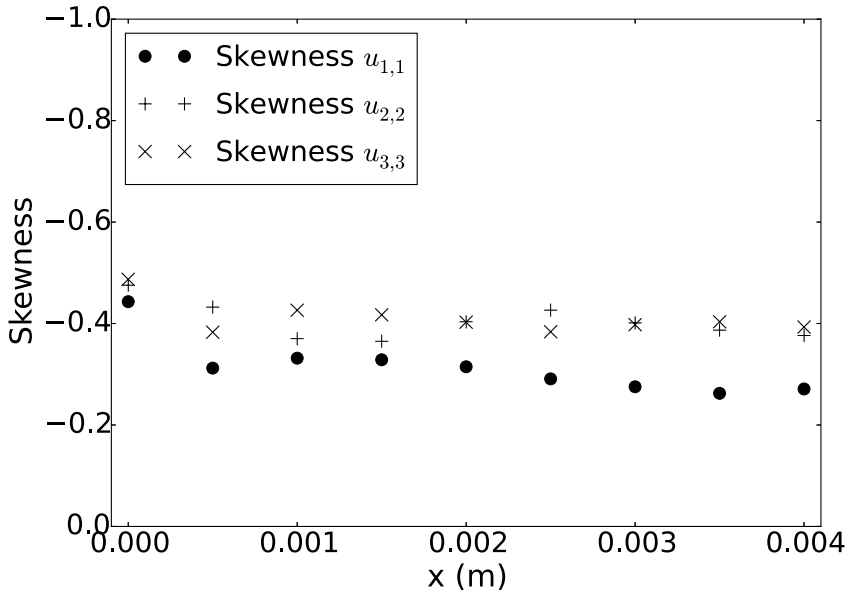

Figure C.7: Skewness of velocity gradient components in channel.

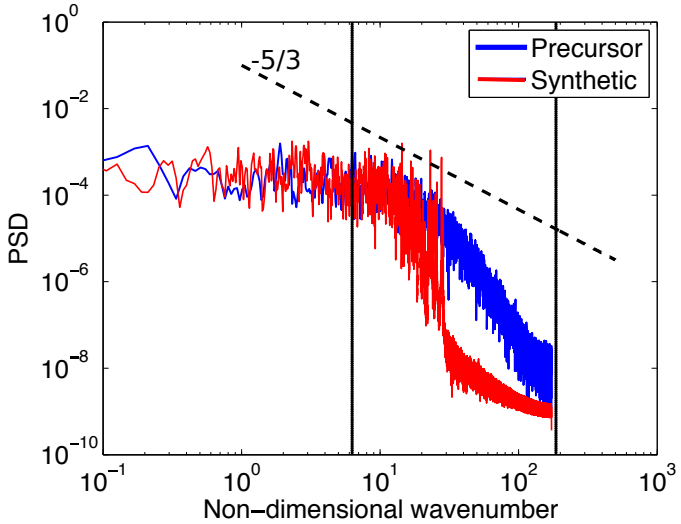

Figure C.8: Spectrum comparison at inlet plane.

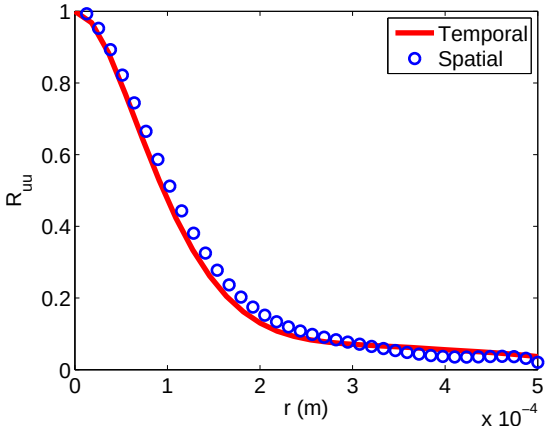

Figure C.9: R_{uu} **at inlet**

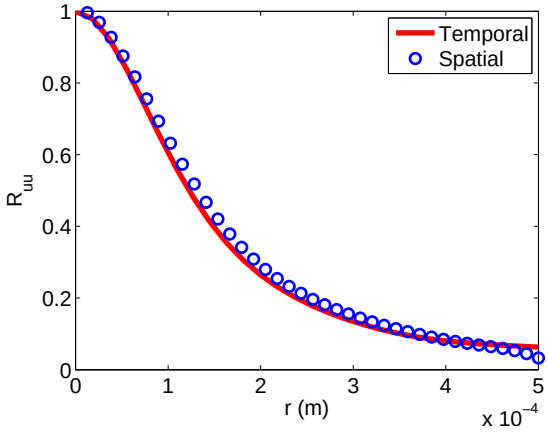

Figure C.10: R_{uu} **at outlet**

Appendix D

Convergence aspects

To ensure the simulation is sufficiently converged, the most limiting case is chosen using the 18% level turbulence at inlet. It is the most limiting as the apparition of turbulent spots with a random spatial and temporal distribution, which increase the heat transfer, introduces a skewness in the measurement distribution. The appearance of a spot is held responsible for the local temporal increase in heat transfer and thus, the skewed histogram. The mean value of the heat transfer profile is compared after averaging for multiple characteristic times obtaining Fig. D.1. Even for the lowest value used, the profile trend does not greatly vary when more time is added to the average.

A histogram of the heat flux is represented at various locations where probes record the temporal signal in Fig. D.2. Although not shown, various probes located at different spanwise positions at the same curvilinear abscissa show the same temporal distribution. The analysis of the histograms show the total number of events during the simulation in Figs. D.2a-D.2b and Fig. D.2c. Moving downstream the number of events grows where larger heat flux values are encountered and so, the latter figure is much more skewed towards the higher values of heat flux. This implies that turbulent spots are more probable as the shock wave is approached and it is these events that cause the increase of heat flux in the plateau region on the suction side.

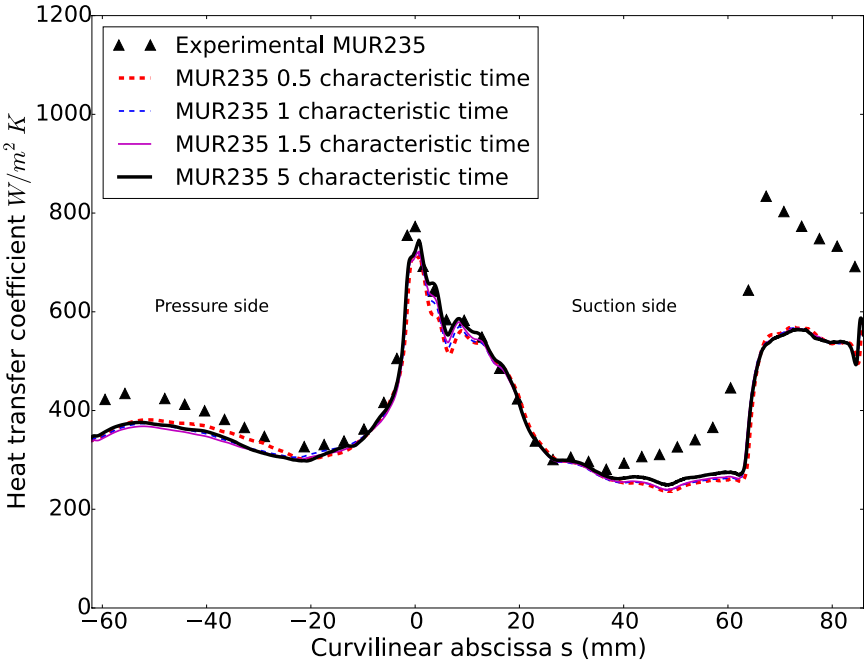

Figure D.1: Heat transfer coefficient profile in most unsteady case for 18% turbulence using M1 mesh.

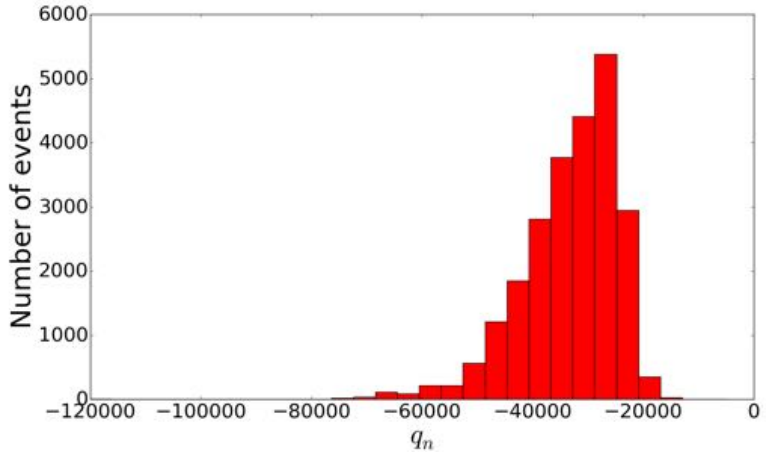

(a)

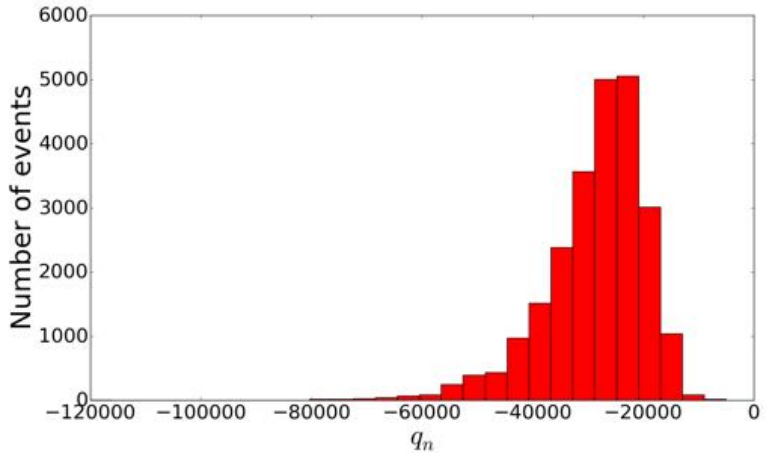

(b)

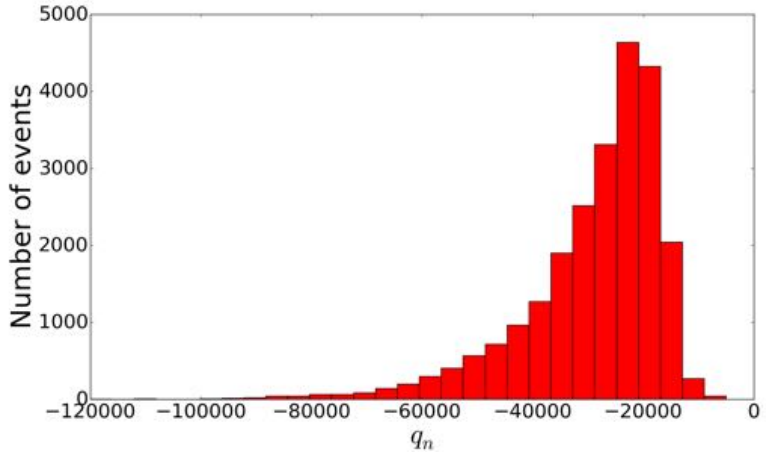

(c)

Figure D.2: Heat flux histogram at a) $s/c = 0.4$ b) $s/c = 0.6$ c) $s/c = 0.8$.

Appendix E

Development of one iteration calculation

In many situations the notation may induce errors that could be avoided by a simple example. This appendix is intended for those wishing to implement such a solver or that require to understand the main steps followed associated to the notation provided.

E.1 First order temporal derivative for triangular elements, L term

The first order temporal derivatives are calculated at a primary cell level using the expression in Eq. (E.1)

$$R_{K_e} = -\frac{1}{n_d V_{K_e}} \sum_{k|k\in K_e} \vec{F}_k \cdot \vec{s}_k \tag{E.1}$$

remembering n_d represents the number of dimensions of the element, V_{K_e} is the volume of the primary element, $\vec{F}$ being the fluxes and $\vec{s}$ the normal to the node represented in Fig. **??**. Subindex k represents each vertex of the cell. Once the residual is calculated, it can be redistributed to the nodes using the distribution matrix previously noted obtaining at each node j as in Eq. (3.5).

So, taking a simple example as in Fig. E.1b, assuming the coordinates for the nodes indicated to be $x = (0, 1, 0)$ and $y = (0, 1, 1)$

$$\vec{F}_k = \begin{pmatrix} F_{1x} & F_{1y} \\ F_{2x} & F_{2y} \\ F_{3x} & F_{3y} \end{pmatrix}; \vec{s}_f|_{edge} = \begin{pmatrix} 0 & 1 \\ -1 & 0 \\ 1 & -1 \end{pmatrix}_{edge} \tag{E.2}$$

The order of $\vec{s}_f$ is taken to be that of the edges, so the first row corresponds to the first edge. Applying $\sum \vec{F}_f \vec{s}_f$ would lead to,

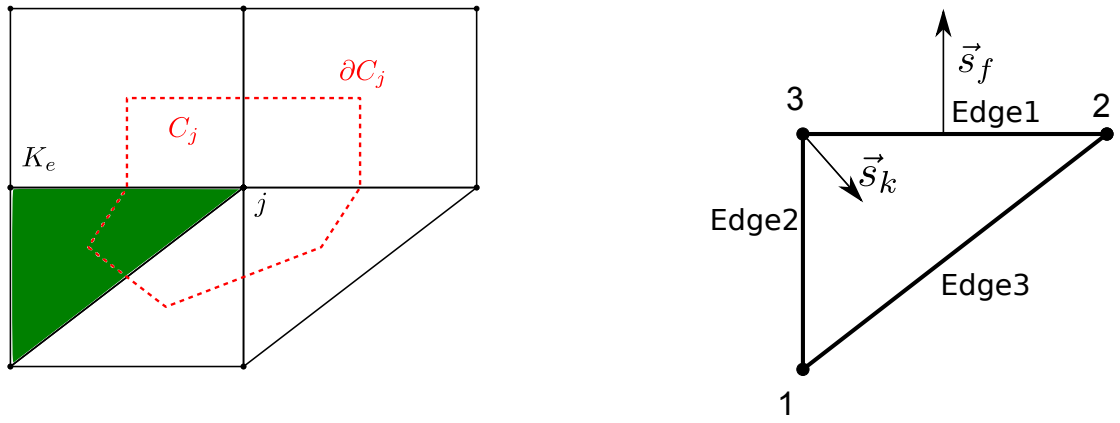

(a) Details of dual cell mesh and notation.

(b) Normal definitions in elementary cell.

Figure E.1: Notation and definitions used for elements in AVBP.

$$R_{K_e} = \frac{1}{V_{K_e}}\Big(\frac{F_{2x}+F_{3x}}{2}s_{f1x} + \frac{F_{2y}+F_{3y}}{2}s_{f1y} + \frac{F_{1x}+F_{3x}}{2}s_{f2x} + \frac{F_{1y}+F_{3y}}{2}s_{f2y} + \frac{F_{1x}+F_{2x}}{2}s_{f3x} + \frac{F_{1y}+F_{2y}}{2}s_{f3y}\Big) = \frac{1}{V_{K_e}}\left(\frac{F_{2x}-F_{3x}}{2} + \frac{F_{3y}-F_{1y}}{2}\right) \tag{E.3}$$

The vertex normals may be recalculated using $\vec{s}_k = \begin{pmatrix} 0 & 1 \\ -1 & 0 \\ 1 & -1 \end{pmatrix}$ at each vertex. Note that the normal to each vertex corresponds to the normal of the opposite edge scaled by the length of the correponding edge. It is easily shown that the same result is obtained,

$$R_{K_e} = -\frac{1}{2V_{K_e}}\left(F_{1y} - F_{2x} + F_{3x} - F_{3y}\right) \tag{E.4}$$

The redistribution process requires to scale the obtained residual by the volume of the intersection of $K_e \cap C_j$, corresponding to the volume of the whole primary cell and divided by the number of vertices in the cell remembering the residual is redistributed equally to each vertex.

For optimisation issues, the redistribution is not done at the end of the calculation of each operation. Also note that the redistribution matrix is done in a fashion such that each node receives a ponderated part of the primary cell residuals surrounding the dual cell. This ponderation corresponds to the area of each primary cell divided by the number of vertices in each cell. The residual of each sub-cell formed by $K_e \cap C_j$ is constant, as assumed in the primary cell, and is concentrated in its centroid. For each cell, residuals are added and finally divided by the total area of the node volume, meaning that the final residual corresponds to that of

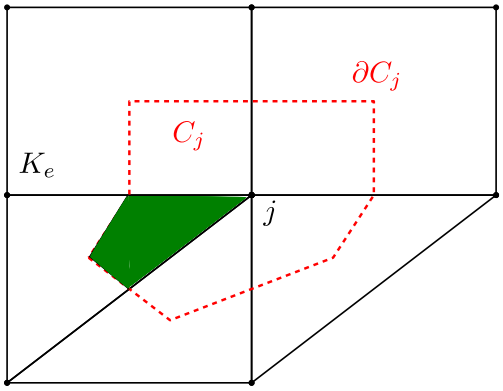

Figure E.2: Detail of mesh dual cell.

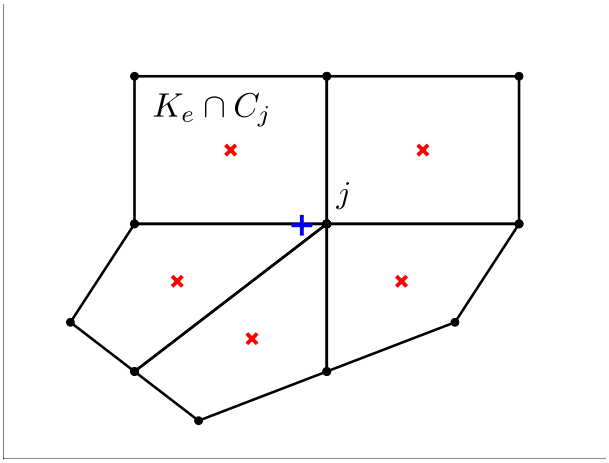

Figure E.3: Dual cell mesh. x represent the centroid of the intersection $K_e \cap C_j$ and $+$ is the global centroid of the cell.

the centroid of the dual cell and not the node. As can be easily shown in Fig. E.3, the centroid of the dual cell does not necessarily coincide with the node position which can lead to large geometrical differences when distorted meshes are used. This is discussed in more detail in Chapter 7.

E.2 First order temporal derivative for quadrilateral elements, L term

It was seen that bilinear elements such as quadrilaterals required an extra correction in relation to linear elements such as triangles. Following the notation in Colin et al. [37], it was seen that,

$$L_j\left(U^n\right)|_c = \sum_{k \in K_e} F_k \Theta_{j,k}|_c, \tag{E.5}$$

where $\Theta_{j,k} = \Theta^0_{j,k} + \Theta^1_{j,k}$.

It can be demonstrated that $\Theta^0_{j,k}$ represents the Finite Volume way of proceeding, being $\Theta^1_{j,k}$ the responsible for the correction. The simplest way to exemplify it is the application of the residual on a quad element. Taking a quadrilateral defined by the coordinates $x = (-1, 1, 1, -1)$ and $y = (-1, -1, 1, 1)$ which is represented by the following shape functions,

$$\begin{aligned}
\phi_1 &= \frac{1}{4}(1-\xi)(1-\eta) \\
\phi_2 &= \frac{1}{4}(1+\xi)(1-\eta) \\
\phi_3 &= \frac{1}{4}(1+\xi)(1+\eta) \\
\phi_4 &= \frac{1}{4}(1-\xi)(1+\eta)
\end{aligned} \tag{E.6}$$

where the shape function gradients,

$$\begin{aligned}
\phi_{1\xi} &= -\frac{1}{4}(1-\eta) \qquad & \phi_{1\eta} &= -\frac{1}{4}(1-\xi) \\
\phi_{2\xi} &= +\frac{1}{4}(1-\eta) \qquad & \phi_{2\eta} &= -\frac{1}{4}(1+\xi) \\
\phi_{3\xi} &= +\frac{1}{4}(1+\eta) \qquad & \phi_{3\eta} &= +\frac{1}{4}(1+\xi) \\
\phi_{4\xi} &= -\frac{1}{4}(1+\eta) \qquad & \phi_{4\eta} &= +\frac{1}{4}(1-\xi)
\end{aligned} \tag{E.7}$$

Variables ξ and η vary between -1 and 1 which means that its mean value is zero. Thus, $\overline{\nabla\phi_k}$ will be determined exclusively by the sign of the gradient and scaled by $\frac{1}{4}$. It can be easily verified that it complies with Eq.(3.44). The correction part then is calculated, proof being provided in [36] that it is a conservative approach as the sum over all the vertices of the correction is zero. For the canonical quadrilateral elements, it is possible then to integrate exactly Eq. (3.40) to obtain the necessary coefficients, as an example for $j = 1$ $k = 1$,

$$\int_{K_e} \phi_j \nabla_\xi \phi_k dV = \int_{-1}^{1}\int_{-1}^{1} -\frac{1}{16}(1-\xi)(1-\eta)(1-\xi)\, d\xi d\eta = -\frac{1}{3} \tag{E.8}$$

It is possible to construct a table with all the coefficients,

$$\int_{K_e} \phi_j \nabla_\xi \phi_k dV = \begin{pmatrix} -\frac{1}{3} & \frac{1}{3} & \frac{1}{6} & -\frac{1}{6} \\ -\frac{1}{3} & \frac{1}{3} & \frac{1}{6} & -\frac{1}{6} \\ -\frac{1}{6} & \frac{1}{6} & \frac{1}{3} & -\frac{1}{3} \\ -\frac{1}{6} & \frac{1}{6} & \frac{1}{3} & -\frac{1}{3} \end{pmatrix} \tag{E.9}$$

$$\int_{K_e} \phi_j \nabla_\eta \phi_k dV = \begin{pmatrix} -\frac{1}{3} & -\frac{1}{6} & \frac{1}{6} & \frac{1}{3} \\ -\frac{1}{6} & -\frac{1}{3} & \frac{1}{3} & \frac{1}{6} \\ -\frac{1}{6} & -\frac{1}{3} & \frac{1}{3} & \frac{1}{6} \\ -\frac{1}{3} & -\frac{1}{6} & \frac{1}{6} & \frac{1}{3} \end{pmatrix} \tag{E.10}$$

and calculate the correction using these coefficients that are constant for quadrilateral elements.

E.3 Second order temporal derivative for quadrilateral elements, LL term

Similarly to the L terms, it is possible to do the same for the LL terms,

$$LL_j\left(U^n\right)|_c = (A, B) \sum_{k \in K_e} F_k \Psi_{j,k}|_c \tag{E.11}$$

where A and B are the Jacobian matrices in cartesian coordinates and,

$$\Psi_{j,k}\Big|_c = \int_{K_e} \nabla\phi_j \nabla\phi_k{}^T dV. \tag{E.12}$$

Rembembering that the transformation matrix is set to the unity matrix in this case, the integration of this Ψ matrix for quadrilaterals can be shown to be,

$$\Psi_{j,k}\Big|_c = \int_{K_e} \begin{pmatrix} \frac{\partial\phi_k}{\partial\xi}\frac{\partial\phi_j}{\partial\xi} & \frac{\partial\phi_k}{\partial\xi}\frac{\partial\phi_j}{\partial\eta} \\ \frac{\partial\phi_k}{\partial\eta}\frac{\partial\phi_j}{\partial\xi} & \frac{\partial\phi_k}{\partial\eta}\frac{\partial\phi_j}{\partial\eta} \end{pmatrix} = \begin{pmatrix} (A) & (B) \\ (C) & (D) \end{pmatrix} \tag{E.13}$$

$$\Psi^{A}_{j,k}\Big|_{c} = \begin{pmatrix} \frac{1}{3} & -\frac{1}{3} & -\frac{1}{6} & \frac{1}{6} \\ -\frac{1}{3} & \frac{1}{3} & \frac{1}{6} & -\frac{1}{6} \\ -\frac{1}{6} & \frac{1}{6} & \frac{1}{3} & -\frac{1}{3} \\ \frac{1}{6} & -\frac{1}{6} & -\frac{1}{3} & \frac{1}{3} \end{pmatrix}; \qquad \Psi^{B}_{j,k}\Big|_{c} = \begin{pmatrix} \frac{1}{4} & -\frac{1}{4} & -\frac{1}{4} & \frac{1}{4} \\ \frac{1}{4} & -\frac{1}{4} & -\frac{1}{4} & \frac{1}{4} \\ -\frac{1}{4} & \frac{1}{4} & \frac{1}{4} & -\frac{1}{4} \\ -\frac{1}{4} & \frac{1}{4} & \frac{1}{4} & -\frac{1}{4} \end{pmatrix} \tag{E.14}$$

$$\Psi^{C}_{j,k}\Big|_{c} = \begin{pmatrix} \frac{1}{4} & \frac{1}{4} & -\frac{1}{4} & -\frac{1}{4} \\ -\frac{1}{4} & -\frac{1}{4} & \frac{1}{4} & \frac{1}{4} \\ -\frac{1}{4} & -\frac{1}{4} & \frac{1}{4} & \frac{1}{4} \\ \frac{1}{4} & \frac{1}{4} & -\frac{1}{4} & -\frac{1}{4} \end{pmatrix}; \qquad \Psi^{D}_{j,k}\Big|_{c} = \begin{pmatrix} \frac{1}{3} & \frac{1}{6} & -\frac{1}{6} & -\frac{1}{3} \\ \frac{1}{6} & \frac{1}{3} & -\frac{1}{3} & -\frac{1}{6} \\ -\frac{1}{6} & -\frac{1}{3} & \frac{1}{3} & \frac{1}{6} \\ -\frac{1}{3} & -\frac{1}{6} & \frac{1}{6} & \frac{1}{3} \end{pmatrix} \tag{E.15}$$

Appendix F

Resampling Strategies to Improve Surrogate Model-based Uncertainty Quantification - Application to LES of LS89

Received <day> <Month>, <year>; | Revised <day> <Month>, <year>; | Accepted <day> <Month>, <year>
DOI: xxx/xxxx

RESEARCH ARTICLE

Resampling Strategies to Improve Surrogate Model-based Uncertainty Quantification - Application to LES of LS89.

Pamphile T. Roy* | **Luis Miguel Segui** | **Jean-Christophe Jouhaud** | **Laurent Gicquel**

[1]CERFACS, 42 Avenue Gaspard Coriolis, 31057 Toulouse cedex 1, France

Correspondence
*Pamphile T. Roy Email: roy@cerfacs.fr

Abstract

Uncertainty Quantification (UQ) is receiving more and more attention for engineering applications in particular from robust optimization. Indeed, running a computer experiment only provides a limited knowledge in terms of uncertainty and variability of the input parameters. These experiments are often computationally expensive and surrogate models can be constructed to address this issue. The outcome of a UQ study is in this case directly correlated to the surrogate's quality. Thus, attention must be devoted to the Design of Experiments (DoE) to retrieve as much information as possible. This work presents two new strategies for parameter space resampling to improve a Gaussian Process surrogate model. These techniques indeed show an improvement of the predictive quality of the model with high dimensional analytical input functions. Finally, the methods are successfully applied to a turbine blade Large Eddy Simulation application: the aerothermal flow around the *LS89* blade cascade.

KEYWORDS:
Design of Experiment, Uncertainty Quantification, Surrogate Model, Gaussian Process, LES

1 | INTRODUCTION

Design process and robust optimization are the major purposes of most engineering works dealing with Computational Fluid Dynamics (CFD), especially in aeronautical or automotive industry (1). Despite the large amount of work that has been devoted to the design of efficient optimization techniques, the design process still requires important investments (financial and human) (2). As a consequence, design errors appear after the industrialization phase (3) and the implications these can have may be critical. This partially explains why CFD tools have been used more and more in the past decades to decrease the number of iterations between conception and experiments to avoid irreversible errors during the preliminary design phase.

Nowadays, CFD codes have reached maturity and represent more accurately physical flow phenomena. Complex flow simulations on high-resolution grids are possible thanks to the continuous developments in numerical models and in High Performance Computing (HPC). Nevertheless, deterministic simulations only provide limited knowledge about a system. Uncertainties in the numerical model as well as in the problem formulation or inputs are necessarily present and translate into uncertainties in the outputs (4).

In fact, the diversity of uncertainties on the CFD boundary conditions or initial conditions, as well as on model parameters (input data, geometry, simplification of the model physics, etc.) limits the validity of the simulations: the quantity of interest (QoI) can be easily affected and shadowed by the conjugation of all types of uncertainties. This assessment explains why Uncertainty Quantification (UQ) is now becoming a mandatory step in application-oriented modelling for operational and industrial purposes (5, 6). It provides insight into the level of uncertainty in the numerical simulation results but also gives access to the Sensitivity Analysis (SA) which aims at describing the respective influences of the input parameters on the QoI. The inclusion of UQ in a design optimization cycle hence allows manufacturers to design quicker and obtain better, cheaper and more robust (i.e. more stable) products.

Classical UQ methods, based on the Monte-Carlo approach, require a large number of CFD simulations (7), which quickly go beyond the limits of available computational resources (CPU cost). This is especially true when it comes to large dimensional problems, both with respect to the domain discretization and to the number of uncertain input parameters. The cost of the UQ study can however be significantly reduced when

the CFD code is replaced by a surrogate model which is formulated in a parameter space and which is fast to evaluate at any set of uncertain variables (8).

Two successful approaches for building a surrogate model are *Polynomial Chaos* (9) and *Gaussian Process* (10). The approach used in this work consists in combining Gaussian Processes with Proper Orthogonal Decomposition (POD) to build response surfaces through interpolation (11, 12). In an industrial context—which is the case here—, some benefits of this method are:*(i)* it does not require any prior knowledge on the probability distribution of the uncertainties on the input parameters ; *(ii)* it does not need a specific sampling of the parameter space which could lead to *curse-of-dimensionality* or mis-evaluation of the space ; *(iii)* it provides an estimation of the predictive error ; and *(iv)* the use of the POD reduces the number of predictors to compute. Details and comparisons can be found in (13, 14).

In any case, the number of CFD simulations that is required for the formulation of the surrogate model is defined by the complexity of the physics and the number of input parameters to take into account. This factor is paramount when considering costly numerical simulations.

The accuracy of an uncertainty quantification being directly correlated to the quality of the surrogate (15), the present study aims at improving its construction by using two new strategies for resampling the parameter space. Industrial applications being targeted, a first UQ analysis of the *LS89* case (16) using Large Eddy Simulation (LES) is presented. LES are high-fidelity full 3D unsteady simulations. This approach comes at a high CPU cost which requires the use of High Performance Computing (HPC) resources.

The paper is tailored as follows; Section 2 starts by presenting the techniques employed to construct the surrogate model as well as its error assessment. Then the UQ tools used are detailed and Section 3.1 describes the two proposed strategies. After this methodological presentation, Section 4 assesses the benefits of these strategies on several difficult analytical functions and presents the results on the application: the aerothermal analysis around the *LS89* blade cascade. Finally, Section 5 will put a closure to this paper by summarizing its contributions along with potential directions for future works or applications.

2 | SURROGATE MODEL FOR UQ

In this study, the surrogate model is created using the *BATMAN* (Bayesian Analysis Tool for Modeling and uncertAinty quaNtification) tool (14) which is written in Python language. Using a non-intrusive approach, BATMAN allows to construct a surrogate model from any *black-box* code. The result obtained is a POD-based Gaussian Process (pGP) surrogate which is computationally inexpensive and able to interpolate any new realization (or snapshot) $\mathbf{x}_*$ not in the sample composed of N_s snapshots. BATMAN's workflow is detailed in Algorithm 1.

All different steps are detailed in the following sections. Section 2.1 presents the POD technique and Section 2.2 reminds the Gaussian process technique. The quality of the surrogate is addressed in Section 2.3 and the UQ methods are detailed in Section 2.4. Finally, in order to improve the surrogate's quality, resampling strategies are presented in Section 3.1. Figure 1 shows the workflow implemented in the BATMAN tool for constructing the surrogate model for UQ.

Algorithm 1 POD-based Gaussian Process

1: Choose the size of the sample N_s
2: Pick N_s samples in the input space $\mathbf{x}$ with a low discrepancy design of experiment (DoE)
3: Perform a POD on the output
4: Formulate the pGP surrogate $\mathcal{M}_{\text{gp}}$ on the POD's coefficients
5: Resample the parameter space if necessary

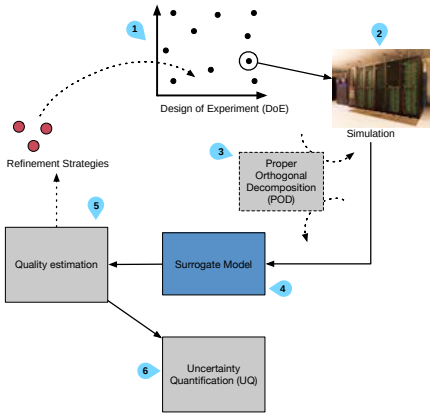

FIGURE 1 Workflow to resample the parameter space in an Uncertainty Quantification framework.

2.1 | POD

A function z can be approximate using a finite sum of terms:

$$z(m, N_i) \simeq \sum_k a_k(N_i)\phi_k(x), \tag{1}$$

with m being the spatial discretization and N_i a realization of the code, a snapshot. The functions $\phi_k(m)$ have an infinite representation and can be Fourier series, Chebyshev polynomials, etc. For a chosen basis of functions, a set of unique snapshot functions $a_k(N_i)$ arises. In the case of POD (17), the basis functions are orthonormal which implies:

$$(\phi_{k_1}, \phi_{k_2}) = \begin{cases} 1 \text{ if } k_1 = k_2 \\ 0 \text{ if } k_1 \neq k_2 \end{cases}, \tag{2}$$
$$a_k(N_i) = z(m, N_i) \cdot \phi_k(m),$$

with $(\cdot, \cdot)$ the inner product. The principle of POD is to choose $\phi_k(m)$ such that the approximation of $z(m, N_i)$ is optimal in a least square

sense. These orthonormal functions are called the *proper orthogonal modes* of the function. Modes can be found using a *Singular Value Decomposition* (SVD) of the snapshot matrix (18). Considering the snapshot matrix $\mathbf{A}$, gathering the output QoI computed spatially on m for the N_s snapshots:

$$\mathbf{A} = \left[\mathbf{z}^{N_1}, \cdots, \mathbf{z}^{N_i}, \cdots, \mathbf{z}^{N_S}\right], \tag{3}$$

with $\mathbf{z}^{N_i}$ the *i-th* snapshot vector stored as a column in $\mathbf{A}$. The SVD is a factorization operation of a matrix expressed as:

$$\mathbf{A} = \mathbf{U}\mathbf{\Sigma}\mathbf{V}^T, \tag{4}$$

with $\mathbf{V} \in \mathbb{R}^{N_s \times N_s}$ diagonalizes $\mathbf{A}^T\mathbf{A}$, $\mathbf{U} \in \mathbb{R}^{m \times m}$ diagonalizes $\mathbf{A}\mathbf{A}^T$ and $\mathbf{\Sigma} \in \mathbb{R}^{m \times N_s}$ is the singular value matrix with its diagonal composed by the singular values σ of $\mathbf{A}$. Thus, the initial matrix can be rewritten:

$$\mathbf{A} = \sum_{i=1}^{r} \sigma_i u_i v_i^T, \tag{5}$$

with u_i and v_i the eigen vectors of respectively $\mathbf{U}$ and $\mathbf{V}$ which form an orthonormal basis. Also $r = \min(m, N_s)$ is the rank of the matrix. Due to the singular value matrix's null terms, the reduced form of the matrices is used which leads to $\mathbf{U} \in \mathbb{R}^{m \times N_s}$, $\mathbf{\Sigma} \in \mathbb{R}^{N_s \times N_s}$. Note that one can apply a filtering on the modes to only keep the basis vectors containing the highest energy of the system. For any $k < r$, an optimal approximation of rank k of the snapshot matrix $\mathbf{A}_k = \mathbf{U}\mathbf{\Sigma}_k\mathbf{V}_k^T$ can be calculated by setting the $\sigma_{i>k} = 0$ in $\mathbf{\Sigma}$. These two steps allow to compress the data as only an extract of $\mathbf{U}$ and $\mathbf{\Sigma}$ need to be stored. But the real benefit is that a surrogate model does not need to be carried out for all points of the spatial discretization of the QoI but only for the matrix $\mathbf{\Sigma}_k\mathbf{V}_k^T$ (a column of this matrix corresponds to a snapshot).

2.2 | The Gaussian Process Regression

A Gaussian Process (GP) is a collection of random variables which have a joint Gaussian distribution (10). GP is equivalent to *Kriging* (19). In this case, the random variable being the POD coefficients computed for each random input vector $\mathbf{x}$ of N_s: $f(\mathbf{x}) = (\mathbf{\Sigma}_k\mathbf{V}_k^T)_\mathbf{x}$. A new prediction consists in a new column of $\mathbf{\Sigma}_k\mathbf{V}_k^T$. A *Gaussian Process* $\mathcal{GP}$ is described by its mean $m(\mathbf{x})$ and covariance $k(\mathbf{x}, \mathbf{x}')$—where $\mathbf{x}, \mathbf{x}'$ are different sets of inputs

$$\begin{aligned} f(\mathbf{x}) &\sim \mathcal{GP}(m(\mathbf{x}), k(\mathbf{x}, \mathbf{x}')), \text{ with} \\ m(\mathbf{x}) &= \mathbb{E}\left[f(\mathbf{x})\right], \\ k(\mathbf{x}, \mathbf{x}') &= \mathbb{E}\left[(f(\mathbf{x}) - m(\mathbf{x}))(f(\mathbf{x}') - m(\mathbf{x}'))\right]. \end{aligned} \tag{6}$$

Here the covariance function k (or kernel) is chosen as a squared exponential

$$K = k(\mathbf{x}, \mathbf{x}') = \sqrt{\pi}\,\sigma_\mathbf{x}^2 \exp -\frac{(\mathbf{x} - \mathbf{x}')^2}{2(\sqrt{2}l)^2}, \tag{7}$$

where l is a length scale that describes the trend in the data and $\sigma_\mathbf{x}$ is the variance of the output signal. Then the GP model consists of a regression providing an interpolation $\hat{f}$ for a new set of input parameters $\mathbf{x}_*$:

$$\begin{aligned} \hat{f}(\mathbf{x}_*) = \bar{f}(\mathbf{x}_*) = \sum_{i=1}^{N_s} \alpha_i k(\mathbf{x}_i, \mathbf{x}_*), \text{ with} \\ \alpha = (K + \sigma_n^2 I)^{-1}\mathbf{y}, \end{aligned} \tag{8}$$

where $\bar{f}$ is the mean realization, $\mathbf{x}_i$ the *i-th* set of parameters, $\mathbf{y}$ the snapshot matrix and σ_n is the variance of the input variables. Indeed, it is the mean realization of the conditioned process considering an artificial noisy observation which gives the prediction. The learning phase of the GP consists in selecting l, σ_n and $\sigma_\mathbf{x}$ so that f passes through or close to the dataset points. These hyperparameters are optimized using a differential evolution strategy. A key advantage of this predictor is that it provides an inference about its prediction variance

$$\mathbb{V}[f(\mathbf{x}_*)] = k(\mathbf{x}_*, \mathbf{x}_*) - \mathbf{k}(\mathbf{x}_*)^T(K + \sigma_n^2 I)^{-1}\mathbf{k}(\mathbf{x}_*). \tag{9}$$

2.3 | Estimation of the error

To correctly adapt the number of snapshots to the required precision, the quality of the model has to be evaluated by comparing expected values and their estimations. A common indicator is to compute the predictivity coefficient Q_2 (20):

$$Q_2 = 1 - \frac{\sum_{i=1}^{N_s}(f_i - \hat{f}_i)^2}{\sum_{i=1}^{N_s}(f_i - \bar{f})^2}, \tag{10}$$

with $\overline{f}$ denoting the mean value, f_i the measured point and $\hat{f}_i$ its prediction by the model. When dealing with a non-analytical function the expected values are not known. However, there are two methods to evaluate the precision:

- The sample can be divided into a validation set and training set. The model is built based on the training set and then evaluations are compared relative to the validation set. However, this technique requires that we do not use the validation simulations which is computationally costly when dealing with high fidelity numerical experiments.

- Another approach is to estimate the quality by *k-fold* Cross Validation (21). A particular case is the *Leave-One-Out Cross Validation* (LOO) with $k = n = 1$—with n the number of observations. The LOO technique derived from statistical learning theory requires the formulation of several surrogates. Each surrogate is built excluding one point from the evaluation sample; the accuracy of the surrogate is then calculated at this particular point. Removing point p from $\hat{f}_p$ gives $\hat{f}_p^{\,(-p)}$ and leads to an error

$$\epsilon_p = \|f_p - \hat{f}_p^{\,(-p)}\|_2. \tag{11}$$

with the Euclidean 2-norm considered for $\mathbb{R}^m$. This is done all over the sample composed of N_s snapshots to get the mean-square-error

$$LOO = \frac{1}{N_s}\sum_{p=1}^{N_s}\epsilon_p^2. \tag{12}$$

Thus, an estimated predictivity coefficient $\hat{Q}_2$ can be retrieved

$$\hat{Q}_2 = 1 - \frac{LOO}{\sum_{p=1}^{N_s}\left(\hat{f}_p - \bar{\hat{f}}\right)^2}. \tag{13}$$

As stated in (15), this estimation tends to be pessimistic. Indeed, a snapshot is removed from an already very small sample which ultimately tends to lower the predictive quality of the model. However the indicator is stable—provided a correct sample size ($N_s > 10n_{dim}$, with n_{dim} the number of dimension (22))—and as the quality increases, the difference between the estimation and the real quality vanishes.

2.4 | Uncertainty Quantification

There are several methods to estimate the contribution of different parameters on quantities of interest (23). Among them, sensitivity methods based on the analysis of the variance allow to obtain the contribution of the parameters on the QoI's variance (24). Here, classical *Sobol'* (25) method is used which gives not only a ranking but also quantifies the importance factor using the variance. This method only makes the hypothesis of the independence of the input variables. It uses a functional decomposition of the variance of the function to explore:

$$\begin{aligned}\mathbb{V}(\mathcal{M}_{gp}) &= \sum_{i}^{p}\mathbb{V}_i(\mathcal{M}_{gp}) + \sum_{i<j}^{p}\mathbb{V}_{ij} + ... + \mathbb{V}_{1,2,...,p}, \\ \mathbb{V}_i(\mathcal{M}_{gp}) &= \mathbb{V}[\mathbb{E}(\mathcal{M}_{gp}|x_i)] \\ \mathbb{V}_{ij} &= \mathbb{V}[\mathbb{E}(\mathcal{M}_{gp}|x_i x_j)] - \mathbb{V}_i - \mathbb{V}_j,\end{aligned} \tag{14}$$

with p the number of input parameters constituting $\mathbf{x}$. This way *Sobol'* indices are expressed as

$$S_i = \frac{\mathbb{V}[\mathbb{E}(\mathcal{M}_{gp}|x_i)]}{\mathbb{V}[\mathcal{M}_{gp}]} \qquad S_{ij} = \frac{\mathbb{V}[\mathbb{E}(\mathcal{M}_{gp}|x_i x_j)] - \mathbb{V}_i - \mathbb{V}_j}{\mathbb{V}[\mathcal{M}_{gp}]}. \tag{15}$$

S_i corresponds to the first order term which apprises the contribution of the *i-th* parameter, while S_{ij} corresponds to the second order term which informs about the correlations between the *i-th* and the *j-th* parameters. These equations can be generalized to compute higher order terms. However, the computational effort to converge them is most often not at hand (15) and their analysis, interpretations, are not simple.

Total indices represents the global contribution of the parameters on the QoI and express as:

$$S_{T_i} = S_i + \sum_{j} S_{ij} + \sum_{j,k} S_{ijk} + ... \simeq 1 - S_i. \tag{16}$$

For a functional output, as for the *LS89* case—see Section 4.4—, *Sobol'* indices can be computed all along the output and retrieve a map or create composite indices. As described by Marrel (26), aggregated indices can also be computed as the mean of the indices weighted by the variance at each point or temporal step

$$S_i = \frac{\sum_{l=1}^{p}\mathbb{V}[\mathbf{f}_l]S_i^l}{\sum_{l=1}^{p}\mathbb{V}[\mathbf{f}_l]}. \tag{17}$$

In this paper the indices are estimated using *Martinez'* formulation. In (27), they showed that this estimator is stable and provides asymptotic confidence intervals—approximated with Fisher's transformation—for first order and total order indices.

3 | IMPROVING THE DESIGN OF EXPERIMENT

3.1 | Description of the new resampling methods

Correctly sampling the parameter space is paramount as it is used to construct the model. Although the golden standard would be to perform a *Monte Carlo* sampling, it would require an unreasonably large sampling which is unfeasible within a costly simulation environment or if considering *real-time* applications. This constrains the number of simulations that can be performed. Cavazzuti (28) provides a comprehensive description of the techniques used to generate the best DoE.

A good criterion for assessing the quality of a DoE technique is the discrepancy (15, 29). It measures the uniformity of the points' coverage of the parameter space. Hence, *low discrepancy sequences*, or *quasi-random sequences*, have good filling properties of the space. To name a few, *Sobol'* and *Halton* sequences are known to perform well when dealing with low-dimensional spaces (30, 7). Furthermore, an advantage over the traditional LHS (31) or optimized LHS (30) sampling is that the sample is deterministic. The sequence can be continued without losing any space-filling quality whereas with traditional LHS, the sample becomes suboptimal. Indeed, LHS algorithms require a number of points to create the sample.

This last observation motivates our choice of a low discrepancy sequence for sampling the parameter space. Indeed, this enables us to increase the design one simulation at the time. A complementary strategy consists in exploring the space using as few points as possible and then refine the exploration around zones of interest.

Starting from the work of (32, 11) with the σ method as a baseline, two novel strategies—LOO-σ and LOO-*Sobol'*—have been developed and are presented in this work. The common strategy is detailed in Algorithm 2.

- Variance (σ),
  As stated in Section 2.2, one of the main advantages of Gaussian processes over other surrogates is to provide an insight into the variance of the solution. The first method consists in using this data and weight it with the eigenvalues of the POD:

$$\sum_{i=1}^{k}\sigma_i^2 \times \mathbb{V}[\mathcal{M}_{gp}(\mathbf{x}_*)]_i. \tag{18}$$

Algorithm 2 Refinement strategy

Require: $N_{max}, threshold$

while $LOO - quality < threshold$ and $N_s < N_{max}$ **do**
  $\mathbf{x}_L \leftarrow$ least stable point of the design
  $\mathcal{H}_\mathcal{L} \leftarrow$ maximum hypercube around $\mathbf{x}_L$
  $\mathbf{x}_o \leftarrow \max \mathbb{V}[\mathcal{M}_{gp}]$, within $\mathcal{H}_\mathcal{L}$
  Compute a new snapshot at $\mathbf{x}_o$
  Update pGP surrogate $\mathcal{M}_{gp}(\mathbf{x}_*)$
end while

Global optimization of this indicator gives the new point to simulate (33).

- Leave-One-Out (LOO) and σ,
  A LOO is performed on the POD and highlights the point where the model is the most sensitive. The strategy here is to add a new point around it. The creation of the hypercube is described in Section 3.2. Within this hypercube, a global optimization over σ is conduced giving the new point.

- LOO-*Sobol'*,
  Using the same steps as with the LOO-σ method, the hypercube around the point is here truncated using prior information about *Sobol'* indices—see Section 2.4. It requires that indices be close to convergence not to bias the result. However, the bias can be intentional depending on the insight we have about the case.

- Hybrid.
  This last method consists of a navigator composed by any combination of the previous methods.

The evaluation of the latter composite method is not presented in this work. Although the computation of the LOO metric is merely an attempt to characterize the model's global quality, this mainly serves to assess the surrogate model's stability. If the model's response surface is not affected by the removal of a particular point, it is interpreted as a stability—or a non sensitivity—of the model to this action. This technique aims at stabilizing the model.

3.2 | Construction of the Hypercube

To resample locally the parameter space, a hypercube is constructed around point p which is the most sensitive in the construction of the surrogate model—LOO point, see Section 2.3. An optimization problem is defined to construct the largest hypercube bounded by the surrounding points $\mathcal{P}$ as shown in Fig. 2 . This allows to only consider the vicinity of the point.

The hypercube is defined by the cartesian product of the intervals of the n parameters *i.e.* $[a_i, b_i]^n$. The constrained optimization problem

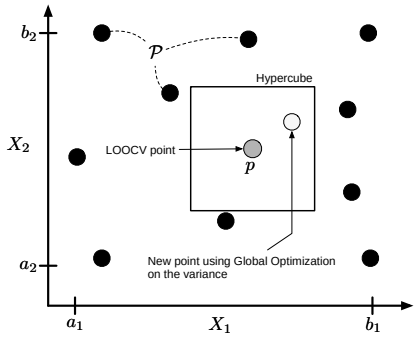

FIGURE 2 Sketch of a Hypercube of size $[a_i, b_i]^2$. The grey dot is the LOO point p, the black dots are the surrounding points $\mathcal{P}$ and the white dot is the new point to evaluate.

can hence be written as:

$$\begin{cases} \max \ \| \ (\mathbf{b} - \mathbf{a}) \ \|_2 \\ \mathcal{P} \quad \notin [a_i, b_i]^n \\ p \quad \in [a_i, b_i]^n \end{cases} . \tag{19}$$

A maximum cube-volume aspect ratio (34) is also defined in order to preserve the locality. This gives the new constrain

$$C : \sqrt[n]{\frac{\max(\mathbf{b} - \mathbf{a})}{\prod_{i=1}^{n} \max(b_i - a_i)}} < \epsilon, \tag{20}$$

with $\epsilon = 1.5$, set arbitrarily to prevent too elongated hypercubes. The global optimum is found using a two-step strategy: first, a discrete optimization using $\mathcal{P}$ gives an initial solution; second a basin-hopping algorithm (33) finds the optimum coordinates of the hypercube. In case of the LOO-*Sobol'* method, the hypercube is truncated using the total order *Sobol'* indices.

4 | RESULTS

The benefits and mechanisms of the methods are first evaluated on complex analytical functions. The chosen functions are defined in Section 4.1. Then, the treatment of the parameter space's boundary is presented in Section 4.2. Taking into account this issue, the analytical functions are tested in Section 4.3. Finally, the methods are evaluated on a realistic application in Section 4.4 with the LES of the LS89 test case (16).

4.1 | Analytical functions

In order to test the new resampling methods, three analytical functions—see Table 1 —with increasing numbers of input dimensions are presented, namely: *(i) Rosenbrock* ; *(ii) Ishigami* ; and *(iii) g-function* (35,

36, 7). They all are widely used because they are nonlinear and non-monotonic. Note that, similar results were obtained on other functions.

4.2 | Restriction of the DoE

The first step when constructing a model is to define the DoE. This is done by defining the range of each input parameter, the boundaries that describe a hypercube. Then, using a low discrepancy sequence as described in Section 3.1, an initial pool of snapshots is computed within the hypercube. However, when constructing a model based on Gaussian Process regression, the error is important at the boundaries of the DoE due to the lack of information. The model is thus not able to extrapolate accurately at these locations. If using the variance technique as it is, the algorithm tends to add points around the corners and only after it considers other parts of the domain. When dealing with a low dimensional case—fewer than three parameters as with the *Michalewicz* function which uses two input parameters, see Fig. 3 —, a few iterations are "wasted" in the process.

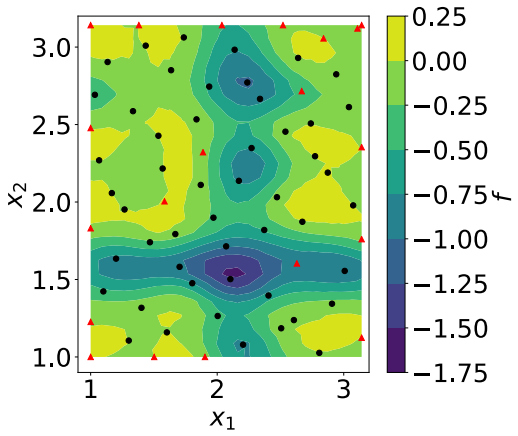

FIGURE 3 *Michalewicz* function: dots represent the initial sample of 50 points and diamonds represent the 20 resampled points. The function was evaluated on the hypercube $[1, \pi]^2$

When increasing the number of parameters, there is a larger number of boundaries to cover. This has been confirmed on the *Ishigami* function (3 input parameters) for which the reported Q_2 values are even worse. As shown in Table 2 , the optimization process is being over constrained in these regions and the global predictions are degraded. To obtain this Table, the initial sample was increased using a constant number of resampling points (10 points) and the error was measured using a uniform distribution on the domain, confirming the importance of the boundary treatment.

The possibility to widen the space by a delta space has been evaluated to address this question. The objective is to condition the predictor around the boundaries by adding information outside the domain of interest. A Halton sequence has been used to generate a sample of size $N_s = 80$ from the space

$$N_i \sim \mathcal{U}(20, 80) \quad \Delta_{space} \sim \mathcal{U}(0, 20\%), \tag{21}$$

with N_i the number of initial snapshots and Δ_{space} the widening factor, the outer delta space. For each case N_i, it is only the proportion of initial sample over the number of resample point that varies. (See Fig. 4). A fixed budget of $N_b = 80$ snapshots was considered. Then, the number of resampling points is equal to $N_{rs} = N_b - N_i$. The strategy used here was the σ model (see Section 3.1). After the resampling phase has been completed, the quality Q_2 of the model is computed. Applied to the *Ishigami* function, N_s simulations each performing N_b evaluations have been used to construct the response surface. These results were compared to a case without resampling: $N_i = N_S = 80$. The resulting predictivity quality being $Q_2 \simeq 0.8$.

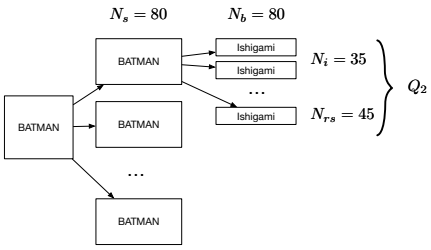

FIGURE 4 Example showing a computation of Q_2 with $N_i = 35$, $N_{rs} = 45$.

As shown in Fig. 5 , there is no benefit of adding points outside the domain. Aside from the uniform distributions usually employed on this function, a standard arcsine distribution was also tested to assess the quality around boundaries but no enhancement was observed. When the delta space is increased, there is a loss of quality due to the presence of points in non-interesting regions.

Complementarily to this analysis using an outer delta space, an inner delta space factor has also been considered. The same methodology was used. Results are shown in Fig. 6 . On the uniform case, the model was not correctly computed due to high discontinuities caused by the 0% inner delta space cases. In (37), optimal design that tends to put more points near the boundaries were shown to be more effective. Our results are coherent with their findings as we observed an improvement of the quality when using a low inner delta space. Indeed, a small value of the parameter limits the trend to add points close to the boundaries.

This work has shown that setting an inner delta space comprised between 5 and 10% is required to ensure the robustness of the model construction. Based on this observation, in the following the inner delta space is set to an arbitrary value of 8%.

Function	Hypercube	Definition
Rosenbrock	$[-2.048, 2.048]^2$	$f(X_1, X_2) = \sum_{i=1}^{d-1}[100(x_{i+1} - x_i^2)^2 + (x_i - 1)^2]$.
Ishigami	$[-\pi, \pi]^3$	$f(X_1, X_2, X_3) = \sin X_1 + 7\sin^2 X_2 + 0.1X_3^4 \sin X_1$.
g-function	$[0, 1]^4$	$f(X_1, X_2, X_3, X_4) = \prod_{i=1}^{4} \frac{\lvert 4X_i - 2\rvert + a_i}{1 + a_i}, \quad a_i = i$.

TABLE 1 Analytical functions considered sorted by increasing number of input parameters.

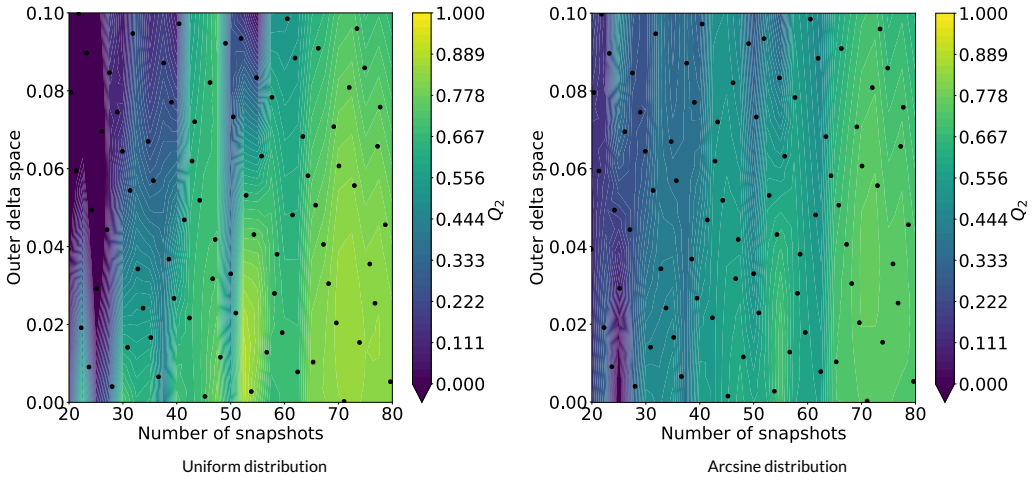

FIGURE 5 Response surface of Q_2 function of the initial sample and the *outer delta space*. Dots represent the simulations.

Initial sample	Total size	Q_2
30	40	0.05
35	45	-0.02
40	50	-0.13
45	55	-0.19
50	60	-0.04
55	65	0.43
60	70	0.51
65	75	0.87
70	80	0.54
75	85	0.86

TABLE 2 Error Q_2 on the *Ishigami* function of the size of the initial sample using a variance strategy with 10 points.

4.3 | Application on analytical functions

The operating mechanism and catches of the method can be visualized on the *Rosenbrock* function—see Fig. 7 . Starting from the σ method: points are first added close to the top boundary despite the inner delta space parameter. However, the lack of surrounding points made this choice fairly legitimate. Other points seem to be located in interesting regions—where there is a gradient and no points. It can be seen as a low discrepancy sequence, which made its use relevant for studying the delta space impact in Section 4.2. On the other hand, the LOO-σ method does not seem to exhibit a boundary preference. But, on the bottom left-hand corner, there is an accumulation of points. Indeed, this method relies on the location of the most sensitive point. Considering the surroundings of a strong extremum—as it is the case here—, the method tends to add points first in this zone preventing further exploration of the domain and, in this case, totally misses the second extremum. Lastly, the LOO-*Sobol'* method seems more balanced. Points have been added preferentially on the X_1 parameter axis, as it is slightly the most influent parameter ($S_{T_{X_1}} \simeq 0.7$).

A convergence study has also been performed. With a fixed total number of simulations, the size of the initial learning sample was changed to evaluate the impact of the ratio of the initial sampling over the total number of samples on the quality of the model. As in Section 4.2, a *Halton* sequence was used. The respective parameters are reported in Table 3 . The *Sobol'* indices for the *Ishigami* function are found in (38), while for the other functions, a deterministic sample of $100\,000$ evaluations was used.

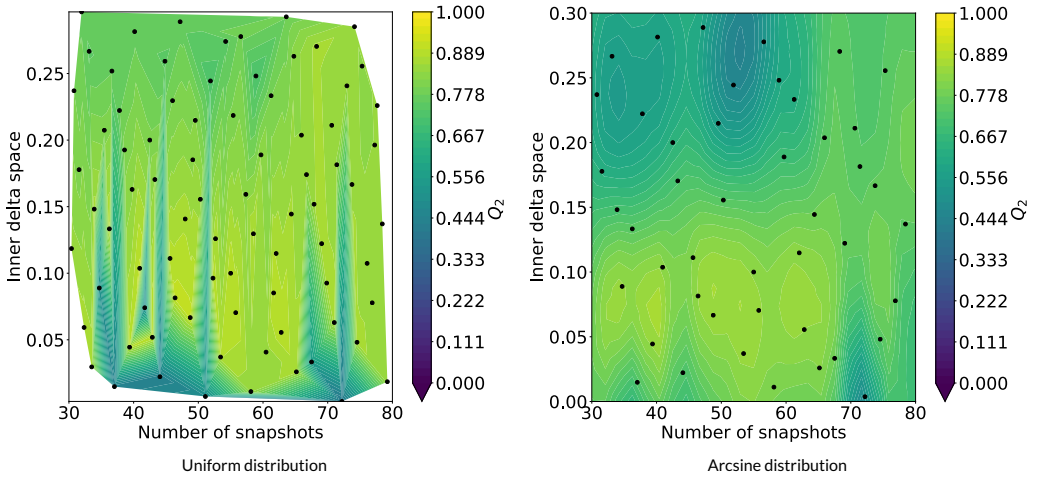

FIGURE 6 Response surface of Q_2 function of the initial sample and the *inner delta space*. Dots represent the simulations.

Function	Sample Budget	Q_2	Total order *Sobol'* indices
Rosenbrock 2-D	25	0.82	[0.71, 0.50]
Ishigami 3-D	80	0.85	[0.557, 0.443, 0.244]
g-function 4-D	65	0.66	[0.61, 0.29, 0.16, 0.09]

TABLE 3 Reference Q_2 and Total order *Sobol'* indices at a fixed budget using a Halton sequence for the analytical functions.

Results are shown in Fig. 8 . The σ method appears to be one of the most, in some cases the most, effective method but it also exhibits more variability. Increasing dimensionality seems only to improve slightly this behaviour. There are multiple explanations to this phenomenon. The method relies on the use of an inference about the variance of the model. Starting from a given sample, if the fitting process does not converge, the prediction of the variance will be far from correct leading to a wrong resampling. Of course, there is a chance for this new point location to be relevant, still this can lead to an even worse model or an overfitting where the model is too closely linked to the outputs, so the model has memorized only the feature but not learned the underlining correlation between the data. Lastly, looking at Fig. 9 , even if the points look well distributed over the parameter space, the pGP model is absolutely wrong. The Gaussian Process reconstruction failed to recover the response surface of the function whereas a Radial Basis Function Networks model successfully did it.

The other two methods share the σ strategy, but the variability is conditioned by the LOO point. Indeed, the former only uses inference about the predictive variance whereas LOO's methods take into account the observed quality of the model. LOO-*Sobol'* is even more stable especially when the contribution of the parameters to the QoI is not even. The quality evolves quasi-linearly with the initial sample size. This is due to the initial guess on the indices. The closer the indices are converged, the better the sizing of the hypercube used by the σ strategy. Indeed, some dimension of the hypercube could be neglected due to the indices. In the *Rosenbrock* case the method behaves like LOO-σ, the importance factors are close enough so that this collapse of dimension does not occur. On the other hand, with the *g-function*, the total order *Sobol'* indice of the last input parameter is so small that the algorithm tends not to take into account this dimension.

For each function, as the initial sample gets close to the budget, the expected improvement is reduced. This is clear with the *Ishigami* function. When the initial sample is too small, the model is so poor that the points are not added efficiently. On the contrary, if we add an insufficient number of points, the impact is close to none but still there is an improvement. From the other cases, the effect of the ratio of the initial learning sample size over the total budget is not so clear. In 2-D the impact is null and after that, a ratio > 0.5 seems appropriate.

Thus, setting aside the possible non-fitting of the data, improving the quality of the surrogate model by resampling the parameter space appears to be guaranteed in high dimensional cases and using no more than half of the budget.

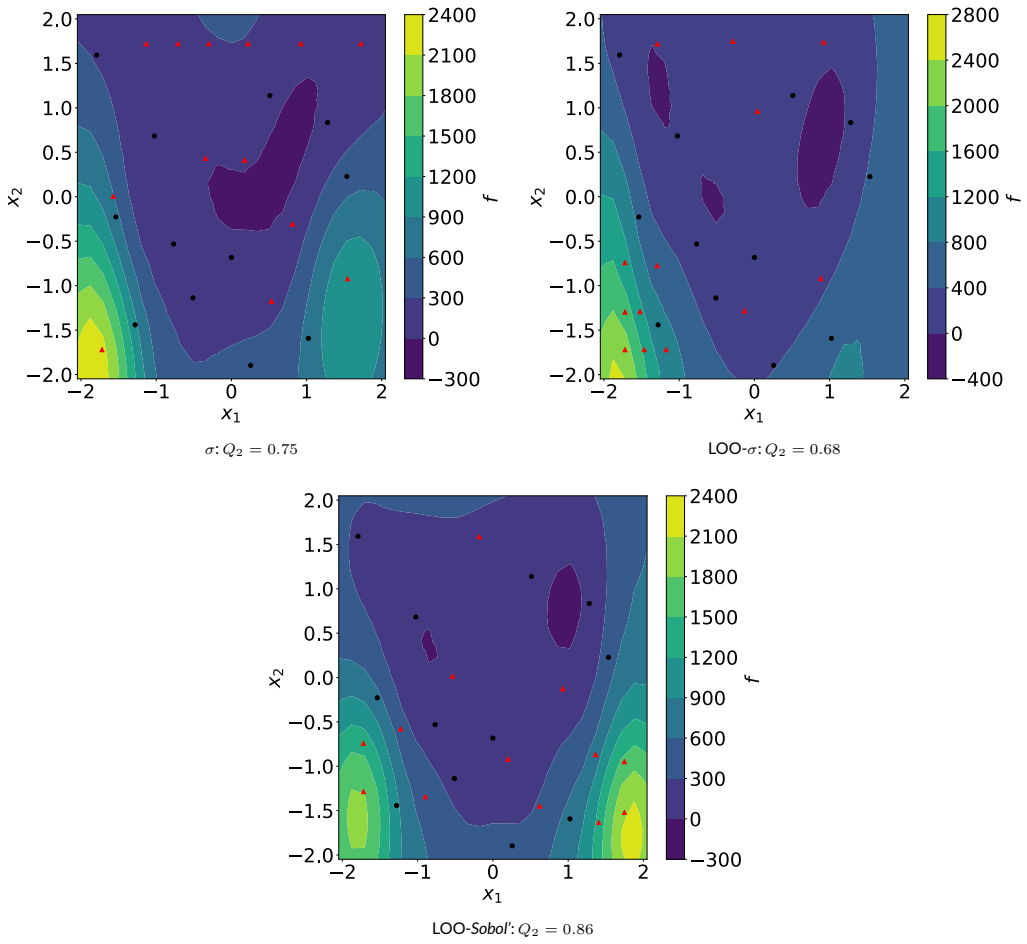

FIGURE 7 Response surface of the *Rosenbrock* function. In each case, the initial learning sample is composed of 12 simulations and there are 13 resampling points—respectively represented in dots and diamonds.

4.4 | LS89 case

4.4.1 | Case description

The *LS89* case is a blade cascade designed and tested experimentally at the Von Karman Institute for Fluid Dynamics (VKI) (16). The linear cascade consists of five high-pressure turbine vanes although only the center vane is studied. The vane is a 2D extruded profile unlike most industrial vanes that are much more complex geometrically. It however remains of great interest because the operating points are representative of values found in real engines today. This test case represents one of the largest turbomachinery databases available for the validation of CFD models in complex geometries.

A large variety of operating points have been successfully simulated until now. Low levels of turbulence injection ($< 1\%$) do not represent an issue for most solvers (39, 40) using either Reynolds-Averaged Navier Stokes (RANS) or Large Eddy Simulation (LES). Higher levels of turbulence have also been studied successfully (41) but difficulties arise for higher Reynolds numbers and larger outlet Mach numbers. Simulations are not able to correctly predict experimentally obtained profiles, notably the heat transfer field which is of great importance for the blade life-cycle.

The operating point addressed in this document, selected from Arts (16), is the MUR235, a very rich case in terms of physics that presents the above mentioned challenges (high Reynolds and outlet

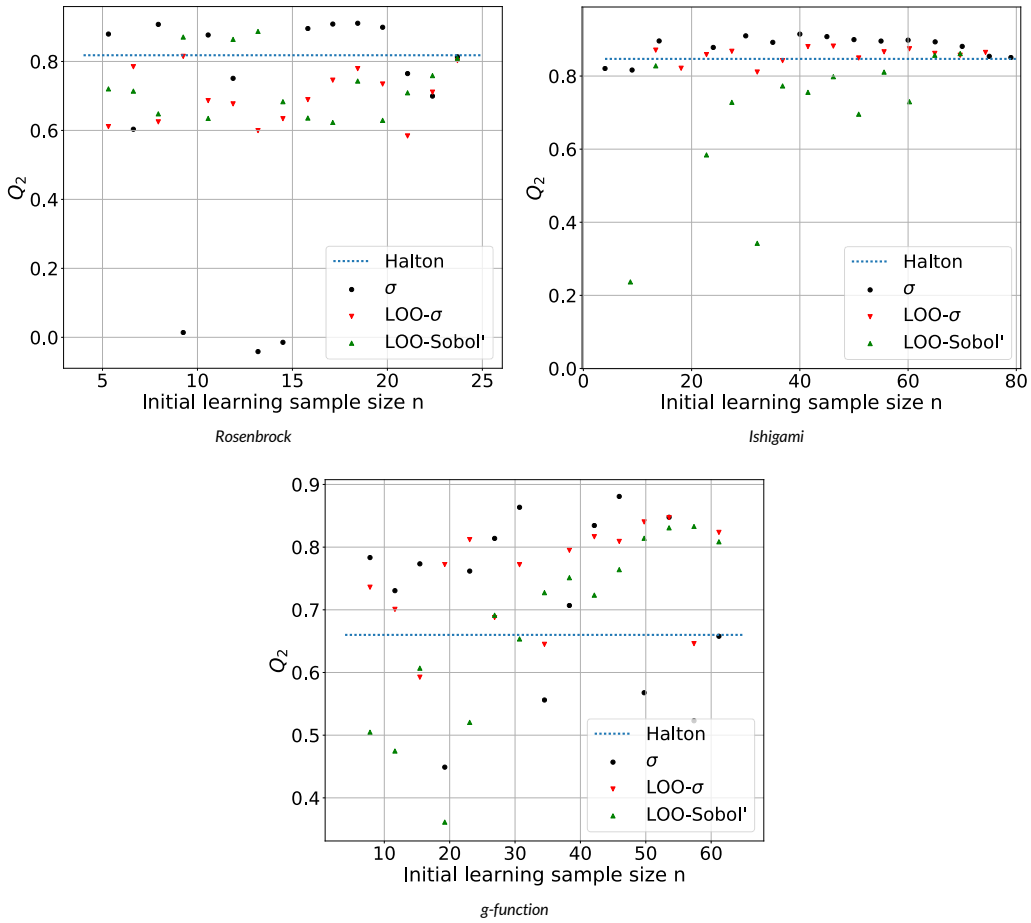

FIGURE 8 Convergence of Q_2 of the different methods on each function by varying the initial learning sample size with a fixed budget.

Mach numbers). Figure 10 highlights the main physical interactions in such a flow. One of the most notable features is the presence of a shock wave on the suction side of the blade. This shock wave interacts with a transitional boundary layer due to the highly curved flow, a potential source of instabilities in the boundary layer which in turn determines the wake downstream. This wake issues acoustic waves that impact the neighbour blade affecting the stability of the boundary layer. Also, there is a high level of free-stream turbulence that undergoes stretching around the leading edge of the blade which modifies the position of the boundary layer transition on the suction side (42).

In the original experiments (16), an increase in heat transfer is observed on the suction side of the blade when a high turbulence intensity level at the inlet ($\sim$ 6%) as well as a large Reynolds number at the outlet ($> 1 \cdot 10^6$) are present. The simulations recover the shock wave that triggers an abrupt transition of the boundary layer, but turbulent spots may be found upstream of this position that can contribute to the overall heat transfer. These spots can be explained due to perturbations in the free-stream turbulence Tu that are capable of trespassing the sheltering effect of the shear layer and thereby increase the heat transfer. Turbulence values upstream of the blade are thus of upmost importance.

The original experiments give only the turbulence intensity level at an upstream distance from the vane, which is insufficient to characterize the turbulent flow at this location. Recent studies on the same test bench have measured the integral length scale for the same intensity level (43). In spite of this newly available information, simulations are not capable of recovering an important part of the heat flux on the

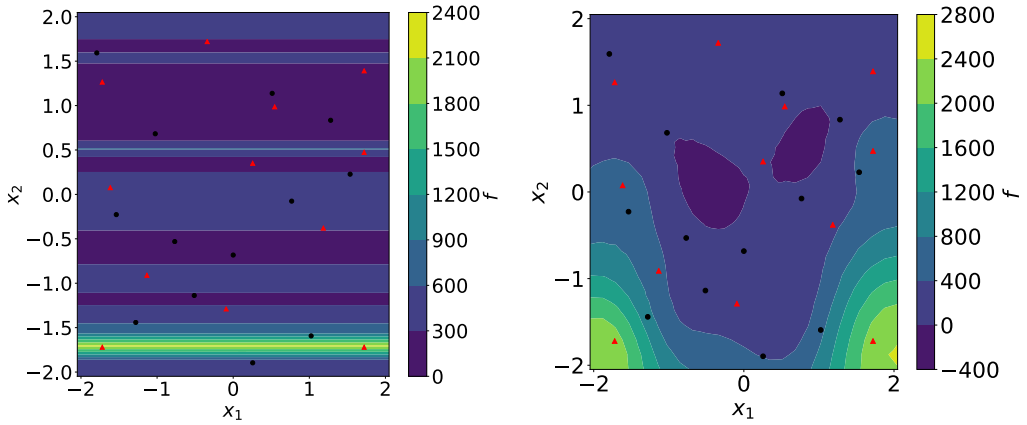

FIGURE 9 Response surface of the *Rosenbrock* function. Comparison between two models. The initial sample is composed of 13 simulations and 12 resampling points—respectively represented in dots and diamonds.

suction side even when taking the correct length scale (44). Uncertainties concerning the measured values in the experiments, that serve as boundary conditions in the simulation, appear as a path to be explored.

Apart from the turbulence intensity and the length scale, the angle of attack α of the incoming flow can also be seen as an uncertain parameter. There is no information related to this parameter in the experimental campaigns. In Fig. 11 , the effect of α was numerically investigated with respect to Tu by studying the heat transfer coefficient response—hereafter defined as the QoI. Due to the computational effort required to modify and simulate correctly a case with a modified integral length scale versus a modification of α, this parameter was not taken into account. Increasing Tu or α causes an increase of the QoI and Tu seems to have a larger impact than α. A deeper analysis would require more computations to obtain: *(i)* a correct response of the influence of these parameters on the QoI ; *(ii)* the contribution of each parameter ; and *(iii)* the probability density function of the QoI by propagating the uncertainties. Thus, the parameter space for this study was defined as

$$Tu \in [0, 30\%] \quad \alpha \in [-5, 5^\circ]. \tag{22}$$

4.4.2 | Numerical setup

The simulations have been performed using *AVBP* (45), a validated CFD LES solver co-developed by CERFACS and IFP-EN. This parallel code solves the three-dimensional compressible Navier-Stokes equations for both steady and unsteady reacting flows. The code is capable of handling hybrid unstructured meshes and allows to address complex geometries. High-order numerical schemes based on the *Taylor-Galerkin* (TTG) family are used (46).

The simulations were performed on a 20 million cells mesh. Five layers of prisms in the near-wall region are present allowing a higher aspect ratio. The mean $\overline{y^+}$ has a value of $\simeq 6.62$ which limits the physical time step to $1{,}94 \cdot 10^{-8}$ s. In this context, a wall-resolved computation using the *WALE* (47) model is used to take into account the proper turbulence scaling in the near-wall region. To gather enough statistics, a simulation time of $\sim 4{,}1$ ms was performed. This lead to a CPU cost, for a single computation, of $\sim$ 7500 hours lasting $\sim$ 5 hours on a cluster of 1440 cores.

The resolution of the mesh and the LES quality must be guaranteed to be sufficient to capture the complex physics encountered. Indeed, the interaction between the free-stream turbulence and the boundary layer requires to carefully mesh the near-wall region. It is reasonable then to compare the profiles of heat transfer obtained using the mesh for this UQ study, from here on denoted as *M0*, to two finer meshes M1 and *M2*, see Fig. 12 . The corresponding spatial distributions of y^+ are shown in Fig. 13 for the three meshes.

The heat transfer coefficient is seen to be different on the pressure side for the finest mesh (M2). However, on the suction side the coarser mesh (M0) leads to approximately the same results as the finest mesh (M2). This suggests that the value of y^+ does not have a first order effect on the heat transfer coefficient for the meshes considered. The sensitivity to other effects such as turbulence intensity and angle of attack may thus be sought. Additionally, it can be noted that the shock wave on the suction side is located at approximately the same position for all meshes. This implies that the upstream boundary layer is similar in all cases although the heat transfer coefficient across the shock wave is affected by the mesh refinement.

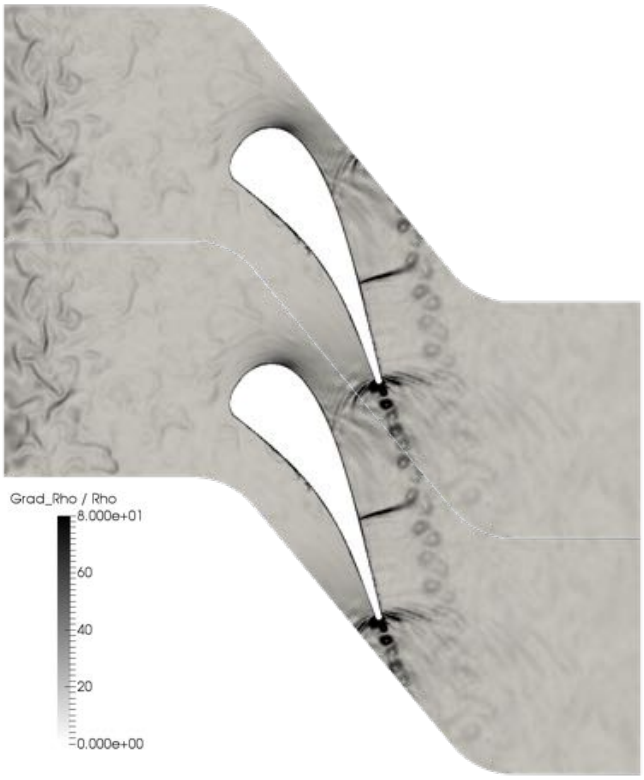

FIGURE 10 $\frac{\nabla \rho}{\rho}$ (m^{-1}) with $Tu = 30\%$.

4.4.3 | Uncertainty Quantification results

This section presents the comparison between the different resampling methods on this complex case. In the following, an existing sample comprised of 16 simulations is used to generate a *Sobol'* low-discrepancy sequence. As seen in Section 3.1, the quality of *Sobol'* sequence is similar to *Halton*'s in low dimensional cases. Using this initial set of simulations, the sequence has been continued adding 4 points to give a total of 20 simulations. Then using the same initial sample, the previous set is compared to the use of the σ method and the LOO-*Sobol'* method. The LOO-σ method gives similar results compared to LOO-*Sobol'* method. It is not tested on this case. Quality results evaluated by LOO as described in Section 2.3 are shown in Table 4 .

As demonstrated in Section 4.1, there is no guarantee that the quality of the model improves when using a refinement strategy other than continuing the low discrepancy sequence, given a low-dimensional case. The σ method was only able to improve a little the quality of the initial design. This improvement was inferior to the simple continuation of the sequence. However, we observed an improved quality using the LOO-*Sobol'* method. The importance factors' difference between the two input parameters make it feasible to improve further the quality of the model—see Fig. 17 .

Method	Number of Simulations	$\hat{Q}_2$
Sobol'	16	0.638
Sobol'	20	0.821
σ	20	0.688
LOO-*Sobol'*	20	0.856

TABLE 4 Estimated Q_2 function of the resampling method compared to an initial sample of 16 simulations.

The response surfaces of the models are plotted in Fig. 14 . The heat transfer coefficient has been integrated over the chord line to obtain this visualization. The first thing to notice is the correct distribution of sample points within the parameter space ensuring that most of the effects are captured. The predictions obtained using the models are

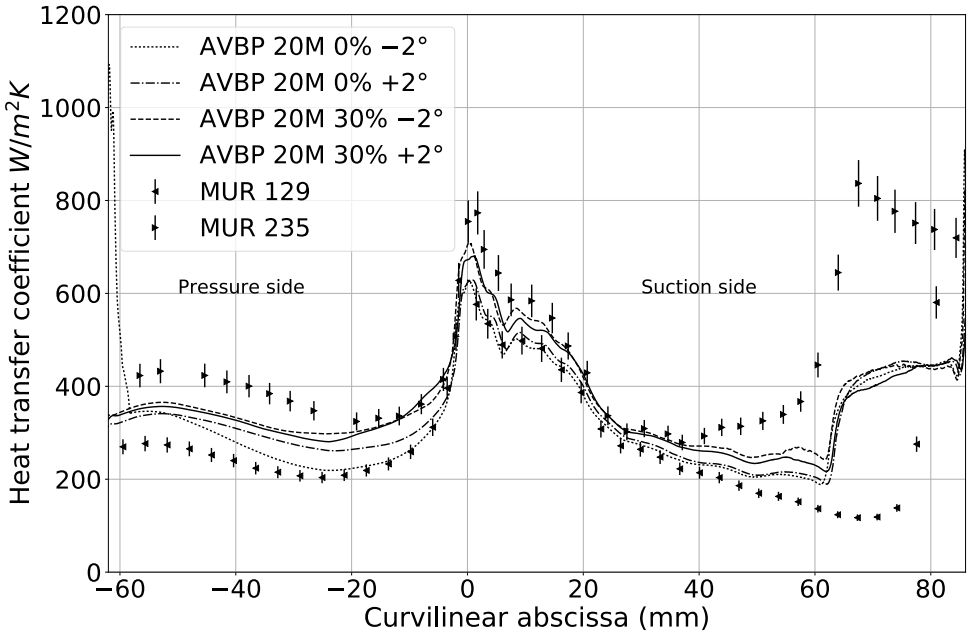

FIGURE 11 Heat transfer coefficient variation compared to experimental data of MUR129 ($Tu = 1\%, \alpha = 0°$) and MUR235 ($Tu = 6\%, \alpha = 0°$).

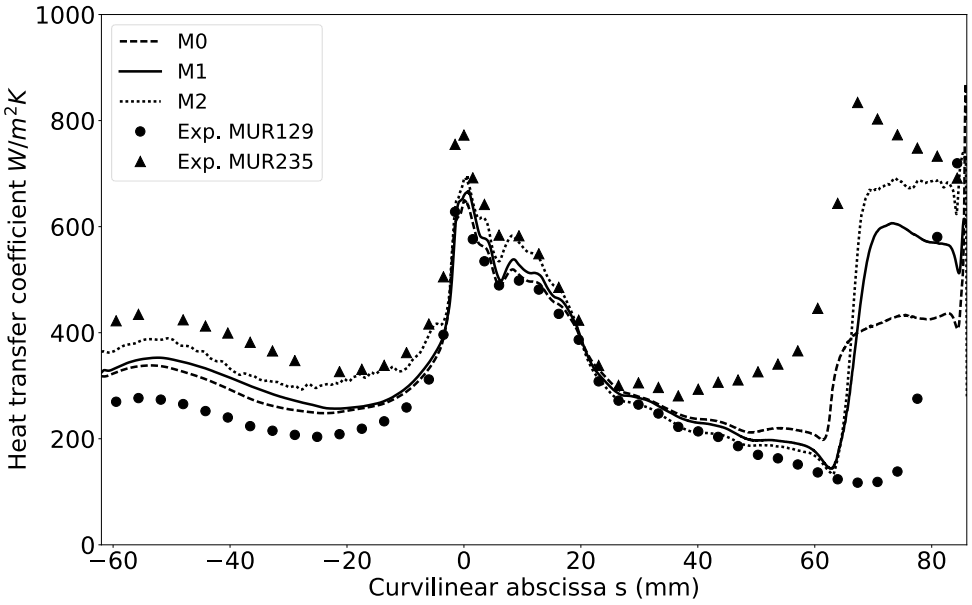

FIGURE 12 Heat transfer coefficient between various meshes using MUR235 setup ($Tu = 6\%, \alpha = 0°$).

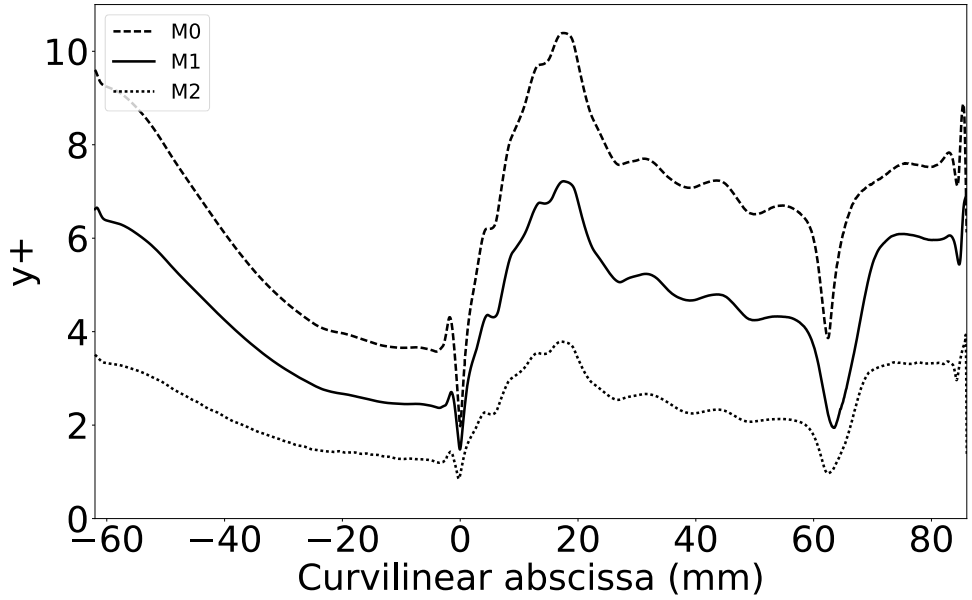

FIGURE 13 Refinement over blade surface measured using non-dimensional y^+ parameter for MUR235 operating point ($Tu = 6\%, \alpha = 0°$).

then found to be in agreement with the observations made previously. The heat transfer coefficient increases with the turbulence intensity and is fairly stable regarding the angle of the incoming flow. The models are said to be additive with respect to the turbulence intensity. Contrary to the *Sobol'* sequence, the LOO-*Sobol'* method detected that the model was sensitive to low values of turbulence intensity. It is this physical information that helped improve the predictivity quality. In the following, the model constructed using the LOO-*Sobol'* method is used.

Without making any assumption on the uncertainties, the Probability Density Functions (PDF) of the input parameters are both defined using uniform distributions over the parameter space

$$Tu \sim \mathcal{U}(0, 30\%) \quad \alpha \sim \mathcal{U}(-5, 5°). \tag{23}$$

Using these PDFs, uncertainties are propagated by $5\,000$ predictions of the heat transfer coefficient along the blade. Then the QoI's PDF is reconstructed using a kernel smoothing procedure (48, 49). Figure 15 reveals the expected concerning the propagation of such uncertainties to the heat transfer coefficient. As the two input distributions are uniform and the model is additive, the mean is centred between the extrema. From the experiments—see Fig. 11 —the envelope of the heat transfer coefficient is correctly captured except after the shock region. Indeed, from past experiences, capturing this region requires a value of $y^+ \sim 1 - 2$ (50).

Finally, the *Sobol'* indices have been estimated using $200\,000$ predictions. As the response surface suggested, the heat transfer coefficient

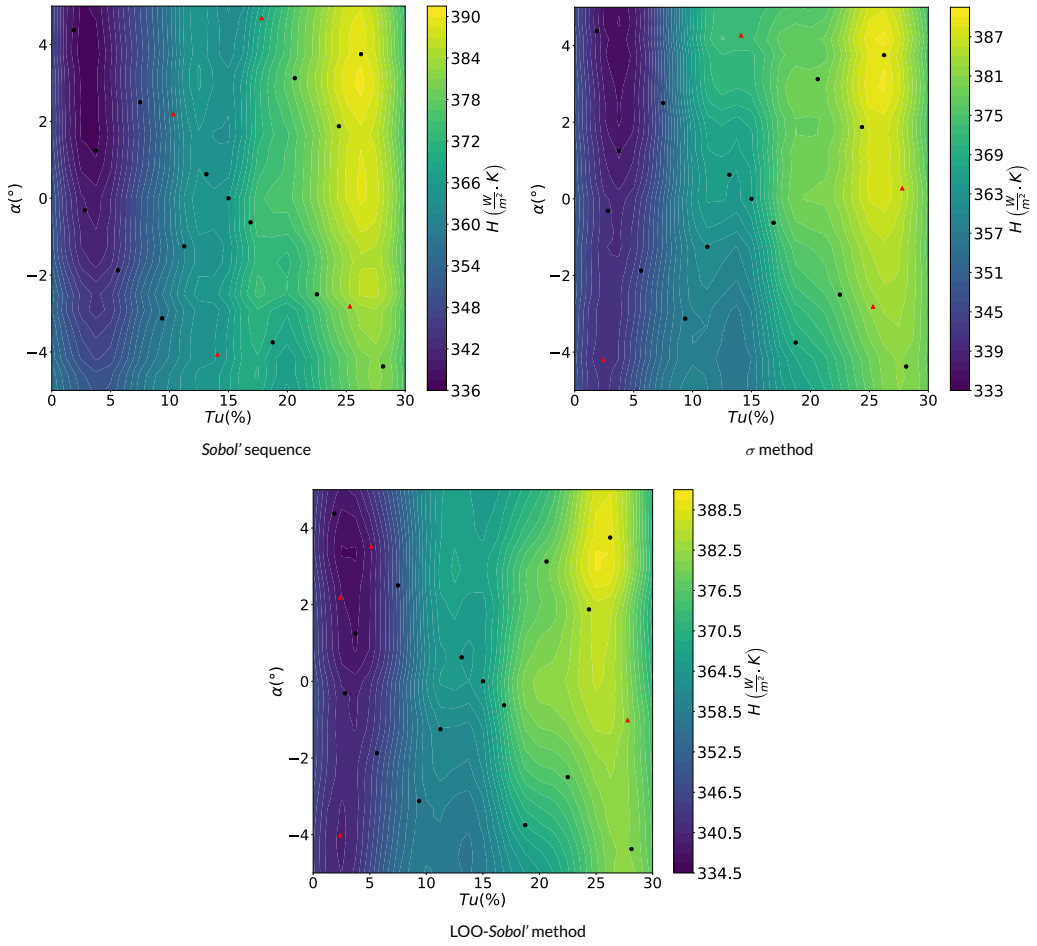

FIGURE 14 Heat Transfer coefficient response surface. DoE is initially composed of 16 simulations sampled with *Sobol'* sequence. Dots represent the initial LES simulations and diamonds represent the resampled points.

is mainly affected by the variation of the turbulence intensity. The spatial evolution of the indices in Fig. 16 , shows a spatial dependency. On the pressure side, the inflow angle has a higher influence as its contribution rises to become the most important parameter at the trailing edge. On the suction side, the turbulence intensity contribution is stable until the shock region. Reaching the trailing edge, the angle contribution increases. Finally, aggregated indices are reported in Fig. 17 . These indices confirm that the turbulence intensity is the most important parameter compared to the inflow angle when studying the heat transfer coefficient and for the range of angle variations retained. The turbulence intensity contributes to 70% of the total variance of the QoI whereas the inflow angle contributes to 30%. This behaviour was expected as downstream the shock, the incoming level of turbulence has little impact. The computation of the second order indices are not presented here because their values are negligible in comparison to the first order indices. This is in agreement with the small differences observed between the first and total order indices. There are no joint effects between the two parameters.

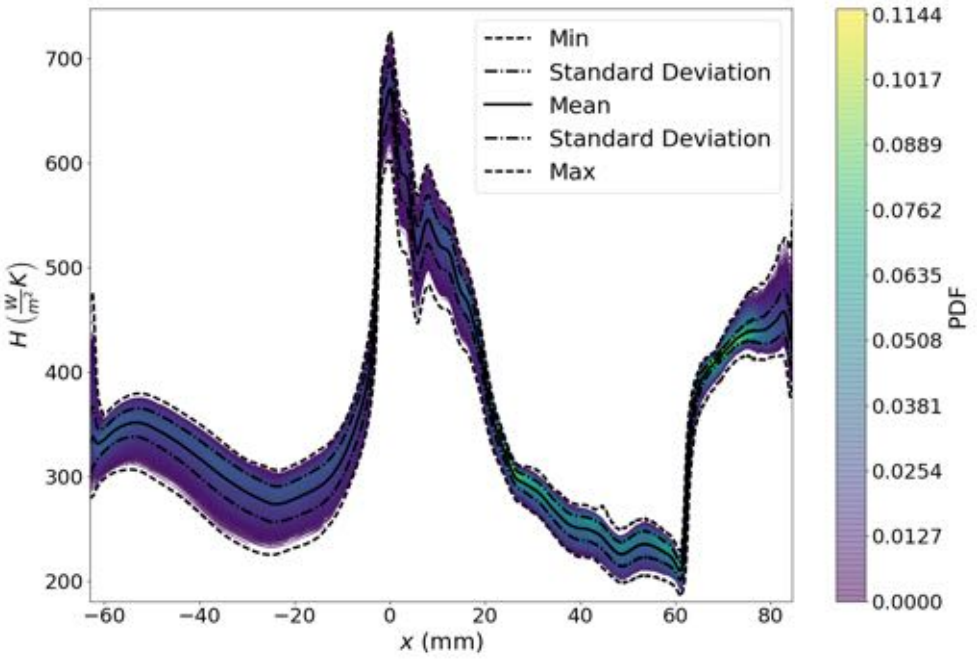

FIGURE 15 Probability Density Function and moments of the heat transfer coefficient along the chord line of the blade.

5 | CONCLUSIONS

Two new methods have been introduced in this work for resampling the parameter space in order to improve the predictivity coefficient of a surrogate model: namely LOO-σ and LOO-*Sobol'* methods. These methods do not only take advantage of the capability of Gaussian Process models to infer a prediction variance, but they use information about the observed quality of the model. It was shown that an improvement of the quality of the model is guaranteed in high dimensional cases. Compared to a resampling method based on the predicted variance only, the proposed methods behaviour appears to be more stable and reliable. We also found that the ratio of the initial learning sample space over the total budget of function evaluation should remain greater than $0,5$. Which is to say that no more than half of the budget should be allocated to resampling the parameter space. In any case, the initial quality of the model should be reasonable when considering these techniques.

A first Uncertainty Quantification LES study of the *LS89* is presented. The parameter space was comprised of the turbulence intensity and the inflow angle. In order to increase the quality of the surrogate model, the LOO-*Sobol'* method was used to refine the parameter space. We showed that it performed better than continuing the sampling sequence. Apart from an analysis of the variance, the model was used to propagate uncertainties. This study reveals that although the turbulence intensity is the main factor impacting the heat transfer coefficient, there is spatial evolution of its contribution along the blade.

In terms of conclusions, by taking into account the physics in this process, the proposed methods will help build better models at lower costs. This will allow also Uncertainty Quantification of high-dimensional or expensive cases to be within reach.

ACKNOWLEDGMENTS

The financial support provided by all the CERFACS shareholders (AIRBUS Group, Cnes, EDF, Météo-France, ONERA, SAFRAN and TOTAL) is greatly appreciated and we thank them to enable the achievement of such research activities. Furthermore, the authors acknowledge GENCI [CCRT/CINES/IDRIS] for giving access to HPC resources under the allocation x20162a6074. These resources have permitted the preliminary studies of the LS89.

References

[1] Duchaine F, Morel T, M. Gicquel L. Y.. Computational-Fluid-Dynamics-Based Kriging Optimization Tool for Aeronautical Combustion Chambers. *AIAA Journal*. 2009;47(3):631–645.

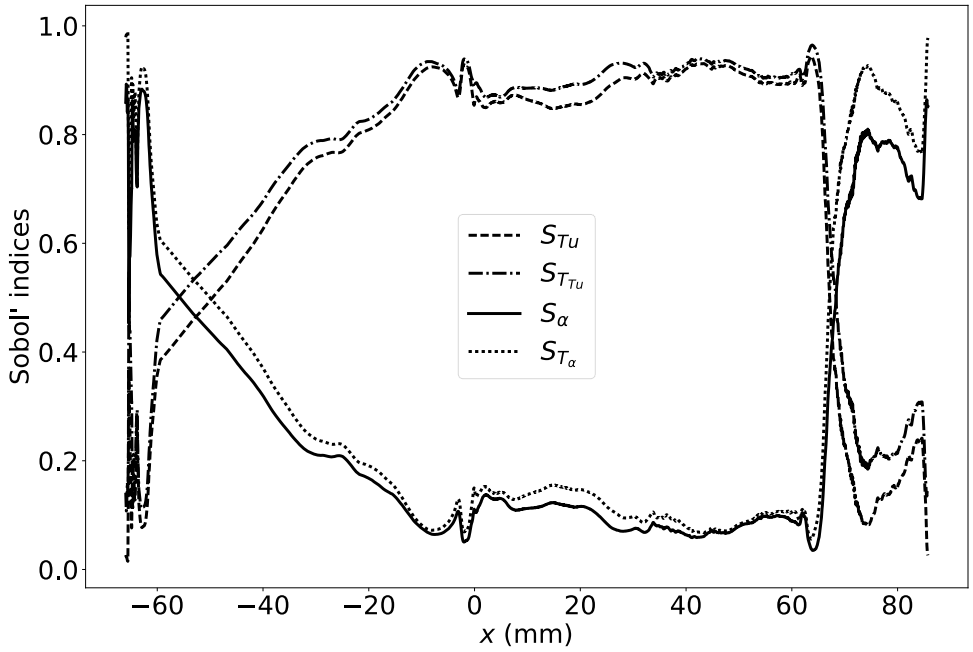

FIGURE 16 First order and total order *Sobol'* indices along the chord line.

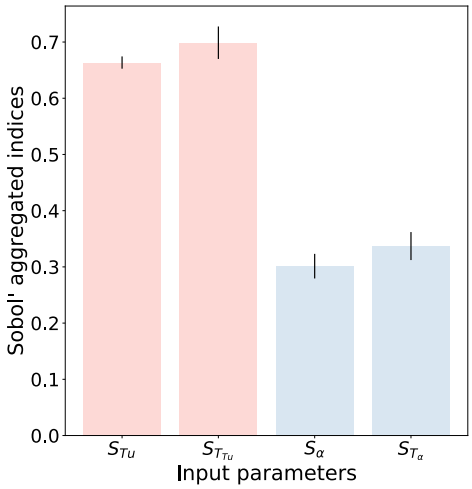

FIGURE 17 Aggregated *Sobol'* indices of the input parameters with their asymptotic confidence intervals.

[2] Forrester Alexander I J, Keane Andy J.. Recent advances in surrogate-based optimization. *Progress in Aerospace Sciences.* 2009;45(1-3):50–79.

[3] Draper David. Assessment and Propagation of Model Uncertainty. *Journal of the Royal Statistical Society B.* 1995;57(1):45–97.

[4] Sacks Jerome, Welch Williams J., Mitchell Toby J., Wynn Henry P.. Design and Analysis of Computer Experiments. *Statistical Science.* 1989;4(4):409–423.

[5] DeGennaro Anthony M., Rowley Clarence W., Martinelli Luigi. Uncertainty Quantification for Airfoil Icing Using Polynomial Chaos Expansions. *Journal of Aircraft.* 2015;52(5):1404–1411.

[6] Masquelet Matthieu, Yann Jin, Dord Anne, et al. Uncertainty Quantification in Large Eddy Simulations of a Rich-Dome Aviation Gas Turbine. In: :1–11; 2017.

[7] Saltelli Andrea, Ratto Marco, Andres Terry, et al. *Global Sensitivity Analysis. The Primer.* Chichester, UK: John Wiley & Sons, Ltd; 2007.

[8] Martin Jay D., Simpson Timothy W.. Use of Kriging Models to Approximate Deterministic Computer Models. *AIAA Journal.* 2005;43(4):853–863.

[9] Najm Habib N. Uncertainty Quantification and Polynomial Chaos Techniques in Computational Fluid Dynamics. *Annual Review of Fluid Mechanics.* 2009;41(1):35–52.

[10] Rasmussen C.E., Williams C. *Gaussian processes for machine learning.* MIT Press; 2006.

[11] Braconnier T., Ferrier M., Jouhaud J.-C., Montagnac M., Sagaut P.. Towards an adaptive POD/SVD surrogate model for aeronautic design. *Computers & Fluids.* 2011;40(1):195–209.

[12] Margheri Luca, Sagaut Pierre. A hybrid anchored-ANOVA âĂŞ POD/Kriging method for uncertainty quantification in unsteady high-fidelity CFD simulations. *Journal of Computational Physics*. 2016;324:137–173.

[13] Owen N. E., Challenor P., Menon P. P., Bennani S.. Comparison of surrogate-based uncertainty quantification methods for computationally expensive simulators. 2015;:1–10.

[14] Roy Pamphile T., El MoĂğayd Nabil, Ricci Sophie, et al. Comparison of Polynomial Chaos and Gaussian Process surrogates for uncertainty quantification and correlation estimation of spatially distributed open-channel steady flows. *Under Final review to Stochastic Environmental Research and Risk Assessment*. 2017;.

[15] Iooss B., Boussouf L., Feuillard V., Marrel A.. Numerical studies of the metamodel fitting and validation processes. *International Journal on Advances in Systems and Measurements*. 2010;3(1):11–21.

[16] Arts Tony, Lambert de Rouvroit M, Rutherford A W. *Aero-Thermal Investigation of a Highly Loaded Transonic Linear Turbine Guide Vane Cascade.* 174: von Karman Institute for Fluid Dynamics; 1990.

[17] Anindya Chatterjee . An introduction to the proper orthogonal decomposition. *Current Science*. 2000;78(7).

[18] Sirovich Lawrence. Turbulence and the dynamics of coherent structures part i: coherent structures. *Quarterly of Applied Mathematics*. 1987;XLV(3):561–571.

[19] Krige D G, Guarascio M, Camisani-Calzolari F A. Early South African geostatistical techniques in today's perspective. *Geostatistics*. 1989;1:1–19.

[20] Marrel Amandine, Iooss Bertrand, Laurent Beatrice, Roustant Olivier. Calculations of Sobol indices for the Gaussian process metamodel. *Reliability Engineering & System Safety*. 2009;94(3):742 - 751.

[21] Kohavi Ron. A Study of Cross-Validation and Bootstrap for Accuracy Estimaiton and Model Selection. In: ; 1995.

[22] Forrester Alexander I.J., Sóbester András, Keane Andy J. Multi-fidelity optimization via surrogate modelling. *Proceedings of the Royal Society A: Mathematical, Physical and Engineering Sciences*. 2007;463(2088):3251–3269.

[23] Iooss B., Saltelli A.. Introduction to Sensitivity Analysis. In: Springer International Publishing 2016 (pp. 1–20).

[24] Ferretti Federico, Saltelli Andrea, Tarantola Stefano. Trends in sensitivity analysis practice in the last decade. *Science of The Total Environment*. 2016;568:666–670.

[25] SobolâĂš I.M. Sensitivity analysis for nonlinear mathematical models. *Mathematical Modeling and Computational Experiment*. 1993;1(4):407–414.

[26] Marrel Amandine, Saint-Geours Nathalie, De Lozzo Matthias. Sensitivity Analysis of Spatial and/or Temporal Phenomena. In: Springer International Publishing 2015 (pp. 1–31).

[27] Baudin Michaël, Boumhaout Khalid, Delage Thibault, Iooss Bertrand, Martinez Jean-Marc. Numerical stability of Sobol' indices estimation formula. In: ; 2016; Réunion Island.

[28] Cavazzuti Marco. Design of Experiments. In: Springer Berlin Heidelberg 2013 (pp. 13–42).

[29] Fang Kai-Tai, Li R Z, Sudjianto A. *Design and modeling for computer experiments*. 2006.

[30] Damblin Guillaume, Couplet Mathieu, Iooss Bertrand, Damblin Guillaume, Couplet Mathieu, Iooss Bertrand. Numerical studies of space filling designs : optimization of Latin Hypercube Samples and subprojection properties. *Journal of Simulation*. 2013;:276–289.

[31] Mckay M. D., Beckman R .J., Conover W. J.. A Comparison of Three Methods for Selecting Values of Input Variables in the Analysis of Output from a Computer Code. *Technometrics*. 1979;21(2):239–245.

[32] Scheidt Céline. Analyse statistique d'expériences simulées : Modélisation adaptative de réponses non-régulières par krigeage et plans d'expériences, Application à la quantification des incertitudes en ingénierie des réservoirs pétroliers. PhD thesisLouis Pasteur2006.

[33] Wales David J., Doye Jonathan P. K.. Global Optimization by Basin-Hopping and the Lowest Energy Structures of Lennard-Jones Clusters Containing up to 110 Atoms. *The Journal of Physical Chemistry A*. 1997;101(28):5111–5116.

[34] Smith Warren D., Wormald Nick. Geometric Separator Theorems and Applications. In: ; 1998.

[35] Molga Marcin, Smutnicki Czesław. Test functions for optimization needs. 2005;(c):1–43.

[36] Ishigami T., Homma T.. An importance quantification technique in uncertainty analysis for computer models. *IEEE*. 1990;:398–403.

[37] Dette Holger, Pepelyshev Andrey. Generalized Latin Hypercube Design for Computer Experiments. *Technometrics*. 2010;52(4):421–429.

[38] Marrel Amandine, Iooss Bertrand, Da Veiga Sébastien, Ribatet Mathieu. Global sensitivity analysis of stochastic computer models with joint metamodels. *Statistics and Computing*. 2012;22(3):833–847.

[39] Gourdain N., Duchaine F., Collado E., Gicquel L.. Advanced Numerical Simulation Dedicated to the Prediction of Heat Transfer in a Highly Loaded Turbine Guide Vane.. In: GT2010-22793 , ed. *ASME Turbo expo*, ; 2010; Glasgow, UK.

[40] Emory Michael, Iaccarino Gianluca, Ma Lynn. Uncertainty Quantification in Turbomachinery Simulations. In: :1–10; 2016.

[41] Wheeler A.P.S., Sandberg R.D., Sandham N.D., Pichler R., Michelassi V., Laskowski G.. Direct numerical Simulations of a High Pressure Turbine Vane. In: :GT2015-43133; 2015; Montreal, Canada.

[42] Segui L.M., Gicquel L.Y.M., Duchaine F., Laborderie J.. LES of the LS89 cascade: influence of inflow turbulence on the flow predictions. In: ; 2017.

[43] Fontaneto F.. Aero-thermal performance of a film-cooled high pressure turbine blade/vane: a test case for numerical codes validation. PhD thesisUniversity of Bergamo2014.

[44] Pichler R., Kopriva J., Laskowski G., Michelassi V., Sandberg R.. Highly resolved LES of a Linear HPT Vane Cascade using structured and unstructured codes. In: GT2016-57189; 2016; Seoul, South Korea.

[45] Gicquel L.Y.M., Gourdain N., Boussuge J.-F., et al. High performance parallel computing of flows in complex geometries. *Comptes Rendus Mécanique*. 2011;339(2-3):104 - 124.

[46] Quartapelle L., Selmin V.. *High-order Taylor-Galerkin methods for non-linear multidimensional problems.*. 1993.

[47] Nicoud F., Ducros F.. Subgrid-scale stress modelling based on the square of the velocity gradient. *Flow Turb. and Combustion*. 1999;62(3):183-200.

[48] Wand M. P., Jones M. C.. *Kernel Smoothing*. Boston, MA: Springer US; 1995.

[49] Hastie Trevor, Tibshirani Robert, Friedman Jerome. *The Elements of Statistical Learning* Springer Series in Statistics, vol. 2: . New York, NY: Springer New York; 2009.

[50] Segui L.M.. Multiphysics Coupled Simulations of Gas Turbines. Unpublished. PhD thesis2017.

How cite this article: P.T. Roy, L.M. Segui, J.-C. Jouhaud, and L. Gicquel (2017), Resampling Strategies to Improve Surrogate Model-based Uncertainty Quantification - Application to LES of LS89., *International Journal for Numerical Methods in Engineering*, *2017;00:1–6*.

Bibliography

[1] Q. Abbas and J. Nordström. Weak versus strong no-slip boundary conditions for the navier-stokes equations. *Engineering Applications of Computational Fluid Mechanics*, 4 (1):29–38, 2010. (page 57)

[2] R. Abgrall and M. Mezine. Construction of a second order accurate monotone and stable residual distribution schemes: the unsteady case. *J. Comput. Phys.* , 188:16–55, 2002. (page 25)

[3] R. Abgrall, A. Larat, and M. Ricchiuto. Construction of very high order residual distribution schemes for steady inviscid flow problems on hybrid unstructured meshes. *Journal of Computational Physics*, 230(11):4103–4136, 2011. (page 28)

[4] B. Abu-Ghannam and R. Shaw. Natural transition of boundary layers-the effects of turbulence, pressure gradient, and flow history. *Journal of Mechanical Engineering Science*, 22(5):213–228, 1980. (page 113)

[5] R. J. Adrian. Hairpin vortex organization in wall turbulence. *Phys. Fluids* , 19(041301): 1–16, 2007. doi: 10.1063/1.2717527. (page 125)

[6] R. A. Antonia, A. J. Chambers, M. Sokolov, and C. W. V. Atta. Simultaneous temperature and velocity measurements in the plane of symmetry of a transitional turbulent spot. *Journal of Fluid Mechanics*, 108:317–343, 1981. (page 127)

[7] T. Arts, M. de Rouvroit, Lambert, and A. Rutherford. Technical report, Von Karman Institute for Fluid Dynamics, 1990. (page 8, 9, 79, 88, 89, 99, 103, 123, 164)

[8] M. Asai, Y. Konishi, Y. Oizumi, and M. Nishioka. Growth and breakdown of low-speed streaks leading to wall turbulence. *Journal of Fluid Mechanics*, 586:371–396, 2007. (page 125)

[9] V. Auffray. *Étude comparative de schémas numériques pour la modélisation de phénoménes diffusifs surmaillages hybrides.* PhD thesis, Institut National Polytechnique de Toulouse, 2007. (page 22, 23, 43)

[10] C. Bailly and C. Bogey. An overview of numerical methods for acoustic wave propagation. In *ECCOMAS CFD 2006: Proceedings of the European Conference on Computational Fluid Dynamics, Egmond aan Zee, The Netherlands, September 5-8, 2006.* Delft University of Technology; European Community on Computational Methods in Applied Sciences (ECCOMAS), 2006. (page 63, 65)

[11] T. Barth. Aspects of unstructured grids and finitevolume solvers for the euler and navier-stokes equations. In *VKI Lecture Series 1994–04*. Von Karman Institute for Fluid Dynamics, 1994. (page 46)

[12] T. Barth and P. Frederickson. Higher order solution of the euler equations on unstructured grids using quadratic reconstruction. In *28th aerospace sciences meeting*, page 13, 1990. (page 162)

[13] T. J. Barth. A 3-d upwind euler solver for unstructured meshes. *AIAA Computational Fluids Dynamics Conference. AIAA paper 1991-1548*, pages 228–238. (page 46)

[14] G. K. Batchelor. An introduction to fluid mechanics. pages 131–132. Cambridge University Press, 1967. (page 2)

[15] G. K. Batchelor and A. A. Townsend. Decay of Vorticity in Isotropic Turbulence. *Proceedings of the Royal Society A: Mathematical, Physical and Engineering Sciences*, 190 (1023):534–550, 1947. (page 183)

[16] G. K. Batchelor and A. A. Townsend. Decay of Turbulence in the Final Period. *Proceedings of the Royal Society A: Mathematical, Physical and Engineering Sciences*, 194 (1039):527–543, 1948. (page xvi, 183, 184)

[17] R. M. Beam, R. F. Warming, and H. C. Yee. Stability analysis of numerical boundary conditions and implicit difference approximations for hyperbolic equations. *J. Comput. Phys.* , 48:200–222, 1982. (page 30)

[18] R. Bhaskaran and S. Lele. Heat transfer prediction in high pressure turbine cascade with free-stream turbulence using les. In *41st AIAA Fluid Dynamics*, Honolulu, Hawaii, 2011. AIAA 2015-3266. (page 88)

[19] R. Blackwelder and H. Eckelmann. Streamwise vortices associated with the bursting phenomenon. *Journal of Fluid Mechanics*, 94(03):577–594, 1979. (page 82)

[20] M. Blair. Boundary-layer transition in accelerating flows with intense freestream turbulence: part 1-disturbances upstream of transition onset. *TRANSACTIONS-AMERICAN SOCIETY OF MECHANICAL ENGINEERS JOURNAL OF FLUIDS ENGINEERING*, 114:313–313, 1992. (page 127)

[21] J. Blazek. *Computational fluid dynamics: principles and applications*. Butterworth-Heinemann, 2015. (page 58, 157)

[22] G. Boudier, L. Gicquel, T. Poinsot, B. D., and C. Bérat. Comparison of les, rans and experiments in an aeronautical gas turbine combustion chamber. *Proceedings of the Combustion Institute*, 31:3075–3082, 2007. (page 18)

[23] J. Boussinesq. Théorie de l'écoulement tourbillant. *Mém. Présentés par Divers Savants. Acad. Sci. Inst. Fr.*, 23:46–50, 1877. (page 17)

[24] P. Bradshaw. 'inactive' motion and pressure fluctuations in turbulent boundary layers. *Journal of Fluid Mechanics*, 30(02):241–258, 1967. (page 128)

[25] P. Bradshaw. *Introduction to turbulence and its measurements*. Pergamon Press, Oxford, 1971. (page 16)

[26] L. Brandt, P. Schlatter, and D. Henningson. Transition in boundary layers subject to free-stream turbulence. *Journal of Fluid Mechanics*, 517:167–198, 2004. (page 85)

[27] H. Brezis. *Functional Analysis, Sobolev Spaces and Partial Differential Equations*. Springer, 2010. (page 2, 24)

[28] J.-C. Carette, H. Deconinck, H. Paillere, and P. Roe. Multidimensional upwinding: its relation to finite elements. *International Journal for Numerical Methods in Fluids*, 20 (8-9):935–955, 1995. (page 28)

[29] CERFACS. *AVBP Handbook - http://cerfacs.fr/∼ avbp/AVBP_ V5.X/HANDBOOK*. CERFACS, 2009. (page xiii, 26, 154)

[30] D. R. Chapman and G. D. Kuhn. The limiting behaviour of turbulence near a wall. *J. Fluid Mech.* , 170:265–292, 1986. (page 115, 177)

[31] H. Choi and P. Moin. Grid-point requirements for large eddy simulation: Chapman's estimates revisited. *Phys. Fluids* , 24(1):011702, 2012. (page 21)

[32] K.-S. Choi and J. Lumley. The return to isotropy of homogeneous turbulence. *Journal of Fluid Mechanics*, 436:59–84, 2001. (page 134)

[33] B. Cockburn and C. W. Shu. Runge-kutta discontinuous galerkin methods for convection-dominated problems. *J. Sci. Comput.* , 16:173 – 261, 2001. (page 30)

[34] O. Colin. *Simulations aux grandes échelles de la combustion turbulente prémélangée dans les statoréacteurs*. Phd thesis, INP Toulouse, 2000. (page 51)

[35] O. Colin. A finite element operator for diffusion terms in avbp. Technical report, Institut Francais du Pétrole, 2003. (page 47, 48)

[36] O. Colin and M. Rudgyard. Development of high-order taylor-galerkin schemes for unsteady calculations. *J. Comput. Phys.* , 162(2):338–371, 2000. (page 45, 46, 65, 198)

[37] O. Colin, F. Ducros, D. Veynante, and T. Poinsot. A thickened flame model for large eddy simulations of turbulent premixed combustion. *Phys. Fluids* , 12(7):1843–1863, 2000. (page 40, 41, 43, 44, 197)

[38] E. Collado Morata, N. Gourdain, F. Duchaine, and L. Gicquel. Effects of free-stream turbulence on high pressure turbine blade heat transfer predicted by structured and unstructured les. *International Journal of Heat and Mass Transfer*, 55(21-22):5754 – 5768, 2012. (page 88, 101, 117)

[39] T. Colonius. Numerically nonreflecting boundary and interface conditions for compressible flow and aeroacoustic computations. *AIAA Journal* , 35(7):1126–1133, 1997. (page 140, 146)

[40] H. Consigny and B. E. Richards. Short Duration Measurements of Heat-Transfer Rate to a Gas Turbine Rotor Blade. *Journal of Engineering for Power*, 104(3):542, 1982. (page 89)

[41] R. Courant, K. Friedrichs, and H. Lewy. On the partial difference equations of mathematical physics. *IBM J.*, 11:215–234, 1967. (page 29)

[42] J. Cousteix. *Turbulence et couche limite*. Cépaduès-éditions, 1989. (page 127)

[43] J. Crank and P. Nicolson. A practical method for numerical evaluation of solutions of partial differential equations of the heat-conduction type. *Mathematical Proceedings of the Cambridge Philosophical Society*, 43(1):50–67, 1947. (page 60)

[44] P. I. Crumpton. An efficient cell vertex method for unstructured tetrahedral grids. Technical Report 95/19, Oxford University Computing Laboratory, 1995. (page 34)

[45] P. I. Crumpton, J. A. Mackenzie, and K. W. Morton. Cell vertex algorithms for the compressible navier-stokes equations. *J. Comput. Phys.* , 109:1–15, 1993. (page xiii, 25, 34, 57)

[46] G. Daviller, M. Brebion, P. Xavier, G. Staffelbach, J.-D. Müller, and T. Poinsot. A mesh adaptation strategy to predict pressure losses in les of swirled flows. *Flow, Turbulence and Combustion*, pages 1–26, 2017. (page 19)

[47] J. W. Deardorff. A numerical study of three-dimensional turbulent channel flow at large reynolds numbers. *J. Fluid Mech.* , 41(2):453–480, 1970. doi: 10.1017/S0022112070000691. (page 20)

[48] H. Deconinck, K. Sermeus, and R. Abgrall. Status of multidimensional upwind residual distribution schemes and applications in aeronautics. In *AIAA CFD Conference*, Denver, CO, 2000. (page 34)

[49] J. C. del Álamo, J. Jiménez, P. Zandonade, and R. D. Moser. Scaling of the energy spectra of turbulent channels. *J. Fluid Mech.* , 500:135–144, 2004. doi: 10.1017/S002211200300733X. (page 18)

[50] N. Dhamankar, G. Blaisdell, and A. Lyrintzis. An overview of turbulent inflow boundary conditions for large eddy simulations. In *22nd AIAA Aviation*, Dallas, 2015. AIAA 2015-3213. (page 96, 181)

[51] S. Diot, S. Clain, and R. Loubère. The mood method in the three-dimensional case: Very-high-order finite volume method for hyperbolic systems. *Int. J. Numer. Meth. Fluids* , 73:362–392, 2013. (page 162)

[52] J. Donea. Taylor-galerkin method for convective transport problems. *Int. J. Numer. Meth. Fluids* , 20(1):101–119, 1984. (page 39, 40)

[53] J. Donea and A. Huerta. *Finite Element Methods for Flow Problems*. John Wiley & Sons Inc, New York, 2003. (page 60, 142)

[54] J. Donea, L. Quartapelle, and V. Selmin. An analysis of time discretization in the finite element solution of hyperbolic problems. *J. Comput. Phys.* , 70:463–499, 1987. (page 40, 58, 61, 68)

[55] P. G. Drazin and W. H. Reid. *Hydrodynamic stability*. Cambridge University Press, London, 1981. (page 84)

[56] E. R. V. Driest. On turbulence flow near a wall. *J. Aeronaut. Sci.* , 23(11):1007–1011, 1036, 1956. (page 178)

[57] A. Dróżdż. Influence of pressure gradient on streamwise skewness factor in turbulent boundary layer. In *Journal of Physics: Conference Series*, volume 530, page 012061. IOP Publishing, 2014. (page 128)

[58] F. Duchaine, S. Jauré, D. Poitou, E. Quémerais, G. Staffelbach, T. Morel, and L. Gicquel. Analysis of high performance conjugate heat transfer with the openpalm coupler. *Journal of Computational Science and Discovery 8*, 015003, 2015. (page 182)

[59] F. Ducros, F. Nicoud, and T. Poinsot. Wall-adapating local eddy-viscosity models for simulations in complex geometries. In *ICFD*, pages 293–300. Baines M. J., 1998. (page 179)

[60] C. Duprat, G. Balarac, O. Métais, P. Congedo, and O. Brugière. A wall-layer model for large-eddy simulations of turbulent flows with/out pressure gradient,. *Physics of fluids*, 23, 2011. (page 21)

[61] H. Emmons. The laminar-turbulent transition in a boundary layer-part i. *Journal of the Aeronautical Sciences*, 2012. (page 84)

[62] M. Emory, G. Iaccarino, and G. Laskowski. Uncertainty quantification in turbomachinery simulations. In *ASME Turbo Expo 2016: Turbomachinery Technical Conference and Exposition*, pages V02CT39A028–V02CT39A028. American Society of Mechanical Engineers, 2016. (page 88)

[63] V. Eswaran and S. B. Pope. Direct numerical simulations of the turbulent mixing of a passive scalar. *Phys. Fluids* , 31:506, 1988. (page 182)

[64] M. Falese. *A study of the effects of bifurcations in swirling flows using Large Eddy Simulation and mesh adaptation*. PhD thesis, Université de Toulouse, 2013. (page 19)

[65] C. A. J. Fletcher. *Computational Techniques for Fluid Dynamics*, volume 1. Springer, 2nd edition, 1991. (page 43)

[66] F. Fontaneto. *Aero-thermal performance of a film-cooled high pressure turbine blade/vane: a test case for numerical codes validation*. PhD thesis, University of Bergamo, 2014. (page 89, 92, 93, 103, 117, 138)

[67] N. Frink. Upwind scheme for solving the euler equations on unstructured tetrahedral meshes. *AIAA journal*, 30(1):70–77, 1992. (page 58)

[68] M. Germano. Turbulence: the filtering approach. *J. Fluid Mech.* , 238:325–336, 1992. (page 177)

[69] G. Ghorbaniasl and C. Lacor. Sensitivity of SGS models and of quality of LES to grid irregularity. In J. Meyers, B. J. Geurts, and P. Sagaut, editors, *Quality and Reliability of Large-Eddy Simulations*, volume 12 of *ERCOFTAC Series*, pages 155–166. Springer Netherlands, 2008. doi: 10.1007/978-1-4020-8578-9_13. (page 19)

[70] S. K. Godunov. A finite difference method for the numerical computation of discontinuous solution of the equations of gas dynamics. *Mat. Sb.*, 47, 1959. (page 3)

[71] N. Gourdain. High-performance computing of gas turbine flows: current and future trends. *Habilitation a diriger des recherches*, 17(60):208, 2011. (page 81)

[72] N. Gourdain, F. Duchaine, E. Collado, and L. Gicquel. Advanced numerical simulation dedicated to the prediction of heat transfer in a highly loaded turbine guide vane. In GT2010-22793, editor, *ASME Turbo expo*, Glasgow, UK, June 2010. (page 88)

[73] P. Gresho and R. Lee. Don't suppress the wiggles-they're telling you something! *Computers & Fluids*, 9(2):223–253, 1981. (page 55)

[74] B. Gustafsson and A. Sundstrøm. Incompletely parabolic problems in fluid dynamics. *SIAM J. Appl. Math.* , 35(2):343–357, 1978. (page 56)

[75] B. Gustafsson, H.-O. Kreiss, and A. Sundström. Stability theory of difference approximations for mixed initial boundary value problems. II. *Math. Comp.* , 26(119):649–686, July 1972. ISSN 0025-5718 (print), 1088-6842 (electronic). (page 57, 74, 144)

[76] M. Hadziabdic and K. Hanjalic. Vortical structures and heat transfer in a round impinging jet. *Journal of Fluid Mechanics*, 596:221–260, 2008. (page 124)

[77] X. He and L.-S. Luo. Theory of the lattice boltzmann method: From the boltzmann equation to the lattice boltzmann equation. *Phys. Rev. E*, 56:6811–6817, Dec 1997. (page 3)

[78] C. Hirsch. *Numerical Computation of Internal and External Flows*, volume 2. John Wiley & Sons, New York, 1990. (page 22, 30, 140)

[79] C. Hirsch. Finite volume method and conservative discretization with an introduction to finite element method. In *Numerical Computation of internal & external flows: Fundamentals of Computational Fluid Dynamics, second edition*, chapter 5, pages 203–248. John Wiley & Sons, New York, 2007. (page xvi, 22, 143, 144)

[80] J. Hunt, O. Phillips, and D. Williams. Turbulence and Stochastic Processes: Kolmogorov's Ideas 50 Years On. *Journal of Fluid Mechanics*, 275:406–408, 1994. (page 181)

[81] R. G. Jacobs and P. a. Durbin. Simulations of bypass transition. *Journal of Fluid Mechanics*, 428:185–212, 2001. (page 85, 116)

[82] A. Jalali and C. Ollivier-Gooch. Accuracy assessment of finite volume discretizations of convective fluxes on unstructured meshes. In *51st AIAA Aerospace Sciences Meeting including the New Horizons Forum and Aerospace Exposition*, page 705, 2013. (page 158)

[83] A. Jameson. Computational fluid dynamics: Past, present and future, 2012. (page xiii, 5)

[84] A. Jameson, W. Schmidt, and E. Turkel. Numerical solution of the euler equations by finite volume methods using runge-kutta time stepping schemes. In A. p. 81-1259, editor, *14th Fluid and Plasma Dynamic Conference*, Palo Alto, 1981. (page 30, 50, 51)

[85] J. Jiménez. Near-wall turbulence. *Physics of Fluids*, 25(10), 2013. (page 82)

[86] J. Jiménez and A. Pinelli. The autonomous cycle of near-wall turbulence. *Journal of Fluid Mechanics*, 389(1999):335–359, 1999. (page 85, 87)

[87] J. Jiménez, J. C. del Álamo, and O. Flores. The large-scale dynamics of near-wall turbulence. *J. Fluid Mech.* , 505:179–199, 2004. doi: 10.1017/S0022112004008389. (page 18)

[88] F. Johnson, E. Tinoco, and J. Yu. Thirty years of development and application of cfd at boeing commercial airplanes, seattle. In *16th AIAA Computational Fluid Dynamics Conference*. AIAA 2003-3439, 2003. (page 4)

[89] Y. Kachanov. Physical mechanisms of laminar-boundary-layer transition. *Annual review of fluid mechanics*, 26(1):411–482, 1994. (page xiv, 85)

[90] G. Kawahara, J. Jiménez, M. Uhlmann, and A. Pinelli. The instability of streaks in near-wall turbulence. 1998. (page 83)

[91] H. Kim, S. Kline, and W. Reynolds. The production of turbulence near a smooth wall in a turbulent boundary layer. *Journal of Fluid Mechanics*, 50(01):133–160, 1971. (page 82)

[92] J. Kim, P. Moin, and R. Moser. Turbulence statistics in fully developed channel flow at low Reynolds number. *J. Fluid Mech.* , 177:133–166, 1987. (page 128, 130)

[93] P. Klebanoff, K. Tidstrom, and L. Sargent. The three-dimensional nature of boundary-layer instability. *J. Fluid Mech*, 12(1):1–34, 1962. (page 84)

[94] S. J. Kline, W. C. Reynolds, F. A. Schraub, and P. W. Runstadler. The structure of turbulent boundary layers. *J. Fluid Mech.* , 30(4):741–773, 1967. doi: 10.1017/S0022112067001740. (page 82, 85)

[95] A. N. Kolmogorov. The local structure of turbulence in incompressible viscous fluid for very large reynolds numbers. *C. R. Acad. Sci. , USSR*, 30:301, 1941. (page 18)

[96] R. Kraichnan. Diffusion by a random velocity field. *Phys. Fluids* , 13:22–31, 1970. (page 96)

[97] A. G. Kravchenko and P. Moin. On the effect of numerical errors in large eddy simulations of turbulent flows. *J. Comput. Phys.* , 131(2):310–322, March 1997. doi: 10.1006/jcph.1996.5597. (page 171)

[98] H.-O. Kreiss. Stability theory for difference approximations of mixed initial boundary value problems. I. *Math. Comp.* , 22(104):703–714, Oct. 1968. ISSN 0025-5718 (print), 1088-6842 (electronic). (page 57)

[99] N. Lamarque. *Schémas numériques et conditions limites pour la simulation aux grandes échelles de la combustion diphasique dans les foyers d'hélicoptère.* Phd thesis, INP Toulouse, 2007. (page xvi, 57, 58, 59, 148)

[100] N. Lamarque and T. Poinsot. Boundary conditions for acoustic eigenmodes computation in gas turbine combustion chambers. *AIAA Journal* , 46(9):2282–2292, 2008. (page 142, 148, 156)

[101] N. Lamarque, M. Porta, F. Nicoud, and T. J. Poinsot. On the stability and dissipation of wall boundary conditions for compressible flows. *International Journal for Numerical Methods in Fluids*, 62:1134–1154, 2010. jx. (page 53, 140, 149)

[102] J. Lambert. Computational methods in ordinary differential equations. 1973. (page 30)

[103] P. Lax and R. Richtmyer. Survey of the stability of linear finite difference equations. *Comm. Pure Appl. Math*, 9:267–293, 1956. (page 3)

[104] P. D. Lax and B. Wendroff. Difference schemes for hyperbolic equations with high order of accuracy. *Commun. Pure Appl. Math.* , 17:381–398, 1964. (page 37)

[105] M. Lee, J. Kim, and P. Moin. Structure of turbulence at high shear rate. *Journal of Fluid Mechanics*, 216:561–583, 1990. (page 82)

[106] S. Lee, S. Lele, and P. Moin. Simulation of spatially evolving turbulence and the applicability of taylor's hypothesis in compressible flows. *Phys. Fluids A*, 4(7):1521–1530, 1992. (page 182)

[107] S. Lele. Compact finite difference schemes with spectral like resolution. *J. Comput. Phys.* , 103:16–42, 1992. (page 19, 26)

[108] H. Lewy, K. Friedrichs, and R. Courant. Uber die partiellen differenzengleichungen der mathematischen physik. *Mathematische Annalen*, 100:32–74, 1928. (page 2)

[109] D. K. Lilly. A proposed modification of the germano sub-grid closure method. *Phys. Fluids* , 4(3):633–635, 1992. URL LES. (page 17, 178)

[110] G. Lodato, P. Domingo, and V. L. Three-dimensional boundary condtions for direct and large-eddy simulation of compressible viscous flow. *J. Comput. Phys.* , 227(10): 5105–5143, 2008. (page 54)

[111] S. Lu and W. Willmarth. Measurements of the structure of the reynolds stress in a turbulent boundary layer. *Journal of Fluid Mechanics*, 60(03):481–511, 1973. (page 129, 134)

[112] J. L. Lumley. Computational modeling of turbulent flows. *Adv. Appl. Mech.* , 18:123–176, 1978. (page 123, 134)

[113] T. S. Lund, X. Wu, and K. D. Squires. Generation of turbulent inflow data for spatially-developing boundary layer simulations. *J. Comput. Phys.* , 140(2):233–258, 1998. doi: 10.1006/jcph.1998.5882. (page 96, 182)

[114] N. Maheu, V. Moureau, P. Domingo, F. Duchaine, and G. Balarac. Large-eddy simulations of flow and heat transfer around a low-mach number turbine blade. In Center for Turbulence Research, NASA Ames/Stanford Univ., editor, *Proc. of the Summer Program* , 2012. (page 21)

[115] I. Marusic, B. McKeon, P. Monkewitz, H. Nagib, A. Smits, and K. Sreenivasan. Wall-bounded turbulent flows at high reynolds numbers: Recent advances and key issues. *Physics of Fluids*, 22(6):065103, 2010. (page 21)

[116] R. Mathis, N. Hutchins, and I. Marusic. Relationship between turbulence modulation and skewness in wall bounded flows. In *TSFP DIGITAL LIBRARY ONLINE*. Begel House Inc., 2011. (page 128)

[117] M. Matsubara and P. Alfredsson. Free stream turbulence induced boundary layer transition. *Bull. Am. Phys. Soc*, 40(12):1956, 1995. (page 85)

[118] J. D. Mattingly. *Elements of gas turbine propulsion*. AIAA, 2nd edition, 2005. (page 7)

[119] D. Mavriplis. Revisiting the least-squares procedure for gradient reconstruction on unstructured meshes. In *16th AIAA Computational Fluid Dynamics Conference*, page 3986, 2003. (page 158)

[120] R. E. Mayle. The role of laminar-turbulent transition in gas turbine engines. *J. Turbomach.* , 113:509–537, October 1991. (page xiv, 84, 86, 87, 110, 123)

[121] W. McMullan and G. Page. Towards large eddy simulation of gas turbine compressors. *Prog. in Astronautics and Aeronautics* , 52(0):30 – 47, 2012. (page 82)

[122] F. Menter. Zonal two equation k-w turbulence models for aerodynamic flows. In *23rd Fluid Dynamics, Plasmadynamics, and Lasers Conference*. AIAA 1993-2906, 1993. (page 4)

[123] M. M. Metzger and J. Klewicki. A comparative study of near-wall turbulence in high and low reynolds number boundary layers. *Physics of Fluids*, 13(3):692–701, 2001. (page 128)

[124] A. R. Mitchell and D. F. Griffiths. *The Finite Difference Method in Partial Differential Equations*. John Wiley and Sons, New York, 1980. (page 61, 144)

[125] M. Morkovin. On the many faces of transition. In *Viscous drag reduction*, pages 1–31. Springer, 1969. (page 84)

[126] K. W. Morton, M. Stynes, and E. Suli. Analysis of a cell-vertex finite volume method for convection-diffusion problems. *Mathematics of Computation*, 66(220):1389–1406, 1997. (page 25)

[127] G. Mouret, N. Gourdain, and L. Castillon. Adaptation of phase-lagged boundary conditions to large eddy simulation in turbomachinery configurations. *Journal of Turbomachinery*, 138(4):041003, 2016. (page 81)

[128] S. Nagarajan, S. Lele, and J. Ferziger. Leading-edge effects in bypass transition. *Journal of Fluid Mechanics*, 572:471–504, 2007. (page 85)

[129] R. Narasimha. On the distribution of intermittency in the transition region of a boundary layer, 1957. (page 127)

[130] R.-H. Ni. A multiple grid scheme for solving the Euler equations. *AIAA Journal*, 101 (20):1565–1571, 1982. (page 34, 38, 40)

[131] F. Nicoud. On the amplitude of waves in characteristic boundary conditions for euler equations. Technical Report TR/CFD/98/21, CERFACS, 1998. (page 53)

[132] F. Nicoud and F. Ducros. Subgrid-scale stress modelling based on the square of the velocity gradient. *Flow, Turb. and Combustion* , 62(3):183–200, 1999. (page 95, 178, 179)

[133] F. Nicoud, H. Baya Toda, O. Cabrit, S. Bose, and J. Lee. Using singular values to build a subgrid-scale model for large eddy simulations. *Phys. Fluids* , 23(8):085106, 2011. doi: 10.1063/1.3623274. (page 177, 179)

[134] K. Nolan, E. Walsh, and D. McEligot. Quadrant analysis of a transitional boundary layer subject to free-stream turbulence. *Journal of Fluid Mechanics*, 658:310–335, 2010. (page xv, 130)

[135] C. Ollivier-Gooch and M. Van Altena. A high-order-accurate unstructured mesh finite-volume scheme for the advection–diffusion equation. *Journal of Computational Physics*, 181(2):729–752, 2002. (page 157, 158)

[136] R. Paoli and K. Shariff. Turbulent condensation of droplets: direct simulation and a stochastic model. *J. Atmos. Sci.* , DOI 10.1175/2008JAS2734.1, 2008. (page 106, 182)

[137] D. Papadogiannis, F. Duchaine, L. Gicquel, G. Wang, and S. Moreau. Effects of subgrid scale modeling on the deterministic and stochastic turbulent energetic distribution in large-eddy simulations of a high-pressure turbine stage. *Journal of Turbomachinery*, 138 (9):091005, 2016. (page 178)

[138] T. Poinsot and S. Lele. Boundary conditions for direct simulations of compressible viscous flows. *J. Comput. Phys.* , 101(1):104–129, 1992. doi: 10.1016/0021-9991(92)90046-2. (page 53, 181, 182)

[139] T. Poinsot and D. Veynante. *Theoretical and Numerical Combustion*. Third Edition (www.cerfacs.fr/elearning), 2011. (page 54, 154, 171)

[140] S. B. Pope. *Turbulent flows*. Cambridge University Press, 2000. (page xiv, 19, 21, 83, 128, 175)

[141] S. B. Pope. Stochastic lagrangian models of velocity in homogeneous turbulent shear flow. *Phys. Fluids* , 14(5):1696–1702, 2002. (page 17, 18, 19)

[142] S. B. Pope. Ten questions concerning the large-eddy simulation of turbulent flows. *New Journal of Physics*, 6:35, 2004. (page 19)

[143] M. Porta. *Développement, vérification et validation des outils LES pour l'étude du bruit de combustion et de l'interaction combustion/acoustique/turbulence - TH/CFD/07/46*. PhD thesis, Institut National Polytechnique de Toulouse, France - Dynamique des Fluides, CERFACS - CFD Team, Toulouse, 2007. (page xix, 142, 154, 156)

[144] R. Prosser. Towards improved boundary conditions for the DNS and LES of turbulent subsonic flows. *J. Comput. Phys.* , 222:469–474, 2007. (page 53)

[145] G. Puigt, V. Auffray, and J.-D. Mueller. Discretisation of diffusive fluxes on hybrid grids. *Journal of Computational Physics*, 229(5):1425–1447, 2010. jx. (page 46)

[146] L. Quartapelle and V. Selmin. High-order Taylor-Galerkin methods for non-linear multidimensional problems., 1993. (page 40, 41, 95, 140)

[147] A. Quarteroni and A. Valli. *Domain Decomposition Methods for Partial Differential Equations*. Oxford Science Publications, 1999. (page 27)

[148] H. Reichardt. Über die geschwindigkeitsverteilung in einer geradlinigen turbulenten couetteströmung. *Z. Angew. Math. Mech.*, (36):26–29, 1959. (page 21)

[149] L. F. Richardson. The approximate arithmetical solution by finite differences of physical problems involving differential equations, with an application to the stresses in a masonry dam. *Philosophical Transactions of the Royal Society of London. Series A, Containing Papers of a Mathematical or Physical Character*, 210:307–357, 1910. (page 2, 3)

[150] A. W. Rizzi and M. Inouye. Time-split finite-volume method for three-dimensional blunt-body flow. *AIAA Journal* , 11(11):1478–1485, 1973. (page 27)

[151] S. Robinson. Coherent motions in the turbulent boundary layer. *Ann. Rev. Fluid Mech.* , 23:601–639, 1991. doi: 10.1146/annurev.fl.23.010191.003125. (page 83, 125)

[152] P. L. Roe. Approximate riemann solvers, parameter vectors and difference schemes. *J. Comput. Phys.* , 43:357–372, 1981. (page 28)

[153] P. Roy, L. Segui, J. Jouhaud, and L. Gicquel. Resampling strategies to improve surrogate model-based uncertainty quantification - application to les of ls89. *Submitted to International Journal for Numerical Methods in Fluids*, 2018. (page 138, 167)

[154] M. Rudgyard. Cell vertex methods for steady inviscid flow. In V. K. I. for Fluid Dynamics, editor, *Lectures Series 1993-04*, volume 1993-04. Von Karman Institute for Fluid Dynamics, 1993. (page 34, 50)

[155] A. Safjan and J. T. Oden. High-order taylor-galerkin methods for linear hyperbolic systems. *J. Comput. Phys.* , 120:206–230, 1994. (page 40)

[156] P. Sagaut. *Large eddy simulation for incompressible flows*. Springer, 2002. (page 173, 178)

[157] J. Scales. *Theory of Seismic Imaging*, volume 2. Springer-Verlag, 1995. (page 55)

[158] P. Schlatter, Q. Li, R. Örlü, F. Hussain, and D. Henningson. On the near-wall vortical structures at moderate reynolds numbers. *European Journal of Mechanics-B/Fluids*, 48: 75–93, 2014. (page 83)

[159] P. C. Schlatter. *Large-eddy simulation of transition and turbulence in wall-bounded shear flow*. PhD thesis, Swiss Federal Institute of Technology of Zurich, 2005. (page 134)

[160] H. Schlichting. *Boundary layer theory*. McGraw-Hill, New York, 1955. (page 84, 111)

[161] T. Schönfeld and M. Rudgyard. COUPL and its use within hybrid mesh CFD applications. In A. Ecer, D. Emerson, J. Périaux, and N. Satofuka, editors, *Proc. of the 10th International Conference on Parallel CFD 98*, Hsinchu, Taiwan, 1998. Elsevier, Amsterdam. (page 8)

[162] G. Schubauer and H. Skramstad. Laminar-boundary-layer oscillations and transition on a flat plate. 1948. (page 85)

[163] U. Schumann. Subgrid scale model for finite difference simulations of turbulent flows in plane channels and annuli. *J. Comput. Phys.* , 18:376–404, August 1975. (page 20)

[164] T. K. Sengupta. *Fundamentals of Computational Fluid Dynamics*. Universities Press, Hyderabad (India), 2004. (page 27)

[165] C. H. Sieverding. Recent progress in the understanding of basic aspects of secondary flows in turbine blade passages. *Transactions of the ASME Journal of Engineering for Gas Turbines and Power*, (April 1985), 1985. (page 110, 111)

[166] R. Simpson. Aspects of turbulent boundary-layer separation. *Progress in Aerospace Sciences*, 32(5):457–521, 1996. (page 86)

[167] J. Smagorinsky. General circulation experiments with the primitive equations: 1. the basic experiment. *Mon. Weather Rev.* , 91:99–164, 1963. (page 178)

[168] E. M. Smirnov and A. Smirnovsky. Turbine vane cascade heat transfer predictions using a modified version of the γ- $re_{\theta t}$ laminar-turbulent transition model. In *ICHMT DIGITAL LIBRARY ONLINE*. Begel House Inc., 2009. (page 88)

[169] T. M. Smith, B. D. Esser, N. Antolin, A. Carlsson, R. E. A. Williams, A. Wessman, T. Hanlon, H. L. Fraser, W. Windl, D. W. McComb, and M. J. Mills. Phase transformation strengthening of high-temperature superalloys. *Nature Communications*, 7:13434 EP –, 11 2016. (page 7)

[170] A. J. Smits, B. J. McKeon, and I. Marusic. High-reynolds number wall turbulence. *Annual Review of Fluid Mechanics*, 43:353–375, 2011. (page 128)

[171] P. Spalart, W.-H. Jou, M. Strelets, and S. Allmaras. Comments on the feasibility of les for wings, and on a hybrid rans/les approach. volume 11, 1997. (page 17, 21)

[172] P. R. Spalart. Strategies for turbulence modelling and simulations. *Int. J. Heat Fluid Flow* , 21(3):252–263, 2000. doi: 10.1016/S0142-727X(00)00007-2. (page 21)

[173] P. R. Spalart and S. R. Allmaras. A one equation turbulence model for aerodynamic flows. *AIAA Journal*, 92(0439), 1992. (page 18)

[174] D. B. Spalding. A novel finite difference formulation for differential expressions. *Int. J. Numer. Meth. Fluids* , 14, 1972. (page 4)

[175] J. C. Strikwerda. Initial boundary value problem for incompletely parabolic systems. *Commun. Pure Appl. Math.* , 30:797, 1977. (page 52)

[176] S. M. Stringer and K. W. Morton. Artificial viscosity for the cell vertex method. Technical report, Oxford University Computing Laboratory, 1996. (page 50, 51, 157)

[177] E. Suli. Finite volume methods on distorted meshes: stability, accuracy, adaptativity. Technical Report NA89/6, Oxford University Computing Laboratory, 1989. (page 25)

[178] S. Tavoularis, J. C. Bennett, and S. Corrsin. Velocity-derivative skewness in small Reynolds number, nearly isotropic turbulence. *Journal of Fluid Mechanics*, 88(01):63, 1978. (page xvi, 183, 184)

[179] G. I. Taylor. The spectrum of turbulence. *Proc. R. Soc. London Ser.*, A 164, 476, 1938. (page 93, 182)

[180] T. Theodorsen. Mechanism of turbulence. In *Proceedings of the Second Midwestern Conference on Fluid Mechanics*, volume 1719. Ohio State University, 1952. (page 83)

[181] K. W. Thompson. Time dependent boundary conditions for hyperbolic systems. *J. Comput. Phys.* , 68:1–24, 1987. (page 53)

[182] E. F. Toro. *Riemann Solvers and Numerical Methods for Fluid Dynamics*. 2009. (page 28)

[183] P. Tucker. Computation of unsteady turbomachinery flows: Part 2?les and hybrids. *Progress in Aerospace Sciences*, 47(7):546 – 569, 2011. (page 82)

[184] J. Tyacke and P. Tucker. Future use of large eddy simulation in aero-engines. *Journal of Turbomachinery*, 137(8):081005, 2015. (page 82)

[185] J. Vanharen, G. Puigt, X. Vasseur, J.-F. Boussuge, and P. Sagaut. Revisiting the spectral analysis for high-order spectral discontinuous methods. *Journal of Computational Physics*, 337:379–402, 2017. (page 53, 162)

[186] R. Vichnevetsky. Propagation and spurious reflection in finite-element approximations of hyperbolic equations. *Comp. & Maths. with Appls.*, 11(7-8):733–746, 1985. (page 56)

[187] R. Vichnevetsky and J. B. Bowles. *Fourier analysis of numerical approximations of hyperbolic equations*. SIAM Studies in Applied Mechanics, Philadelphia, 1982. (page xiii, 55, 56, 68)

[188] J. von Neumann and R. Richtmeyer. A method for the numerical calculation of hydrodynamic shocks. *J. Appl. Phys.* , 21:231, 1950. (page 3, 60, 61)

[189] G. Wang, F. Duchaine, D. Papadogiannis, I. Duran, S. Moreau, and L. Gicquel. An overset grid method for large eddy simulation of turbomachinery stages. *Journal of Computational Physics*, 274:333–355, 2014. (page 21, 165)

[190] M. Wang and P. Moin. Dynamic wall modeling for large-eddy simulation of complex turbulent flows. *Phys. Fluids* , 14(7):2043–2051, July 2002. doi: 10.1063/1.1476668. (page 21)

[191] R. F. Warming and B. Hyett. The Modified Equation Approach to the Stability and Accuracy of Finite Difference Methods. *Journal of Computational Physics*, 14:159–179, 1974. (page 59)

[192] A. Wheeler, R. Sandberg, N. Sandham, R. Pichler, V. Michelassi, and G. Laskowski. Direct numerical simulations of a high pressure turbine vane. In *ASME Turbo Expo 2015*, pages GT2015–43133, Montreal, Canada, 2015. (page 19, 82, 88, 89)

[193] F. M. White. *Viscous fluid flow*. McGraw-Hill, New-York, 1991. (page 84)

[194] F. Wlassow, F. Duchaine, G. Leroy, and N. Gourdain. 3d simulation of coupled fluid flow and solid heat conduction for the calculation of blade wall temperature in a turbine stage. In GT2010-22513, editor, *ASME Turbo expo*, Glasgow, UK, June 2010. (page xiii, 17)

[195] A. A. Wray. Minimal storage time advanced schemes for spectral methods. *J. Comput. Phys.* , 1990. (page 3)

[196] X. Wu and P. Durbin. Evidence of longitudinal vortices evolved from distorted wakes in a turbine passage. *Journal of Fluid Mechanics*, 446:199–228, 2001. (page 81)

[197] X. Wu and P. Moin. Direct numerical simulation of turbulence in a nominally zero-pressure-gradient flat-plate boundary layer. *J. Fluid Mech.* , 630:5–41, 2009. doi: 10.1017/S0022112009006624. (page 83)

[198] X. Wu, R. G. Jacobs, J. C. R. Hunt, and P. A. Durbin. Simulation of boundary layer transition induced by periodically passing wakes. *Journal of Fluid Mechanics*, 398:109–153, 1999. (page 86)

[199] C. Yoo and H. Im. Characteristic boundary conditions for simulations of compressible reacting flows with multi-dimensional, viscous, and reaction effects. *Combust. Theory and Modelling* , 11:259–286, 2007. (page 53)

[200] C. Yoo, Y. Wang, A. Trouvé, and H. Im. Characteristic boundary conditions for direct simulations of turbulent counterflow flames. *Combust. Theory and Modelling* , 9:617–646, 2005. (page 53, 91)